Conference Proceedings

The 5th Conference on MicroFluidic Handling Systems

21-23 February 2024

Munich
Germany

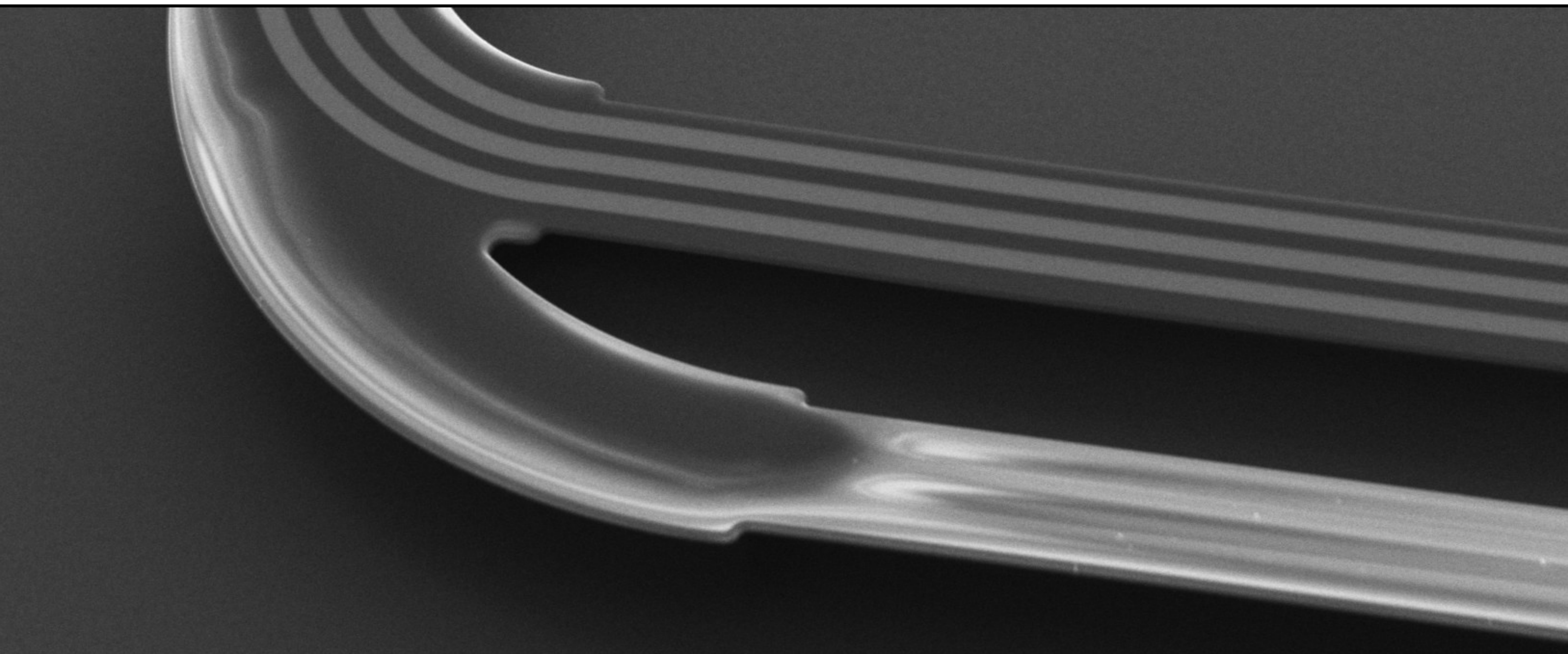

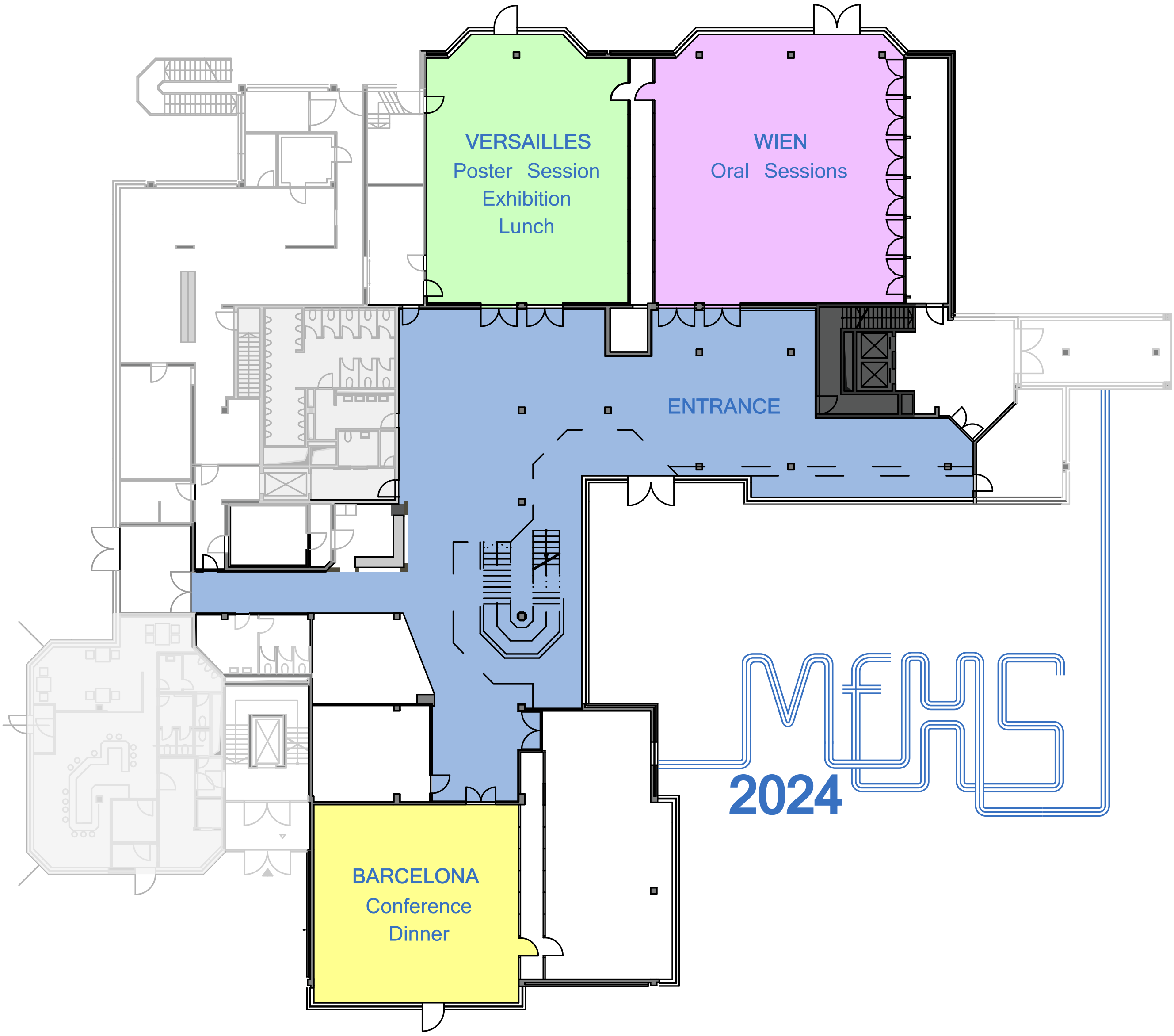

Conference: The 5th Conference on MicroFluidic Handling Systems (MFHS 2024).
Dates: 21-23 February 2024.
Chairs: Joost Lötters and Martin Richter.
Technical program committee: Dennis Alveringh, Roland Zengerle, Sabrina Kartmann, Klaus Drese, Mathieu Odijk, Urs Staufer, Loes Segerink, Karin Bauer, Gabriele Schrag, Agnes Bussmann, and Remco Wiegerink.
Sponsors: Hahn-Schickard, NWO, Kloé, Innovative Sensor Technology, Truedyne, Fraunhofer EMFT, Bronkhorst High-Tech, University of Twente, MESA$^+$, PI Ceramic, BioFluidiX, KLA, MDPI Micromachines, and Krohne.
Location: smartvillage Bogenhausen, Rosenkavalierplatz 13, 81925 Munich, Germany.
Organisation: Agnes Bussmann, Remco Wiegerink, Shirin Azadi Kenari, Maarten Bonnema, Elisa Göbel, and Marthe Kampman.
Proceedings: Dennis Alveringh and Maarten Bonnema.

Welcome to the 5th International Conference on MicroFluidic Handling Systems

From 21 to 23 February 2024, the 5th International Conference on Microfluidic Handling Systems (MFHS 2024) will be held in Munich, in the smartvillage Bogenhausen, as a follow-up to the successful first four conferences in Enschede in 2012, 2017 and 2019, and in Freiburg in 2014.

Worldwide, accurate handling — i.e. analysis, dosage, measurement and control — of small and extremely small flows of both gases and liquids is becoming more and more important, driven by numerous applications. Examples of economically and societally relevant applications are e.g. medical multi-infusion systems, respiratory systems for patients with lung diseases, equipment for high-pressure liquid chromatography (HPLC) and mass-spectrometry (MS), flow and pressure control in organ-on-a-chip systems, research on catalysts, energy content measurement in (mixtures of) fuel gases including biogas and hydrogen, dosage systems for accurately dosing additives like e.g. vitamins to food and beverages, production of specialty baby food with high nutritional value, production of vaccines and pharmaceuticals by means of flow chemistry and fermentation, and production of solar cell panels with CVD and ALD processes.

Whether in analytical instrumentation, flow chemistry, energy, semiconductor industry, food and beverage or life sciences – microfluidic handling systems are facing several major trends: (1) a need for accurate measurement and calibration facilities; (2) a need for complete functional systems rather than for the individual components; (3) commercialisation of academic research results; (4) standardisation of fabrication technology & materials, modules & connections, and quality assurance & test equipment; (5) cross-overs between technologies, e.g. microfluidics and electronics, and microfluidics and robotics, and last but not least (6) the rise of machine-learning enhanced fluidic systems.

In the future, the impact of this field of research may become even bigger and potentially large target markets may arise, especially when spin-off companies start manufacturing and selling their products, systems or pilot plants.

The focus of this conference is mainly on the technology, components, devices and systems that enable the application in microfluidic systems. We invite submission of papers on systems and devices for accurate handling (e.g. dosing, measurement, analysis and control) of (extremely) small flows of both gases and liquids, and corresponding measurement and control principles, including cross-over technologies with e.g. electronics and robotics, and machine learning enhanced fluidic systems. The most recent academic and industrial developments in the field of microfluidic actuators, sensors, fluidic systems, machine learning, and applications will be presented in five oral sessions and a poster session.

We are looking forward to seeing you at the MFHS 2024 conference!

Prof. dr. Joost Lötters	Dr. Martin Richter
Conference Co-chair	Conference Co-chair

Sponsors

Platinum

Hahn Schickard

NWO

Gold

KLOÉ

iST Innovative Sensor Technology
physical. chemical. biological.

truedyne

Fraunhofer
EMFT

Bronkhorst®
Flow Technology

UNIVERSITY OF TWENTE.

PI

BioFluidiX
a HAMILTON Company

KLA
INSTRUMENTS

Silver

micromachines
an open access journal by MDPI

KROHNE

UNIVERSITY OF TWENTE. | MESA+ INSTITUTE

Conference committee

Chairs

Prof. dr. ir. Joost Lötters
Integrated Devices and Systems Group, University of Twente, Enschede, the Netherlands
Bronkhorst High-Tech BV, Ruurlo, the Netherlands

Dr. Martin Richter
Fraunhofer Institute for Electronic Microsystems and Solid State Technologies EMFT
Munich, Germany

Technical program committee

Prof. dr. Roland Zengerle
Institut für Mikrosystemtechnik (IMTEK), Albert-Ludwigs-Universität
Freiburg, Germany

Dr. ir. Dennis Alveringh
Integrated Devices and Systems Group, University of Twente
Enschede, the Netherlands

Dr. Sabrina Kartmann
Hahn-Schickard Institute for Microanalysis System
Stuttgart, Germany

Prof. dr. Klaus Drese
Coburg University of Applied Sciences and Arts
Coburg, Germany

Prof. dr. ir. Mathieu Odijk
BIOS Lab-on-Chip Group, University of Twente
Enschede, the Netherlands

Prof. dr. Urs Staufer
Micro and Nano Engineering Laboratory, Technical University of Delft
Delft, The Netherlands

Prof. dr. ir. Loes Segerink
BIOS Lab-on-Chip group, University of Twente
Enschede, The Netherlands

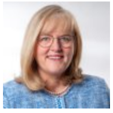

Dr. Karin Bauer
Fraunhofer Institute for Electronic Microsystems and Solid State Technologies EMFT
Munich, Germany

Prof. dr. Gabriele Schrag
Technical University of Munich
Munich, Germany

Dr. Agnes Bussmann
Fraunhofer Institute for Electronic Microsystems and Solid State Technologies EMFT
Munich, Germany

Dr. ir. Remco Wiegerink
Integrated Devices and Systems Group, University of Twente
Enschede, the Netherlands

Program

Wednesday, 21st of February

17:00 – 19:00	Registration & welcome reception	Versailles

Thursday, 22nd of February

8:00 – 8:45	Registration	Versailles
8:45 – 9:00	Opening & announcements	Wien
9:00 – 9:30	Invited talk 1: “Postoperative pain control system: COOPDECH AmyPCA, based on the technology of piezoelectric-actuated metal micropump”	Wien
9:30 – 10:50	Session 1: Actuators	Wien
10:50 – 11:20	Coffee break & exhibition	Versailles
11:20 – 12:40	Session 2: Sensors	Wien
12:40 – 13:40	Lunch & exhibition	Versailles
13:40 – 14:10	Invited talk 2: “Perspectives for fully-electric organs-on-chip”	Wien
14:10 – 15:30	Session 3: Fluidic systems	Wien
15:30 – 16:00	Coffee break & exhibition	Versailles
16:00 – 17:45	Poster session & exhibition	Wien
18:00 – 21:00	Conference dinner	Barcelona

Friday, 23rd of February

8:00 – 8:45	Registration	Versailles
8:45 – 9:00	Opening & announcements	Wien
9:00 – 9:30	Invited talk 3: “Unlocking the potential of machine learning and small data in microfluidics”	Wien
9:30 – 10:30	Session 4: Machine learning	Wien
10:30 – 11:00	Coffee break & exhibition	Versailles
11:00 – 11:30	Invited talk 4: “Microfluidics ballistics and its commercialization potential for biomedical and chemical engineering”	Wien
11:30 – 12:30	Session 5: Applications	Wien
12:30 – 13:00	Closing session & awards ceremony	Wien
13:00 – 14:00	Lunch & exhibition	Versailles
14:30 – 16:00	Optional lab tour	Fraunhofer EMFT

Session 1: Actuators

Thursday, 22nd of February, 9:30 – 10:50
Chairs: Martin Richter & Roland Zengerle

9:30 – 9:50	**Fully integrated micropump and mass flow sensor based on a standard MEMS technology platform** M. Seidl, G. Schrag	15
9:50 – 10:10	**Flow ripple reduction in reciprocating micropumps – an electrical circuit simulation study** Z. Wang, J. C. Lötters, M. K. Ghatkesar	19
10:10 – 10:30	**Investigation of metal jet printing for homogeneous lines with starjet technology** D. Straubinger, Z. Khan, P. Koltay, R. Zengerle, S. Kartmann, Z. Shu	21
10:30 – 10:50	**Highly parallel droplet dispensing approach to fabricate homogeneous, functional layers for diagnostic test manufacturing** O. Rajabnia, A. Ernst, N. Lass, L. Riegger	25

Session 2: Sensors

Thursday, 22nd of February, 11:20 – 12:40
Chairs: Joost Lötters & Klaus Drese

11:20 – 11:40	**Non-invasive ultrasonic flow measurement method for the detection of flow rates in the microliter range** A. Backer, P. Arneth, P. Linke, K. S. Drese	29
11:40 – 12:00	**Thermal flow sensor with liquid characterisation feature by combining 3omega method and constant temperature anemometry** C. J. Hepp, K. Gajo, R. E. Bernhardsgrütter, K. Schmitt, J. Wöllenstein	33
12:00 – 12:20	**Velocity-independent thermal conductivity and volumetric heat capacity measurement of binary gas mixtures** S. Azadi Kenari, R. J. Wiegerink, R. G. P. Sanders, J. C. Lötters	37
12:20 – 12:40	**Particle detection in free falling nanoliter droplets** F. Sturm, V. Zieger, P. Koltay, D. Frejek, S. Kartmann	41

Session 3: Fluidic systems

Thursday, 22nd of February, 14:10 – 15:30
Chairs: Mathieu Odijk & Urs Staufer

Session 4: Machine learning

Friday, 23rd of February, 9:30 – 10:30
Chairs: Dennis Alveringh & Sabrina Kartmann

Session 5: Applications

Friday, 23rd of February, 11:30 – 12:30
Chairs: Loes Segerink & Karin Bauer

Poster session

Thursday, 22nd of February, 16:00 – 17:45

Actuators

Sensors

Fluidic Systems

Machine learning

Applications

Invited talks

Invited talk 1, Thursday 22 February 09:00 – 09:30

Dr. Yamada Keiichi
CEO Daiken Medical Co. Ltd.
Postoperative pain control system: COOPDECH AmyPCA, based on the technology of piezoelectric-actuated metal micropump.

Abstract - In 2021 in Japan, we launched an innovative micro-dosing system of medicine for postoperative pain control, that is COOPDECH AmyPCA. AmyPCA is very compact and user-friendly-designed dosing/patient-controlled analgesia (PCA) system operated with a smartphone. This compact dosing system has been accepted for postoperative pain control due to its higher portability and smart operation system to improve "Quality-of-Life" of patients as well as good pain management. We have widely supplied AmyPCA in the Japanese market for 2021 so far, now we are promoting the product to spread in the European market. Such an innovative dosing system has been achieved by piezoelectric-actuated metal micropump based on metal MEMS and diffusion bonding technology under the research collaboration with Fraunhofer EMFT, which enables robust and compact pump with low manufacturing cost. And this micropump is a diaphragm pump that has a chamber of nanoliter volume, and it makes constant flowrate by periodic push/pull stroke of its diaphragm actuated by piezoelectrically generated force. Then, the metal micropump makes it possible to precisely control the flowrate of drug administration at nanoliter level. Hence, these key features of compact and precise dosing by the micropump have the wide range of possibility for medical dosing applications, and we are going to next challenges on the state-of-the-arts dosing system, such as proximal dosing system during the medical operation and insulin patch pump for home healthcare field. In this talk, I introduce key features of metal micropump succeeded as micro-dosing system of AmyPCA, and show you our next challenges of new micro-dosing systems.

Invited talk 2, Thursday 22 February 13:40 – 14:10

Dr. Massimo Mastrangeli
Delft University of Technology
Perspectives for fully-electric organs-on-chip.

Abstract - Organ-on-chip (OoC) technology is rapidly being established as a valid approach to develop in-vitro models of human (patho)physiology of unprecedented relevance. Advances in the technology involve co-development of the biological substrates and the design of supporting hardware enabling microfluidic perfusion, actuation and sensing. In this lecture, I will present the state of the art in OoC platforms, and introduce the perspective of fully-electric OoCs meant to foster ease of use, adoption and reproducibility of the technology. I will argue that virtually all relevant functions in OoCs can be driven and controlled electrically, and exemplify that this is best achieved by a seamless integration of electric and fluidic layers in the architecture of the platforms.

Invited talk 3, Friday 23 February 09:00 – 09:30

Dr. Daniela Blanco
CEO and co-founder Sunthetics
Unlocking the potential of machine learning and small data in microfluidics.

Abstract - Improving the performance and understanding of complex fluidic systems is a focal point for researchers in industry and academia. Machine learning (ML) stands out as a promising solution, offering unparalleled opportunities to propel knowledge generation and accelerate optimizations in microfluidics. From refining process optimization and predictive modeling, to device design optimization, automated experimentation, and advanced data analysis, ML is reshaping the landscape of microfluidic research. Despite the evident advantages of ML in microfluidics, its implementation has faced challenges, particularly with the limited performance of predictive algorithms operating on small datasets. Additionally, the absence of user-friendly interfaces has posed barriers for scientists across disciplines. SunthetiscML introduces an enhanced Bayesian optimization (BO) approach, enabling a chemistry-agnostic pathway for designing and implementing intelligent experimental campaigns. SunthetiscML is an accessible online ML platform tailored for researchers without coding or ML expertise. Moreover, scientists can upload data from as few as 5 experiments and instantly leverage ML-distilled insights for enhanced reaction understanding and smart experimental campaigns. The approach demonstrates compelling returns on material and experimental efficiency, enabling up to 32x faster R&D and optimizations, as well as 9-12% increase in previously-optimized systems. Recognizing the limitations and opportunities of ML as a catalyst for innovation is key as the field moves towards the integration of ML into microfluidic research. Technologies that provide easy access and effective ML analysis will play a pivotal role advancing microfluidics into an era of accelerated and intelligent R&D with deeper understanding of fluidic behaviors at the microscale.

Invited talk 4, Friday 23 February 11:00 – 11:30

Prof. dr. David Fernandez Rivas
Mesoscale Chemical Systems, University of Twente
Microfluidics ballistics and its commercialization potential for biomedical and chemical engineering.

Abstract - How can chemistry, process intensification, applied physics and engineering contribute to reducing painful needle-based injections? I will share salient moments on an ongoing quest to develop a needle-free injection technology, using lasers and microfluidics [1].

In the BuBble Gun project (https://bubble-gun.eu) we make high speed microjets with thermocavitation: laser-driven evaporation of the liquid inside a microchannel, creates rapidly expanding bubbles that generate jets through flow focusing.

We have studied the impact and traversing of such jets on pendant liquid droplets, and other skin surrogate materials [2-3]. The jets can reach velocities in the order of 100 m/s, with diameters ranging from 50-120 µm. We have used controlling techniques such as additives modifying liquid properties, and demonstrated that changing the wetting properties of the microchannels gives a better control over jetting phenomena. The combination of microchannel geometry and coating on its inner surfaces influences the jet breakup, the resulting drop size distribution, the trajectory of the jet tip, and the consistency of jet characteristics across trials [4].

A typical thermocavitation-induced injection takes less than 1 ms, and it can be repeated for delivering with precise control over volumes (pL to mL) and penetration depths (mm to mm). Our results increase the knowledge of the jet interaction with materials of well-known physical properties, and it is being applied to better control injections in real tissue, e.g., skin.

Lastly, I am excited to present progress in the commercialization of BuBble Gun's technology via the academic start-up FlowBeams, based on the novel framework 'Knowledge, Persuasiveness and Empathy' [5].

[1] Schoppink J, Rivas DF. Jet injectors: Perspectives for small volume delivery with lasers. Advanced drug delivery reviews. 2022 Mar 1;182:114109.

[2] Quetzeri-Santiago MA, Rivas DF. Cavity dynamics after the injection of a microfluidic jet onto capillary bridges. Soft matter. 2023;19(2):245-57.

[3] van der Ven DL, Morrone D, Quetzeri-Santiago MA, Rivas DF. Microfluidic jet impact: Spreading, splashing, soft substrate deformation and injection. Journal of colloid and interface science. 2023 Apr 15;636:549-58.

[4] Schoppink JJ, Mohan K, Quetzeri-Santiago MA, McKinley G, Rivas DF, Dickerson AK. Cavitation-induced microjets tuned by channels with alternating wettability patterns. Physics of Fluids. 2023 Mar 1;35(3).

[5] Rivas, D.F. "Empathic Entrepreneurial Engineering." De Gruyter, 2022.

FULLY INTEGRATED MICROPUMP AND MASS FLOW SENSOR BASED ON A STANDARD MEMS TECHNOLOGY PLATFORM

Martin Seidl and Gabriele Schrag
Technical University of Munich, Chair of Physics of Electrotechnology, Munich, Germany

ABSTRACT

We present a micropump concept and an associated miniaturized mass flow sensor design, which in combination have the potential to form the basis for an integrated microfluidic development platform. Both devices exhibit a very small footprint and can, in principle, be combined in a single, joint manufacturing process, to form very compact, fully integrated micro-dosing systems. The devices can be manufactured using standard MEMS technology based on a modified silicon microphone process.

KEYWORDS

MEMS, microfluidics, micropump, mass flow sensor, anemometry, electrostatic actuation, electrostatic pull-in, microdosing, integrated.

INTRODUCTION

Silicon technology has enabled major advances in the miniaturization of microsystems. While sensor technology for mobile devices is already in widespread use, miniaturized microfluidic components that meet the requirements for integration into mobile devices or other compact systems are rare, despite the advances in the field of actuator technology. However, increasing packaging and functional density as well as shorter product cycles are continuously tightening the requirements for miniaturized sensors and actuators.

Recent developments regarding micropumps focus mainly on reliability and miniaturization. However, conventional concepts seem to hit a downsizing limit at edge lengths above 3 mm. [1,2]

FULLY INTEGRATED MICROPUMP

The concept [3] of the miniaturized membrane pump (see Fig. 1) consists of a central, bi-directionally electrostatically driven cylindrical pump chamber and a surrounding valve area. The pump membrane is suspended from radial support structures around its circumference, between which fluid channels connect the pump chamber with the valve area. An elevation in the centre of the pump chamber base reduces the actuation voltage required for the pump membrane without significantly reducing the available stroke volume. This design feature also contributes to the fact that the pump membrane first comes into contact with the lower counter electrode in the centre and then rolls off towards the corners, facilitating the complete expulsion of the fluid from the pump chamber.

The design is tailored to a low flow resistance inside the device in order to achieve high flow rate. To reduce the flow resistance, two primary solutions are pursued.

Firstly, actively controlled valves are used. The valve membrane is driven by electrostatic actuation in the same way as the pump membrane. However, both can be moved independently from each other using separate actuation signals. In contrast to passive valves, these active valves do not have to be opened by the positive or negative pressure from the pump chamber, which reduces the usual problems caused by dead volume and reduces the maximum required drive force of the pump membrane.

Secondly, the largest possible flow cross-sections are provided at the points with the highest volume flow. This is achieved, for example, by arranging the valve in a ring around the central, cylindrical pump chamber. On the one hand, this maximises the flow cross-section in the channels between the pump chamber and the valve area, but on the other hand, it also allows the largest possible intake and outlet cross-sections.

The chip plane itself separates the intake and outlet, which facilitates integration into compact microfluidic systems.

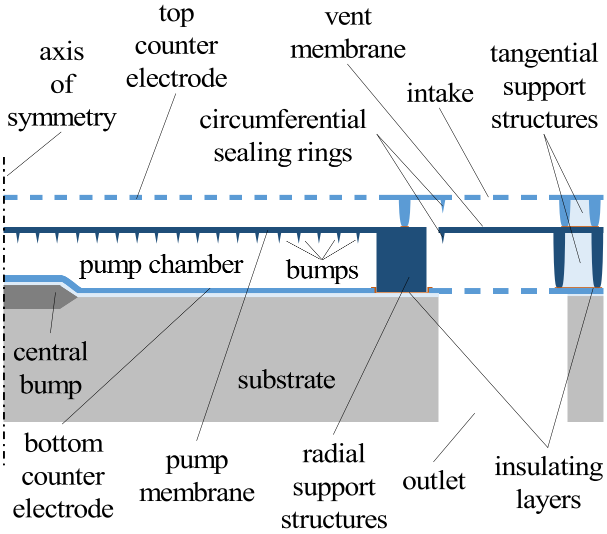

Figure 1: Design of the micropump: A half-cut through the device is shown, with the axis of rotational symmetry at the left side.

The working principle is shown in Fig. 2. Starting from the condition depicted in the upper right corner, the valve membrane is actuated in the direction of the top counter electrode and closes the intake of the micropump. In the next step, the pump membrane is pulled towards the bottom counter electrode, causing the fluid to be expelled through the open outlet. As soon as this process is complete, the valve membrane is actuated in the direction of the bottom counter electrode, closing the outlet and connecting the pump chamber to the intake. As the pump diaphragm is released, the pump chamber is filled with liquid from the top of the micropump chip. Then the cycle repeats.

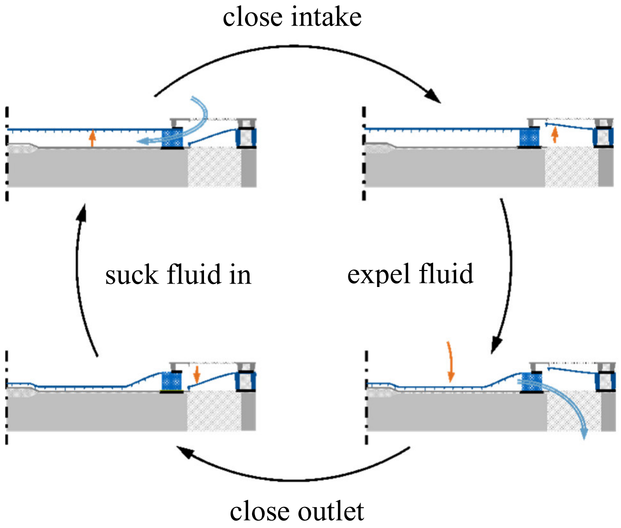

Figure 2: Working principle of micropump: each stage of the pumping cycle is depicted.

Taking into account the results of previous tests and FEM simulations [4], new micropump prototypes with a chip edge length of 1.86 mm (see Fig. 3) are developed and produced.

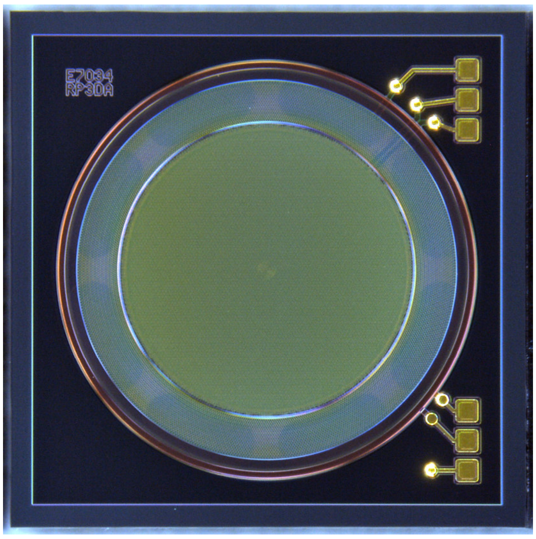

Figure 3: Microscope image of a prototype micropump chip. The chip dimensions are 1.86 mm x 1.86 mm x 0.3 mm.

Figure 4: Measurement setup: Polytech MSA-500 laser-doppler vibrometer with purpose built test jig for prototypes and Bronkhorst EL-Flow Prestige mass flow meter.

The prototypes are glued and bonded to printed circuit boards and fitted with protective covers, which have a central port that doubles as fluid intake and opening for the optical measurements. The assembled printed circuit boards are clamped in a purpose built test fixture and placed on a mechanical stage under microscope optics of the Polytech MSA 500 laser Doppler vibrometer for characterisation. A Bronkhorst EL-Flow Prestige mass flow sensor is used to measure the flow rate. (see Fig. 4).

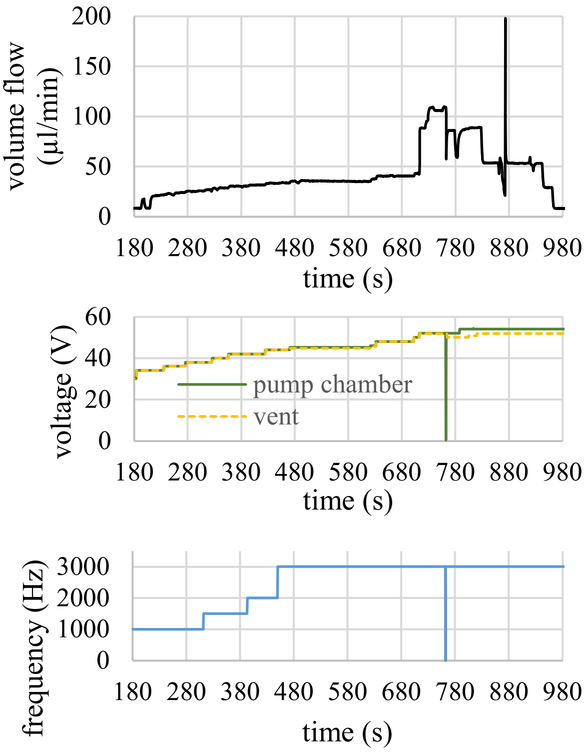

Figure 5: Measured volume flow: A flow rate of 110 µl/min (air) is achieved for this design.

Fully coupled FEM simulations [5] are used to determine optimised parameter sets for the control signals. Fig. 5 shows the measurement result of a test run in which a maximum volume flow of 110 µl/min was achieved by further adjusting the control signals in terms of control voltage, operating frequency, phase offset between pump and valve diaphragm and the duty cycle of the pump and valve control signals.

MEMS-BASED MASS FLOW SENSOR

The mass flow sensor combines the principle of hot-wire anemometry with the miniaturisation made possible by applying semiconductor manufacturing processes. As with the micropump, the manufacturing process used for the mass flow sensor chips is based on a standard MEMS process as well.

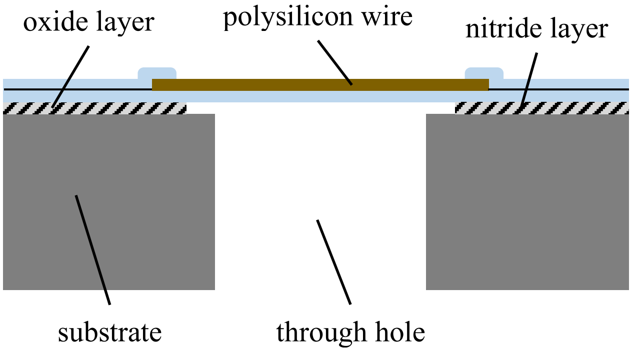

Figure 6: Design of the mass flow sensor.

The main innovation of the design [3] is that the measured flow passes perpendicularly through the chip (see Fig. 6), which is enabled by etching a through hole applying DRIE (Deep Reactive Ion Etching). This way, the centre of the heated wire, which exhibits a tapered shape to improve its robustness, is placed at the centre of the mass flow to be measured. In addition, the constriction of the hot wires ensures increased electrical resistance in the centre, at their thinnest point. Most of the conversion of electrical energy into heat therefore takes place at the centre of the flow channel, where the highest flow velocities are expected. Both factors enhance the sensitivity of the mass flow meters.

In addition to the highly localised heat generation in the centre of the heat wires, the heat wires are very efficiently thermally decoupled from the substrate due to the very small contact surfaces of the heat wires to the chip and the additional insulation layers, making the system less prone to external disturbances.

Different variants with one wire (see Fig. 7) as well as several wires connected to a Wheatstone bridge (see Fig. 8) are realized on chips with an edge length of 1.4 mm.

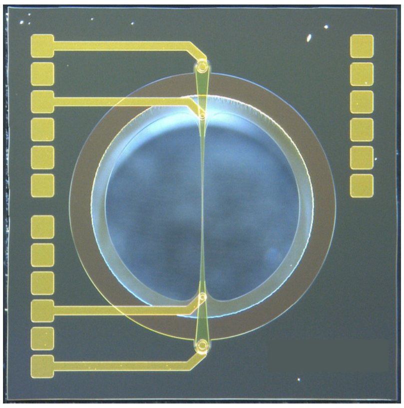

Figure 7: Microscope images of a silicon-based hot-wire anemometer chip. Standard design with single wire configuration and force/sense contact pairs.

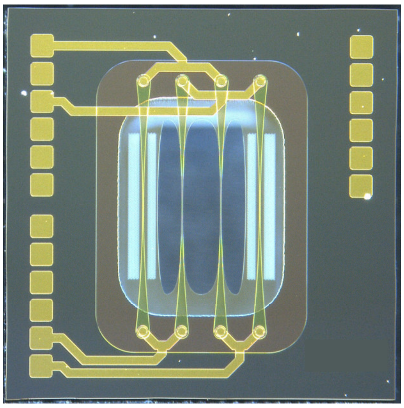

Figure 8: Microscope images of a silicon-based hot-wire anemometer chip. Improved design with a fully integrated Wheatstone bridge.

The characterisation setup for the mass flow meter prototypes consists of a specially manufactured syringe pump, a reference sensor (Bronkhorst EL-FLOW® Prestige series) which is connected in series between the syringe pump and the prototypes to be tested, a constant current source to supply the prototype sensors and a desktop multimeter to measure the sensor voltage.

Characterisation of the different prototypes clearly shows that the best variant is one of the variants with an integrated measuring bridge (see Fig. 8). This sensor prototype exhibits a detection threshold of about 10 µl/min and a measuring range up to at least 20 ml/min, without any dedicated evaluation electronics.

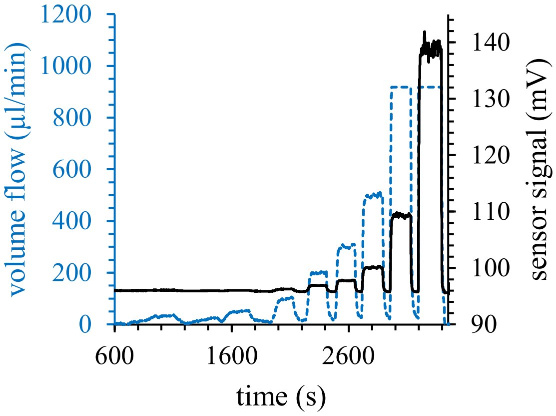

Figure 9: Exemplary measurement of an integrated Wheatstone bridge variant compared to a reference sensor (Bronkhorst EL-FLOW® Prestige series). For high flow rates the reference sensor saturates.

Fig. 9 shows an exemplary measurement in which it can be clearly seen that the reference sensor is already clipping the signal while the prototype is still able to measure. The last two applied volume flows are 1600 µl/min and 2400 µl/min respectively.

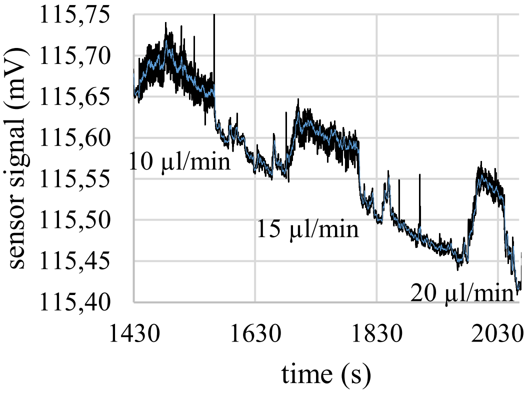

Figure 10: Exemplary result of an integrated Wheatstone bridge variant of the anemometer demonstrating its capability to measure very low flow rates in the range of 10 µl/min to 20 µl/min.

Fig. 10 shows the behaviour of the sensor close to its detection limit. This is a very promising result; however, issues like drift and non-linearities, have to be addressed in future work.

CONCLUSION

The presented micropump and flow sensor designs are very compact compared to the state of the art, fully integrated, and manufacturable within the same process platform. Since pump and sense direction are the same (perpendicular to the chip) the anemometers can be easily integrated into the counter-electrodes of the micropumps and, e.g., clamped over the outlet. This way a fully integrated microdosing system can be realized, which can be easily combined with other silicon-based (electronic) components.

At a size of only 1.86 mm x 1.86 mm x 0.3 mm, the micropumps are capable of pumping gaseous media at flow rates of up to 110 µl/min when applying an optimized parameter set for the actuation signal.

The miniaturised mass flow sensors (1.4 mm x1.4 mm x 0.4 mm) are able to detect liquid flows of around 10 µl/min up to 20 ml/min. The drift and non-linearities still have to be compensated for by a dedicated, application-specific integrated circuit. However, well-known methods already exist for this purpose.

REFERENCES

[1] Bhuiyan, N.H., Hong, J.H., Uddin, M.J. & Shim, J.S., Artificial Intelligence-Controlled Microfluidic Device for Fluid Automation and Bubble Removal of Immunoassay Operated by a Smartphone. Analytical Chemistry, 94(9), 2022, pp. 3872-3880.

[2] Richter, M., Leistner, H., Congar, Y., Drost, A., Kibler, S., Röhl, S., & Wackerle, M. Piezoelectrically driven silicon micropump of the size 3.5 x 3.5 x 0.6 mm3. MST Kongress, Proceedings, 2019, pp. 382-385.

[3] Seidl, M. Integrated Silicon-Based Miniaturized Pumps and Flow Sensors for Mobile Microfluidic Systems, Doctoral dissertation, Technical University of Munich, 2023, https://nbn-resolving.de/urn/resolver.pl?urn:nbn:de:bvb:91-diss-20231103-1713917-1-1

[4] Seidl, M., Schrag, G., Klein, W., Vobl, M. & Krumbein, U. Design of a Micropump Based on an Industrial Microphone Manufacturing Process, DTIP, 2019, pp. 1-4, doi: 10.1109/DTIP.2019.8752688.

[5] Hölzl, W., Seidl, M. & Schrag, G. Fully-Coupled Transient Modelling of Highly Miniaturized Electrostatic Pull-In Driven Micropumps, EuroSimE, 2023, pp. 1-11, doi: 10.1109/EuroSimE56861.2023.10100814

CONTACT

* mart.seidl@tum.de

FLOW RIPPLE REDUCTION IN RECIPROCATING MICROPUMPS – AN ELECTRICAL CIRCUIT SIMULATION STUDY

Z. Wang[1], *J.C. Lötters*[1,2] *and M.K. Ghatkesar*[1]
[1] Delft University of Technology, Department of Precision and Microsystems Engineering, Delft, The Netherlands
[2] Bronkhorst High-Tech BV, Ruurlo, The Netherlands

Reciprocating micropumps are miniaturized pumps delivering fluid by reciprocating mechanical movement which are widely developed for engineering and biomedical applications. However, undesired ripple may occur in the flowrate when actuating these micropumps in a low frequency range (<10 Hz) due to the reciprocating mechanism [1]. One effective method to reduce the flow ripple is multi-phase rectification [2]. In this abstract, a study on actuation strategies for multi-phase rectification is introduced by building an equivalent electrical circuit to rapidly model the fluidic system.

A diaphragm micropump is used in this model. For a single actuator/chamber configuration, there are two modes during one cycle of reciprocation as shown in Fig. 1(a) and (b). With check valves on both sides, the micropump first collects fluid from the inlet into a chamber and then pushes it out through the outlet, generating a ripple flow when continuously actuated. It is possible to reduce the ripple by increasing the actuation frequency (>100 Hz). However, this method has two main limitations, namely, higher power consumption and reduced backpressure. One of the methods to enable steady flow delivery at low frequencies of actuation is multi-phase rectification. Equally divided phase shift in actuation is applied to parallel reciprocating micropumps. All flowrates compensate for each other to deliver a steadier flow through the system. To describe the flow ripple scale, the fluidic ripple factor is introduced [2]:

$$RF_{fl} = \sqrt{\left(\frac{Q_{rms}}{Q_{mean}}\right)^2 - 1} \qquad (1)$$

in which Q_{rms} and Q_{mean} are root-mean-square value and mean valve of flowrate signal, respectively.

In this work, different parts of a microfluidic system are modeled as electrical components and their connection also follows the electrical analogy [3,4]. As shown in Table 1, the micropump chamber, check valve, hydraulic resistance and fluid inertia are represented by electrical capacitance, diode, resistance and inductance, respectively. The pressure applied by the diaphragm is modeled as a voltage applied on the capacitor and the flowrate at outlet is modeled as a current through the inductor. A multi-phase rectification system is shown in Fig. 1(c) and a four-phase rectification model is shown in Fig. 2. In this model, the parameters valve resistance, tubing resistance and capacitance are neglected as their contribution is negligible. The electrical circuit is simulated by NI Multisim.

Fig. 3 shows flowrate signals of one to four phase rectifications at 1 Hz actuation. For a single pump, a clear pulsation behavior can be observed. The phase difference is generated because of the differential effect on the capacitor (diaphragm). When pressure decreases, a small amount of leakage is observed, which represents a threshold pressure below which the check valves do not completely close. For three-phase rectification, the fluidic ripple is greatly reduced. The results match with the experimental results reported [2].

The frequency dependence study of average flowrate and fluidic ripple factor are shown in Fig. 4 and 5. In the lower frequency range (<10 Hz), the flowrate is proportional to frequency and the ripple factor is close to the theoretical value. This demonstrates the feasibility and effectivity of multi-phase rectification in micropump ripple reduction. At higher frequencies (>100 Hz), an extremely low ripple factor can be achieved without reduction in the average flowrate. This shows the potential of multi-phase rectification in extremely stable low flowrate delivery while keeping high backpressure.

In conclusion, an electrical circuit simulation for multi-phase rectification of parallel reciprocating micropumps is introduced. The results obtained match with the experimental results obtained validating the electrical model shown here. The flow ripple reduces to >90% for a three-phase rectification.

Table 1. Parameters used in the equivalent electrical circuit and their corresponding fluidic parameters.

Electrical Component	Fluidic Component	Value
Voltage V (V)	Pressure P (Pa)	400 V_{pp} $sine$
Current I (A)	Flowrate Q (m^3/s)	-
Capacitor C (F)	Hydraulic Capacitance (m^3/Pa)	9.1×10^{-14}
Resistor R (Ω)	Hydrodynamic Resistance R_{load} ($Pa \cdot s/m^3$)	5.5×10^{10}
Inductor L (H)	Fluidic Inertia (Water) L_{load} ($Pa \cdot s^2/m^3$)	4.0×10^{8}
Diode	Check Valve	-

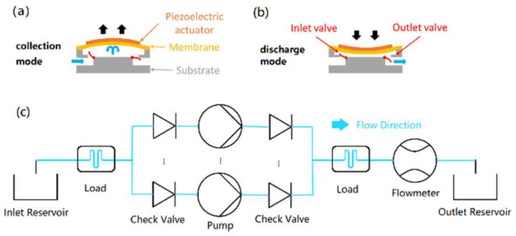

Figure 1: Schematic diagram of micropump and microfluidic system. Piezoelectric diaphragm micropump in liquid (a) collection mode and (b) discharge mode [2] (c) Microfluidic system of multi-phase rectification.

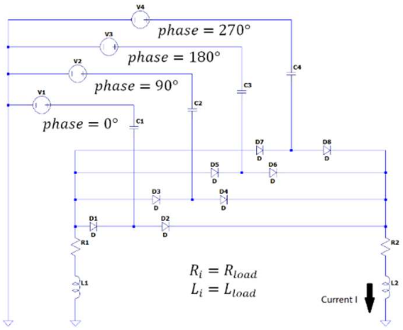

Figure 2. Example of equivalent electrical circuits (four phase rectification).

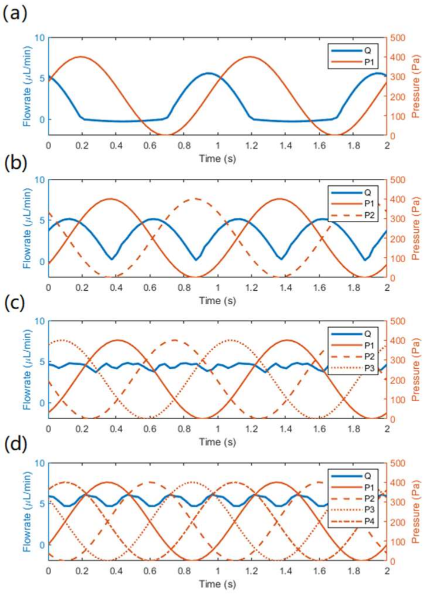

Figure 3. Flowrate and applied pressure (at 1Hz) waveform in multi-phase rectification: (a)one-phase, (b)two-phase, (c)three-phase and (d)four-phase. In the legend, Q is the flowrate and P is the applied pressure in each pump connected in parallel.

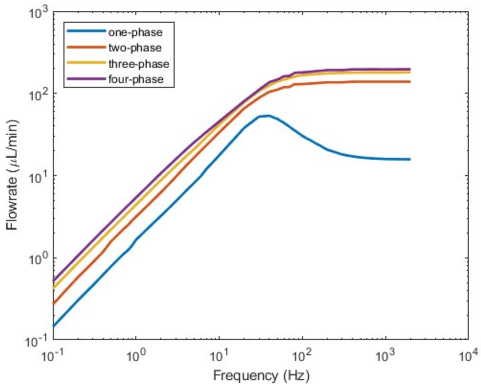

Figure 4. Frequency dependence of the average flowrate in multi-phase rectification.

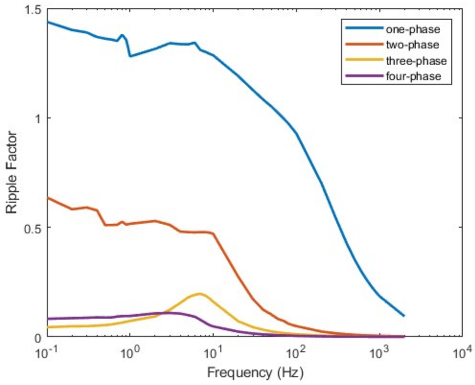

Figure 5. Frequency dependence of the fluidic ripple factor in multi-phase rectification. The cut-off frequency of 10Hz is with the resonance frequency of the micropump chamber diaphragm.

REFERENCES

[1] S. Mohith, P. Navin Karanth, S.M. Kulkarni, “Recent Trends in Mechanical Micropumps and Their Applications: A review.” Mechatronics, pp. 34-55, 2019.

[2] G. Özkayar, Z. Wang, J.C. Lötters, M. Tichem, M.K. Ghatkesar, “Flow Ripple Reduction in Reciprocating Pumps by Multi-Phase Rectification”, Sensors 23, no. 15: 6967, 2023.

[3] T. Bourouina, J.P. Grandchamp, "Modeling Micropumps with Electrical Equivalent Networks." Journal of Micromechanics and Microengineering 6, no. 4, pp. 398, 1996.

[4] K.W. Oh, K. Lee, B. Ahn, E.P. Furlani, "Design of Pressure-driven Microfluidic Networks Using Electric Circuit Analogy." Lab on a Chip 12, no. 3, pp. 515-545, 2012.

INVESTIGATION OF METAL JET PRINTING FOR HOMOGENEOUS LINES WITH STARJET TECHNOLOGY

D. Straubinger[1], *Z. Khan*[1,2], *P. Koltay*[2,3], *R. Zengerle*[1,2], *S. Kartmann*[1,2], *Z. Shu*[1,2]
[1] Hahn-Schickard, Georges-Koehler-Allee 103, 79110 Freiburg, Germany;
[2] Laboratory for MEMS Applications, IMTEK - Department of Microsystems Engineering, University of Freiburg, Georges-Koehler-Allee 103, D-79110 Freiburg, Germany;
[3]Actome GmbH, Georges-Köhler-Allee 103, D-79110 Freiburg.

ABSTRACT

Jet printing of metal lines with high shape fidelity on variable substrates without the need for post-processing is a technology desired in various fields, such as 3D printing flexible and biodegradable electronics or electrodes for solar cells. This paper provides an experimental investigation and a deeper understanding of printing uniform metal lines with the StarJet technology. The jet and its spreading behaviour are analysed on PET sheets. Robust printing parameters are provided to produce uniformly shaped, bulge-free, highly conductive lines suitable for additively manufactured electronic devices.

KEYWORDS

Liquid metal, jet, solder alloy, 3D printing, lines, printed electronics, flexible electronics, StarJet

INTRODUCTION

Flexible electronics is an emerging topic and has significantly advanced in recent years [1]. Wearable sensors enable Industry 4.0 concepts to be implemented in medical applications and smart-care [2, 3]. Manufacturing cost is a crucial factor enabling the widespread adoption of flexible and wearable electronic devices [4]. A process step is the realisation of conductive traces and electrical connections on the different substrates. Inkjet-printing is a frequently used technology for additive manufacturing, but silver-nanoparticle based inks have a high material cost. The need for sintering at elevated temperatures further limits substrate compatibility [5].

The StarJet technology [6] is capable of direct, non-contact printing of conductive metal onto flexible polymer substrates with commercially used solder alloys without the need for post-processing (Fig. 1). However, realizing consistent line width (desired to improve reliability, signal integrity, and resistivity along the interconnect) without spherical bulging (solder spheres formed along the line) is challenging, especially at lower printing speeds [6]. The bulging behaviour is a well-known phenomenon in inkjet-printed structures [7, 8]. Direct printing of molten metal is a novel field. Due to its complex nature (polymer-metal interaction, wetting behaviour, phase change, alloy-specific properties), most paper focus on droplet printing [9-11]. Continuous jet metal printing provides faster printing speed than drop-on-demand mode, eliminates the risk of missing or printing extra droplets, and can be an essential step towards the printability of 3D metal objects.

This paper provides an experimental investigation to achieve a deeper understanding of molten metal jet interaction with a polymer substrate for electrical interaction applications with the StarJet technology.

MATERIALS AND METHODS

The experiments were performed using a 3-axis robotic system (Nordson Asymtek Spectrum II) equipped with a StarJet printhead (Fig. 1.) and employed a low-temperature 57Bi-42Sn-1Ag solder alloy (melting range of 137-139 °C), often used in biodegradable electronics [12]. The StarJet nozzle had an orifice diameter of 44 µm. The printhead was pressure-actuated using actuation and rinse nitrogen gas pressures of 800 mbar and 860 mbar, respectively. The substrate holder was heated with PID control. The substrate temperature was monitored with a K-type thermocouple (±1 °C accuracy).

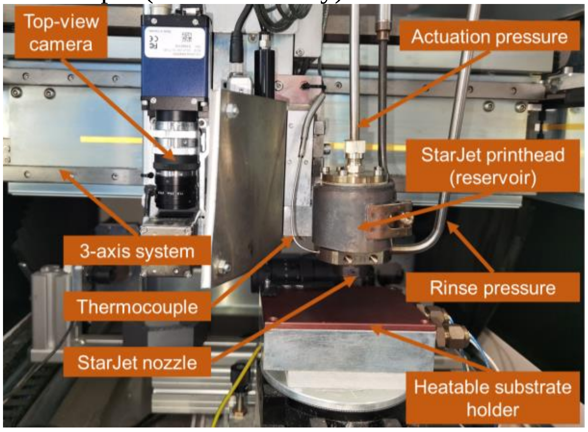

Figure 1: StarJet printhead and its main parts integrated into a 3-axis robotic system with a heatable substrate holder

The tests were performed on 125 µm thick PET sheets characterized by a smooth surface and high transparency. The experimental parameters encompassed the following variables: the movement speed of the printhead (v), which ranged from 35 to 120 mm/s with increments of 5 mm/s; printing distances (d), varying between 6 and 30 mm with 2 mm increments; elevated reservoir temperature (T_{res}, 400 °C) with different printing distances; and substrate temperatures (T_{sub}), ranging from 45 to 110 °C with a step size of 5 °C. A summary of these experimental conditions is presented in Table 1.

Table 1: Investigated test cases

Test case (TC)	v [mm/s]	d [mm]	T_{res} [°C]	T_{sub} [°C]
Printing speed (A)	**35-120**	12	330	20
Printing distance (B)	30	**6-30**	330	20
Reservoir temperature (C)	30	6-20	**400**	20
Substrate temperature (D)	30	20	330	**45-110**

The solder jet and line printing were video-recorded and analysed with Phantom Miro 310 high-speed camera and Canon 5D cameras. The printed structure was measured with a Zeiss Axiophot optical microscope. The printed solder lines were imaged from the underside through the transparent substrate (Fig. 2.). This way, the shadowing effect of the printed traces due to their high aspect ratio is avoided, and the spreading behaviour at the edges is observable.

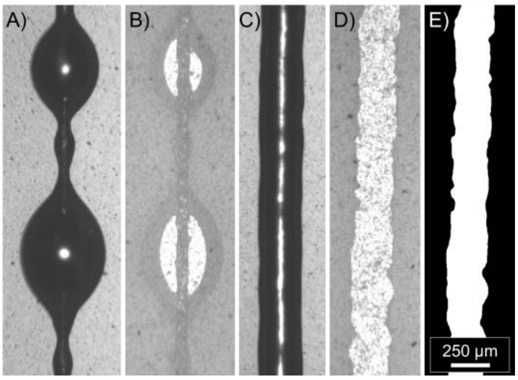

Figure 2: Solder line with bulging (A - top view, B - bottom view), optimized bulge-free line (C - top view, D - bottom view), binary representation of bulge-free line (E)

The investigation aims to establish a process window where bulging is eliminated. A bulge-free nature and consistent width of lines are essential. For further analysis of line fidelity, if no spherical bulging was detected (i.e., Fig. 2. C, D), at least two images were taken for quantitative analysis: one close to the start location of the printing and one close to the end. The images were evaluated using image processing. The printed lines were automatically segmented using machine learning based CVAT [13]. This enables precise segmentation of the printed traces, even on low-contrast images, where conventional approaches (edge detection, thresholding) were not applicable. After segmentation, the images were binarised, and the width of the traces alongside the images was automatically measured.

RESULTS

Solder jet generation

The high framerate video recording reveals the jet dynamics: in many cases, a small volume fraction can be separated from the jet after the printing is started ("head", Fig. 3.).

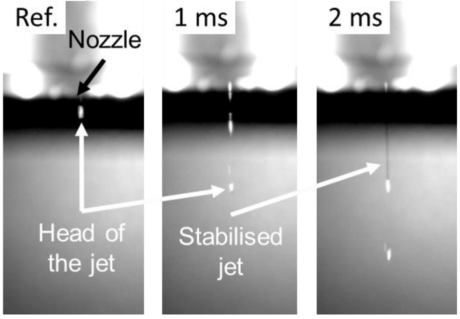

Figure 3: High-framerate recording of jet printing. A nozzle orifice of 60 µm was used for better visibility in jet behaviour (frames are 1 ms apart).

After that, the jet stabilises, and the volumetric flow is assumed to be constant during the printing. In most cases, the head part of the jet is not a concern since it melts with the jet on the substrate. Priming the printhead or masking the structure is a suitable solution to eliminate its potential effects. The stabilised jet shows no disturbance on the high-speed recording and has high directional stability.

Printing speed and spherical bulging (TC-A)

This paper focuses on low-speed printing (i.e., less than 120 mm/s) so that more complex structures can be directly printed. Thinner, bulge-free lines are achievable with high speeds [6], but the required speed is about one order of magnitude higher (i.e., ~900 mm/s), which limits applicability for sudden changes in the printing direction. For Test Case A (TC-A), the printing distance was 12 mm. Results show that increasing the speed up to 4 times (120 mm/s) did not eliminate the formation of bulging (Fig. 4). Only a decrease was observable in the line width between the bulges.

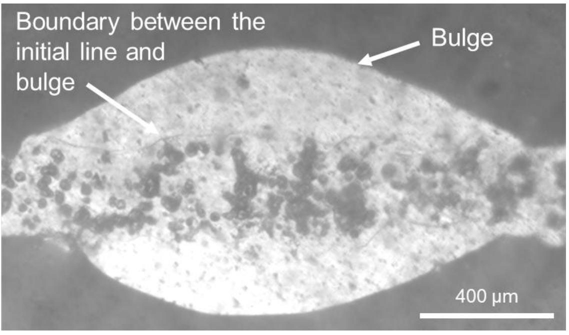

Figure 4: Optical microscope image of the underside of a solder line with noticeable bulging printed onto a PET foil.

Investigation of the underside of the lines with bulging revealed two different types of surfaces with a clear interface between them. The circular black spots are present along the line, while the spherical bulge has a smoother surface. The reason for the spots' formation is still unclear, but it could be attributed to the hot metal creating blisters on the polymer by locally melting it or encapsulating gas under it, which was reported before for metal droplets [14, 15].

It was assumed that the bulging happened at a different time due to its different nature. This assumption was validated with video recordings, where the bulge accumulated after the liquid front had passed the point, but the metal was still in a liquid phase. J. Yang et al. proposed for bulging in the case of inkjet-printed lines, that the bulges are formed due to pre-existing surface defect-induced pressure gradient and internal flow [16]. On the contrary, in the case of StarJet printed lines, the bulging frequency is very different for different printing parameters (on the same substrate). This suggests that the bulging depends not on surface defects but printing parameters (such as initial spreading width and internal pressure).

Printing distance (TC-B)

StarJet printing's non-contact nature allows for structures with a substantial printhead distance (around a couple of times 10 mm). This distance, while enabling printing on uneven surfaces, is unique to StarJet technology. However, closer proximity is beneficial for minimizing heat loss and oxidation (droplet printing is usually performed below a 10 mm distance). Bulging was observed to be eliminated at a printing distance of 16 mm or higher, but variations in width and uniformity persist in printed metal lines (see Fig. 5) for distances ranging from 16 to 30 mm. Only parameters achieving bulge-free lines are illustrated for TC-B, TC-C, and TC-D, as these are the desired outcome.

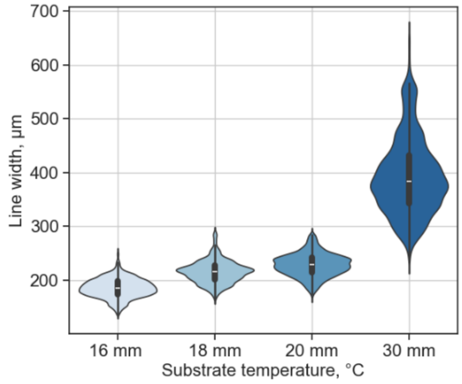

Figure 5: Effect of different printing distances without bulging.

The average line width shows a slight increase under 20 mm (185 µm, 216 µm and 228 µm for 16 mm, 18 mm and 20 mm, respectively). The line width is around five times higher than the orifice diameter. The distance of 30 mm showed a significant increase in average line width (398 µm) and standard deviation (71.4 µm). The increased line width can be attributed to a resulting higher impact velocity of the jet, which changes the nature of the printing towards an impact-driven kinetics from capillary-driven [11]. The higher surface area and time of flight also increase the cooling rate and result in faster solidification.

Reservoir temperature (TC-C)

In this test case, a reservoir temperature of 400 °C was used. The higher initial temperature results in lower viscosity, density and surface tension [17] of the molten solder. In addition, the alloy is in a liquid phase for longer after being jetted from the StarJet reservoir. Due to the low solder volume, no degradation (i.e., warpage) was observed on the PET sheet at a substrate level. The results without bulging can be seen in Fig. 6.

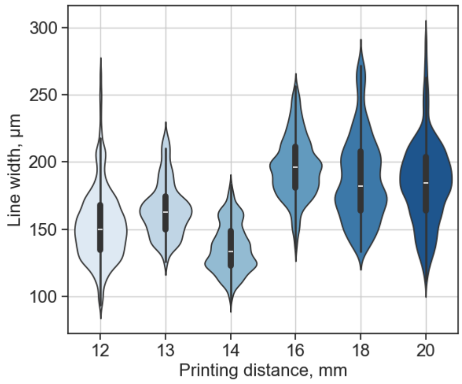

Figure 6: Effect of 400 °C reservoir temperature at different printing distances

The critical printing distance without bulging was reduced to 12 mm from 16 mm. At identical distances, the line width slightly decreased, while the standard deviation slightly increased compared to TC-B. This might be attributed to the higher retraction of the line because of the longer time in a molten state. The line's underside exhibited many more dark spots, resulting in low-contrast images. This observation suggests potential localized polymer melting induced by the higher-temperature metal.

Substrate temperature (TC-D)

This test case investigates the effect of elevated substrate temperatures (Fig. 7.).

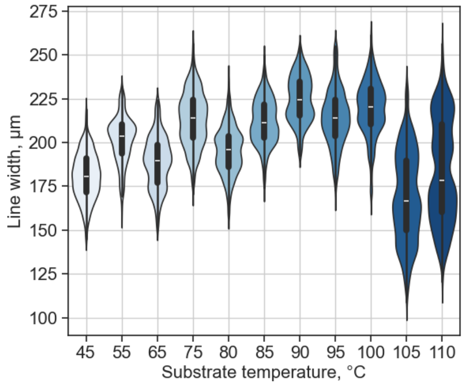

Figure 7: Effect of different substrate temperatures without bulging

No apparent pattern in line width was observed across varying temperatures. Over 100 °C, which is already over the glass transition temperature (T_g) of the PET sheet, the standard deviation was increased. The shape non-uniformity (standard deviation) is also slightly increased.

CONCLUSIONS

This paper establishes a process window for achieving bulge-free metal lines using StarJet jet technology, investigating printing speed and distance, substrate temperature, and reservoir temperature for a chip nozzle opening of 44 µm and a 57Bi-42Sn-1Ag solder alloy. The derived parameters serve as a robust foundation for producing uniform metal lines.

The following key findings are concluded:

- The bulges occur after the passage of the liquid front, indicating a likely association with the internal pressure of the molten metal.
- The printing distance was a critical parameter for bulge formation for the investigated lower printing speeds (<120 mm/s).
- Higher reservoir temperature can extend the process window of bulging-free metal line printing: The critical printing distance can be reduced to 12 mm at a reservoir temperature of 400 °C from 16 mm at 330 °C.
- Maintaining a maximum distance of 20 mm is recommended due to the splashing behaviour (resulting in less uniform and wider lines) of solder at excessive distances.

Future research will assess the process window's applicability to different substrate materials and explore polymer-metal interactions.

REFERENCES

[1] Corzo, D., Tostado-Blázquez, G., & Baran, D. "Flexible electronics: status, challenges and opportunities." *Frontiers in Electronics*, vol. 1, 2020, article 594003

[2] Javaid, M., & Haleem, A. "Industry 4.0 applications in the medical field: A brief review." *Current Medicine Research and Practice*, vol. 9, no. 3, 2019, pp. 102-109

[3] Binyamin, S. S., & Hoque, M. R. "Understanding the drivers of wearable health monitoring technology: an extension of the unified theory of acceptance and use of technology." *Sustainability*, vol. 12, no. 22, 2020, article 9605

[4] Gao, W., Ota, H., Kiriya, D., Takei, K., & Javey, A. "Flexible electronics toward wearable sensing." *Accounts of Chemical Research*, vol. 52, no. 3, 2019, pp. 523-533

[5] Perelaer, J., Schubert, U. S., & Jena, F. "Inkjet printing and alternative sintering of narrow conductive tracks on flexible substrates for plastic electronic applications." *Radio frequency identification fundamentals and applications, design methods and solutions*, 2010, 265-286.

[6] Shu, Z., Gerdes, B., Fechtig, M., Riegger, L., Zengerle, R., & Koltay, P. "Direct printing of conductive metal lines from molten solder jets via StarJet technology on thin flexible polymer substrates." *Proc. NIP Digit. Fabr. Conf.*, vol. 2018, no. 1, 2018, pp. 72-75, doi:10.2352/ISSN.2169-4451.2018.34.72.

[7] Duineveld, P. C. "The stability of inkjet printed lines of liquid with zero receding contact angle on a homogeneous substrate." *Journal of Fluid Mechanics*, vol. 477, 2003, pp. 175-200

[8] Soltman, D., & Subramanian, V. "Inkjet-printed line morphologies and temperature control of the coffee ring effect." *Langmuir*, vol. 24, no. 5, 2008, pp. 2224-2231

[9] Aziz, S. D., & Chandra, S. "Impact, recoil and splashing of molten metal droplets." *International Journal of Heat and Mass Transfer*, vol. 43, no. 16, 2000, pp. 2841-2857.

[10] Wang, C. H., Tsai, H. L., Wu, Y. C., & Hwang, W. S. "Investigation of molten metal droplet deposition and solidification for 3D printing techniques." *Journal of Micromechanics and Microengineering*, vol. 26, no. 9, 2016, article 095012.

[11] Yi, H., Wang, Z., Cao, H., Liu, M., & Li, J. "Metal droplet deposition: from foundation to engineering manufacturing." *Advanced Engineering Materials*, vol. 25, no. 3, 2023, article 2201003.

[12] Géczy, A., et al. "Thermal and RF Characterization of Novel PLA/Flax Based Biodegradable Printed Circuit Boards." *2022 IEEE 24th Electronics Packaging Technology Conference (EPTC)*, 2022, pp. 329-333

[13] *CVAT Open Data Annotation Platform*, www.cvat.ai/. Accessed 12 Jan. 2024.

[14] Xiong, W., & Cheng, P. "Numerical investigation of air entrapment in a molten droplet impacting and solidifying on a cold smooth substrate by 3D lattice Boltzmann method." *International Journal of Heat and Mass Transfer*, vol. 124, 2018, pp. 1262-1274.

[15] Yi, H., Qi, L. H., Luo, J., Jiang, Y., & Deng, W. "Pinhole formation from liquid metal microdroplets impact on solid surfaces." *Applied Physics Letters*, vol. 108, no. 4, 2016.

[16] Yang, J., Zheng, F., & Derby, B. "Stability of lines with zero receding contact angle produced by inkjet printing at small drop volume." *Langmuir*, vol. 37, no. 1, 2021, pp. 26-34.

[17] Sklyarchuk, V., Plevachuk, Y., Novakovic, R., & Kaban, I. "Surface properties and wetting characteristics of liquid Ag–Bi–Sn alloys." *Monatshefte für Chemie-Chemical Monthly*, vol. 143, 2012, pp. 1249-1254.

HIGHLY PARALLEL DROPLET DISPENSING APPROACH TO FABRICATE HOMOGENEOUS, FUNCTIONAL LAYERS FOR DIAGNOSTIC TEST MANUFACTURING

O. Rajabnia[1]*, A. Ernst*[1]*, N. Lass*[1]*, and L. Riegger*[1]
[1] BioFluidix GmbH, Freiburg, Germany

ABSTRACT

We introduce a novel approach for highly parallel droplet dispensing with precise control over the droplet parameters. This approach facilitates the fabrication of homogeneous and precise thin layers with uniform coverage on defined small areas (e.g., a specific area of 1x1.4 mm^2 in microfluidic channels or microwell). The presented approach ensures layer uniformity and high precision in X/Y extent and edge resolution, making it well-suited for achieving precise and controlled coating for a variety of applications. Our approach is based on direct liquid displacement employing a piston that is in direct contact with the liquid. Based on a variety of nozzle chip designs (i.e., nozzle diameter and pitch), we evaluated a multitude of parameters to derive general design rules for the nozzle chip design. Thus, we achieved a tunable droplet volume from 200 to 800 pl and droplet velocities from 0.5 to 2.5 m/s, applying a nozzle diameter of 50 μm and a nozzle pitch of 165 μm. The presented results showcase the versatility of the approach, offering precise dispensing capabilities.

KEYWORDS

Surface coating; Biochips; highly parallel; Droplet dispensing; Homogeneous droplets; Microfluidic.

INTRODUCTION

Surface coating processes play a pivotal role in industries ranging from electronics to biomedical devices such as biochips to modify surface interaction with bioactive materials. Uniformity and optimal thickness are crucial for achieving the full functionality of surface coatings [1]. Therefore, pursuing precision, efficiency, homogeneity, and scalability in manufacturing has driven the development of innovative techniques for small-scale and high-throughput diagnostic applications. This paper presents an innovative approach for highly parallel droplet dispensing [2] to fabricate homogeneous and precise thin layers for functionalizing defined small surfaces such as microfluidic channels.

Common surface coating methods in diagnostic applications such as spray coating, inkjet printing [3], and microcontact printing often rely on single-nozzle, parallel-nozzles [4], and batch processes [5] which present various challenges. These methods frequently encounter issues like non-homogeneous liquid distribution on the surface, liquid handling limitations, material inefficiency, and varying coating precision and thickness. In contrast, the presented approach distinguishes its ability to achieve a homogeneous and precise surface coating in a defined small surface area by dispensing highly parallel droplets as array-on-demand (microarray) in a low volume range. Furthermore, this approach can reduce the coffee stain effect and enhance the surface coating quality by depositing a multitude of smaller droplets. This decreases the impact of evaporation and capillary flow, which ensures the solutes within the microarray remain uniformly distributed, resulting in a more even and consistent deposition pattern. Thus, this method has the potential capability of homogeneous distribution of solids.

MATERIAL AND METHOD

Principle, design, and fabrication

The principle of the employed dispensing approach is based on a direct liquid volume displacement to eject highly parallel droplets through a nozzle array. The device comprises a cartridge designed with feeding channels directing the flow from the reservoir to the chamber. A piezo actuator, linked to a piston, facilitates the direct displacement of volume within the cartridge chamber. Additionally, a nozzle chip is incorporated for the controlled ejection of a droplet array positioned beneath the chamber. This arrangement effectively seals the microfluidic channels within the cartridge, as illustrated in Figure 1.

The cartridge is made of PMMA material by milling and is designed to contain two feeding channels with a height of 200 μm. The channels are connected to the circular chamber located in the center of the cartridge. Underneath the cartridge, a nozzle chip that is fabricated in silicon through deep reactive ion etching (DRIE) is attached to the cartridge, where the nozzle array is located beneath the chamber. In addition, a piston that is fabricated in resin material using SLA printing, including a cut out for placement of an O-ring to seal the chamber, is positioned inside the chamber while being connected to the piezo actuator. The chamber's volume is adjustable by the piston position, which was set to a height of 400 μm for the presented results. The nozzle chip is made from a 300 μm thick silicon wafer and has a nozzle inlet at a depth of 150 μm and through-etched nozzles. (Figure 2).

The nozzle surface is selectively coated with a fluorosilane [6] as a hydrophobic surface so that the nozzle inlet remains hydrophilic.

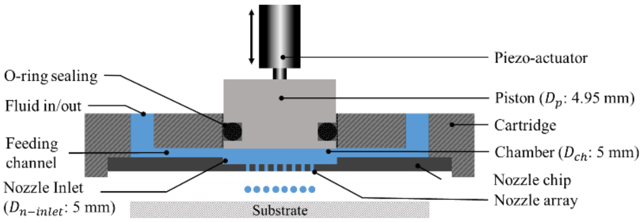

Figure 1: Dispensing device schematic.

Operational process and experiment

For a reliable coating procedure, a stable operation is essential. To achieve this operation, a bubble-free priming process is established to ensure that the fluidic path, especially the chamber, is free of any air bubbles that can negatively impact the dispensing process, such as fluctuations in droplet volumes resulting in unstable dispensing. In the priming process, the liquid flows from one side of the feeding channel to the other side to fully prime and wet the fluidic path and the chamber using a pressure setting of 0.5 mbar.

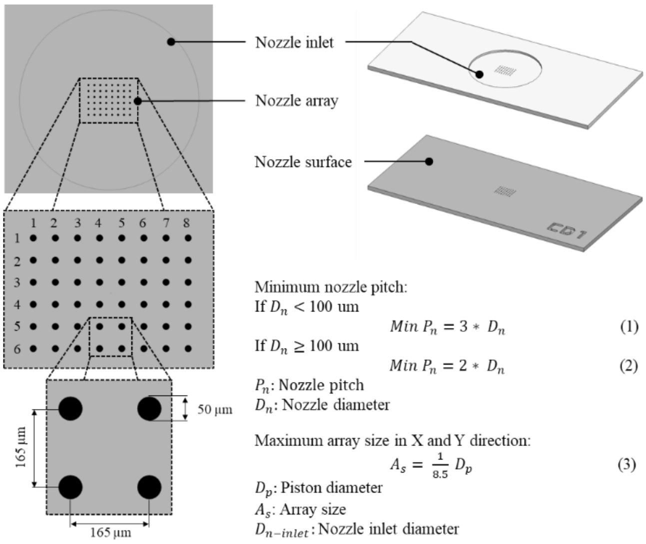

Figure 2: An example nozzle chip design according to the determined empirical design rules.

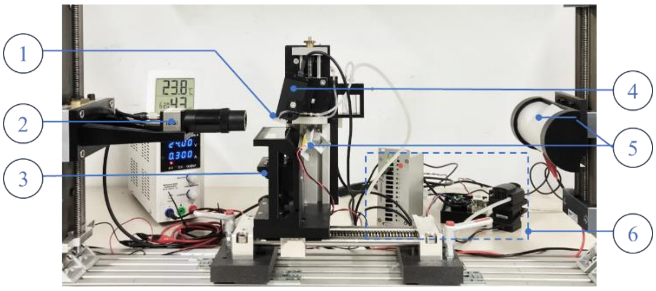

Figure 3: Experimental setup, (1) Cartridge, (2) SmartDrop camera, (3) Bottom view camera, (4) Actuator, (5) Illuminations, (6) Control units.

To achieve droplet ejection through the nozzle array, a defined liquid volume is directly displaced by the piston inside the chamber without any interface, such as a membrane, air cushion, or a deformable medium (e.g., rubber.) This movement is precisely controlled by a piezo-stack actuator that tunes the amplitude and the speed of the piston, which directly controls the dynamics of droplet ejection. Therefore, the applied energy must be constrained within the specific range of exceeding the surface energy of the liquid within the nozzles up to a point when satellite droplets appear.

In this paper, we introduce an empirical design rule for nozzle chips by specifying nozzle diameter, nozzle pitch, and array size relative to factors such as droplet volume and piston surface area (Figure 2). The underlying data is acquired by characterizing nozzle chips with different configurations and designs. We investigated nozzle diameters ranging from 40 to 200 µm and nozzle pitch to nozzle diameter ratio of 1 to 3.

Our implemented experimental setup (Figure 3) allowed us to analyze the droplet tear-off, measure the droplet volume in flight using image processing [7], and visualize the spotted array on the substrate.

RESULT AND DISCUSSION

The study evaluates various nozzle array configurations, exploring nozzle diameter, nozzle pitch, maximum array size, and droplet volume relationships. The characterization of different nozzle chip configurations indicates two distinct regimes to calculate the minimum required nozzle pitch relative to the nozzle diameter (Figure 2).

Formulas (1), (2), and (3), derived from this characterization and shown in Figure 2, provide practical insights for nozzle chip design. A nozzle chip with $P_n \geq Min\ P_n$ results in successful dispensing, whilst $P_n < Min\ P_n$ leads to unsuccessful dispensing (Figure 5). Additionally, the issue with a smaller surface area between nozzles (smaller than the defined minimum nozzle pitch) in the context of hydrophobic coating may result in the compromised quality of the coating, and it becomes challenging to maintain a uniform and effective hydrophobic coating on the surface between the nozzles. Therefore, insufficient coverage could lead to areas with lower contact angles, especially around nozzles, demanding increased energy to overcome surface energy for droplet ejection. However, if the energy exceeds the optimal range, it can contribute to issues such as droplet merging, bulging, and wetting, which ultimately results in unsuccessful dispensing.

The evaluation of droplet volume measurement over the experiment of different nozzle diameters ranging from 40 to 200 µm, encompassing achievable dispensed droplet volumes from 140 pl to 20 nl (Figure 4).

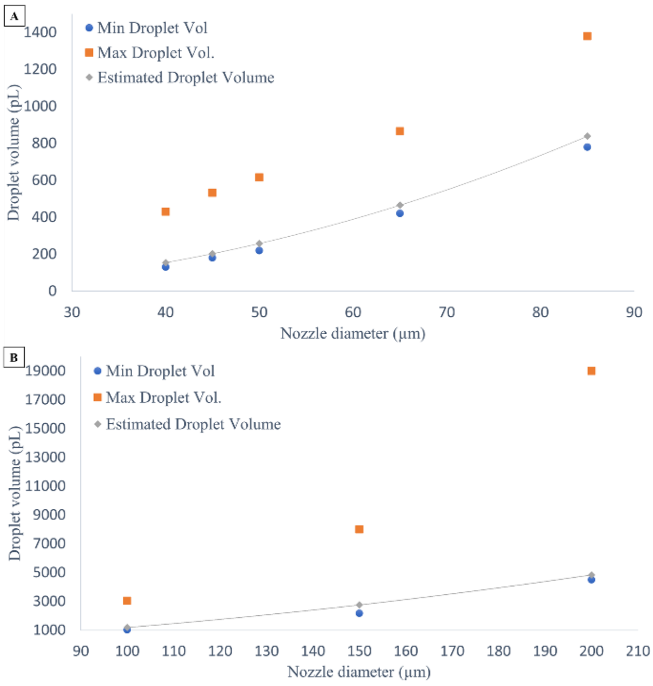

Figure 4: Estimated minimum droplet volume calculated by empirical formula compared to measured minimum and maximum dispensed droplet volume based on experimental results A: nozzles between 40 and 85 µm, B: nozzles between 100 and 200 µm.

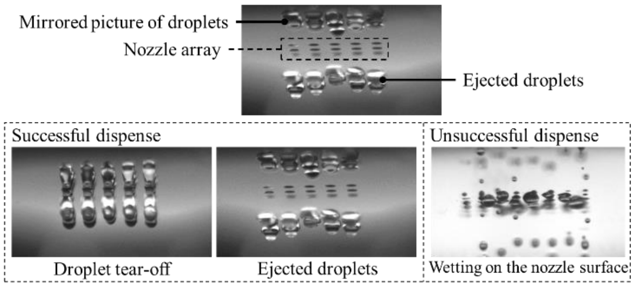

Figure 5: Successful and unsuccessful dispense.

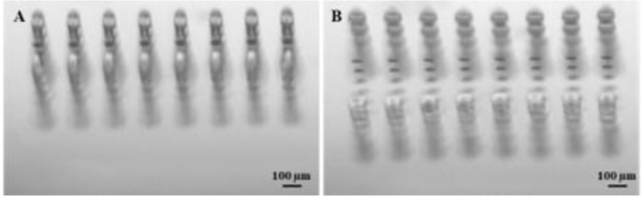

Figure 6: A: droplets during tear-off. B: droplets after tear-off.

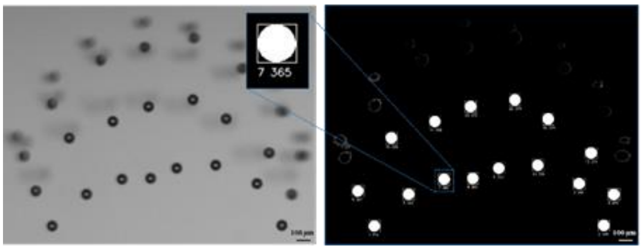

Figure 7: Parallel droplet measurement in flight.

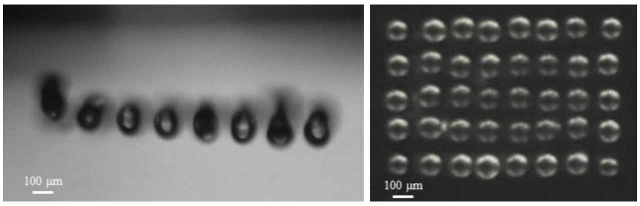

Figure 8: Dispensed droplet array in the fly (left) and spotted array on an objective slide (made of PMMA) with a contact angle of ~ 80° (right).

We utilized a specific nozzle chip configuration featuring a 50 µm nozzle diameter, a 165 µm nozzle pitch, and an 8x6 rectangular pattern to demonstrate droplet tear-off (Figure 6), droplet volume measurement (Figure 7), and spotted array on a substrate (Figure 8). Achievable droplet volumes range from 200 to 800 pl, dispensed with piezo strokes from 1 to 4 µm and stroke velocities from 20 to 45 µm/ms. The calculated coefficient of variation (CV) for droplet volume remains below 2.5% for a piezo stroke of 1.7 µm and stroke velocity of 30 µm/ms. This resulted in a dispensed mean droplet volume of 366 pl.

The dispensed droplet volume was quantified as a function of the piezo stroke, shown in Figure 9.

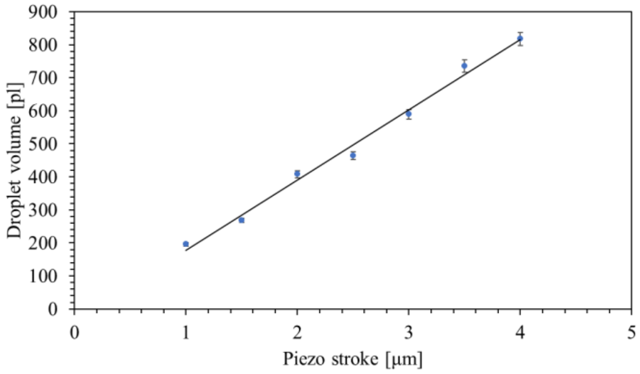

Figure 9: The dispensed droplet volume of the nozzle chip with 5o µm nozzle diameter vs Piezo stroke.

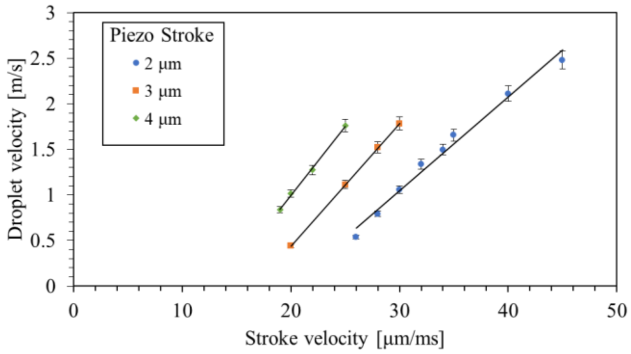

Figure 10: The effect of piezo actuator velocity on droplet velocity for three different piezo strokes.

The R-squared value of 0.98 implies a high degree of linearity between droplet volume and piezo stroke, as referred to in Figure 9.

Experiments were conducted with three specific piezo strokes over different time intervals to analyze the relationship between the stroke velocity and droplet velocity, as shown in Figure 10. The direct linkage between the piston and droplet ejection implies an anticipated direct proportionality between droplet velocity and stroke velocity. The linearity of the droplet and stroke speed relationship is shown in Figure 10 as a factor of approximately 3. The velocity measurements revealed that, for every droplet volume, a specific speed range exists within which dispensed droplets remain stable without the appearance of satellite droplets. For instance, smaller droplets of 300 pl exhibits stable ejection within the range of 0.5 to 2.5 m/s, while larger droplets of 800 pl maintain stability between 0.8 and 1.8 m/s.

CONCLUSION

In conclusion, the approach showcased a robust mechanism for the direct displacement of liquid volume, resulting in the precise and stable dispensing of highly parallel droplets onto a substrate.

This displacement of the liquid volume by the piston in the chamber, which is controlled by the piezo stack actuator, enables direct control of the droplet ejection dynamics.

Experimental evaluations provided empirical design rules for nozzle chips, defining relationships between nozzle diameter, pitch, and array size. The study identified successful dispensing conditions, outlined challenges, and devised formulas for the minimum required nozzle pitch relative to nozzle diameter, which offered practical guidelines for successful dispensing.

The characterization of nozzle chip configurations highlighted the device's versatility, allowing for the dispensing of volumes ranging from 140 pl to 20 nl with different nozzle diameters from 40 to 200 um. The specific configuration with a 50 µm nozzle diameter, 165 µm nozzle pitch, and an 8x6 rectangular pattern demonstrated successful dispensing in the range of 1 to 4 µm and 20 to 45 µm/ms of piezo stroke and Stroke velocity, respectively. Furthermore, specific dispensing parameters used to indicate successful droplet tear-off, droplet volume measurement, and spotted array on the substrate result in a mean droplet volume with a CV of 2.5% in an array of droplets.

Quantification of dispensed droplet volume as a function of the piston stroke revealed a consistent linear relationship, indicating precise volume control. The experiments analyzing the relationship between piezo actuator velocity and droplet velocity underscored the device's capability to maintain stability within specific velocity ranges for different droplet volumes.

Overall, this approach addresses several key aspects and challenges of the surface coating technology for diagnostic test manufacturing. Additional research will be conducted to assess all system variables to establish definitive design rules to determine droplet volume associated with specified liquid.

REFERENCES

[1] Zhao, W. (2006). Characterization of titanium dioxide pigment particles by high-resolution and analytical transmission electron microscopy (hrtem and aem). Microscopy and Microanalysis, 12(S02).

[2] J. Ducree; H. Gruhler; N. Hey; M. Muller; S. Bekesi; M. Freygang; H. Sandmaiser; R. Zengerle, “TOPSPOT-a new method for the fabrication of microarrays”, Proceedings of the IEEE MEMS, February 2000.

[3] Robert Mau, Gerrit Paasche, Thomas Lenarz and Hermann Seitz, “Inkjet printing for localized coating and functionalization of medical devices.”, Current Directions in Biomedical Engineering 2018.

[4] Christopher G. Lausted, Charles B. Warren, Leroy E. Hood, Stephen R. Lasky, “Printing Your Own Inkjet Microarrays”, Methods in Enzymology, Academic Press, Volume 410, 2006, Pages 168-189.

[5] Cheng-En Ho, Ching-Chang Chieng, Ming-Hung Chen, Fan-Gang Tseng, “Micro-Stamp Systems for Batch-Filling, Parallel-Spotting, and Continuously Printing of Multiple Biosample Fluids”, SLAS Technology, 2008, ISSN 2472-6303.

[6] S. Breisch, B. de Heij, M. Loehr, M. Stelzle, Selective chemical surface modification of fluidic microsystems and characterization, J. Micromech. Microeng. 14 (2004) 497–505.

[7] Kerstin Thurow, Thomas Kruger, and Norbert Stoll, “An Optical Approach for the Determination of Droplet Volumes in Nanodispensing”, Journal of Automated Methods and Management in Chemistry 2009, Article ID 198732, doi:10.1155/2009/198732.

CONTACT

* O. Rajabnia, omid.rajabnia@biofluidix.com

NON-INVASIVE ULTRASONIC FLOW MEASUREMENT METHOD FOR THE DETECTION OF FLOW RATES IN THE MICROLITER RANGE

A. Backer[1], P. Arneth[1], P. Linke[2] and K. S. Drese[1]
[1] Institute for Sensor and Actuator Technology, Coburg University of Applied Sciences and Arts, Am Hofbräuhaus 1B, 96450 Coburg, Germany.
[2] ibidi GmbH, Lochhamer Schlag 11, 82166 Gräfelfing, Germany.

ABSTRACT

Particularly in medical technology, biotechnology or the pharmaceutical sector, very small quantities of fluids often have to be transported or dosed. Non-invasive measuring methods for flow rate or volume flow measurement that work without direct contact to the fluid and thus meeting the high hygiene standards of these industries hardly exist. Sensors available on the market are either not suitable for precise measurement of the smallest flow rates in the microliter range or are very expensive.

For this field of applications, a retrofittable ultrasound-based flow sensor was developed in cooperation with the company ibidi GmbH, which can be integrated into an existing system consisting of very thin tubes or cannulas or capillaries as well as thin flexible tubes.

KEYWORDS

Micro flow metering, non-invasive flowmeter, guided acoustic waves, ultrasonic sensing

INTRODUCTION

For medical applications, e. g. drug dosing, a relevant flow range of 50 µl/min to 50 ml/min with an error below 10% is required. The most commonly used thermal sensors achieve this performance, but have a thermal impact on the fluid. Ultrasound as an alternative has no impact on the fluid however, the commonly used oblique transmission of sound through the pipe using wedge transducers, combined with low fluid velocities, does not provide sufficient accuracy and is therefore unsuitable as a measurement system for applications outlined above. In the developed sensor concept, the time difference method is also applied, but the sound propagation occurs along the pipe. Special guided ultrasound modes are excited, which propagate as coupled wall fluid mode, i.e., sound travels both in the wall and in the fluid [1-3]. The sensor system acts as a cylindrical waveguide. Due to the entrainment of the sound wave by the fluid, the modes propagate faster in the direction of flow than against the flow direction.

MATERIALS AND METHODS

At first the resulting measurement effect was calculated based on finite element method (FEM) simulation of a liquid-flowing cannula. The dispersion diagram in Fig. 1 shows the frequency-dependent phase velocity of propagating modes in a liquid-filled cannula. In addition to longitudinal modes, shear modes, and bending modes, there is also a fluid mode, whose phase velocity is significantly influenced by the flow velocity and which shows very low dispersion. Fig. 1 on the right illustrates the velocity change caused by flow in the same and opposite direction to the sound propagation, ultimately leading to a well-measurable difference in signal transit time.

The coupling of the wave propagating along the tube's

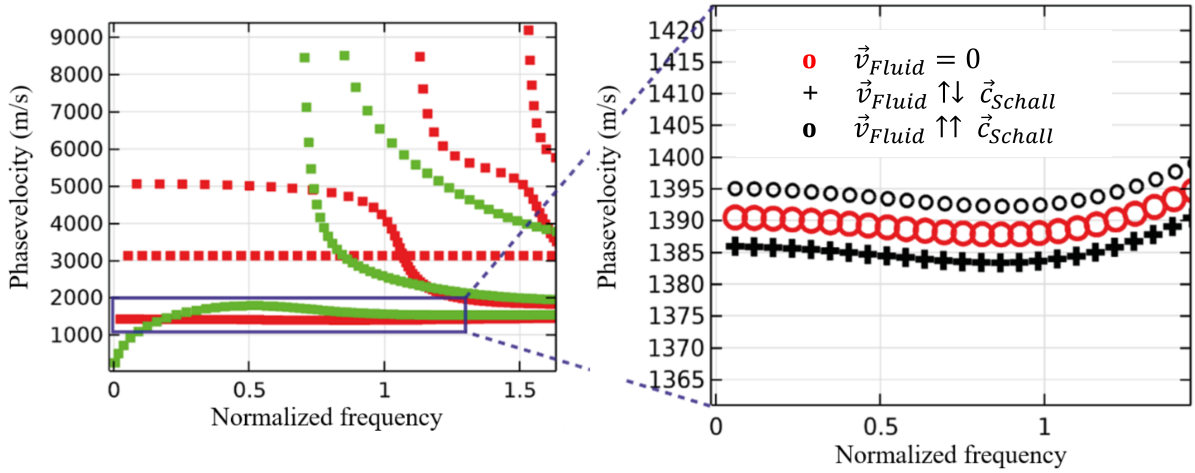

Figure 1: left: Dispersion relation of a cylindrical waveguide with modes with different propagation velocities to derive a suitable operating point for flow measurement, green: bending modes, red: longitudinal modes; right: dispersion relation of the fluid mode. Red circle: Fluid at standstill. Black circle: dispersion along the background flow. Black plus: dispersion against the background flow.

wall and the fluid is depicted in Fig. 2.

It has to be emphasized that the wave uniformly propagates across the entire cross-section of the cannula, and the measured signal transit time shift corresponds to an averaged flow velocity over the entire cross-section.

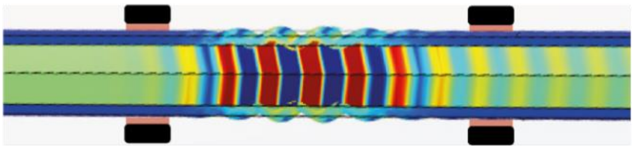

Figure 2: Propagation of the excited fluid mode in the cannula and schematic diagram of the attached piezo sensors

Preliminary investigations indicated this holds true for various flow profiles, making the sensor less sensitive to differently shaped flows. The existing flow velocity can be described using the following formulas. However, simulation results have indicated that the change in phase velocity does not precisely match the flow velocity and tends to be slightly lower. Therefore, calibration of the sensor was necessary for the accurate determination of the flow rate.

In the evaluation of the zeros of the measurement signal in both the flow and counter-flow directions, the time difference is approximated using formulas (1) and (2) with formula (3). Here, L is the distance between the transmitting and receiving piezos, c_{phase} is the phase velocity of the fluid mode, and v_{mean} is the mean flow velocity.

$$t_{+} = \frac{L}{c_{phase} + v_{mean}} \tag{1}$$

$$t_{-} = \frac{L}{c_{phase} - v_{mean}} \tag{2}$$

$$\Delta t = t_{-} - t_{+} = \frac{2 \cdot L \cdot v_{mean}}{c_{phase}^2 - v_{mean}^2} \tag{3}$$

Under the assumption $\mathrm{c_{phase}} \gg v_{mean}$ this leads to:

$$\Delta t \approx \frac{2 \cdot L \cdot v_{mean}}{c_{phase}^2} \tag{4}$$

By rearranging formula (4), the mean flow velocity (5) is derived from the measured phase difference. Additionally, with the known cross-sectional area A_{quer} of the cannula, the volumetric flow rate $\dot{V}$ is calculated to be:

$$v_{\mathrm{mean}} \approx \frac{c_{phase}^2}{2 \cdot L} \cdot \Delta t \tag{5}$$

$$\dot{V} = A_{quer} \cdot v_{\mathrm{mean}} \quad . \tag{6}$$

It is important to note that the phase velocity c_{phase} of the fluid mode is below the longitudinal velocity of the liquid and approaches it at higher frequencies. Therefore, for flow rate calculations, it must first be determined by calculating the dispersion diagram. In traditional ultrasound flow meters, the speed of sound in the fluid is calculated through the determination of the signal transit time of the received wave group. However, due to the dispersive nature of the fluid mode used, the phase velocity and group velocity deviate from each other. Determining the signal transit time of the wave group and thus establishing the group velocity is not sufficient to accurately determine the phase velocity.

Since the calculation of the dispersion diagram and, consequently, the required phase velocity involves often using imprecisely known material properties of the cannula and liquid, as well as the inner and outer diameters of the cannula, calibration of the sensor based on reference measurements are indispensable for highly accurate measurements. Only through this calibration flow rates can be accurately measured down to 50 µl/min.

In the developed system, a 50 cm long stainless-steel capillary with an inner diameter of 0.8 mm and an outer diameter of 1.2 mm served as a waveguide. Piezoelectric ring transducers were mounted at defined distances on the capillary, alternating between acting as transmitters and receivers. Excitation and detection of the modes occurred externally, i.e., at the wall of the capillary, ensuring that the sensor elements were not in direct contact with the medium, thereby eliminating the risk of contamination. The fluid mode used for flow measurement here primarily contained energy in the liquid at the operating point. Consequently, the sensor prototype, consisting of a transducer and capillary, was integrated into a 3D-printed housing with highly damping silicone. Undesirable wave components were strongly attenuated, while the evaluated fluid mode arrived nearly undampened at the receiving piezo. This allowed the evaluation of a pure mode and ensured precise measurement of the transit time shift with minimal interference. Electrical contact was established via BNC connectors. By spirally winding the cannula inside the housing, the prototype shown in Fig. 3 had compact dimensions of 8 x 8 x 4 cm³ and was easily connected to various pipe or tubing systems using a Luer-lock.

A pressure-controlled pump (P2CS 4 Plus, Biophysical Tools GmbH) was utilized to generate constant flow rates down to the µl/min range. Signal generation for exciting the acoustic waves was performed using a function generator (AFG 3022B, Tektronix). The signals were captured with a digital storage oscilloscope (WaveRunner 604Zi, Teledyne

LeCroy) with a sampling rate of 1 GHz and 20 averages. Python was used to control the devices and analyse the data.

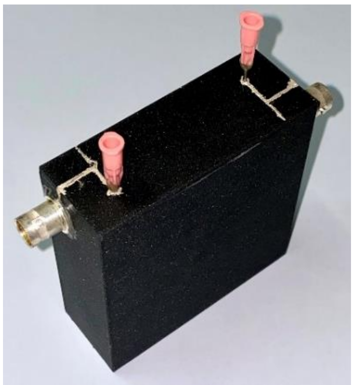

Figure 3: 3D-printed housing with internal sensor elements and connection via Luer-Lock adapter

The system calibration, and thus the conversion of the measured signal transit time difference into a flow rate, was carried out by holding different pressures and determining the pumped liquid volume with a precision balance (TED224S-OCE, Sartorius).

RESULTS AND DISCUSSION

With the system calibrated in this manner, ibidi measured Dulbecco's Modified Eagle's Medium (DMEM) at various pump pressures and determined the resulting flow rate. Each pressure level was retained for 5 minutes. Before switching between pressure levels, the zero position was first set to detect and compensate for possible long-term drifts in the measurement system. As depicted in Fig. 4 and Fig. 5, the developed sensor can measure flow rates up to 50 µl/min.

The temporary dips in the calculated flow rate, as shown in Fig. 4 at around 2 and 4 minutes, were observed in several measurements with different liquids and flow rates. The width of the signal dips was assigned to the time required by the liquid to cover the distance between the two sensors. It is assumed that these are air bubbles. An air bubble that is pushed through the cannula causes a pressure drop and thus increases the flow resistance in the cannula [4]. In combination with flow generation by a pressure-regulated pump, a higher resistance results in a reduced flow rate.

The use of laboratory devices is unsuitable for the industrial use of the developed sensor. For this reason, work is currently underway on stand-alone electronics, which can be seen in Fig. 6. This system is designed to handle data generation, data acquisition, and data analysis. The transmission signals, which are freely programmable in the range from 300 kHz to 1 MHz, are generated via a digital analog converter (DAC) operating at 30 MHz. Data is recorded by means of an analog-to-digital converter (ADC) which samples the signals at a frequency of 60 MHz. The transmitter and receiver piezo are interchanged by means of built-in multiplexers, thus enabling transit time difference measurement in and against the direction of flow. The entire control of the components and the data evaluation are realized via several Complex Programmable Logic Devices (CPLDs). To increase the signal-to-noise ratio, the measurement signals are differentially pre-amplified in the sensor housing. In combination with twisted and shielded data cables, cable lengths of 10 m can be realized between the sensor and the measuring electronics.

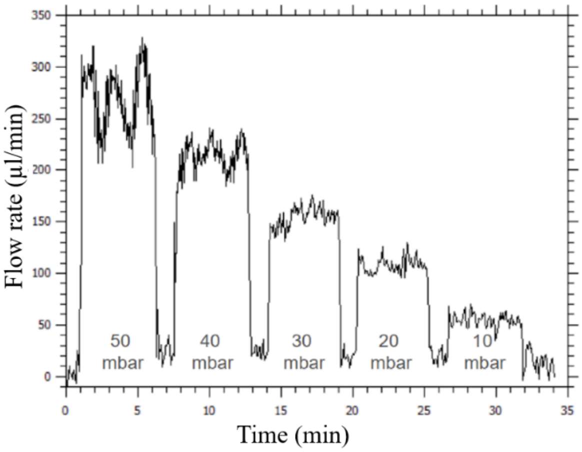

Figure 4: Measuring signal at different pressure levels, Medium: DMEM

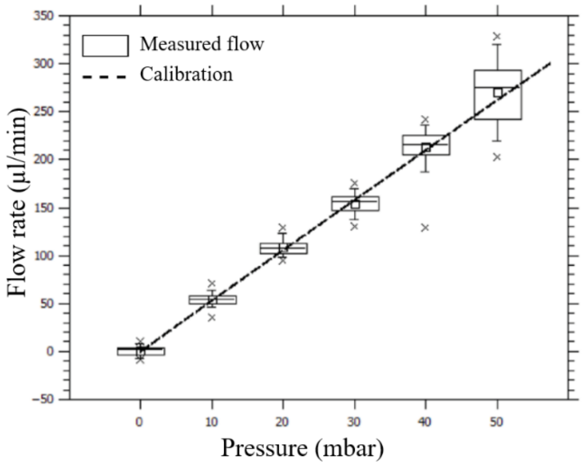

Figure 5: Boxplot of the pressure stages from Fig.4

The measurement signal is a 430 kHz, 12-fold sine burst with Hanning windowing. The electronics automatically detect the maximum of the wave group and search for the five closest zero points. During a measuring cycle, a total of 48 individual measurements are carried out and offset against each other to determine the current flow rate. To reduce temperature influences during a measuring cycle, a measurement is first carried out in the direction of flow, then against and then again in the direction of flow and the individually determined signal transit times are combined.

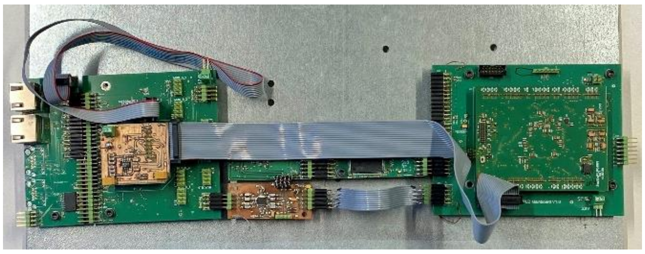

Figure 6: Control electronics with CPLDs, ADC, DAC, multiplexer, and adjustable differential amplifier

The further development of the measuring system also includes a redesign of the sensor. The key difference to the previous sensor is the integration of differential preamplifiers directly into the sensor housing. The direct proximity to the piezos significantly reduces the influence of interference signals and therefore also increases the signal-to-noise ratio. The BNC connections have also been replaced by RJ45 sockets to provide the power supply for the preamplifiers.

A cross-section of the sensor housing with installed electronics can be seen in Fig. 7 as a CAD model.

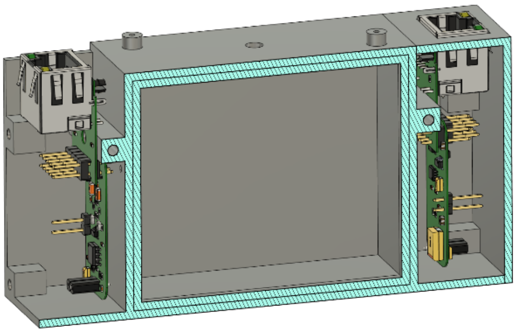

Figure 7: CAD model of the inside of the sensor

The finished sensor with built-in cannula and Luer-Lock connections is shown in Fig. 8. Like the first generation of the sensor, the housing is 3D printed.

Figure 8: Second generation sensor with integrated differential amplifiers

Initial measurements with the developed electronic system in combination with the modified sensor have shown a significantly greater signal-to-noise ratio. Due to the increased signal quality, slow drifting of the calculated flow rates in the two-digit µl range was also observed. This drift can currently only be compensated for by pausing the flow rate for a short time and making a baseline correction. Possible causes such as temperature effects are to be investigated in the future and compensated for without baseline correction.

OUTLOOK

The housing 3D printed from polylactide (PLA) can be replaced by a stainless-steel housing in the future. In addition to the increased mechanical and chemical resistance, the sensor can also be shielded from electromagnetic interference, which further improves the signal-to-noise ratio. For the medical sector, it is also possible to autoclave the sensor after use.

It is also conceivable to control the pressure-regulated pump based on the measured flow rates, which makes it possible to set specific flow rates even in the µl range. This is particularly relevant if the liquid to be pumped may contain gas bubbles. As measurements have shown, maintaining a constant pressure is not sufficient to ensure a constant flow rate of the liquid. Even the smallest air bubbles can significantly increase the pressure drop across the measurement section, leading to a substantial reduction in flow.

FUNDING

The development work of ISAT and ibidi were funded by the Federal Ministry for Economic Affairs and Climate Action (BMWK) as part of the Central Innovation Program for SMEs (ZIM) (funding reference 16KN070933, Microflowsense project)

REFERENCES

[1] J.L. Rose, “Ultrasonic Guided Waves in Solid Media”, Cambridge University Press, 2014

[2] H. Sato, H. Ogiso, “Guided waves propagating in a water-filled stainless steel pipe”, Jpn. J. Appl. Phys., 53 07KC13, 2014

[3] H. Kwun, K. A. Bartels, C. Dynes, „Dispersion of longitudinal waves propagating in liquid-filled cylindrical shells“, J. Acoustic. Soc. Am., Vol. 105, Nr. 5, pp. 2601 – 2611, 1999

[4] P. Garstecki, M. J. Fuerstman, H. A. Stone, and G. M. Whitesides, “Formation of droplets and bubbles in a microfluidic T-junction-scaling and mechanism of break-up“, Lab on a chip, Vol. 6(3), pp. 437-446, 2006

CONTACT

* A. Backer, Alexander.Backer@hs-coburg.de

THERMAL FLOW SENSOR WITH LIQUID CHARACTERISATION FEATURE BY COMBINING 3OMEGA METHOD AND CONSTANT TEMPERATURE ANEMOMETRY

C. J. Hepp[1]*, K. Gajo*[1]*, R. E. Bernhardsgrütter*[1]*, K. Schmitt*[2,3]*, and J. Wöllenstein*[2,3]
[1]Innovative Sensor Technology IST AG, Ebnat-Kappel, Switzerland
[2]Department of Microsystems Engineering, University of Freiburg, Freiburg, Germany
[3]Fraunhofer Institute for Physical Measurement Techniques IPM, Freiburg, Germany

ABSTRACT

In this paper, we investigate in a new approach for a thermal flow sensor, allowing to obtain flow speed and characteristic information about the liquid. The fluid dependency of thermal flow sensors is overcome by combining the 3ω-method and constant temperature anemometry (CTA). We apply the 3ω-method to characterise the thermal properties of the liquid and obtain the flow speed by using the CTA. A theoretical approach is presented to parameterize the thermal properties of the liquid, which is verified by experimental results. It is shown that the flow rate can be measured within 10% accuracy for different concentrations of a binary mixture of water and isopropanol.

KEYWORDS

Thermal flow sensor, liquid characterization, 3ω/3omega method, constant temperature anemometer, binary mixture, concentration, flow speed

INTRODUCTION

Flow measurements are utilized in many applications. Most flow measurement principles require an information about certain physical properties of the fluid a priori, to determine flow velocity. Coriolis flow meters measure flow velocity, as well as the density of the liquid and are an exception in this field [1]. Several researchers are targeting this approach by using MEMS technologies to reduce size and complexity of the measurement device.

Thermal flow sensors are widely used in various, low flow applications, like process control and life science. The big advantages are the small sensor size and easy implementation in the flow channel [2]. These sensor's biggest drawback is the fluid dependence; hence the sensor must be calibrated to the gas, or liquid used in the application or correction factors must be implemented [3]. Applications where the fluid or the concentration varies over time can also not be addressed. Research is done to overcome the mentioned drawbacks for gas applications [4]. The sensor presented in this paper describes a proof of concept for liquid applications to measure flow speed with liquid characterization feature.

For the first time, the 3ω-method is applied on a meander-shaped thin-film structure made of platinum on a Al_2O_3-substrate, which is attached to a stainless steel tube. The main challenges are the sensor's multilayer structure and the meander-shaped thin film structure [5].

OPERATING PRINCIPLE

The operating principle of the sensor is designed to obtain flow rate and information of the liquid. Liquid concentration can be obtained for a binary mixture; however, the components of the mixture have to be known in advance.

Combining two different measurement principles allow a precise measurement of flow speed and either the concentration of a binary liquid mixture, or the detection of a single liquid type:

- The liquid is characterized by the 3ω-method in no flow condition leading to the liquid type or concentration of the binary mixture [6]. No flow condition can be set by deploying a valve for example.
- The flow speed is measured with the constant temperature anemometry principle.

Our measurement procedure is based on theoretical investigations on the 3ω-method and CTA. The information of the liquid is implemented in the CTA model to compensate different physical properties of the liquid. A detailed scheme of the measurement and compensation procedure is shown in Fig. 1. If only the flow speed changes, the measurement is performed by following loop 1. The fluid characterization in combination with flow rate is indicated by loop 2.

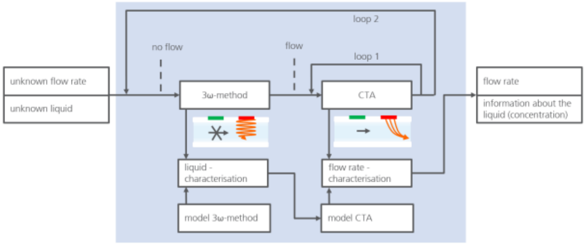

Figure 1. Measurement and compensation routine to obtain flow speed and concentration/type of a liquid. Concentration of a binary liquid can be obtained if the components are known a priori.

THEORETICAL INVESTIGATION

A theoretical model was developed based on the differential equations of the 3ω-method and CTA [7]. In a first step the 3ω-method was analysed theoretically with respect to the drive frequency for different fluids. For this investigation, the current amplitude I_0 is set to 20mA. The implemented physical properties for the sensor and the fluids are shown in Tab. 1. The result of the temperature 3ω term is shown in Fig. 2. The amplitude decreases monotonically if the drive frequency increases. Different liquids show a different temperature amplitude of the 3ω term. For example, air shows the largest, water the smallest temperature amplitude. The amplitude of the 3ω term depends on several parameters, like, drive frequency, thermal conductivity, volumetric heat capacity, and can be expressed by $\Delta T_{3\omega} \simeq g(\omega, \rho c_p, k)$. The dominant physical parameter however is the fluid's thermal conductivity. The sensor's fluid dependency is visible until a drive frequency of about 10 Hz. An explanation can be that for frequencies over 10 Hz the thermal wave does not expand into the fluid.

Table 1: Physical properties for density ρ, thermal conductivity k and specific heat capacity c_p at 25 °C for different materials used in the theoretical and experimental investigation [8-10].

Material	**Density [kg/m3]**	**Thermal conduct. [W/(mK)]**	**Specific heat capacity [J/(kgK)]**
Al_2O_3	3720	25	880
stainless steel	7900	15	500
air	1.12	0.03	1000
water	997	0.61	4187
isopropanol	786	0.14	2680
engine oil	873	0.15	1880

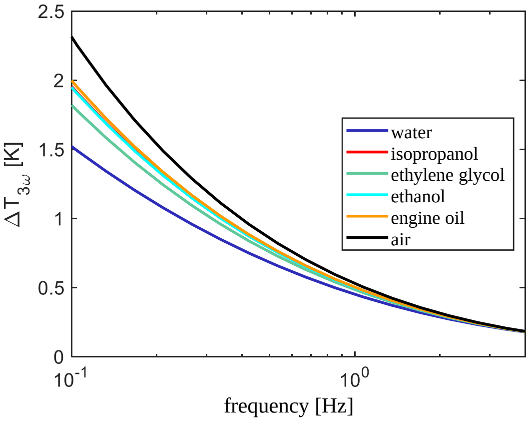

Figure 2. Theoretical result of the 3ω-method – temperature amplitude of the 3ω term as a function of the drive frequency. The signal is shown for different liquids and air. A fluid dependency is clearly visible until a drive frequency of around 10 Hz.

In a second phase, a similarity between the two theoretical models (3ω-method and CTA) was investigated. The idea is to combine the different theoretical approaches leading to correlations between thermal conductivity and volumetric heat capacity.

Thus, the theoretical investigation leads to a combination of:

- The amplitude of the signal of the 3ω-method as a function of thermal conductivity (k) and volumetric heat capacity ($\rho * cp$) for a given drive frequency.
- The CTA power signal as a function of thermal conductivity, volumetric heat capacity and flow.

Fig. 3 and 4 show the isolines of the amplitude for the 3ω-method and power signal for CTA as function of thermal conductivity and volumetric heat. The model assumes identical isolines for both methods - 3ω-method and CTA.

Based on this assumption, determination of the isolines is sufficient to characterizes the fluid. Furthermore, it is possible to parameterize the thermal conductivity as a function of the volumetric heat capacity.

The equation for the parametrization can be given by

$$k = a \cdot (\rho c_p)^n \qquad (1)$$

Where a and n are constants.

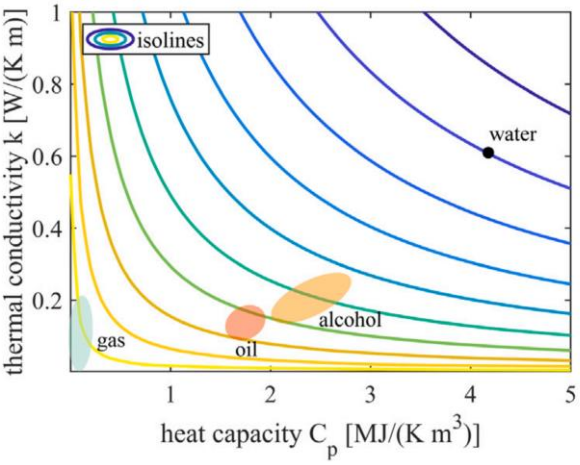

Figure 3. Theoretical result – isolines of the amplitude by the 3ω-method. Covering a wide range of thermal conductivity and volumetric heat capacity to obtain Equation 1 by including Fig. 4.

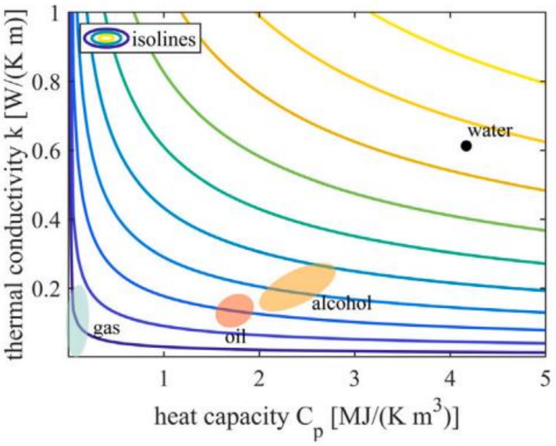

Figure 4. Theoretical result - isolines of the power signal by the Constant Temperature Anemometry with respect to thermal conductivity and volumetric heat capacity.

SENSOR DESIGN

The sensor is designed for liquid applications with a high corrosion resistance for long lifetimes.

Therefore, a stainless-steel tube is used as flow channel with an inner diameter of 3.7 mm and wall thickness of 150 µm. The length of the tube is 40 mm to ensure a laminar flow profile. A Pt50 element is deployed as a heater and a Pt1000 serves as a temperature sensor. The fluid is only in contact with the stainless-steel tube. A thin Al_2O_3-substrate with backside metallization is ensures good heat transfer from the thin film platinum layer into the liquid. The metallised backside allows for the elements to be soldered onto the stainless-steel tube. Furthermore, an Al_2O_3-substrate with extra high thermal conductivity is chosen. The 3ω-method uses the Pt50. Both elements (Pt50 and Pt1000) are used by the CTA.

A photo of the sensor is shown in Fig. 5 a), a cross section in Fig. 5 b), a layout of the heater Pt50 showing the meander structure in Fig. 5 c).

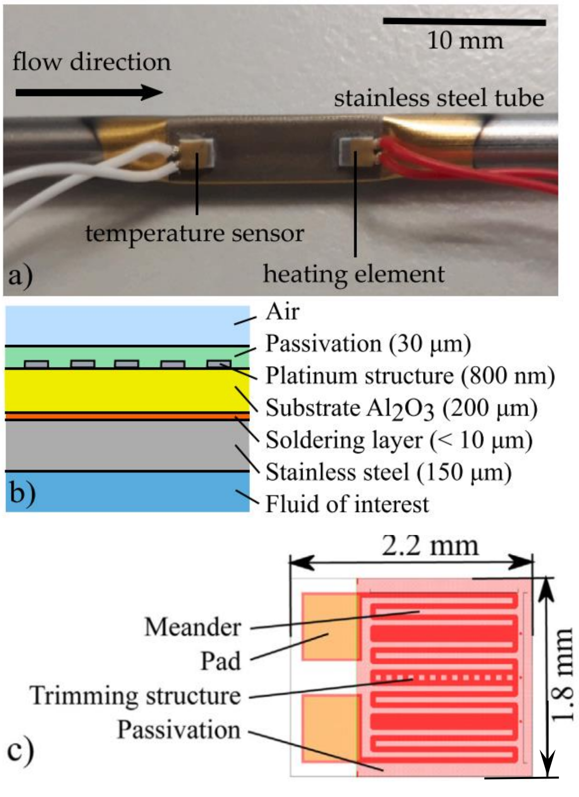

Figure 5. (a) Photograph of the sensor. The flow channel has an inner diameter of 3.7 mm and a wall thickness of 150 µm (b) cross section of the sensor, the liquid is described by the fluid of interest (c) layout view - meander structure of the Pt50. This layout ensures a homogeneous heating surface.

ELECTRONICS AND MEASUREMENT SETUP

As the signal of interest is around three magnitudes smaller than the drive signal, a Lockin-Amplifier based on a data acquisition card from National Instruments (NI USB 6225) is developed for performing the measurements with the 3ω-method.

Joule heating is used for the 3ω- method. An alternating current is applied on the heater: $I(t) = I_0\ \cos(\omega t)$,where ω contains the drive frequency. The amplitude of the AC current is set to I_0 = 30 mA. This leads to temperature oscillation on the heater $T_{h(t)}$:

$$T_h(t) = \Delta T_{DC} + \Delta T_{3\omega} \cdot \big(1 + \cos\,(2\omega t + \phi)\big) \qquad (2)$$

The temperature oscillation $\Delta T_{3\omega}$ contains information about the thermal properties of the liquid, which is analysed.

For CTA-mode, the temperature difference between liquid and heater is set to 8 K.

In the experiments, the flow rate was adjusted between 0 m/s and 0.05 m/s using a syringe pump. Therefore, a laminar flow profile is assumed. A binary mixture with different concentrations of isopropanol and water is investigated.

EXPERIMENTAL RESULTS

The experimental results for the 3ω-method are shown in Fig. 6. It can be clearly seen that the 3ω-signal is:

- monotone decreasing for an increasing drive frequency.
- monotone increasing for an increase of isopropanol concentration for a binary water-isopropanol-mixture.
- fluid dependent up to a drive frequency of 4 Hz. If the drive frequency is higher than 4 Hz, the thermal wave does not expand into the liquid.

The results of the heating power as function of flow speed for CTA-excitation is shown in Fig. 7. The graph includes the theoretical prediction using the compensation routine and experimental results for a flowing, binary mixture of water and isopropanol with different concentrations. The power signal is monotone increasing towards flow speed. In addition, the output decreases monotonically with increasing isopropanol content. The offset (power signal at stationary condition) also shows a fluid dependency.

Based on the model, equation (1) can be given with n=3 for the best compensation performance of this mixture. The experimental results and the model fit very well for flow rates above 0.005m/s. There is a slight deviation below this value. The deviation between theory and experiment can be explained by the employed model: Thermal conductivity is expressed with a constant for CTA mode. This might be a bit inaccurate especially at extreme low flow speeds.

The accuracy investigation of the experimental results is illustrated in Fig. 8. The graph shows the deviation of a set value to the measured value including the fluid compensation. Based on the presented results, flow rates can be predicted with an accuracy of +/- 10% (compensated flow rate). As rule of thumb, the measurement accuracy of mass flow meters without fluid characterisation is around +/- 3%.

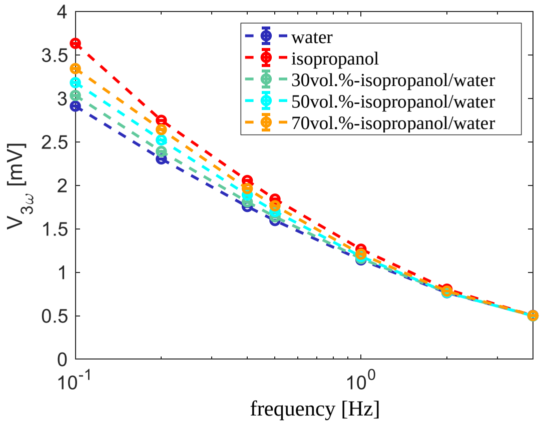

Figure 6. Experimental result - signal of the 3ω-method for various concentrations of isopropanol and water. The signal is monotonically increasing regarding the increase of isopropanol concentration. Signal depends on concentration below a drive frequency of 4 Hz.

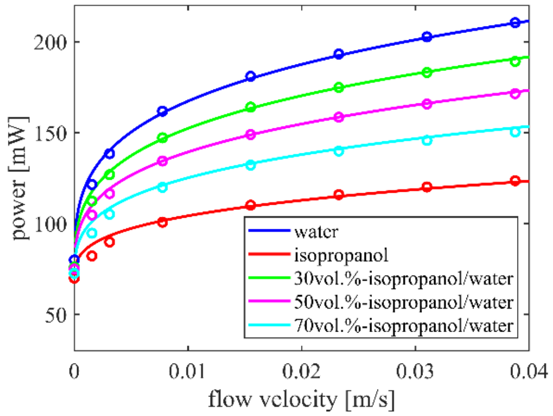

Figure 7. Prediction and experimental results – fluid compensation of CTA signal according to measurement procedure illustrated in Fig 1. Graph shows the prediction (line) of the model and experimental data (dot) for various concentrations of the investigated mixture.

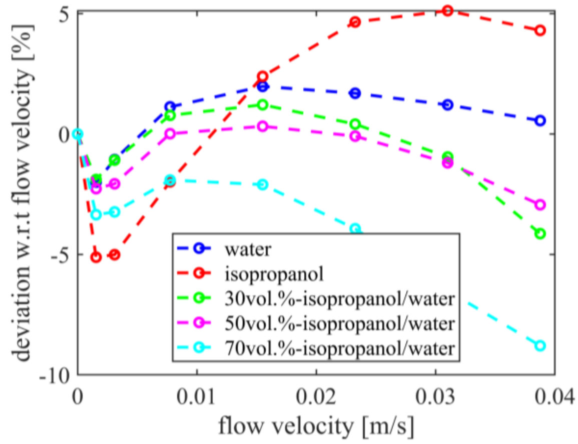

Figure 8. Accuracy analysis of experimental data – deviation of measured value towards set flow speed. The compensated flow speed has an accuracy of +/- 10%.

CONCLUSION

This research presents a concept to obtain both, flow speed and information of the liquid, using a thermal sensor. A combination of the 3ω-method and CTA enables measuring flow speed of an unknown, flowing liquid. The sensor consists of a stainless-steel tube, wherein the fluid is streaming. On the outside of the tube, two platinum thin film sensors are soldered enabling a good heat transfer from the platinum layer into the fluid. A new readout and evaluation algorithm has been developed to combine the 3ω-method in no flow condition and CTA for a flowing fluid. By correlating the measurements of these two methods the thermal parameters of the liquids can be determined. Thus, flow speed of an unknown liquid can be measured with an accuracy of 10%. Furthermore, the concentration of a binary mixture can be determined if the components are known in advance. This concept was proven experimentally for a mixture of water and isopropanol. To increase the measurement accuracy, future investigations aim to analyse the liquid under flow conditions by the 3ω-method.

REFERENCES

[1] T. Wang, R. Baker, Coriolis flowmeters: A review of developments over the past 20 years, and an assessment of the state of the art and likely future directions, Flow Meas. Instrum. 40, 2014, pp. 99–123
[X] Coriolis
[2] N.T. Nguyen, "Micromachined flow sensors—a review", Flow Meas. Instrum. 8 (1), 1997, pp.7–16
[3] J.T. Kuo, L. Yu, E. Meng, Micromachined thermal flow sensors-A review, Micromachines 3 (3), 2012, pp. 550–573
[4] C.J. Hepp, et al., "Multi-parameter monitoring of binary gas mixtures: Concentration and flow rate by DC excitation of thermal sensor arrays", Sensors Actuators A, Vol. 265, 2017, pp. 32–39
[5] R.E. Bernhardsgrütter, et al., "3ω Method in combination with a meander shaped heater: Theoretical and experimental investigation", Sensors Actuators A, Vol. 332, part 2, 2021, 113175
[6] R.E. Bernhardsgrütter, et al., "Towards a robust thin film sensor for distinguishing fluids using the 3ω-method", Sensors Actuators A, Vol. 321, 2021, 112419
[7] R.E. Bernhardsgrütter, et al., "Fluid-compensated thermal flow sensor: A combination of the 3ω-method and constant temperature anemometry", Sensors Actuators A, Vol. 350, 2023, 114116
[8] Care, CRC Handbook of Chemistry and Physics, nineth ed., CRC Press, Boca Raton, 2009
[9] Accuratus Ceramic Corporation, 96% Alumina properties - datasheet, 2013
[10] Deutsche Edelstahlwerke GmbH, Datasheet 1.4301 - X5CrNi18 -10, 2015

CONTACT

* Christoph Hepp; Christoph.hepp@ist-ag.com

VELOCITY-INDEPENDENT THERMAL CONDUCTIVITY AND VOLUMETRIC HEAT CAPACITY MEASUREMENT OF BINARY GAS MIXTURES

S. Azadi Kenari[1], *R.J. Wiegerink*[1], *R.G.P. Sanders*[1], *and J.C. Lötters*[1,2]
[1] University of Twente, Integrated Devices and Systems, Enschede, The Netherlands
[2] Bronkhorst High-Tech BV, Ruurlo, The Netherlands

ABSTRACT

In this paper, we present a single hot wire suspended over a V-groove cavity that is used to measure the thermal conductivity (k) and volumetric heat capacity (ρc_p) for both pure gases and binary gas mixtures through DC and AC excitation, respectively. The working principle and measurement results are discussed.

KEYWORDS

Binary gas mixtures, thermal conductivity, volumetric heat capacity, ω - 3ω technique.

INTRODUCTION

Thermal flow sensors are used in various applications, like industry, farming, medical, etc., where flow rate of gases needs to be monitored in real-time [1]. Thermal flow sensors are cost-effective, have a simple fabrication process, and straightforward working principle. However, the main problem with these sensors is their dependency on the type of fluid due to the differences in thermal conductivity k and volumetric heat capacity ρc_p. Whenever the gas or fluid changes, the sensor needs to be calibrated. Researchers have tried to overcome this problem by implementing different measurement principles and applying different designs to the sensor or the channel in which the sensor is placed. One of the methods to measure the gas properties is using ω - 3ω excitation. In this technique, an AC current with frequency ω is used for Joule heating, resulting in temperature variations at frequency 2ω, and the heater voltage will contain a component at frequency 3ω due to the dependence of the heater resistance on temperature. In [2], AC excitation was used to measure the gas properties from the third harmonic voltage amplitude and phase, and then correct the flow rate. In [3], the 3ω-method and constant temperature anemometry (CTA) were used. In [4], a thermal flow sensor was used consisting of a heater and upstream and downstream temperature sensors to determine the flow speed and thermal properties of binary gas mixtures.

In this paper, we will show that a single hot wire can be independent of the flow rate and can measure the gas properties via different types of excitation.

DESIGN AND THEORY

The sensor chip consists of a single wire suspended above a V-groove cavity, as shown in Fig. 1. The dimensions of the wire are listed in Table 1. The sensor chip is inserted in a tube with circular cross-section, such that the wire and V-groove cavity are perpendicular to the flow direction. When the gas enters the tube, it fills the cavity, but the influence of variations in flow velocity on the wire temperature is negligible. The only parameters that affect the wire's temperature are the gas properties. The amount of heat transferred from the wire to the heat sink depends on the thermal gas properties, such as thermal conductivity, density, and heat capacity. A schematic illustration of the gas properties measurement is shown in Fig. 2. DC and AC excitation are used to measure k and ρc_p, respectively.

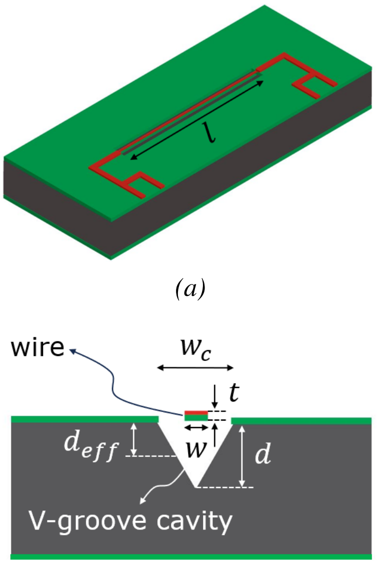

(a)

(b)

Figure 1: Schematic drawing of the single wire suspended above a V-groove cavity. (a) The top view, and (b) cross-section view of the sensor ($d_{eff} \approx \frac{d}{2}$).

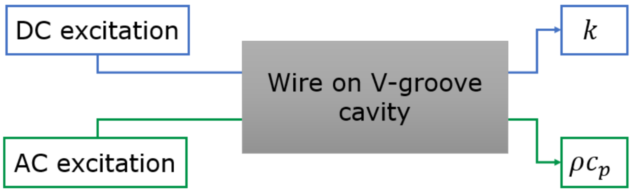

Figure 2: Gas physical properties measurement by DC and AC excitation.

Table 1: Dimensions of wire and cavity.

Parameter	Term	Value
Beam length	l	2 mm
Beam width	w	3 μm
Beam thickness	t	400 nm
V-groove width	w_c	80 μm
V-groove depth	d	58 μm

Thermal conductivity measurement

If the wire is heated by a DC current I, the temperature distribution along the wire can be calculated analytically [5]. If the wire is sufficiently long, heat conduction inside the wire can be neglected and only conduction through the gas needs to be considered, as indicated by the equivalent circuit shown in Fig. 3a. The temperature of the wire is proportional to the heating power P and the thermal resistance R_{th} of the gas, which is inversely proportional to k. The resulting voltage over the wire can now be calculated from:

$$V = R_a(1 + \alpha P R_{th})I \tag{1}$$

with R_a the wire resistance at room temperature, and α the temperature coefficient of resistance of the platinum wire. Fig. 4 shows a plot of the calculated voltage as a function of $\frac{1}{k}$.

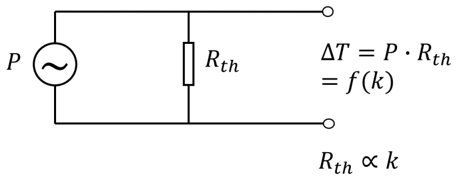

(a) DC excitation

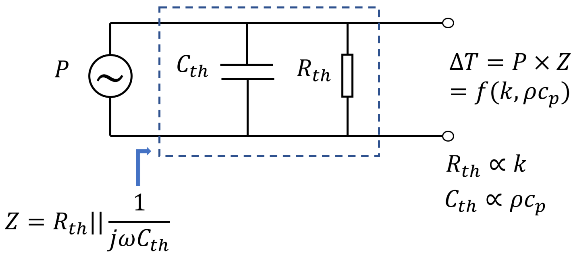

(b) AC excitation

Figure 3: Equivalent circuit model of the wire when heated by (a) a DC, and (b) an AC current. R_{th} and C_{th} are the thermal resistance and thermal capacitance of the fluid.

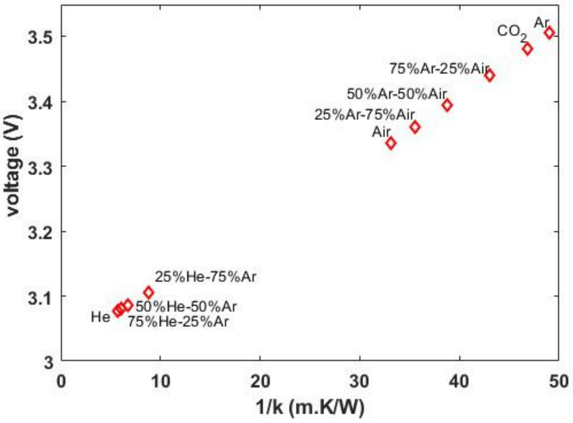

Figure 4: Calculated voltage over the wire for various pure and binary-mixtures of gases using equation (1).

Volumetric heat capacity

In case of an AC heating current the equivalent circuit model needs to include the thermal capacitance of the wire and gas, as shown in Fig. 3b. If the current has a frequency ω, the dissipated power will have a frequency 2ω, giving temperature and resistance variations at frequency 2ω. As a result, the voltage over the resistor will contain a component at frequency 3ω, which contains information about the thermal conductivity and volumetric heat capacity of the fluid. The voltage over the heated wire can be expressed as follows [6]:

$$\begin{aligned} V(t) &= I_{ac}(1 + \alpha \Delta T_{dc}) cos(\omega t) \\ &+ \frac{I_{ac} R_a \alpha \Delta T_{ac}}{2} cos(\omega t + \angle Z_{2\omega}) \\ &+ \frac{I_{ac} R_a \alpha \Delta T_{ac}}{2} cos(3\omega t + \angle Z_{2\omega}) \end{aligned} \tag{2}$$

The voltage has two time-dependent terms at frequencies ω and 3ω. The amplitude of the 3ω component can be described as:

$$|V_{3\omega}| = \frac{I_{ac}^3 R_a^2 \alpha}{4} |Z_{2\omega}| \tag{3}$$

Two parameters play a role, $R_{th} = \frac{l}{kA}$ and $C_{th} = \rho c_p V$, since the impedance (Z) is a function of R_{th} and C_{th}, which relate to k and ρc_p, respectively. V is the volume of the V-groove cavity, A the cross-section area of the V-groove, and l is the trajectory from the heated element to the heat sink. COMSOL simulations were used to calculate the 3ω component for different gases. Time domain simulations were performed and 3ω amplitude was obtained by a Fast Fourier Transform (FFT). Fig. 5a shows the result for Ar, CO_2, air, and He, showing a clear dependence on the product $k\rho c_p$.

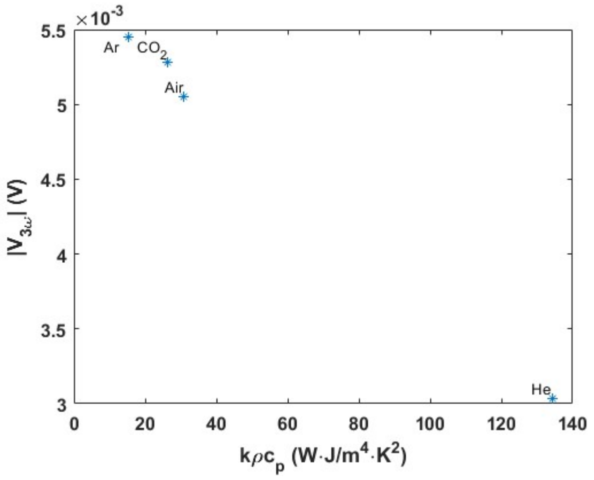

Figure 5: COMSOL simulation result showing the dependence of the $|V_{3\omega}|$ component on $k\rho c_p$.

FABRICATION

The fabrication process is very similar to the process described in [6], except that processing is only needed at one side of the wafer. Fig. 6 shows photographs of the fabricated chip.

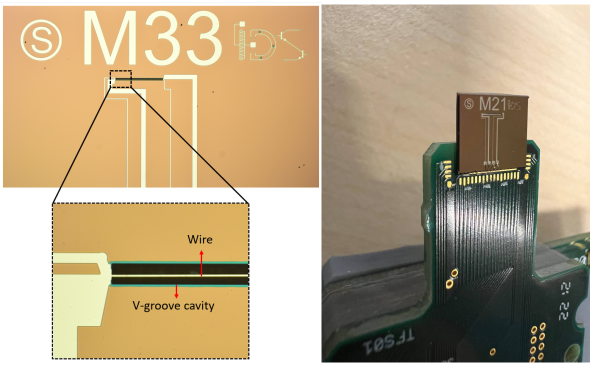

(a) (b)

Figure 6: (a) Microscope photograph of the released sensor, (b) chip mounted on a PCB with electrical connections.

RESULTS AND DISCUSSIONS

The schematic drawing of the measurement setup is shown in Fig. 7. There are two flow controllers (Bronkhorst ML120V21) and pressure controllers (Bronkhorst M19205673D) to apply the pure gases and binary gas mixtures into the sensor tube.

To measure k, a 2 mA DC current is applied to the wire, and the voltage across the wire is measured with a digital multimeter. Fig. 8 shows the measurement results together with the theoretical prediction and simulation results for comparison. The blue error bars show the voltage variations due to flow velocity changes from 0 to 40 g/h, confirming that the influence of flow is very small. The red error bars show the theoretical variations in k due to temperature changes. The calculated points are based on the thermal conductivity at $80°C$ and 1 bar from FLUIDAT (https://www.fluidat.com).

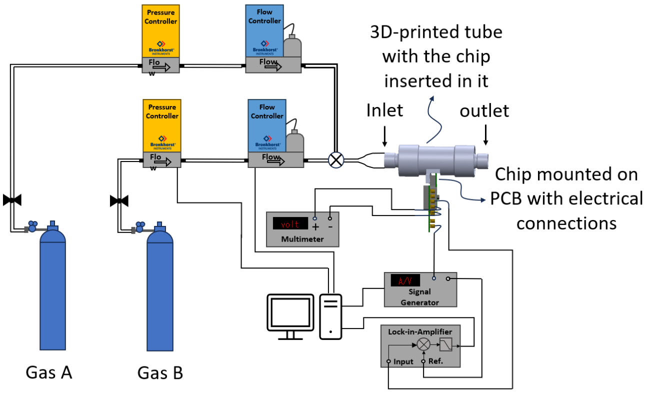

Figure 7: Schematic drawing of the measurement setup.

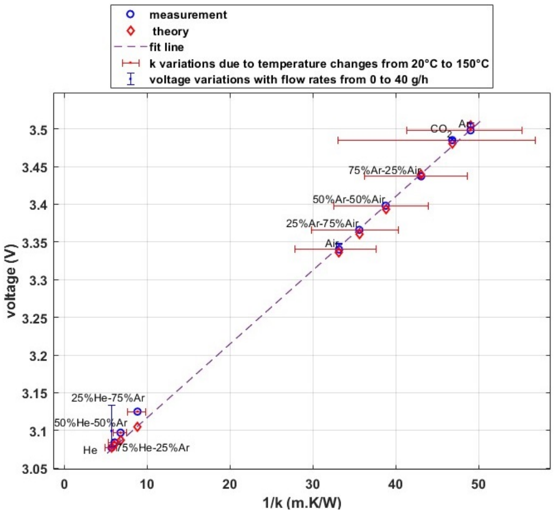

Figure 8: Voltage of the wire with a DC excitation of 2 mA. The voltage depends on the thermal conductivity of the pure and binary mixture of gases.

An AC current of 4 mA peak to peak is applied to the wire, and the third harmonic amplitude of the voltage is measured with a lock-in amplifier for the ρc_p measurement. Fig. 9 shows the third harmonic amplitude of the wire as a function of frequency. The derived frequency for the AC excitation must be higher than the cut-off frequency to contain the gas's volumetric heat capacity (C_{th}) as well as thermal conductivity (R_{th}) information. It is shown in Fig. 10 that the third harmonic component is a function of $k\rho c_p$.

The temperature of the wire is also simulated in COMSOL for four different gases, and the third harmonic voltage is calculated with a fast Fourier transform (FFT). The amplitude is plotted for three different frequencies. The red error bar shows the k variations due to the temperature. The measurement results show that a single wire suspended over a V-groove cavity can be used to measure thermal conductivity and volumetric heat capacity of gases through different types of excitation since the wire temperature is only dependent on the medium, not the fluid velocity. The dependency on the velocity is eliminated by positioning the wire perpendicular to the flow direction.

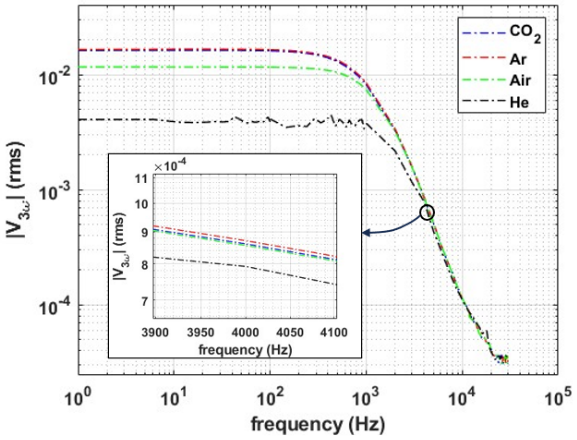

Figure 9: 3ω voltage amplitude of the wire as a function of frequency.

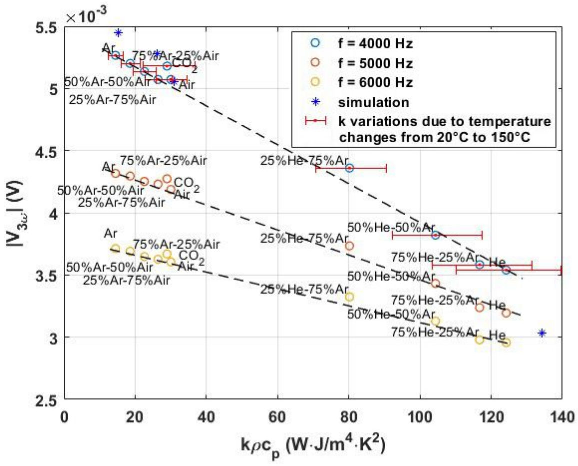

Figure 10: 3ω amplitude of the wire with an AC excitation of 4 mA (p-p). The amplitude depends on k and $k\rho c_p$ of the pure and binary mixture of gases.

CONCLUSION

A single wire suspended over a V-groove cavity is used to measure the fluid's thermal conductivity and volumetric heat capacity. DC excitation is applied to the wire and the voltage is measured to detect the thermal conductivity. AC excitation is used for detecting the volumetric heat capacity. The measurement results are compared to the theory and simulations. It is shown that a single wire can be used to measure the thermal properties of a fluid independent of the velocity. Only the measurements with helium show a small dependence on the flow velocity, because He is a very light gas which easily mixes with air entering from the outlet of the tube. The thermal conductivity and volumetric heat capacity ranges used in this paper are from 0.01652 $[\frac{W}{m \cdot K}]$ to 0.1554 and 864 to 1558 $[\frac{j}{K \cdot m^3}]$, respectively.

Future steps include using the physical parameters, thermal conductivity and volumetric heat capacity, of pure and binary mixtures of different gases to correct the flow rate of the proposed calorimetric flow sensor in [5].

ACKNOWLEDGEMENTS

The authors like to thank Bronkhorst High-Tech B.V. and TKI for financially supporting this project.

REFERENCES

[1] V. Balakrishnan, H.-P. Phan, T. Dinh, D.V. Dao, and N.-T. Nguyen, “Thermal flow sensors for harsh environments”, Sensors 17, 2017.

[2] D. F. Reyes, “Development of a medium independent flow measurement technique based on oscillatory thermal excitation”, Ph.D. dissertation, Albert-Ludwigs-Universität Freiburg, Breisgau, 2014.

[3] R. E. Bernhardsgrütter, C. J. Hepp, J. Wöllenstein, and K. Schmitt, “Fluid-compensated thermal flow sensor: A combination of the 3ω-method and constant temperature anemometry”, Sensors and Actuators: A. Physical 350, 2023.

[4] C.J. Hepp, F.T. Krogmann, G.A. Urban, ”Flow rate independent sensing of thermal conductivity in a gas stream by a thermal MEMS-sensor—Simulation and experiments”, Sens. Actuators A 253, 2017.

[5] S. Azadi Kenari, R. J. Wiegerink, R.G.P. Sanders, J.C. Lötters, “Thermal flow meter with integrated thermal conductivity sensor”, Micromachines 14, 2023.

[6] S. Azadi Kenari, R. J. Wiegerink, R.G.P. Sanders, J.C. Lötters, “Gas independent thermal flow meter based on real-time velocity-independent k And ρc_p measurement”, IEEE MEMS, Austin, USA, 21–25 January 2024.

CONTACT

* S. Azadi Kenari, s.azadikenari@utwente.nl

PARTICLE DETECTION IN FREE FALLING NANOLITER DROPLETS

F.Sturm[1], V. Zieger[1], P. Koltay[1], D. Frejek[2], S. Kartmann[1,2]
[1] Laboratory for MEMS Applications, IMTEK – Department of Microsystems Engineering,
University of Freiburg, Freiburg, Germany
[2]Hahn-Schickard, Freiburg, Germany

This work presents a system that can detect micrometer sized synthetic or biological particles within free-falling droplets with a volume of around 30 nanoliters. Different illumination modalities and detection algorithms were tested and detection accuracies of up to 95 % were achieved for polymer particles and MCF-7 spheroids with diameters above 80 µm. For smaller particles the detection accuracy was still in a range of 70 %.

This makes the demonstrated method suitable for improving the accuracy and quality control of particle detection in droplets for Drop-on-Demand techniques and for bioprinting.

KEYWORDS

Optical particle detection, Spheroid detection, Nanoliter dispensing, Drop-on-Demand, Glare point illumination, Bioprinting

INTRODUCTION

Lately, Drop-on-Demand approaches have been used to precisely deposit distinct amounts of spheroids, for example for drug screenings or in tissue engineering [1, 2]. The number of dispensed spheroids is usually tracked by monitoring the nozzle region of the dispenser head. However, this method depends on the optical transparency of the observed nozzle region and can therefore be disturbed by residual dirt on the nozzle. Additionally, the opaqueness of the meniscus region of the dispensing nozzle can obscure a particle, hence making the detection whether the particle has been dispensed or is hidden in the meniscus impossible. Therefore, we propose the detection of spheroids in dispensed free-falling droplets.

Solutions for characterization of droplets mainly focus on size and velocity of the droplets [3].

In contrast to that, Heinisch investigated content-dependent glare point changes on the droplet surface [4]. With that they were able to detect the position and size of enclosed air bubbles. Here, our goal is to use glare point changes to detect enclosed spheroids in droplets for more simplified, low-cost application.

THEORY

In order to optically detect particles inside a spherical object it is necessary to understand the propagation of light through the spherical object. Light scattering properties on droplets or translucent spherical particles is described by the Gustav Mie theory. It enables a way to simulate and characterize the scattering properties of all sizes of spherical objects depending on their material properties. For this purpose, the propagation of electromagnetic waves is considered. For spherical particles without an inclusion this theory can be easily applied and is already the basis of many measurement techniques. Nevertheless, for objects or droplets with an inclusion such as air bubbles or cellular aggregates this theory must be extended to a much more complex form which leads to increased computational efforts [5].

To investigate the light propagation for the illumination concepts in this work the ray optic theory is sufficient for a basic understanding. The light propagation that results for illuminating a droplet with different wavelengths can be seen in Figure 1.

From the point of geometrical ray optics, the droplet surface causes a refraction of the incident beam that hits the droplet surface. The ray enters a medium that has a higher refractive index than the ambient medium causing a refraction towards the center of the droplet. Subsequently, the light is partially reflected at the phase transitions from optically denser medium to optically thinner medium (ambient air) on the back of the droplet. A total reflection can be achieved depending on the droplet media and the incident angle.

The reflected light beam is pointed back to the front side of the droplet. In this way characteristic glare points become visible that depend on the droplet size, the incident angle of the light and the wavelength.

Enclosed particles cause changes in the described light propagation due to absorption and scattering effects.

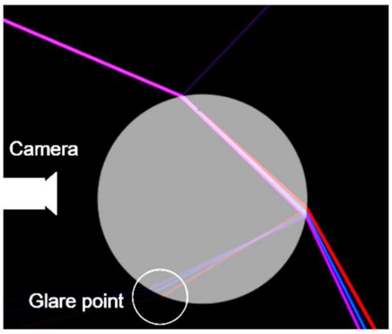

Figure 1: Simulation of the ray propagation of different wavelength (405 nm, 465 nm, 635 nm) hitting a droplet. The difference in the reflection results in slightly shifted position of the glare points depending on the wavelength.

For cellular aggregates like spheroids, organoids or microtissue the light penetration is limited by the different nonhomogeneous refractive index distributions which result from the different components of the cells. Changes in the speed and angle of the light propagation are induced and promote the scattering and absorption of the light [6].

These changes in light propagation, which depend on particles inside the droplet are expected to be visible as newly appearing glare points or changes in the size and brightness of the already present glare points on the droplet surface. However, this assumes that the light hits the particle during the propagation through the droplet.

MATERIALS AND METHODS

Spheroid culture

Spheroids are three-dimensional cell culture aggregates that can mimic tissue as well as micro tumors much better than two-dimensional cell culture models can do. They provide strong cell to cell bonds and the three-dimensional structure realistically mimics the resulting drug diffusion barrier. This makes spheroids especially interesting for drug and cancer research. [7]

In case of this study spheroids which are made of MCF-7 breast cancer cells are used. They are generated by means of the hanging drop method [1] or the use of Corning® Elplasia® 12K Flasks. The seeding concentration is chosen to generate spheroids with a diameter between 80 µm and 130 µm.

Illumination concept

Droplets with a volume of 30 nl are continuously dispensed by a non-contact piezoelectric dispenser (PipeJet, BioFluidiX, Germany). In a first step we use LED light with either 405 nm (violet), 465 nm (blue) or 635 nm (red) for the illumination of ejected droplets. The LEDs are arranged on top and bottom of a specially designed housing in an angle of 40° towards the optical axis of a CMOS camera and in an angle of 60° around the dispense axis as shown in Figure 2 & 3. The camera captures images triggered by the dispensing impulse signal of the PipeJet.

The light setup depicted in Figure 3 show the arrangement of four LEDs which are aligned posterior towards the camera. The setup with six LEDs contains two more LEDs which are additionally oriented anterior to the camera.

Image acquisition and evaluation

Calculating the mean value of pixel values of an image is one possibility to determine differences in images depended on the droplet inclusion.

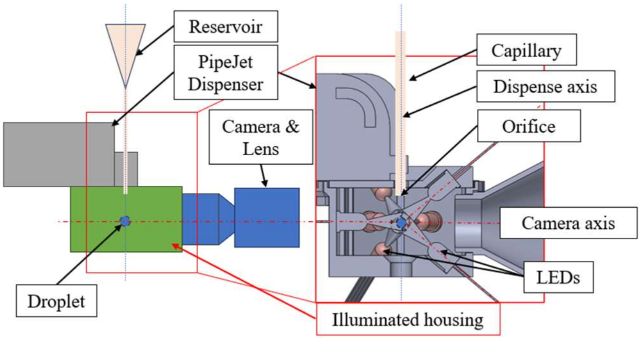

Figure 2: Housing, which includes the LEDs and adapts the camera as well as the dispenser for the detection of the droplets.

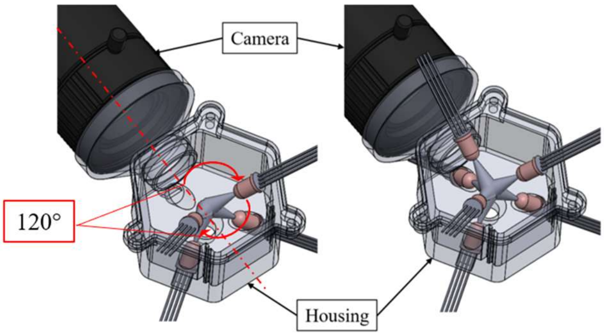

Figure 3: Left: Setup with four LED illumination posterior, Right: Setup with six LED posterior and anterior illumination.

Therefore, the images are first cropped to a size of 200 x 200 pixels. This is the range of image sizes that are well-suited for faster image processing and suits as well to the size of the droplets. In the second step a threshold (Otsu threshold) is applied to convert the image to a binary image. Now the number of white pixels is counted and divided by the total number of pixels of the image. Images of droplets that contain particles should have a higher number of white pixels. This is because the glare points change in their appearance, which leads to an increase in the number of white pixels. Consequently, the mean pixel value also increases. A threshold value is defined by calculating the average mean value of ten empty droplet images. A margin of 15 % of that value is added to define the particle detection threshold. All images of droplets above that threshold are considered to contain a particle. This method is entitled with white pixel count (WPC).

Another method to determine differences in images of droplets with or without an enclosed particle is the calculation of the droplet image similarity (DIS) which is determined based on the printing accuracy model developed by Fritz Koch [8]. It consists of three scores. One counts the number of black pixels that newly appear in an image compared to a reference image (OD). The other score counts the number of pixels that are missing compared to a reference image (UD). Both scores combined lead to the third score which gives the similarity of the captured image to the reference image (DIS). The reference image in case of the droplet images is calculated by averaging 20 images of empty droplets. The formulas of the scores as well as the determination of the scores by the image processing are shown in Figure 4. The binarization of the images is performed by applying the Otsu threshold to the images. By calculating the three scores, a detection can be counted as soon as two of the three scores simultaneously deviate from a defined threshold.

$$UD = \frac{missing\ pixels}{reference\ pixel} * 100\ \% \tag{2}$$

$$OD = \frac{additional\ pixels}{black\ pixels\ in\ captured\ image} * 100\ \% \tag{3}$$

$$DIS = 100\ \% - \frac{UD+OD}{2} \tag{4}$$

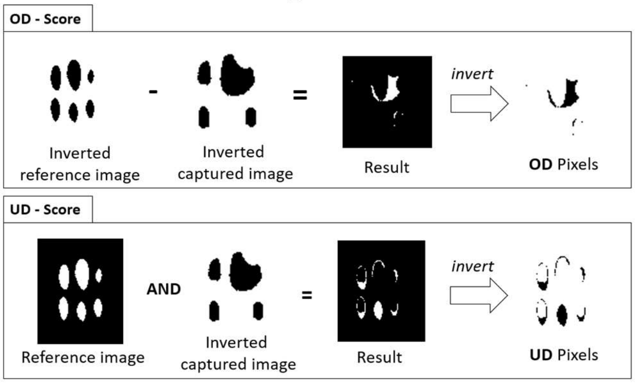

Figure 4: Image processing for calculating the droplet image similarity coefficient.

RESULTS AND DISCUSSION

Wavelengths and number of light sources

We first investigated the characteristic glare points of pure water drops depending on the anterior and posterior light modalities.

An even droplet illumination with characteristic, bright glare points was achieved with either anterior or anterior-posterior illumination for all wavelengths (see Figure 5). The main difference between the illumination concepts can be seen in the number of glare points on the droplet surface as well as in the different brightness levels of the glare points depending on the wavelength and number of light sources.

In further experiments MCF-7 spheroids within a size range of 80 µm up to 130 µm were cultivated, harvested resuspended in phosphate buffered saline (PBS) for printing. For the tests, five image series with 200 images in each series were captured with the spheroid PBS suspension. This process was repeated for each wavelength. The droplets are dispensed onto a microscope slide. After each run the number of spheroids that was dispensed was counted under the microscope. The images were evaluated manually and the number of images with a potential detection were counted by an experienced researcher. In Figure 6 exemplary images of droplets are shown. Either new bright points or large points with lower intensity appear as soon as a spheroid is encapsulated in the droplet. For 405 nm this effect is most pronounced.

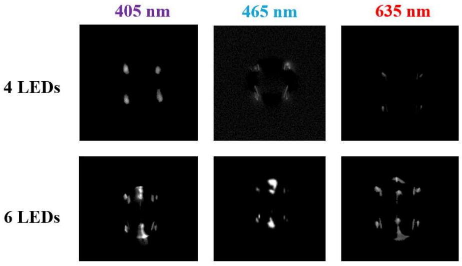

Figure 5: Empty droplets illuminated by four and six LEDs in the arrangement as shown in Figure 2 with different wavelengths.

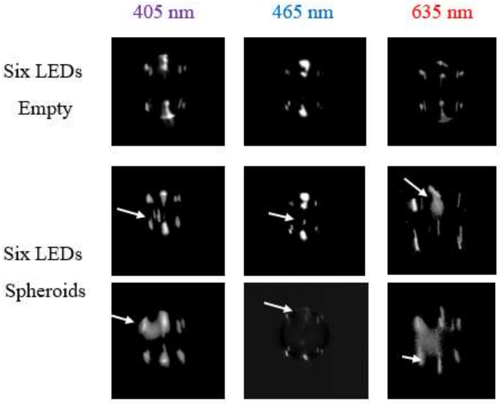

Figure 6: Series of captured images of droplets with different wavelengths of the illuminating light. The appearance of the spheroids is marked with arrows.

In the next step, the number of images in which the researcher detected a spheroid within the droplet as well as the number of spheroids counted by means of the microscope are compared to calculate the manual detection accuracy according to equation 1:

$$A = \frac{Counted\ particles\ images}{Counted\ particles\ microscope} * 100\ \% \tag{1}$$

The detection accuracy of the version with violet light was more constant and in average higher (93.8 %) than with red (59.2 %) and blue (84.3 %) light. The distribution of the accuracies can be seen in Figure 7.

Code assisted evaluation

For further experiments and to capture pictures that can be processed towards an automated evaluation only the setup with six 405 nm LEDs is considered. It showed the most promising results in terms of clearness of the glare points and difference between an empty

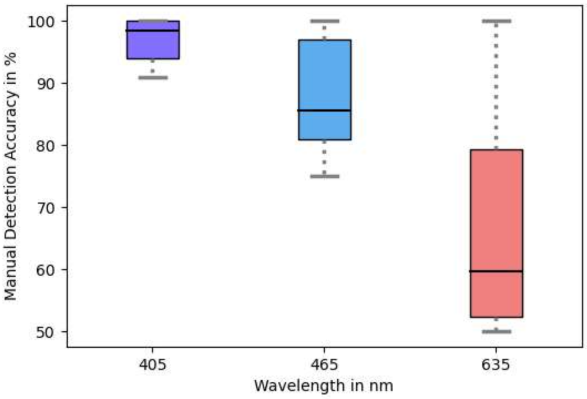

Figure 7: Particle detection accuracy of the different wavelengths. Each wavelength was tested five times with 200 images each time.

droplet and a droplet containing a spheroid.

In the next step, we evaluate the effect of the particle type on the detection accuracy. We use either blue colored polyethylene beads within a diameter range of 90 µm – 106 µm (cospheric BLPMS-1.08 Polyethylene microspheres) as well as within a diameter range of 45 µm – 53 µm (cospheric BLPMS-1.08 Polyethylene microspheres) and transparent polyethylene beads with a diameter of 75 µm (Polysciences Inc. Polybead, Polyethylene 75 µm).

For each particle three image series with 200 pictures each are captured and later evaluated by either the white pixel count or the droplet similarity algorithm as explained in the materials and methods section. After each run, the total number of dispensed particles is counted by means of a second camera which points towards the microscope slide onto which the droplets are dispensed. The number of particles varied between six and 30 particles per run, all other dispensed droplets did not contain any particle.

Table 1 shows the detection accuracies received with the two considered detection algorithms.

Both algorithms show a strong performance with particles that are larger than 75 µm. For particles which are below 75 µm, glare point changes get less significant and cannot be distinguished from noise effects. Noise can be caused by slight position shifts of droplets within the captured images e.g. due to trigger errors. This results in a default change of glare points due to changed incident illumination angle.

CONCLUSION & OUTLOOK

The concept study which was presented in this work showed that it is possible to determine if a particle is within a droplet by means of glare points that are projected onto its surface by 405 nm LED lights that are arranged in an anterior and posterior arrangement. Further, algorithms for the image analysis were proposed and tested. The achieved computer-based detection accuracy was in the same range as the detection accuracy achieved with manual image evaluation. The detection accuracy decreases for particles with a size smaller than 75 µm.

Nevertheless, this technique can help to improve the quality of Drop-on-Demand bioprinting process by a more precise determination of actual dispensed amounts of particles and therefore makes results in terms of drug screening research on the printed models more reliable.

Table 1: Accuracy of white pixel count (WPC) and droplet image similarity (DIS) compared to each other based on the same images.

Particles	**A – WPC [%]**	**A – DIS [%]**
Beads 90 – 106 µm	93,0 ± 2,2	95,0 ± 4,1
Beads 45 – 53 µm	73,7 ± 4,7	36,7 ± 15,3
Beads 75 µm	95,0 ± 7,1	95,3 ± 6,1
Spheroids 80 – 130 µm	88,7 ± 8,1	97,3 ± 3,8

REFERENCES

[1] L. Gutzweiler et al., “Large scale production and controlled deposition of single HUVEC spheroids for bioprinting applications”, Biofabrication Vol.9, 2017.

[2] J. Dornhof et al., “Bioprinting-based automated deposition of single cancer cell spheroids into oxygen sensor microelectrode wells”, Royal Society of Cemistry Lab Chip Vol. 22, p.4369-4381, 2022.

[3] C. Tropea, “Opticle Particle Characterization in Flows”, Annual Review of Fluid Mechanics, Vol.43 p.399-426, 2011.

[4] C. Heinisch, “Optische Messtechnik für umströmte Tropfen in einer neuen elektrodynamischen Falle“, Technische Universität Darmstadt, 2008.

[5] U. Kreibig, “Hundert Jahre Mie-Theorie. Optische Eigenschaften von Nanopartikeln.“ Physik in unserer Zeit 39, 2008

[6] E. C. Costa et al., “Optical clearing methods: An overview of the techniques used for the imaging of 3D spheroids”, Biotechnology and bioengineering, Vol.116, 2019

[7] W. Zhang et al., “Optimization of the formation of embedded multicellular spheroids of MCF-7 cells: How to reliably produce a biomimetic 3D model.

[8] F. Koch, “Quantitative assessment of generic processes to enable 3D-bioprinting of artificial tissue” Albert-Ludwigs-Universität Freiburg im Breisgau, 2023

CONTACT

* F. Sturm fabian.sturm@imtek.uni-freiburg.de,
V. Zieger viktoria.zieger@imtek.uni-freiburg.de

COMPACT MULTI-PARAMETER SENSING SYSTEM FOR IN-LINE DENSITY AND VISCOSITY MEASUREMENTS

J. Groenesteijn[1], *T.S.J. Lammerink*[2] *and J.C. Lötters*[1,2]
[1] Bronkhorst High-Tech BV, Ruurlo, The Netherlands
[2] University of Twente, Integrated Devices and Systems, Enschede, The Netherlands

ABSTRACT

We demonstrate a multi-parameter measurement system that combines a micro Coriolis mass flow meter with integrated up- and downstream pressure sensors. Using these sensors, the mass flow, density and pressure can be measured and the pressure drop over the chip and the dynamic viscosity of the fluid can be derived. Measurements using water, acetone, isopropanol and ethanol show an accuracy for pressure within 0.4%, for massflow within ±0.2% fullscale ± 1% reading, for density within 0.2% and for viscosity within 1.6% for a temperature range of 20°C to 30°C, input pressure between 4 and 6 bar and flow up to 5g/h.

KEYWORDS

Multi-parameter sensor, viscosity, density, massflow

INTRODUCTION

Advances in microfluidic flow sensors make it possible to measure and control very low flowrates, in the order of nanoliters per minute. However, it is becoming increasingly important to not only measure the flowrate, but to also measure physical parameters of the fluid that is being controlled. For this purpose, a micro Coriolis mass flow sensor has been integrated on the same chip with an upstream and downstream pressure sensor. Unlike other flow sensing principles, a Coriolis flow sensor measures true mass flow by detecting the inertial forces caused by a fluid flow through a vibrating tube, independent of fluid properties. The resonance frequency of this vibration depends on the mass of the tube and can thus be used to derive the density of the fluid inside the tube. The mass flow and density can be combined with the pressure drop, measured by the up- and downstream pressure sensors, to derive the viscosity of the fluid. The sensor chip and read-out electronics has been integrated into one compact tabletop housing as shown in Figure 1.

THEORY

The fabrication process used to fabricate the multi-parameter mass flow sensor is based on [1]. The sensor design is based on the micro Coriolis mass flow sensor with two in-line pressure sensors described in [2].

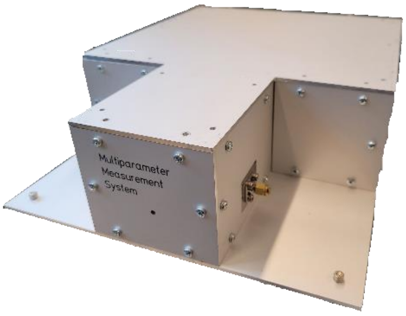

Figure 1: Photograph of the compact multi-parameter sensing system

Temperature

The temperature of the liquid inside the vibrating channel is measured using a metal track on top of the channel. The resistance of the metal track is related to the temperature via the temperature coefficient of resistivity:

$$\mathrm{R}_{track} = R_0\big(1 + \alpha(T - T_0)\big) \tag{1}$$

Where R_{track} is the resistance of the track, T_{track} the temperature of the track, R_0 the resistance of the track at reference temperature T_0 and α the thermal coefficient of resistivity. Since the track is right on top of the channel with the fluid, its temperature will be very close to that of the fluid.

Pressure

Figure 2 shows the operating principle of the integrated pressure sensors. The sensors uses metal resistors to measure the deformation of the flat ceiling of the channel. Four identical resistors are placed in a Wheatstone bridge configuration. When the pressure P is equal to the ambient pressure, the ceiling will be flat and all resistors will have equal resistance *R*. When a pressure is applied inside the channel, the flat ceiling will bend upwards. Two resistors, R2 and R3, are placed at the center of the channel and will elongate, increasing their resistance. Two resistors, R1 and R4, are placed at the edges of the ceiling and will be compressed due to the deformation of the ceiling, reducing their resistance. The output voltage of the Wheatstone bridge can then be calculated using:

$$V_{out} = \left(\frac{R_2}{R_1+R_2} - \frac{R_4}{R_3+R_4}\right)V_{in} \tag{2}$$

Where V_{out} is the output voltage, V_{in} the input voltage of the Wheatstone bridge and R_i the resistors on the channel.

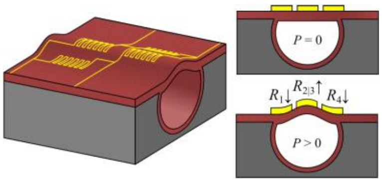

Figure 2: Operating principle of the resistive pressure sensors showing the deformation due to pressure.[2]

Mass flow

Figure 3 shows the basic operating principles of a Coriolis mass flow sensor [3]. A mass flow Φ_m through a free hanging channel, vibrating around rotational axis ω_{act} will cause a Coriolis force F_C along the side perpendicular to the rotational axis with length L_x. This force is proportional to the mass flow and can be calculated using [3]:

$$\overrightarrow{F_C} = -2L_x\left(\overrightarrow{\omega_{act}} \times \overrightarrow{\Phi_m}\right) \tag{3}$$

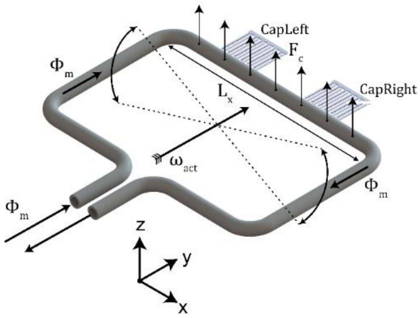

Figure 3: Operating principle of the Coriolis mass flow sensor showing the vibrating tube and the capacitive read-out structures.

This force will induce a secondary motion in the channel. The movement of the channel can be measured by placing two capacitive read-out structures on both sides of the rotational axis. This way the actuated movement will be measured 180 degrees out of phase. The movement caused by the Coriolis force will be an additional phase shift $\Delta\varphi$ between the two read-out signals:

$$\Delta\varphi = \tan^{-1}\left(\frac{\dot{C}_s}{\dot{C}_t}\right) \tag{4}$$

Where $\dot{C}_t$ is amplitude of the actuated twist mode, while $\dot{C}_s$ is the amplitude of the swing mode induced by the Coriolis force.

Density

Using the resonance frequency of the channel, the Coriolis mass flow sensor can also be used to derive the density of the fluid:

$$\omega_0 = \sqrt[2]{\frac{k_{eff}}{\rho_{fl}V_{ch}+m_{ch}}} \tag{5}$$

Where ω_0 is the resonance frequency, k_{eff} is the effective spring constant, ρ_{fl} is the density of the fluid, V_{ch} the volume inside the channel and m_{ch} the mass of the channel.

Viscosity

Using the above sensors, the dynamic viscosity μ_{fl}, can be calculated using the Hagen-Poiseuille equation:

$$\Delta p = \frac{128\mu_{fl}L\Phi_m}{\pi\rho_{fl}D_h^4} \tag{6}$$

Where Δp is the pressure drop between the upstream and downstream pressure sensors, L the length of channel between the pressure sensors and D_h the hydraulic diameter of the channel. This in shown schematically in Figure 4.

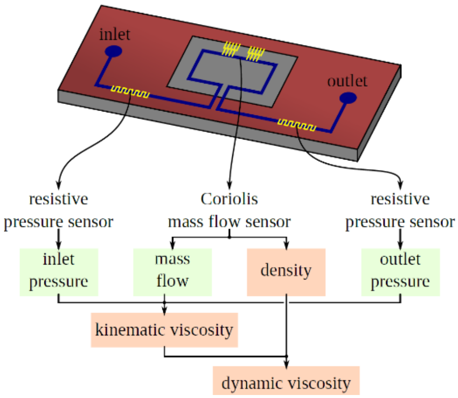

Figure 4: Overview off the integrated multi-parameter measurement system and the measured and derived parameters. [2]

Accuracy improvements

The various sensors on the chip can be used to derive extra parameters, but the accuracy of each measurement will limit the accuracy of any parameter derived from it. However, each measured parameter can also be used to compensate for cross sensitivity to that parameter in another sensor. For instance, the pressure sensors work because the channel will deform under pressure. This will also happen with the vibrating channel, changing the effective spring constant, k_{eff}, used in equation (5) to derive the density. By using the measured pressure in the tube, the sensitivity to pressure of the density and mass flow measurement can be reduced, reducing the measurement error over the whole measurement range.

MEASUREMENT SETUP

Figure 5 shows a schematic overview of the measurement setup. A Bronkhorst EL-PRESS P-602CV is used to apply a pressure to a vessel filled with the measurement liquids. The liquid is then degassed before it goes to the multi-parameter measurement system (MPMS). The MPMS is placed inside an incubator to be able to control the environmental temperature during the measurements. Finally, a Bronkhorst mini CORI-FLOW ML120V21 is used to control the liquid flowrate.

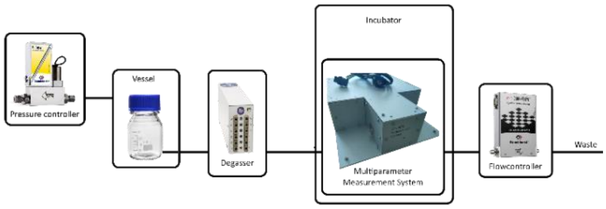

Figure 5: Schematic overview of the measurement setup.

The applied pressure is in the range of 4bar(a) to 6bar(a) in steps of 0.5bar, the flow is varied from 0g/h to 5g/h in steps of 0.5g/h and the temperature is varied from 20°C to 30°C in steps of 5°C. Note that the tube temperature is higher than the temperature of the incubator due to the power dissipated by the electronics inside the demonstrator and by the actuation track.

Table 1 shows and overview of the density and viscosity of the liquids used during the measurements. The shown values are at a temperature of 20°C and 1 bar(a). The theoretical density and viscosity used to calculate the error with the measured values is taken from [4] at the pressure and tube temperature measured by the MPMS.

Table 1: Density and viscosity at 20°C and 1bar(a) of the liquids used during measurements

Liquid	Density (kg/m^3)	Viscosity (Pa*s)
Water	998.2	1.018E-03
Isopropanol	792.6	2.311E-03
Acetone	791.4	3.174E-04
Ethanol	804.9	1.145E-03

MEASUREMENT RESULTS

Temperature

If there is a temperature difference between the channel and the fluid flowing through it, the channel will cool down. So, to measure the thermal coefficient of resistivity, measurements have been done without flow. This resulted in an thermal coefficient of resistivity of 0.00123/K which is in accordance of values previous measured for these tracks.

Pressure

Alveringh et al [2] have shown that the used pressure sensors have a linear relation with pressure when measured at constant temperature. However, a small imbalance in the four measurement resistors will introduce an offset that depends on the resistance of each resistor and thus on temperature. This can be seen in Figure 6, which shows the measurement error of the inlet pressure sensor and the applied pressure by the pressure controller when there is no flow and a linear relation is assumed as proposed in [2]. The three different temperature setpoints can be clearly seen when temperature is not included in the fit (blue markers). The measurement error is improved to better than ±0.4% for all liquids, temperatures and pressures when a polynomial surface fit is done which also includes the measured tube temperature (red markers). The outlet pressure sensor shows similar improvements.

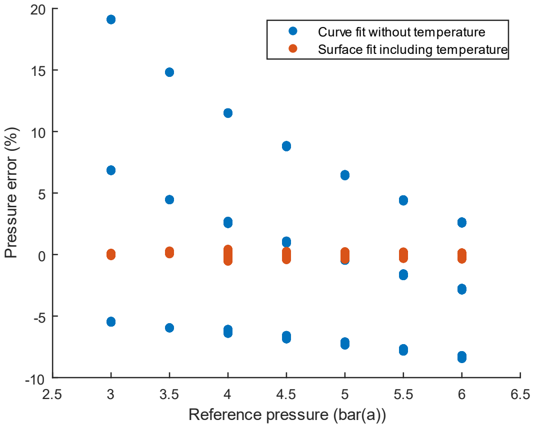

Figure 6: Measurement error of the inlet pressure sensor with and without temperature compensation

Density

Equation (5) shows that the density can be derived by measuring the resonance frequency, however the effective stiffness of the channel is sensitive to temperature and deformation due to pressure. By including the measured temperature and pressure, the density measurement was improved from a maximum error of ±1% to ±0.25%. The error of the final model for each fluid is shown in Figure 7.

Mass flow

While the Coriolis mass flow principle itself is independent of fluid and environmental parameters, the mechanical resonance structure is not. Deformation due to pressure and different thermal expansion coefficients of the used materials will change how far

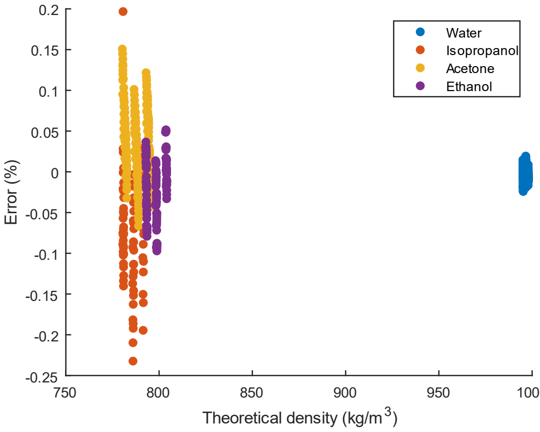

Figure 7: Error between the density as measured by the DUT and the theoretical density from [4] at the measured temperature and pressure.

the electrodes of the capacitive read-out are from each-other and thus the zero-flow position. Similarly, the density of the fluid will change the resonance frequency and thus ω_{act} in equation (3). By using not only the phaseshift, but also the temperature, pressure and frequency while fitting, the accuracy of the Coriolis massflowmeter is increased to ±0.2% fullscale ± 1% reading as shown in the Trumpet curve in Figure 8.

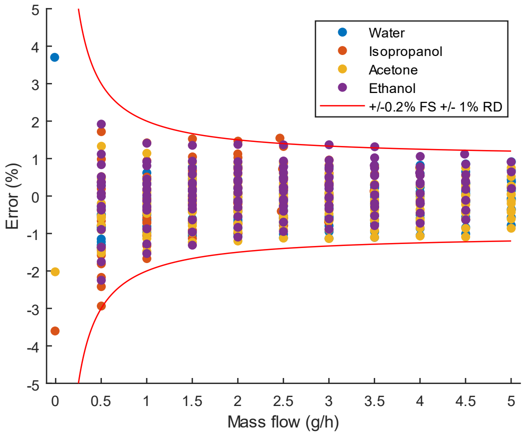

Figure 8: Error between the flow as measured by the DUT and the reference flow controller

Viscosity

Equation (6) assumes straight circular channels, however, this isn't the case for the microchannels used in the MPMS, which means that filling in equation (6) would result in large errors mainly based on temperature and geometrical parameters. By using the measured parameters (pressure drop, density and mass flow) in equation (6) and fitting for the temperature and geometrical parameters, the viscosity can still be derived. Since this relies on the presence of a pressure drop, a minimum flow of 2g/h is used. The error for all liquids is within ±20μPa*s. This means that for all liquids, except acetone, the error is within ±1.6% as shown in Figure 9.

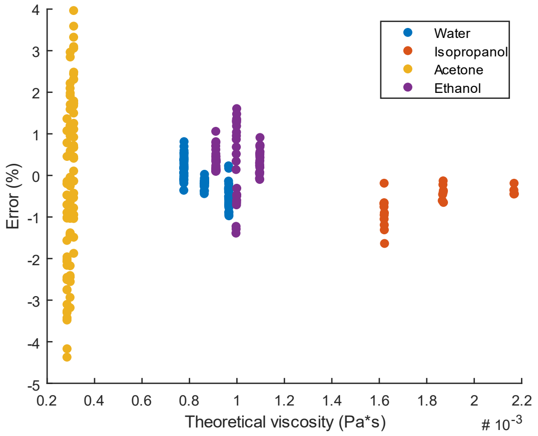

Figure 9: Error between the viscosity as measured by the DUT and the theoretical density from [4] at the measured temperature and pressure.

CONCLUSION

We demonstrate a tabletop multi-parameter measurement system that combines a micro Coriolis mass flow meter with integrated up- and downstream pressure sensors. By combining the measurement data of these sensors, the individual measurements can be improved and new parameters, density and viscosity, can be measured. The accuracy reached for viscosity measurement is competitive with state-of-the-art micro-pipe viscometers [5], but offers the advantage of a single tabletop instrument that also provides measurements of pressure, mass flow and density.

REFERENCES

[1] J. Groenesteijn et al., Microfluid Nanofluid 21, 2017, pp. 127, doi: 10.1007/s10404-017-1961-0
[2] D. Alveringh et al., 19th International Conference on Solid-State Sensors, Actuators and Microsystems (TRANSDUCERS), Taiwan, 2017, pp. 1167-1170, doi: 10.1109/TRANSDUCERS.2017.7994261.
[3] J. Haneveld et al., Journal of Micromechanics and Microengineering, vol. 20, no. 12, 2010, doi:10.1088/0960-1317/20/12/125001
[4] Fluidat on the net; 2023. Available from: https://www.fluidat.com/default.asp.
[5] H. Bissig et al. Biomedical Engineering / Biomedizinische Technik, 68(1), 39-50, doi: 10.1515/bmt-2022-0039

CONTACT

* J. Groenesteijn, J.Groenesteijn@Bronkhorst.com

CALIBRATION OF FLOW DEVICES UNDER ACTUAL FLOW CONDITIONS WITH INLINE MEASUREMENT OF THE VISCOSITY OF THE LIQUID

H. Bissig, M. de Huu
Federal Institute of Metrology METAS, Bern, Switzerland

ABSTRACT

In order to simulate any dosing process, calibrations of flow devices with the process-oriented and dynamic flow profile changes are performed under actual flow conditions and liquid properties (e.g. dynamic viscosity). METAS has developed facilities with METAS piston provers to address the issue of measuring with process-oriented liquids and non-constant flow profiles. Moreover, the gravimetric method has been upgraded with a so-called capillary beaker allowing the characterisation of flow generators such as high precision syringe pumps or insulin pumps. Additionally, a pipe viscometer has been implemented in the Milliflow facility where the dynamic viscosity of the liquid is determined under actual flow conditions. This allows the calibration of flow devices for traceable flow rates and dynamic viscosity of the liquid.

KEYWORDS

Calibration, process-oriented liquid, dynamic flow profile changes, pipe viscometer

INTRODUCTION

Dosage of process liquids or accurate measurement of the flow rate are processes applied in industries for pharmaceutical, flow chemistry and microfluidic applications. The calibration of flow meters or microfluidic devices with the process-oriented liquids is important, because some sensor technologies depend on fluid properties [1]. Performing dynamic flow profile changes to simulate any dosing process gives important insight in the behavior of these flow devices and their accuracies under actual flow conditions and liquid properties such as the dynamic viscosity.

METAS has developed facilities with METAS piston provers and the implementation of a pipe viscometer to address the issue of measuring non-constant flow profiles with process-oriented liquids, where the dynamic viscosity of the liquid can be determined under flow conditions. Moreover, the gravimetric method has been upgraded with a so-called capillary beaker allowing the characterisation of flow generators. The upgraded METAS facilities as well as characterisation and validation measurements will be described in this paper.

METAS FACILITIES

METAS Piston Prover

METAS has developed facilities with METAS piston provers to address the issue of measuring with process-oriented liquids non-constant flow profiles for flow rates as low as 20 nl/min (see Figure 1) [2-4].

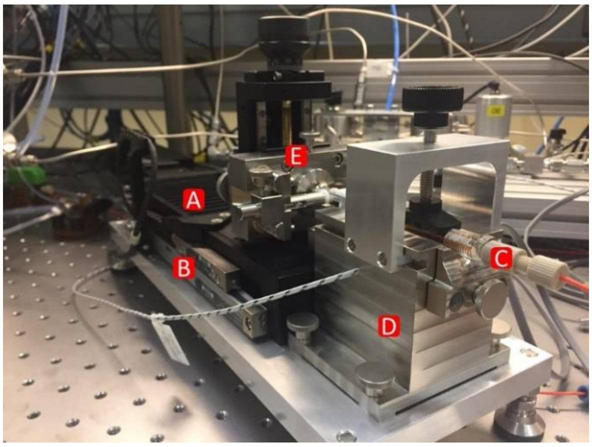

Figure 1: METAS piston prover of the Microflow facility. (A) high precision linear stage, (B) linear measuring system, (C) syringe, (D) mounting syringe body, (E) mounting and positioning for syringe plunger. The same design and components are used for the METAS piston prover of the Milliflow facility, but with a different speed range.

Upgrade gravimetric method

The gravimetric method of the Microflow facility has also been upgraded with a so-called capillary beaker, where a vertically mounted capillary is used to collect the water by placing the outlet needle inside the top of the capillary (Figure 2) [3,5].

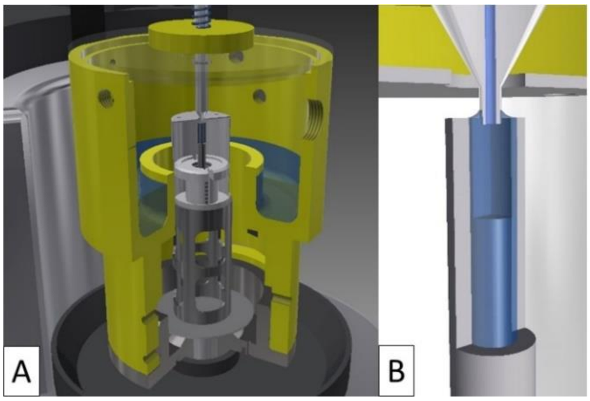

Figure 2: (A) Weighing zone on the balance of the Microflow facility showing outlet needle and beaker with cover. (B) Insight into the contact of the outlet needle in the capillary.

The gravimetric methods of the Microflow and Milliflow facilites use also a similar glass filter beaker, which contains a vertically mounted glass filter, where the outlet needle is positioned just above the glass filter avoiding droplet formation for a continuous collection of the water. (see Figure 3) [2,3]. Thus, the water contact between the outlet needle and the glass filter remains the same, independent on the water level inside the beaker.

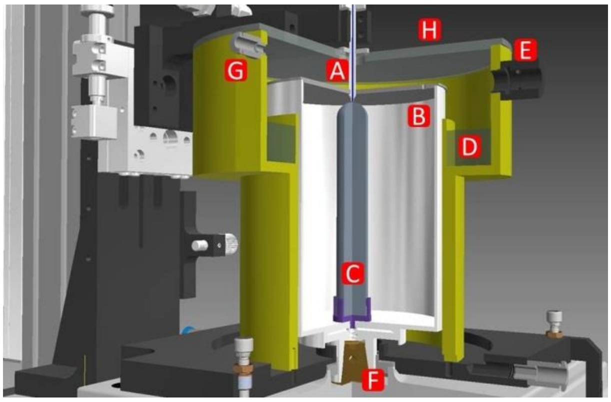

Figure 3: Weighing zone on the balance of the Milliflow facility. (A) outlet needle, (B) beaker with cover, (C) glass filter, (D) water in evaporation trap, (E) mount for T and rH sensor, (F) balance, (G) tubing for humidity exchanger.

Dynamic flow profiles

Similar to the determination of the steady flow rate, the collected weighing data and the data of the linear measuring system are fitted by means of a least square linear fit to obtain the instantaneous flow rate [2,3]. In this case we choose a fixed time window as short as 0.5 s to perform the least square linear fit to determine the flow rates of the piston prover and as well the dynamic gravimetric method. By shifting the starting time of the fixed time window by each time step the instantaneous flow rates can be determined continuously in time as shown in Figure 4.

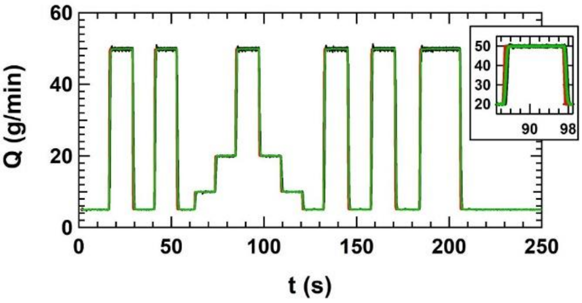

Figure 4: The determined mass flow rate Q of the gravimetric method (black line), the piston prover (red line) and the Coriolis flow meter (green line) as a function of time t.

For these measurements at the Milliflow facility the glass filter beaker is used and the change of the capillary force at the flow rate changes are slightly visible. These measurements allow the characterization of the response time of the Coriolis flow meter Cubemass DCI DN01 from Endress+Hauser AG with incompressible and compressible liquids as mentioned in the reference [3].

Dynamic flow profiles were performed with the thermal flow meter: L01 from Bronkhorst High-Tech B.V. for flow rates below 100 nL/min with the Microflow facility, where the capillary beaker was used to collect the water for the gravimetric method. Three cycles were measured after a stabilisation time of 2 h with the L01 as shown in Figure 5.

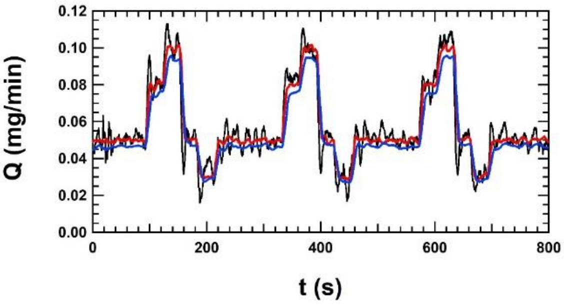

Figure 5: Dynamic flow profile generated by the piston prover (red line) and measured with a thermal flow meter (blue line). The gravimetric method (black line) is also shown.

Obviously, the data from the gravimetric method are noisy due to the fact that we use a fit window of only 5 s and that the gravimetric method (black line) is getting to its limits for such short fit windows at these low flow rates. The influence of the variation of the capillary forces at the water contact between the outlet needle and the capillary gets more important than at higher flow rates. The piston prover measures directly the position of the plunger with the linear measuring system and therefore corresponding instantaneous speed. The deviation of the flow meter can be determined for each of the plateaus (constant flow rates) of the three cycles and the average of several deviations at each flow rate is calculated and shown in Figure 6 as full red circles. The average of the flow rates over a full cycle can also be analysed. The deviations determined by the piston prover or the gravimetric method are shown as open red circle or open black circle in Figure 6.

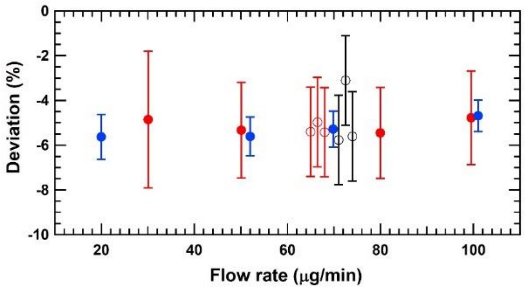

Figure 6: The deviations of the thermal flow meter. Constant flow calibration (full blue circle), plateau values from dynamic flow profile calibration (full red circle). Calibration over a full cycle with piston prover (open red circle) and with the gravimetric method (open black circle).

These deviations from the dynamic flow profile measurements are compared to the deviations obtained from constant flow calibration over several hours (full blue circle). The results are consistent even for these short measurement times.

Validation METAS facilities

The piston prover and the gravimetric method have been validated by means of an European interlaboratory comparison EURAMET project 1508 "Pilot study: Intercomparison of ultra-low liquid flow rates in range below 100 nL/min", where the METAS calibration results of two thermal flow meters and a flow generator are consistent with the reference value [4,7].

CHARACTERISATION INSULIN PUMP

The characterization of insulin pumps is discussed as example of discontinuous flow. The pump mechanism of the insulin pump consists of a stepper motor that moves the plunger in one or more steps, which pushes forward the piston in the container to deliver a discrete dose of insulin in a given cycle time.

The delivery of discrete doses is visible in the raw data of the gravimetric method and the optical front track method, as shown in Figure 7 [6]. The weight increase of the gravimetric method shows a significant increase followed by a flattening of the curve before the delivery of the next dose (Figure 7, black line). The same behaviour is observed for the front track methods, shown as blue and red lines.

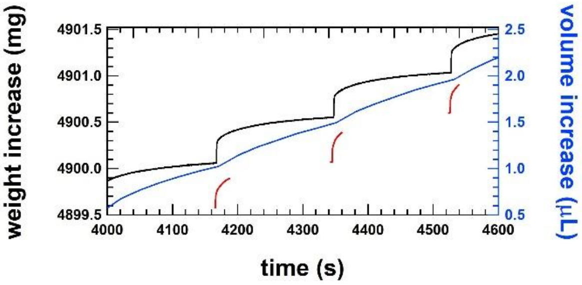

Figure 7: Smooth step increase of the weight of single shots of the order of 500 nL at a cycle time of 3 minutes for a flow rate of 10 µL/h or 1.0 U/h measured by the gravimetric setup at METAS (black line), by the front track setup at IPQ (blue line) and by the front track setup at THL (red line) [6].

The red line is discontinuous because the optical front track method at THL is limited to a measurement time of 167 s and the gaps are caused by the time needed to transfer the images from the high-speed camera to the PC. Nevertheless, the increase of the position for a dose can be calculated from the positions prior the increase.

The blue line representing the position data of the optical front track method at IPQ shows step increases that are heavily smoothed out. This is due to the fact that the tubing is not very stiff and the pressure wave caused by the dose is absorbed by the tubing, resulting in a very smooth increase in position due to pressure relaxation. Nevertheless, the single doses can be identified by the wave-like increase in position.

The histogram of the weight increments is shown in Figure 8, where the average of the discrete dose volume is 496.6 nL with a standard deviation of 21.2 nL, resulting in a deviation of +0.68 %. Furthermore, the corresponding cycle times of the discrete doses range between 179.80 s and 180.30 s with a mean value of 180.00 s.

The cycle time of the discrete doses is an important time constant for calculating the average flow rate of such smooth step functions. The average flow rate must be calculated over a time window which is an integer multiple of this cycle time to avoid accounting for an artefact from the analysis method [6].

This discrete dose analysis method also makes it possible to detect irregularities from an insulin pump with its infusion set. However, the stabilization time of the measurement setup must comply with the requirements in order to not misinterpret irregularities at the beginning of the measurements.

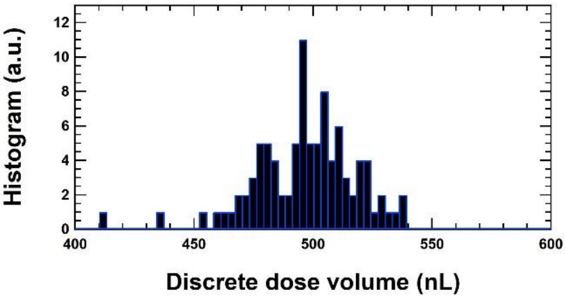

Figure 8: The dose volumes at 10 µL/h for the measurements at METAS are represented in a histogram. The average of the dose volumes is 496.6 nL.

METAS PIPE VISCOMETER

Setup Pipe Viscometer

The micro pipe viscometer consists of a flow generator (piston prover) connected to a tube (see Figure 9).

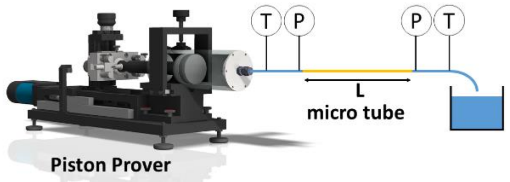

Figure 9: Schematic setup of the pipe viscometer. Temperature and pressure sensors upstream and downstream of the micro tube.

Appropriate temperature and pressure sensors are installed upstream and downstream of the micro tube to determine the pressure drop as a function of flow rate for the calculation of the dynamic viscosity of the liquid.

A detailed description of the METAS Pipe Viscometer can be found in the references [8,9].

Validation Pipe Viscometer

The validation of the micro pipe viscometer has been performed with eight different liquids typically found in hospitals [8]. The kinematic viscosity of these liquids are also calibrated with conventional capillary viscometers (instruments with sampling) and converted to dynamic viscosity with the measured density. The results show the consistency between these conventional capillary viscometers and the micro pipe viscometers, as can be seen in Figure 10.

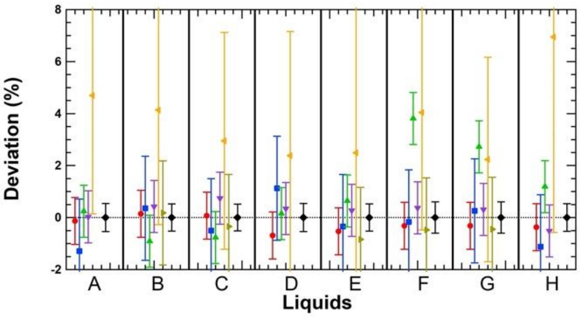

Figure 10: Results for the deviations of the dynamic viscosity measurements performed by the different laboratories with respect to the reference value after applying the χ^2-test consistency check. METAS (red circle), RISE (blue square), NEL (green triangle up), EIM (violet triangle down), IPQ (orange triangle left), KRISS (dark yellow triangle right), Reference value (black diamond) [8,10]

CONCLUSION

The METAS piston provers and the upgraded gravimetric methods for measuring non-constant flow profiles as well as the pipe viscometer for measuring the dynamic viscosity have been described as an overview of the upgrade of the flow facilities at METAS. Details of the presented characterisation and the validation measurements can be found in the references mentioned in this paper.

Most of the work has been performed in the framework of the EMPIR project 18HLT08 MEDDII [11]. The project 18HLT08 MEDDII has received funding from the EMPIR programme co-financed by the Participating States and from the European Union's Horizon 2020 research and innovation programme.

REFERENCES

[1] H. Bissig, M. Tschannen and M. de Huu, "Liquid properties effects on Coriolis and thermal mass flow meters at very low flow rates", Proceeding Paper, Flomeko Conference, Lisbon, Portugal, 2019. https://www.imeko.org/publications/tc9-2019/IMEKO-TC9-2019-003.pdf

[2] H. Bissig, M. Tschannen and M. de Huu, "Recent Innovations in the field of traceable calibration of liquid milli-flow rates with liquids other than water", Proceeding Paper, Flomeko Conference, Sydney, Australia, 2016

[3] Bissig H, Tschannen M and de Huu M, "Dynamic vs constant liquid flow calibrations down to 20 nL/min", Proceeding Paper, Flomeko Conference, Chongqing, China, 2022. https://www.imeko.org/publications/tc9-2022/IMEKO-TC9-2019-135.pdf

[4] Mills C, Batista E, Bissig H et al. "Calibration methods for flow rates down to 5 nL/min and validation methodology" *Biomedical Engineering / Biomedizinische Technik*, vol. 68, no. 1, 2023, pp. 13-27. https://doi.org/10.1515/bmt-2022-0049

[5] Wright J D and Schmidt J W, "Reproducibility of Liquid Micro-Flow Measurements", in *Flomeko Proc.*, 2019. https://www.imeko.org/publications/tc9-2019/IMEKO-TC9-2019-097.pdf

[6] H. Bissig, O. Büker, K. Stolt et al. "Calibration of insulin pumps based on discrete doses at given cycle times" *Biomedical Engineering / Biomedizinische Technik*, vol. 68, no. 1, 2023, pp. 67-77. https://doi.org/10.1515/bmt-2022-0040

[7] NEL, "Pilot study intercomparison of ultra-low liquid flow rates in range below 100 nL/min", Reg. No. 1508. https://www.euramet.org/technical-committees/tc-projects/

[8] H. Bissig, O. Büker, K. Stolt et al. "In-line measurements of the physical and thermodynamic properties of single and multicomponent liquids" *Biomedical Engineering / Biomedizinische Technik*, vol. 68, no. 1, 2023, pp. 39-50. https://doi.org/10.1515/bmt-2022-0039

[9] S. Neuhaus, H. Bissig, B.A. Bircher and M. de Huu. "Presentation of the METAS pipe viscometer", in *Flomeko Proc.*, 2022. https://www.imeko.org/publications/tc9-2022/IMEKO-TC9-2019-062.pdf

[10] H. Bissig, O. Büker, K. Stolt et al. "First comparison of inline measurements of dynamic viscosity", in *Flomeko Proc.*, 2022. https://www.imeko.org/publications/tc9-2022/IMEKO-TC9-2019-061.pdf

[11] EMPIR project 18HLT08 MEDDII, https://www.drugmetrology.com

CONTACT

* H. Bissig, hugo.bissig@metas.ch

MICROFABRICATION TECHNOLOGY FOR ISOLATED SILICON SIDEWALL ELECTRODES AND HEATERS

Maarten J.S. Bonnema[1], *Henk-Willem Veltkamp*[1], *Remco J. Wiegerink*[1], *and Joost C. Lötters*[1,2]
[1]MESA+ Institute for Nanotechnology, University of Twente, The Netherlands, and
[2]Bronkhorst High-Tech B.V., The Netherlands

ABSTRACT

This paper presents a novel microfabrication technology for highly doped silicon sidewall electrodes parallel to – and isolated from – the microchannel. The sidewall electrodes can be utilised for both electrical and thermal actuation of sensor systems. The technology is scalable to a wide range of channel geometries, simplifies the release etch, and allows for further integration with other Surface Channel Technology-based systems. Furthermore, the fabrication technology is demonstrated through the fabrication of a relative permittivity sensor. The sensor measures relative permittivity values ranging from 1 to 80, within 3% accuracy of full scale, including water and water-containing mixtures.

KEYWORDS

Microfabrication, Surface Channel Technology, sidewall heating elements, sidewall electrodes.

INTRODUCTION

The miniaturisation of microfluidic systems, including sensor and actuator blocks and their interconnects, is often limited due to the large variety of fabrication techniques and materials that are used [1,2]. Monolithic approaches can significantly enhance the integration of microfluidic systems [3].

Moreover, the positioning of the electrodes and heaters is essential in the design, actuation, and read-out of sensor and actuator systems. Thermal flow sensors currently use heaters on top of the microchannel, resulting in significant heat loss and large thermal gradients across the microchannel [2,4]. 3-D heater structures, like additional sidewall heating elements (SHEs), can significantly reduce these gradients and losses [5]. Similarly, relative permittivity sensors that use electrodes only on one side of the microchannel, yield large parasitic capacitance [3], that can be overcome by the additional sidewall electrodes. Furthermore, the release step of microfluidic channels is often performed using multi-step dry etching approaches [2,6,7]. These techniques are often more expensive and have more complicated process parameters than wet etching.

This paper starts with an overview of the proposed fabrication technology, divided into three main phases. Secondly, intermediate and overall fabrication results are presented. Lastly, the proposed technology is demonstrated through a relative permittivity sensor.

FABRICATION METHOD

A complete overview of the process flow is shown in Figure 1. The process can be divided into three main phases: the layout of microfluidic channels and sidewall electrodes or SHEs, the channel formation, and the metallisation and release etch. Afterwards, the main advantages of the proposed technology over conventional methods are considered. The fabrication flow is designed for highly doped (*p*+-type in this work) silicon wafers with a ⟨100⟩ crystal orientation. However, the process is also suitable for other doping types and a large range of doping levels.

1. Isolating Trench Formation

The process starts with etching 3 µm wide trenches into the silicon substrate. The layout of the trenches defines the width of both the microchannels and the electrodes. From an electrical point of view, the trenches ensure a capacitive contact with the fluid. Additionally, for heater purposes, the contact area of the heaters with the fluid should be maximised to enhance heat transfer.

Firstly, the silicon wafer is thermally oxidised using wet oxidation to grow a 1.5 µm layer of thermal SiO_2 (t-SiO_2) serving as a hard mask. By means of UV-photolithography and CHF_3/O_2-based reactive ion etching (RIE), the layout of the trenches is patterned in the t-SiO_2 (Figure 1a). When designing trenches with T-junctions, it is essential to incorporate indentations. The indentations guarantee that the width of the trenches does not exceed 3 µm, ensuring adequate refilling later on in the process. The trenches are realised via a two-step Bosch-based process: a layer of C_4F_8 is deposited, after which a single step is used for both the breaking of the C_4F_8 at the bottom of the trench and etching of silicon beneath. An aspect ratio of approximately 20 is achievable without significant tapering. Subsequently, the t-SiO_2 hard mask is stripped using 50% HF (Figure 1b). Before the trenches are refilled, the wafers are thoroughly dried via a heated nitrogen gas flow for two days. The refilling is done by a conformal low-pressure chemical vapour deposition (LPCVD) of 1.6 µm of low-stress (50 MPa) silicon-rich silicon nitride (SiRN) [8] (Figure 1c). To enhance the uniformity of the substrate – hence reducing the inherent V-grooves at the refilled trenches – the SiRN

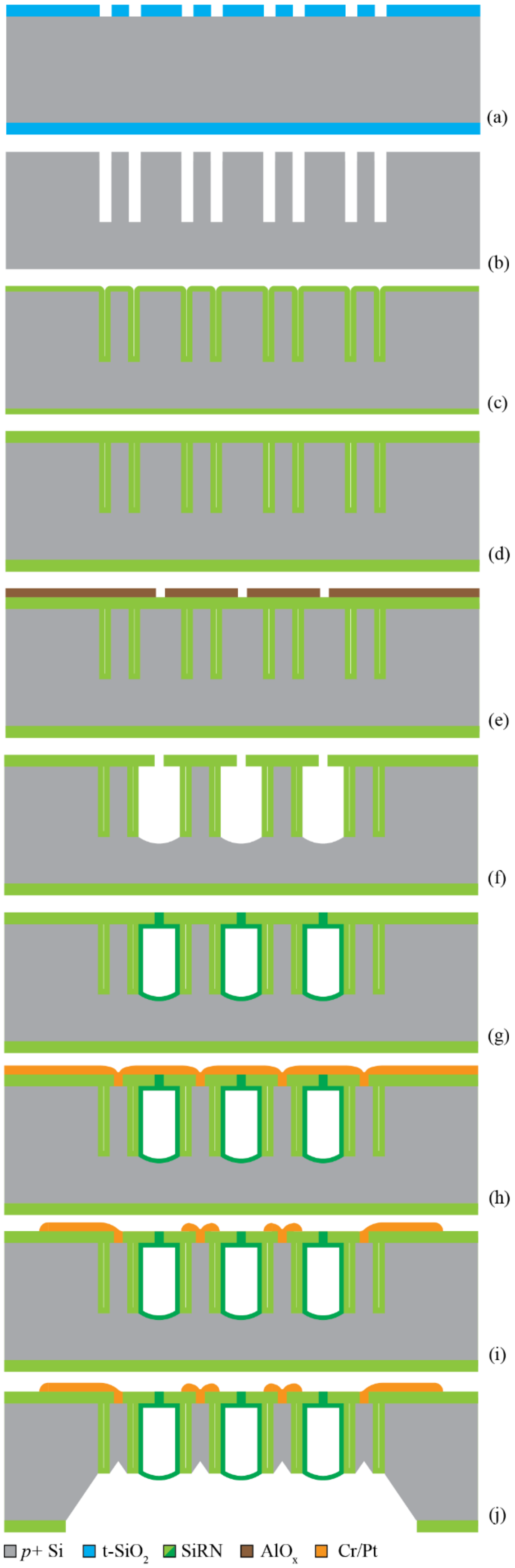

Figure 1: Fabrication process flow with cross-sectional schematics, (a) until (j), for three parallel microchannels having isolated silicon electrodes in the sidewalls.

layer is etched back using CHF_3/O_2-based RIE. This etch is performed on both sides of the wafer to reduce internal stresses and curvature of the wafer. A new and more uniform layer of 500 nm SiRN is deposited via LPCVD (Figure 1d).

2. Channel Formation

The second phase concerns the formation of the microchannels. The channels are etched through a slit pattern in the SiRN. The depth of the channel is – besides the etch time – controlled by the density of slits, defined as $\rho_\mathrm{s} = A_\mathrm{s}/A_\mathrm{u}$, where A_s is the area of the slit and A_u the area of the unit cell containing the slit. Due to the low selectivity and harshness of the SF_6-based channel etch [3], another hard mask is required. For this purpose, a 200 nm layer of AlO_x is e-beam evaporated on the front side of the substrate. A pattern of slits of 2 µm wide and 4 to 8 µm long – depending on the local ρ_s – is transferred into the hard mask by a UV-photolithography step in combination with a BCl_3/HBr-based inductively coupled plasma RIE (ICP-RIE) (Figure 1e). Using an SF_6/O_2-based ICP-RIE, the slit pattern is transferred into the SiRN layer. The channels are semi-isotropically etched using SF_6 with 4 kW of ICP power. The depth of parallel channels should not surpass the depth of the trenches, which is controlled by the etch time. The remaining AlO_x layer is removed using HF (Figure 1f). Before the microchannels are sealed, the wafer is again thoroughly dried using a heated nitrogen flow. The sealing of the microchannels is done using another LPCVD of 1.6 µm of low-stress SiRN. Simultaneously, the channel walls are formed by a thin layer of SiRN (Figure 1g).

3. Metallisation and Release Etch

The last phase is the metallisation and the release etch, during which the electrodes are contacted and isolated. These two steps are strongly dependent on each other and should thus be considered simultaneously. Via UV-photolithography and a CHF_3/O_2-based RIE step, contact windows to the highly doped silicon are realised. The resulting native SiO_2 layer is removed using a vapour HF etch. After which a layer of 5 nm Pt is immediately sputtered. To reduce the contact resistance, the Pt is annealed at 400 °C to form low-ohmic PtSi. The metal stack is completed by sputtering another 10 nm of Cr and 200 nm of Pt (Figure 1h). The Cr layer serves as an adhesion layer to the SiRN underneath. The metal stack is patterned by a UV-photolithography step followed by an Ar-based ion beam etch (Figure 1i). The last step is the release of the microchannel structure, required to isolate the individual highly doped silicon electrodes. At the back side, release windows are opened in the SiRN layer by a UV-photolithography step followed by a CHF_3/O_2-based RIE step. The entire structure is released via a self-limiting etch step: submerging the wafer in 25% wt. diluted KOH at 75 °C (Figure 1j). When the deposited metals are unaffected by KOH [9], the fabrication process simultaneously allows for release windows at the front side of the substrate. Otherwise, a clamp is needed during etching.

The proposed fabrication method has multiple advantages compared to conventional methods. Firstly, the widths and heights of the microchannels can be scaled to a large extent. Additionally, within the same design and fabrication process, different channel depths and widths can be realised. Secondly, the silicon sidewall electrodes are fully isolated from the fluid flowing through the microchannel by a chemically inert layer of SiRN. Moreover, the electrodes can also be utilised as silicon SHEs through Joule heating, due to the high stress tolerance of SiRN, as demonstrated in [6]. Thirdly, large sensor or actuator structures can be released simultaneously in this process. Furthermore, this release etch is a self-limiting process, simplifying the fabrication.

RESULTS

After the first phase of the fabrication process, a cross-sectional scanning electron microscope (SEM) image is made. Figure 2 shows an SEM image of four refilled trenches spaced 5 and 40 µm apart, with a close-up of the remaining V-groove. The trenches show minimal tapering over the 60 µm. Moreover, a keyhole is visible, indicating that the neck of the trench has been sealed prematurely, an often encountered problem in refilling [10]. The keyhole contains precursor or product gasses from the LPCVD process, like SiH_2Cl_2 and NH_3. However, subsequent processing – like spin-coating photoresist – only requires that the necks of the trenches are thoroughly sealed. The close-up in Figure 2 indicates at least 1 µm of SiRN that seals the trenches.

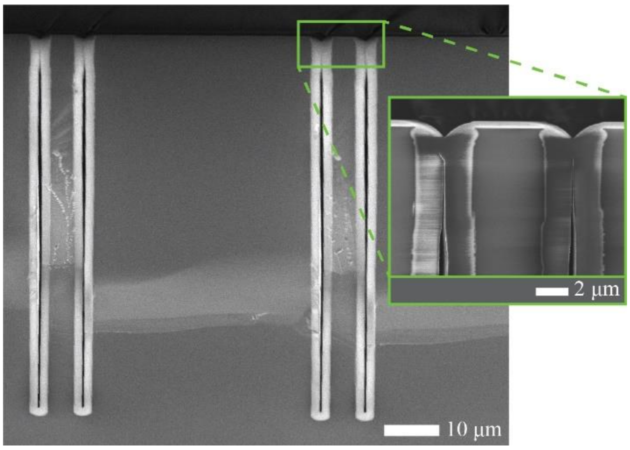

Figure 2: Cross-sectional SEM image of refilled trenches with a close-up. Corresponding to Figure 1d.

During the formation of the microchannels, ρ_s can be used in the mask design to obtain both varying channel depths and equal depths for varying channel widths. Figure 3a shows a cross-sectional SEM image of six microchannels having equal ρ_s with widths ranging from 5 to 50 µm. Furthermore, locally designing deeper channels can be desired, for example, when connecting two microfluidic devices on-chip. The hydraulic resistance – and hence the pressure drop – of the connection can be reduced significantly by increasing ρ_s. Figure 3b shows a cross-sectional SEM image of a microchannel at which ρ_s is increased to 22%. Despite the high ρ_s, the SiRN membrane at the top remains intact.

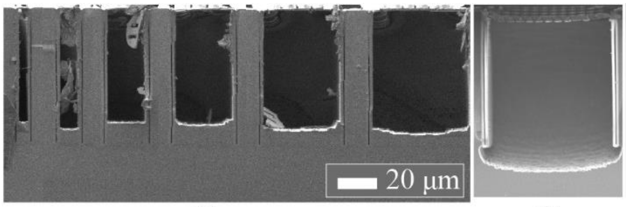

(a) (b)

Figure 3: Cross-sectional SEM image of: (a) six microchannels having $\rho_s = 13\%$ and depth within 4% deviation, and (b) microchannel having $\rho_s = 22\%$. Widths are, from left to right: 5, 10, 20, 30, 40, 50, and 60 µm, scale bar applies to both figures. Corresponding to Figure 1f.

After the formation of the microchannels, the structure is released during which the electrodes are simultaneously isolated from each other. Figure 4 shows a cross-sectional SEM image of multiple released parallel microchannels after being submerged in the diluted KOH for 7 hours and 45 minutes. The close-up image shows various distinct features of the fabrication process: the refilled trenches with a keyhole, the nearly rectangular microchannel of SiRN, and the self-limiting feature of the inverted KOH pits at the bottom side of the silicon electrodes.

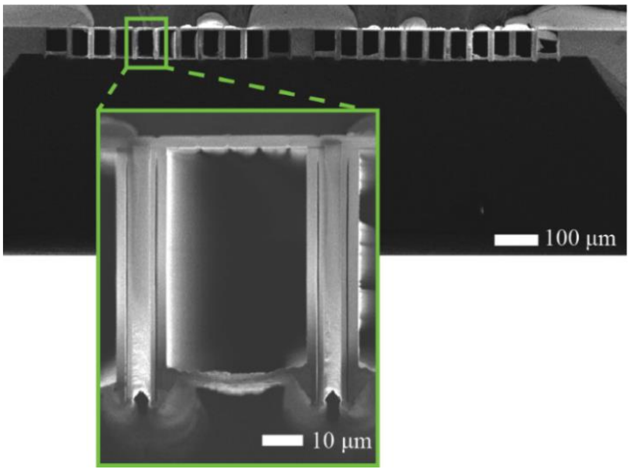

Figure 4: Cross-sectional SEM image of 22 parallel microchannels after the KOH release etch with close-up. Each channel is 40 µm wide. Corresponding to Figure 1j.

DEMONSTRATOR CHIP

The proposed process technology is used to fabricate four proof-of-principle relative permittivity sensors. Figure 5 shows a photograph of the mounted sensors. The relative permittivity sensor with nine parallel channels of 40 µm wide (top left) has been characterised. Ten different homogeneous fluids with relative permittivity values ranging between 1 and 80, including water and a water-containing mixture, have been measured. The measurement results have an accuracy within 3% of full scale. More details on the sensor performance can be found in [11].

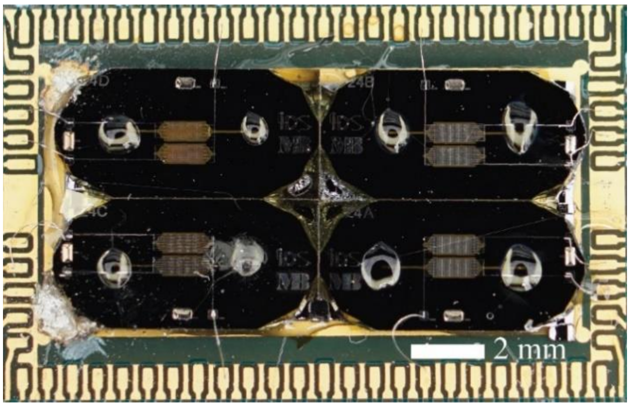

Figure 5: Relative permittivity demonstrator consisting of four sensor systems using the proposed fabrication technology. The widths of the parallel channels of the four sensors are: 5 µm (bottom right), 10 µm (top right), 20 µm (bottom left), and 40 µm (top left).

DISCUSSION

The proposed method also contains limitations. Firstly, the height of the channels is limited by the aspect ratio of the trench etch, which relates to a maximum allowed tapering. Secondly, for wide channels, ρ_s is limited by the mechanical stability of the resulting suspended SiRN membrane. Thirdly, at the fluidic inlets, the fluid is in contact with a native SiO_2, instead of the SiRN as elsewhere in the sensor. Lastly, the release etch is done via a crystallographic orientation dependent wet etch, which limits the angle to the $\langle 111 \rangle$ planes. Hence, large release windows are necessary, limiting the freedom in the mask design, especially for release windows at the front side.

Furthermore, two aspects of the fabrication process are further examined. Firstly, to make fluidic contact with the microchannels fabricated in this process, the thin SiRN membrane at the top or bottom side must be opened. For the demonstrator device, the membrane at the bottom side has been manually punctured using a syringe needle. Although a deeper and larger channel – as shown in Figure 3b – is favourable for this approach, it remains challenging to open the connection without damaging the microchannel. Secondly, the thickness of the SiRN layer between the electrode and the fluid should be kept to a minimum, reducing the effect of series capacitance and thermal isolation. However, a layer of SiRN is deposited both in the trench refill phase and in the sealing of the microchannel. Both contributions add up to the layer thickness and degrade the performance of the device.

CONCLUSION AND OUTLOOK

This work presents a novel fabrication process in which highly doped silicon sidewall electrodes and SHEs can be realised parallel to and isolated from the microchannel. The process flow allows for a wide range of microchannel dimensions. Moreover, large structures can be released simultaneously from the substrate during the simple and self-limiting etch step. The fabrication process is demonstrated through a microfluidic relative permittivity sensor which can measure relative permittivity values over a range from 1 to 80 within a 3% deviation of full scale.

For future work, it is desirable to have a wafer-scale method for making fluidic connections without the risk of damaging the device. Additionally, exploring narrower slits and higher aspect ratio trenches should reduce the SiRN layer between the electrode and the fluid, enhancing the performance of the device. Furthermore, additional characterisation of the micro-heaters proposed in this method is needed to demonstrate the thermal performance.

REFERENCES

[1] R. Ecker *et al.* IEEE Access, vol. 11. pp. 82882–82893, 2023.

[2] Z. Wang *et al.*, *IEEE Sensors J.*, vol. 20, no. 19. pp. 11122–11127, Oct. 2020.

[3] J. Groenesteijn *et al.*, *Microfluidics and Nanofluidics*, vol. 21, no. 7, Jul. 2017.

[4] B. Jiang *et al.*, *Sensors and Actuators B: Chem.*, vol. 175. pp. 218–224, Dec. 2012.

[5] H. Bian *et al.*, J. MEMS, vol. 26, no. 3. 2017.

[6] H.-W. Veltkamp *et al.*, *IEEE MEMS*, Jan. 2019.

[7] Y. Zhao et al., J. Micromech. and Microeng., vol. 31, no. 4. IOP Publishing, Mar. 03, 2021.

[8] J.G.E. Gardeniers *et al.*, *J. Vac. Sci. Technol. A: Vac., Surf., Films*, vol. 14, no. 5. Amer. Vac. Soc., pp. 2879–2892, Sep. 01, 1996.

[9] P. Walker *et al.*, Handbook of Metal Etchants, *CRC Press*, 1991.

[10] H.-W. Veltkamp *et al.*, *Micromachines*, vol. 13, no. 11. MDPI AG, p. 1908, Nov. 04, 2022.

[11] M.J.S. Bonnema *et al.*, *IEEE MEMS*, Jan. 2024.

CONTACT

Maarten J.S. Bonnema - m.j.s.bonnema@utwente.nl

FLUID-INDEPENDENT THERMAL GAS FLOW SENSOR

C. Huber[1], S. Schwab[1], F.Lütolf[1], D. Dienemann[1], R. Bernhardsgrütter[2] and C. Hepp[2]
[1] TrueDyne Sensors AG, Reinach, Switzerland
[2] Innovative Sensor Technology AG, Ebnat-Kappel, Switzerland

ABSTRACT

Thermal flow sensors are widely used as they are based on a simple measuring principle, can be used very flexibly and are inexpensive to manufacture. However, thermal flow sensors have the disadvantage that the signal is dependent on the fluid, as the thermal parameters can differ between the fluids and therefore a fluid-specific calibration is required. This paper presents a new approach to compensate for the gas dependency of a gas flow meter. The approach uses a combination of a thermal flow sensor and a vibronic density sensor. The information from the density sensor is used to determine the gas or gas mixture and thus allows the gas dependency of the thermal flow sensor to be compensated automatically. The result is a fluid-independent gas flow meter.

KEYWORDS

Thermal gas flow, gas density, gas mixtures

INTRODUCTION

Thermal gas flow sensors can be found in many everyday applications, in industry and research. They convince with their small size, flexibility in countless applications and cost efficiency. However, conventional thermal gas flow sensors are fluid-dependent, which has the following consequences:

- Thermal flow sensors must be gas-specifically calibrated to achieve the highest accuracy.
- Thermal flow sensors cannot distinguish whether the gas or the flow has changed.

This is particularly problematic if a gas mixture with a variable composition is to be measured. Approaches to solve these issues have been presented that use different thermal principles to compensate for fluid dependence. In most of these cases, the same sensitive sensing element is used, and the different thermal principles are executed sequentially. However, this has the disadvantage of increasing the response time.

Here we present a combination of a thermal flow sensor and a vibronic density sensor to compensate for the fluid dependence. The result is a fluid-independent thermal flow sensor that works for pure gases as well as for binary gas mixtures with varying concentrations.

SENSOR DESIGN

The complete flow sensor system (Figure 1) consists of the sensor bord, the fluid block and the main electronics. The sensor board contains the thermal flow sensor and the density sensor, which are the two core elements of this sensor system. In addition, a pressure and temperature sensor are installed on the board for pressure and temperature compensations of density and flow.

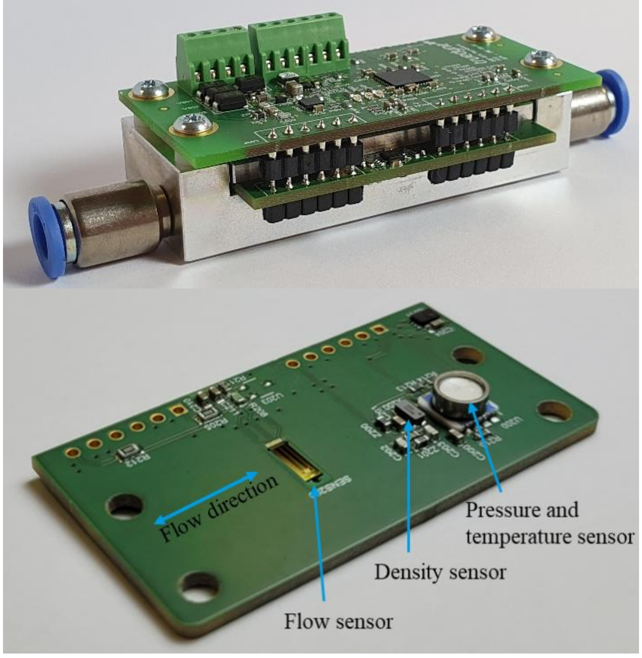

Figure 1. Assembled sensor system with the aluminum fluid block on the bottom, the sensor board in the middle and the main electronics on top (above). Detailed view of the sensor board (below).

The fluid block contains a defined measuring channel for the flow sensor and typically also a bypass channel which is designed in such a way that the resulting flow velocity is matched to the flow sensor. The measuring range of the flow measurement system can be defined via the dimensioning of the bypass channel. The fluid block also contains a measuring chamber for the density sensor.

The main electronics contains the microcontroller which controls the measurement of density and flow, calculates the correction factor and performs the fluid compensation.

Thermal Flow Sensor Element

The sensor works according to the calorimetric measuring principle [1]. It is based on conventional silicon technology and consists of a heating element and two thermopile elements, which are positioned next to the heating element upstream and downstream, respectively (Figure 2). The thermopiles act as relative temperature sensors. The difference between the two thermopile signals is the desired temperature difference that characterizes the flow (Figure 3).

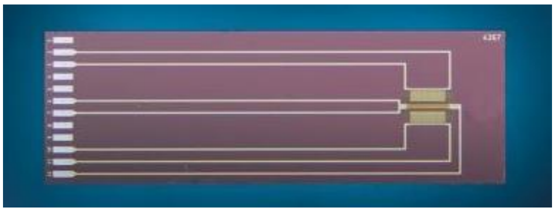

Figure 2. Flow sensor element with the heater in the center and two thermopile elements symmetrically arranged above and below the heater. The size of the entire chip is 6 mm x 2 mm.

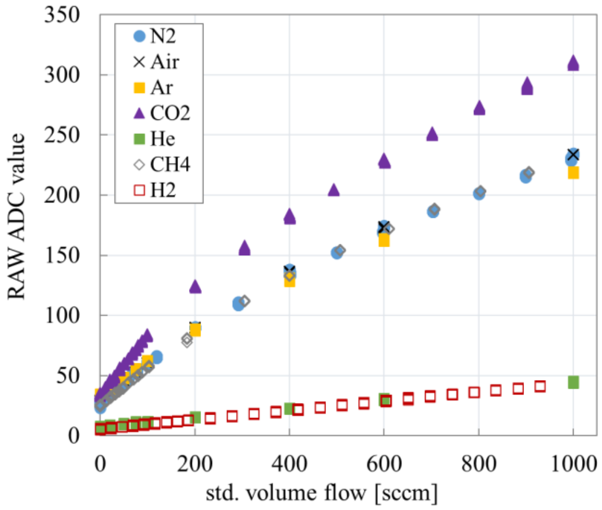

Figure 3. Raw flow signal (difference of voltages of two thermopiles as analog-to-digital converter (ADC) values) versus standard volume flow for different gases. The fluid dependency is clearly evident.

Density Sensor

The density sensor operates according to the oscillator principle [2,3]. As sensor element we use a modified quartz crystal oscillator. These are tuning fork-shaped oscillators made of quartz (Figure 4), which are typically used as clock-pulse generator in quartz watches. Quartz is a piezoelectric material. The oscillation is excited and read out by electrodes placed on the surface and on the side of the two prongs.

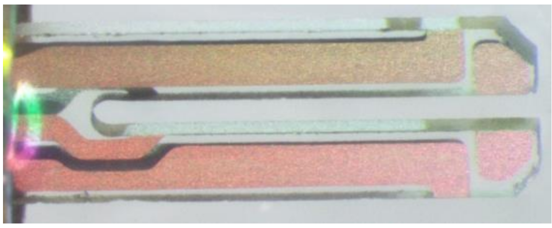

Figure 4. Picture of a quartz tuning fork. The length of the tuning forks used for these experiments is < 3 mm. The encapsulated chip has a dimension of 3.2 mm x 1.5 mm.

In our case the tuning fork is exposed to the gas. For this purpose, small openings are carved into the side of the housing, through which a gas exchange can take place. Thus, the resonant frequency f depends now not only on properties of the vibrating element (e.g. stiffness) but also on the density and, to a lesser extent, on the viscosity of the touching fluid (Figure 5). Equation (1) describes the relationship between density ρ, dynamic viscosity η, and resonant frequency of the tuning fork [4]:

$$f = f_0 + A\rho + B\sqrt{\rho\eta} \qquad (1)$$

where A and B are determined by the properties (geometry and Young's modulus) of the vibrating element and f_0 is the resonant frequency in vacuum. If the properties of the vibrating component are known, the density can be determined from the measured resonant frequency. Due to the very small volume and the high frequency, the oscillator reacts almost instantly to changes in density.

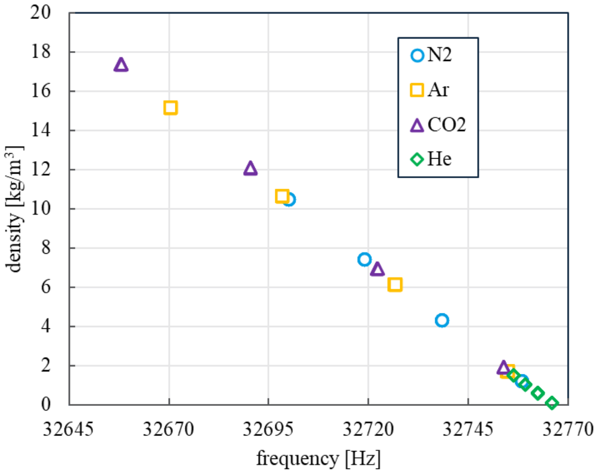

Figure 5. Dependence of resonant frequency on gas density at room temperature and pressures 1.1, 3.8, 6.6 and 9.4 bar abs.

If such a sensor is calibrated with different gases over pressure and temperature, a density measurement accuracy in the range of 0.05 kg/m^3 can be achieved over a measuring range from 0 to 20 kg/m^3 (pressure 0 to 10 bar, temperature -20°C to 60°C). This measurement accuracy is sufficient to be able to clearly distinguish the gases from Table 1 by means of density measurements or, in the case of binary mixtures of two gases, to determine the composition with an accuracy of approx. 1% vol.

WORKING PRINCIPLE

The basic idea of the flow sensor system is that both density and flow measurement take place simultaneously. The density measurement is used to identify the gas, and this knowledge makes it possible to determine the specific conversion factors that make it possible to compensate for the fluid dependency of the thermal flow sensor as described in equation (2)

$$\dot{V}_{STD} = \frac{\dot{m}}{\rho_{STD}} = G(C, S_{Raw}, ZP) \cdot \frac{CF}{\rho_{STD}} \qquad (2)$$

$\dot{V}_{STD}$ is the volume flow rate at standard conditions, $\dot{m}$ is the mass flow rate, ρ_{STD} is the density at standard conditions, G is the model function for flow, C stands for calibration coefficients, S_{Raw} is the measured raw signal, ZP is the zero point of the raw signal and CF the flow conversion factor. ZP and CF are both fluid-dependent. This principle works for pure gases as well as for binary mixtures, where the two initial gases are known.

The *CF* of such a flow element can be estimated from theoretical considerations [1]. From the heat conduction equation (3) it can be deduced that the mass flow rate must be proportional to the ratio of thermal conductivity, *k*, and heat capacity, *Cp*. See equations (4) and (5).

$$\frac{dT(\vec{x},t)}{dt} - \frac{k}{Cp \cdot \rho} \nabla^2 T(\vec{x},t) = q(\vec{x},t) \qquad (3)$$

$$\frac{\dot{m}}{A} \frac{dT(\vec{x},t)}{dx} - \frac{k}{Cp} \nabla^2 (\vec{x},t) = \rho q(\vec{x},t) \qquad (4)$$

$$\dot{m} \approx CF \approx \frac{k}{CP} \qquad (5)$$

In reality, however, the measuring system does not behave in quite the same way as in theory. The factor also depends on the design of the fluid and bypass channel of the flow sensor. But the basic behavior can be explained by this relationship.

Table 1: Thermophysical properties and flow conversion factors of measured gases at 25°C and 1,013 bar.

Gas	Density [kg/m³]	Thermal conductivity [mW/(m K)]	Heat capacity [J/(kg K)]	CF
N_2	1.145	25.84	1.04	1.00
Air	1.184	26.25	1.01	1.04
Ar	1.634	17.75	0.52	1.68
CO_2	1.808	16.63	0.85	1.00
CH_4	0.657	33.96	2.23	0.55
He	0.164	155.31	5.19	1.25
H_2	0.082	185.80	14.31	0.61

Flow Calibration

Hence an individual flow conversion factor must be determined experimentally for each gas that is to be measured with the sensor. However, the factor can then be regarded as sensor type-specific and can be fixed. *CF* can be determined by measuring mass flow with different gases as shown in Figure 6. Once the gas conversion factors are known a sensor calibration with a single gas, e.g. nitrogen or air is sufficient.

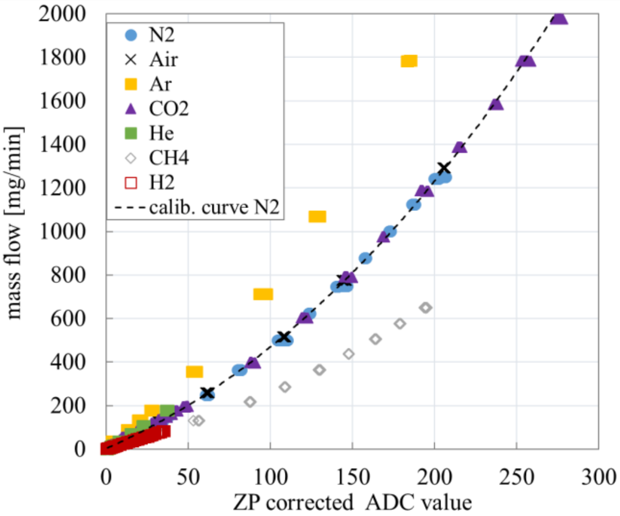

Figure 6. Mass flow versus zero point corrected ADC signal. Dashed line shows the sensor calibration with nitrogen.

Zero Point Correction

Besides the flow conversion factor, another parameter is gas-dependent, namely the zero point which is the measured raw signal without flow. It has been shown that in addition to the nitrogen calibration, a fluid specific zero point correction is required in order to be able to accurately measure volume flow also at low flowrates.

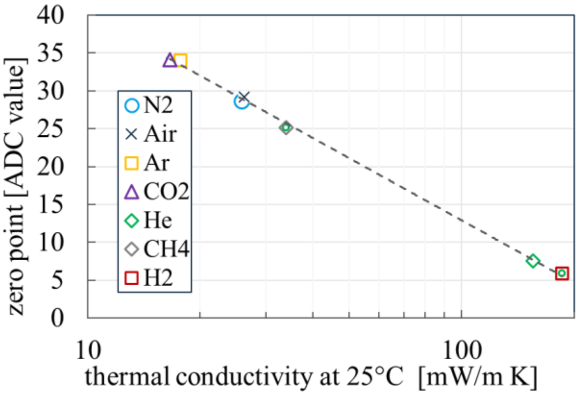

Figure 7. Zero point (measured raw ADC signal without flow). See the measurement data at x = 0 in Figure 3

Zero point is caused by slight asymmetries in the sensor structure. A change of zero point can be observed well with helium or hydrogen measurements, both of which have a very high thermal conductivity. Figure 7 shows a clear correlation of zero point with the thermal conductivity. Hence zero point can be determined and corrected when the thermal conductivity of the measured gas is known.

MEASUREMENT PERFORMANCE

Figure 8 shows the measurement performance of the measuring system, calibrated with nitrogen, with automatic clean gas detection. A measuring accuracy of < 2.5% form full scale can be achieved for clean gases besides helium and hydrogen which, due to their very low density, generate much smaller measurement signals per volume flow (Figure 6) and therefore have a slightly lower measurement accuracy and a greater scattering of measured values.

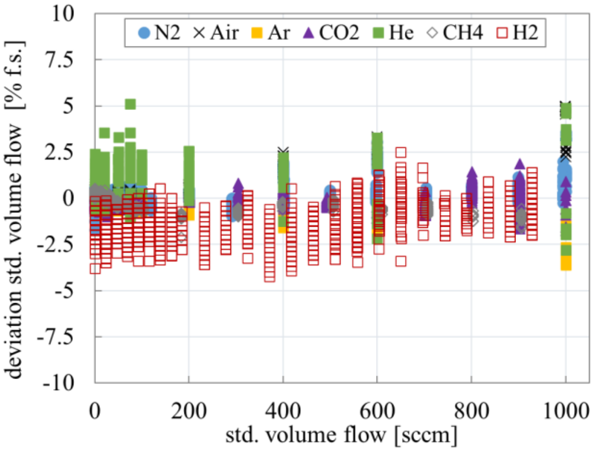

Figure 8. Measuring deviation from master meter of gas compensated std. volume flow rate for clean gases.

Automatic gas detection and adjustment with a thermal flow sensor is a nice and useful function. However, the real benefit of the measuring system lies in the measurement of binary gas mixtures with variable concentrations.

When measuring binary gas mixtures, conversion factors and zero points between clean gas values must be adjusted depending on the concentration. The density sensor can determine the gas concentration almost in real time (t90 < 2 sec) and adjust the fluid compensations accordingly. Look-up tables or gas mixture models can be used for this purpose. It should be noted that mixtures with helium or hydrogen in particular behave in a highly non-linear manner (see Figure 9 above). This can be expected from the relationship in equation (5). With the implemented models, our sensor system is able to achieve a measurement accuracy in the range <5% f.s. for gas mixtures (see Figure 9. below).

CONCLUSION

The combination of thermal flow measurement and density measurement allows to compensate the fluid dependence of the thermal flow sensor for pure gases or binary mixtures. On the one hand, the sensor allows to identify pure gases from a predefined list and to adjust the fluid compensations automatically. The main advantage, however, is the accurate flow measurement of binary gas mixtures with varying gas compositions. The sensor is able to determine the gas concentration in real time and to adjust the fluid compensations accordingly. In our experiments we achieved measurements accuracies <2.5% f.s for clean gases and <5% f.s. for binary gas mixtures comparable with gas-specific calibrations of thermal flow sensors.

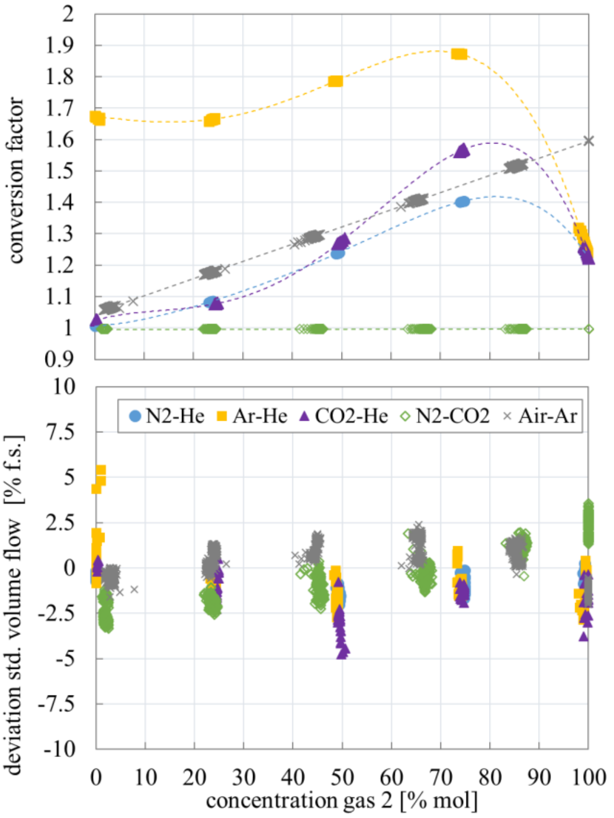

Figure 9. Measurements of binary gas mixtures. Conversion factors (above) and measuring deviation form master meters (below) versus gas concentration.

REFERENCES

[1] M. Elwenspoek, “Thermal flow micro sensors”, *CAS '99 Proceedings - International Semiconductor Conference*, 1999

[2] C. Huber, P. Reith, A. Badarlis, “Gas Density and Viscosity Measurement with a Microcantilever for Online Combustion Gas Monitoring”, *Sensors and Measuring Systems; 19th ITG/GMA-Symposium*, 2018

[3] C. Huber, “MEMS-based micro-Coriolis technology for high precision density measurement”, *tm – Technisches Messen*, 83(3), 2016, pp. 157–162

[4] M. Christen, “Air and Gas Damping of Quartz Tuning Forks”, *Sensors and Actuators*, 4,1983, pp. 555-564

CONTACT

* C. Huber, christof.huber@endress.com

CAMERA-BASED JET VOLUME ESTIMATION USING DEEP LEARNING

G. Miotto[1,] and R. Voelckner[1,*], R. Zengerle[1,2], S. Kartmann[1,2]*
[*]contributed equally [1] Hahn-Schickard, Freiburg, Germany
[2] Laboratory for MEMS Applications, IMTEK, University of Freiburg, Freiburg, Germany

ABSTRACT

This paper presents a computer vision system designed to determine the volume of liquid jets generated by non-contact microdispensing devices. The volume is estimated by a neural network that processes data recorded online by a line-scan camera. Compared to other methods, our system has many advantages, for instance, simple and affordable hardware, real-time measurements, no liquid contact and hence no liquid loss. In the measurement range of 100 nl to 1.1 µl, the mean relative error (MRE) achieved is as low as 1.3%.

INTRODUCTION

The investigation of small liquid jets and their fragmentation into droplets is a well-established domain within microfluidics [1, 2, 3]. Extensive research led to the development of microdispensers, i.e. high-precision devices for controlled liquid delivery. This technology finds widespread applications in diverse fields, including biological tissue engineering [4, 5, 6], high-throughput screening for drug discovery [7, 8], additive manufacturing (also known as 3D printing) [9, 10, 11], and various other domains falling under the umbrella term of non-contact dispensing [12, 13].

In certain scenarios, such as during dispenser calibration, the accurate measurement of jet volume becomes essential. In this regard, computer vision offers an elegant and inexpensive solution compared to well-established gravimetric solutions [14]. Nonetheless, existing camera-based methodologies have focused exclusively on calculating the volume of discrete droplets, overlooking the quantification of liquid jets. In response to this gap in knowledge, we present a system that addresses this limitation.

DEEP LEARNING AND COMPUTER VISION

Deep learning, a subset of machine learning, empowers algorithms to acquire knowledge without explicit programming. Although conventional machine learning historically has been utilized for data processing, the emergence of deep learning approaches in the early 2010s marked a significant shift towards effectively handling large amounts of diverse data types, including images, videos, text, audio, and other domains. The impact of deep learning on automated data processing has been revolutionary, achieving unprecedented precision levels in pattern recognition [15, 16].

RELATED WORK

The usage of deep learning in microfluidics is still in its early stages [17]. Some studies have introduced deep learning vision systems for microfluidics. For instance, Dressler et al. [18] devised a vision system based on deep reinforcement learning to regulate the size of water-in-oil droplets on a microfluidic chip. Huang et al. [19] trained networks on videos of dispensed droplets using unsupervised learning. They show that the network can predict the evolution of droplet shape when given the initial frames of the video. Hadikhani et al. [20] conducted a study showcasing a system to estimate the flow-rate of oil-in-water droplets on a microfluidic chip. They illustrate that the utilization of deep learning significantly enhances the accuracy of flow rate estimates.

All the aforementioned studies share the commonality of working with images as input data and of investigating the behavior of (single or multiple) fluidic droplets.

What however has not yet been attempted, to the best of our knowledge, is the utilization of deep learning for estimating the volume of liquid jets. Owing to the variable lengths of fluid jets, there is no individual camera frame that captures the entirety of the dispensed liquid. Consequently, techniques for estimating liquid jet volume must account for image sequences. Given the typically non-rotational symmetry of jets, a minimum of two cameras positioned at varying angles is usually necessary for accurate volume prediction. However, our strategy involves adopting a naively axisymmetrical assumption for the jet shape, a deliberate measure aimed at streamlining the hardware requirements by utilizing a single camera instead of the conventional two.

In the following sections, we detail the configuration of our system used for data acquisition as well as the methodology employed to transform high-resolution input image sequences into low-dimensional time series.

— METHODOLOGY —

A. SYSTEM DESCRIPTION

There are many types of non-contact microdispensing devices, but they all comprise three main parts: a liquid reservoir, a nozzle, and an actuation mechanism. The reservoir stores the liquid and is connected to the nozzle through which the liquid can be expelled. The actuation mechanism is responsible for increasing the liquid pressure to a threshold, or allowing the flow of an already pressurized liquid. In both cases, the liquid will be expelled and travel freely in the air until it makes contact with the intended substrate.

Our experimental setup (see Fig. 1) includes the aforementioned three components and additional components for image capture, including illumination and a high-speed camera. We selected a telecentric camera objective to minimize image distortions. A microbalance was employed to obtain the volume ground truth. The high-speed camera was configured to emulate a low-cost line scan camera, producing two horizontal lines with a vertical pitch of 36 µm at a frequency of 150k fps, see Fig. 2. Note that the ordinate axis in Fig. 2(b) represents both time and jet speed, therefore the full image encodes information about the jet flowrate.

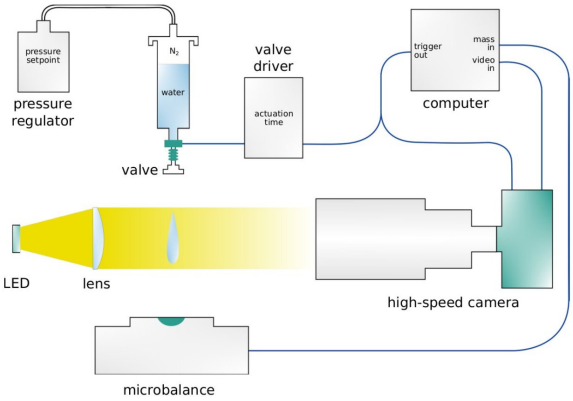

Figure 1: The experimental configuration comprises a pressurized liquid reservoir, a valve for dispensing jets, an illumination system, a high-speed camera, and a precision microbalance for data acquisition. The high-speed camera was configured to emulate a line scan camera, generating two lines with a spacing of 36µm, operating at a frequency of 150k fps. It is important to note that this camera will be subsequently replaced by an authentic line scan camera in future experiments.

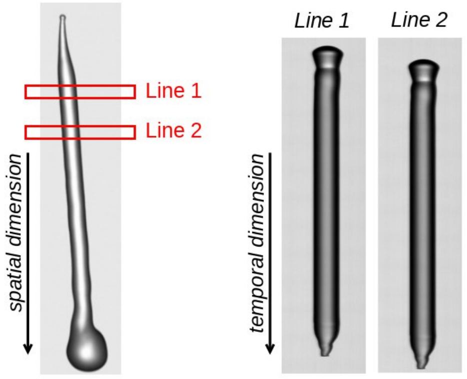

(a) (b)

Figure 2. Panel (a) illustrates a single exemplary high-speed camera frame, while panel (b) displays the outcome of capturing two arbitrary lines over a sequence of frames. The two images presented in (b) result from a temporal concatenation, transforming the ordinate axis of the image into a time axis.

B. FEATURE EXTRACTION

In contrast to the previously mentioned studies, we have chosen not to directly input the two line scan images into our deep learning model. Instead, our approach involves preprocessing these images to extract essential features. The rationale behind this decision is to streamline the input data presented to the model, thereby enhancing the efficiency and expediting the learning process of the network. We postulate that reducing the complexity of the input data facilitates a more effective learning experience for the model. Another notable benefit is a reduction in the inference runtime of the resulting network.

Initially, the two images are segmented using thresholding. Next, for each pixel row in the line scan images, jet diameter and x-shift are determined. Finally, the four resulting time series are partitioned into their corresponding jet sections: head, body, and tail (Fig. 3). Subsequently, in preparation for integration into the deep learning model, the head and tail segments of each of the four time series are concatenated. This operation yields four resultant vectors, each possessing a length of 250, ensuring uniformity for further analysis and modeling.

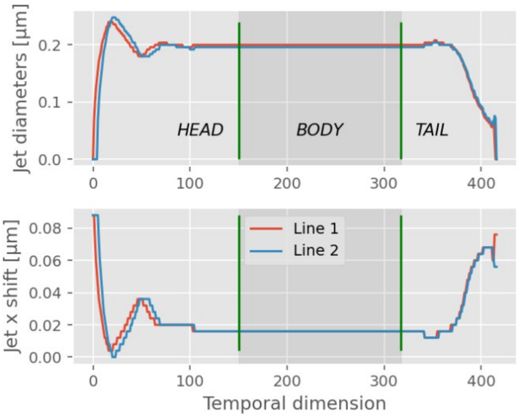

Figure 3. The four time series representing the key features of the two line scan images (two jet diameter and two x-shift series). These can be segmented into the three distinct sections, namely head, body, and tail. The body is defined as the region of permanent regime, head an tail represent the initial and final transients.

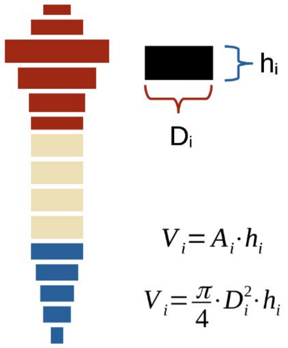

$$V_i = A_i \cdot h_i$$

$$V_i = \frac{\pi}{4} \cdot D_i^2 \cdot h_i$$

Figure 4. Illustration of the segmentation process of a

liquid jet into a stack of cylinders. The parameter D_i represents the true jet diameters at specific positions, while the heights h_i, each equivalent to one pixel row, do not accurately reflect the actual jet height at the particular position, as the ordinate axis represents both time and jet speed.

We model the jet shape as a stack of cylinders, to express the jet volume as discrete sum of the cylinder volumes, as shown in Eq. (1) and Fig. 4. The assumption hereby is the axisymmetry of liquids during flight.

$$V_{jet} = \frac{\pi}{4} \sum_i D_i^2 h_i \qquad (1)$$

D_i and h_i represent diameters and heights of the individual cylinders, with diameters measured as explained above. The heights, however, cannot be directly determined from the jet images, due to the non-constant jet flowrate. Therefore, we train a neural network to estimate $\hat{h}$, an average cylinder height that satisfies Eq. (2).

$$V_{jet} = \hat{h} \frac{\pi}{4} \sum_i D_i^2 \qquad (2)$$

To render the estimation independent of jet length, we segregate the constant body diameters from the head and tail diameters. Eq. (3) illustrates the final equation utilized for jet volume estimation.

$$\hat{V}_{jet} = \hat{h} \cdot \frac{\pi}{4}\left(D_b L_b + \sum_i D_i^2\right) \qquad (3)$$

D_b and L_b correspond to body diameter and length. Note that the second part of Eq. (3) serves as multiplicative factor after $\hat{h}$ estimation, which can be calculated from input data directly.

C. DEEP LEARNING FOR JET VOLUME ESTIMATION

Our dataset comprises approx. 1300 experimentally acquired datapoints. We chose a split of 60% for training, 20% for validation, and 20% for test.

Extensive experimentation with various architectures, including LSTM and a one-dimensional CNN, led to the determination that the latter provides the optimal model performance in both accuracy and runtime. Consequently, our focus will be exclusively on the CNN architecture. The model receives input in the form of the four aforementioned concatenated 250-element vectors from the head and tail partitions, where each of the vectors serves as an individual input channel. Configured for a regression task, the network outputs the estimated value for $\hat{h}$ as a single floating-point value.

To identify the optimal set of hyperparameters, including the network architecture, a hyperparameter optimization study was conducted using Bayesian Optimization. Each experiment involved training a model for 1000 epochs. The optimal network architecture, as determined through this optimization, is detailed as follows: incorporating batch normalization in the input layer, employing eight convolutional layers with channel configurations of 64, 128, 256, and 512 (each repeated twice). Both the convolutional kernel size and stride were optimized to 3. The network concludes with two dense layers, each comprising 128 hidden neurons. The following list outlines the training parameters, all derived from the hyperparameter optimization:

- Learning rate (LR): $125.7 \cdot 10^{-6} \rightarrow 39.3 \cdot 10^{-9}$
- LR scheduler: Cosine anneal
- Dropout: $33.3 \cdot 10^{-3}$
- Batch size: 16
- Weight decay: $1.65 \cdot 10^{-3}$
- Train loss function: L1 loss

Consequently, our network encompasses approximately 1.9 million trainable parameters. The complete deep learning pipeline is presented in Fig. 5.

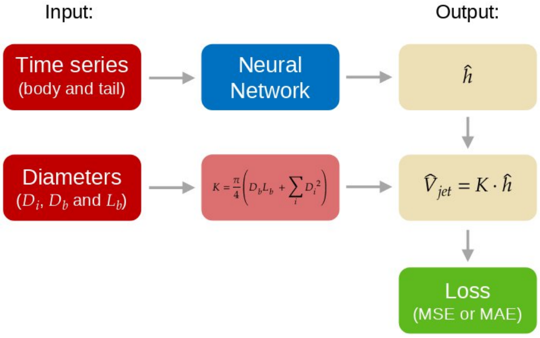

Figure 5. Deep learning architecture overview. The neural network undergoes training to predict the parameter $\hat{h}$, symbolizing the average height of each individual cylinder slice. Subsequently, the coefficient K is applied as a multiplicative factor to obtain the jet volume estimate.

D. EXPERIMENTAL RESULTS

Our validation results, derived from our experimental dataset, demonstrate the capability of our method to estimate jet volumes with an MRE of 1.3% and a median relative error of 1.1%. The highest relative error observed is 7.4%, hence none of the relative errors exceeds the 10% threshold. The distribution of error values is visualized in Fig. 6.

However, it's important to note that the test split of our dataset comprises approximately 260 samples. In future research, we aspire to validate and refine our findings with a more extensive dataset.

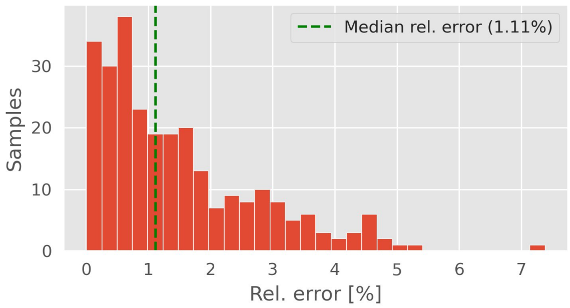

Figure 6. The distribution of relative errors from our optimal model over the test dataset. The MRE is calculated at 1.3%, and the median relative error is recorded at 1.1%. The maximum relative error observed is 7.4%.

SUMMARY AND OUTLOOK

The integration of a simulated line scan camera and our novel feature extraction methodology represent a cost-effective, yet accurate solution for jet volume estimation from nanoliter to microliter range. Future investigations will entail the use of a real line scan camera and an exploration into reducing the camera frame rate—initial experiments indicate that a decrease from 150kfps to 30kfps does not compromise results.

Furthermore, our future research initiatives aim to significantly augment the dataset size through both synthetic and experimental means. This expansion will encompass diverse types of liquids and a broader spectrum of jet volumes. Lastly, our objectives include integrating the prediction of confidence intervals, and the refinement of the algorithm for deployment on embedded hardware.

ACKNOWLEDGEMENT

Financed by THE MINISTRY OF ECONOMICS, LABOR AND TOURISM OF THE STATE OF BADEN-WÜRTTEMBERG within the framework of the investment competition Invest BW, funding code BW1_1512/02.

REFERENCES

[1] H. Bruus, “Theoretical microfluidics”, volume 18, Oxford university press, Oxford, 2008.

[2] N. Convery and N. Gadegaard, “30 years of microfluidics”. *Micro and Nano Engineering*, 2:76–91, 2019.

[3] S. Sohrabi, M. K. Moraveji, et al., “Droplet microfluidics: fundamentals and its advanced applications”, *RSC Advances*, 10(46):27560–27574, 2020.

[4] W. Zhu, X. Ma, M. Gou, D. Mei, et al., “3d printing of functional biomaterials for tissue engineering”, *Current opinion in biotechnology*, 40:103–112, 2016.

[5] S. Derakhshanfar, R. Mbeleck, K. Xu, et al., “3d bioprinting for biomedical devices and tissue engineering: A review of recent trends and advances”, *Bioactive materials*, 3(2):144–156, 2018.

[6] M. Hospodiuk, M. Dey, et al., “The bioink: a comprehensive review on bioprintable materials”, *Biotechnology advances*, 35(2):217–239, 2017.

[7] M. Choi, J. Hwang, et al., “Multicomponent high-throughput drug screening via inkjet printing to verify the effect of immunosuppressive drugs on immune t lymphocytes”, *Scientific reports*, 7(1):1–7, 2017.

[8] R. Daly, T. S. Harrington, et al., “Inkjet printing for pharmaceutics – A review of research and manufacturing”, *International journal of pharmaceutics*, 494(2):554–567, 2015.

[9] Z. Khan, P. Koltay, et al., “One-Stop Hybrid Printing of Bulk Metal and Polymer for 3D Electronics”, *Advanced Engineering Materials*, 2300922, 2023.

[10] Z. Shu, B. Gerdes, M. Fechtig, et al., “Direct Printing of Conductive Metal Lines from Molten Solder Jets via StarJet Technology on Thin, Flexible Polymer Substrates”, *The Society for Imaging Science and Technology, 2018.*

[11] K. V. Wong, A. Hernandez, “A review of additive manufacturing”, *International scholarly research notices*, 2012.

[12] M. Singh, H. M. Haverinen, P. Dhagat, and G. E Jabbour, “Inkjet printing—process and its applications”, *Advanced materials*, 22(6):673–685, 2010.

[13] G. Cummins and M. P. Y. Desmulliez, “Inkjet printing of conductive materials: a review”, *Circuit world*, 2012.

[14] D. Liang, C. Steinert, S. Bammesberger et al., “Novel gravimetric measurement technique for quantitative volume calibration in the sub-microliter range”, *Measurement Science and Technology*, 2013.

[15] Y. LeCun, et al., “Deep learning”, *Nature* 521(1)436–444, 2015.

[16] A. Krizhevsky, I. Sutskever, G. E. Hinton, “ImageNet classification with deep convolutional neural networks”, *Communications of the ACM*, 60(6)84–90, 2012.

[17] J. Riordon, D. Sovilj, et al., “Deep learning with microfluidics for biotechnology”, *Trends in biotechnology*, 37(3):310–324, 2019.

[18] O. J. Dressler, P. D. Howes, et al., “Reinforcement learning for dynamic microfluidic control”, *ACS omega*, 3(8):10084–10091, 2018.

[19] J. Huang, L. J. Segura, et al., “Unsupervised learning for the droplet evolution prediction and process dynamics understanding in inkjet printing”, *Additive Manufacturing*, 35:101197, 2020.

[20] P. Hadikhani, N. Borhani, et al., “Learning from droplet flows in microfluidic channels using deep neural networks”, *Scientific reports*, 9(1):1–7, 2019.

MACHINE LEARNING-ENHANCED MASS FLOW MEASUREMENTS USING A CORIOLIS MASS FLOW SENSOR

R. Zubavicius, D. Alveringh[1]*, M. Poel*[2]*, J. Groenesteijn*[1,3]*,*
R. G. P. Sanders[1]*, R. J. Wiegerink*[1]*, J. C. Lötters*[1,3]
[1] MESA+ Institute, University of Twente, Enschede, The Netherlands
[2] Data Management and Biometrics, University of Twente, Enschede, Netherlands
[3] Bronkhorst High-Tech BV, Ruurlo, The Netherlands

ABSTRACT

We present machine learning-enhanced mass flow measurements based on microfabricated Coriolis mass flow sensors with integrated pressure and temperature sensors. Two machine learning techniques have been applied: linear regression (LR) and support vector regression (SVR) on four features extracted from the raw sensor data to improve mass flow estimation. In contrast to conventional mass flow detection, LR and SVR use information from all integrated sensors to estimate the mass flow, which results in a full-scale accuracy improvement of a factor 4 for trained fluids.

KEYWORDS

Coriolis, mass flow, machine learning, linear regression, support vector regression, sensors, microfluidics.

INTRODUCTION

Miniaturization of flow sensors using microfabrication techniques has enabled the measurement and control of very low flows, i.e., in the order of a few micro or nano liters per minute [1]. Accurate flow sensing and control has applications in pharmaceutical, biomedical and many other fields [2, 3, 4]. Thermal flow sensors are capable of measuring down to a few nano liters per minute. However, thermal flow sensing principles are highly dependent on liquid properties; the sensors need to be calibrated per liquid [5].

In contrast to thermal flow sensors, Coriolis mass flow sensors (CMFS) are capable of measuring the true mass flow without the need for calibration per fluid. Last decades, a few different fabrication techniques have been developed to miniaturise these type of flow sensors [6, 7, 8]. The latter has been used to integrate multiple fluid sensors into a single chip [9] and to find accuracy limits for CMFS [10, 11]. Recent work has focused on applying machine learning for fluid classification [12] and extraction of fluid parameters [13]. In the work presented in this paper, the improvement of the accuracy for mass flow sensing by applying machine learning to the raw sensor signals has been investigated.

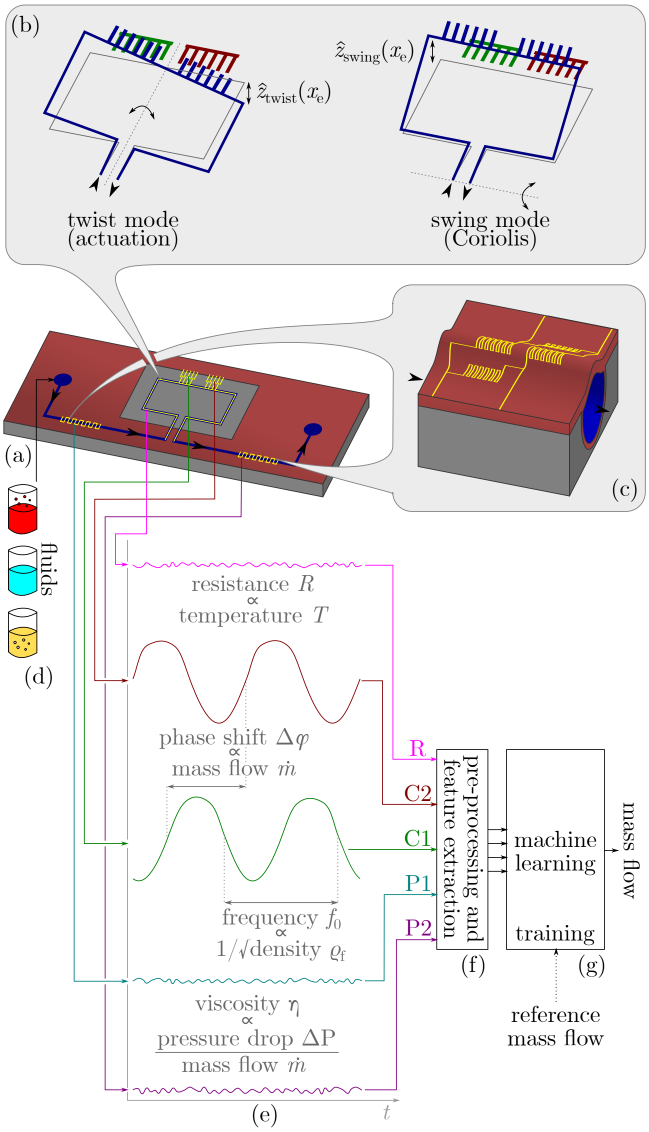

Figure 1: Illustration of the proposed principle using a CMFS, temperature and pressure sensors, with (a) the chip, (b) the swing and twist mode of the CMFS, (c) the pressure sensor, (d) different fluids, (e) five output signals, (f) pre-processing and (g) the regression-based machine learning. Adapted from [12].

SENSOR THEORY AND DESIGN

The sensor chip consists of a CMFS, two pressure sensors (upstream and downstream with respect to the CMFS) and a temperature sensor, see Figure 1a. The

CMFS utilizes the Coriolis principle, where inertia caused by a fluid flow (φ_m) in a twisting microchannel induces a swing mode (Figure 1b). The swing mode is proportional to the mass flow and is theoretically independent of fluid properties. However, temperature and pressure influence the movement of the channel [11, 14], which includes the magnitude of the swing mode. Therefore use of the signals from the already integrated temperature and pressure sensors potentially improves the accuracy.

The CMFS has two capacitive readout structures on each side with respect to the twist mode axis. The phase shift at the fundamental frequency between these electrodes is proportional (for low flows) to the mass flow [8]. The pressure sensors consist of a membrane that deforms proportional to the pressure in the channel. To measure the pressure, there are golden resistive tracks deposited on top of the channel and connected in Wheatstone bridge configuration. On top of the CMFS, there are also a resistive track deposited to enable temperature measurements. The signals (R, C1, C2, P1 and P2) from these five sensing structures are illustrated in Figure 1e.

REGRESSION BASED APPROACH

Regression could be applied directly to the sampled sensor signals. However, this would result in very long training times and complex regression models due to the enormous amount of data points in the signals. As indicated in Figure 1f, feature extraction has been implemented to reduce the sampled data to a set of numbers that is relevant for accurate mass flow sensing. This included:

- Fast Fourier Transforms (FFT) of CMFS signals C1, C2 and D;
- resonance frequency f_0 and phase shift between C1 and C2 $\Delta\varphi$ detection;
- min-max normalization.

Four features have been chosen as these are expected to be most related to the mass flow: phase shift $\Delta\varphi$, resonance frequency f_0, resistance of the temperature-dependent track R and upstream pressure P_1.

Two regression methods have been investigated: Linear Regression (LR) and Support Vector Regression (SVR). LR models the linear relationship between dependent and independent variables. The dependent variable $\dot{m}$ can be estimated by LR using:

$$\begin{aligned} \dot{m} &= \beta_0 + \beta_1 x_1 + w_2 x_2 + \ldots + \beta_n x_n + \epsilon && (1) \\ &= \beta_0 + \beta_1 \Delta\varphi + w_2 f_0 + \beta_3 R + \beta_4 P_1 + \epsilon && (2) \end{aligned}$$

with β_0 the intercept (or constant), ϵ the noise and β_1 to β_n the weights corresponding to features x_1 to x_n. Finding values for the weights β_0 to β_4 for LR is based on the Ordinary Least Squares (OLS) method.

Similar to LR, SVR fits data linearly. However, SVR fits given an error margin: instead of a single linear fit, support vectors are fitted for the loss-sensitive region. This potentially improves the fit due to providing flexibility with its hyperparameters. The optimization of this algorithm is accomplished by applying Lagrange multipliers which satisfy Karush-Kuhn-Tucket (KKT) conditions.

In contrast to kernel-based SVR, where the kernel performs nonlinear mapping $\kappa(\cdot) : \mathcal{X} \mapsto \mathcal{H}$, transforming features $\mathcal{X}$ to a feature space $\mathcal{H}$. The κ transformation used in this research is the Radial Basis Function (RBF) kernel [15].

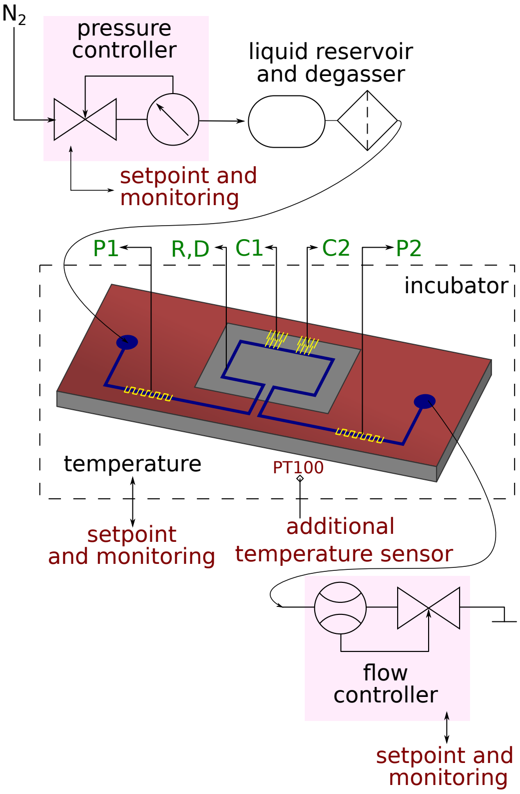

Figure 2: Illustration of the experimental measurement setup. This setup enables the chip to be exposed to different combinations of flows, pressures, temperatures and liquids. The raw pressure sensor signals (P1 and P2), CMFS (C1 and C2), driving signal (D) and temperature-dependent resistive track (R) were recorded. Adapted from [12].

EXPERIMENTAL SETUP

The fabrication of the CMFS is based on [8], see Figure 3 for a photograph of the chip. Electronic interfacing of all sensors is based on [12], where the capacitance has been measured using a combination of charge amplification and demodulation and the pressure sensors using lock-in amplification. Both capacitance signals (C1 and C2) and driving signal (D) have been sampled at $250\,\mathrm{kS\,s^{-1}}$ for 1 second. In that second one sample for each of the pressure sensor signals (P1 and P2) and the resistive track are also captured.

Four different liquids (ethanol, water, acetone, isopropanol) and one gas (nitrogen) were measured with the experimental setup illustrated in Figure 2. The mass flow has been controlled using a Bronkhorst® mini CORI-FLOW™ ML120V21, pressures were controlled by a Bronkhorst® EL-PRESS P-602CV and temperature has been controlled by a Peltier-cooled incubator IPP55 from Memmert. As shown in Figure 4, measurements were performed with varying parameters: temperatures between 15 and 35 °C, pressures between 4 and 6 bar and mass flows between 0 and $5\,\mathrm{g\,h^{-1}}$. In total, 5540 experiments were performed, and 1662 (30%) of these measurements were randomly selected as a training set.

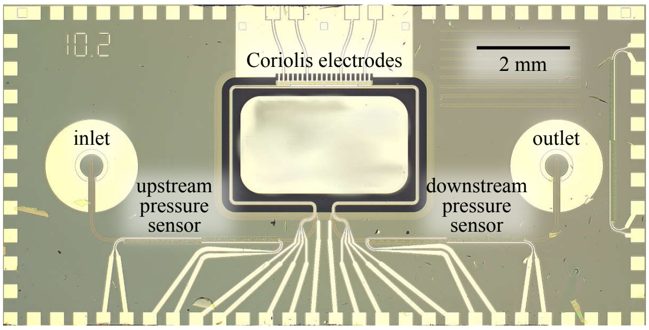

Figure 3: Microscopy image of the sensor.

RESULTS AND DISCUSSION

The data that has not been used for training (70% of the dataset) has been used for testing.

Table 1 shows an overview of the Pearson correlations between the mass flow $\dot{m}$ and extracted features $\Delta\varphi$, f_0, R and P_1. As expected, the CMFS phase difference $\Delta\varphi$ has a very high Pearson correlation of > 0.99. However, also resonance frequency f_0 and upstream pressure P_1 show significant correlations of respectively -0.32 and 0.40. The correlation between mass flow and the resistance on the track can be neglected (0.04).

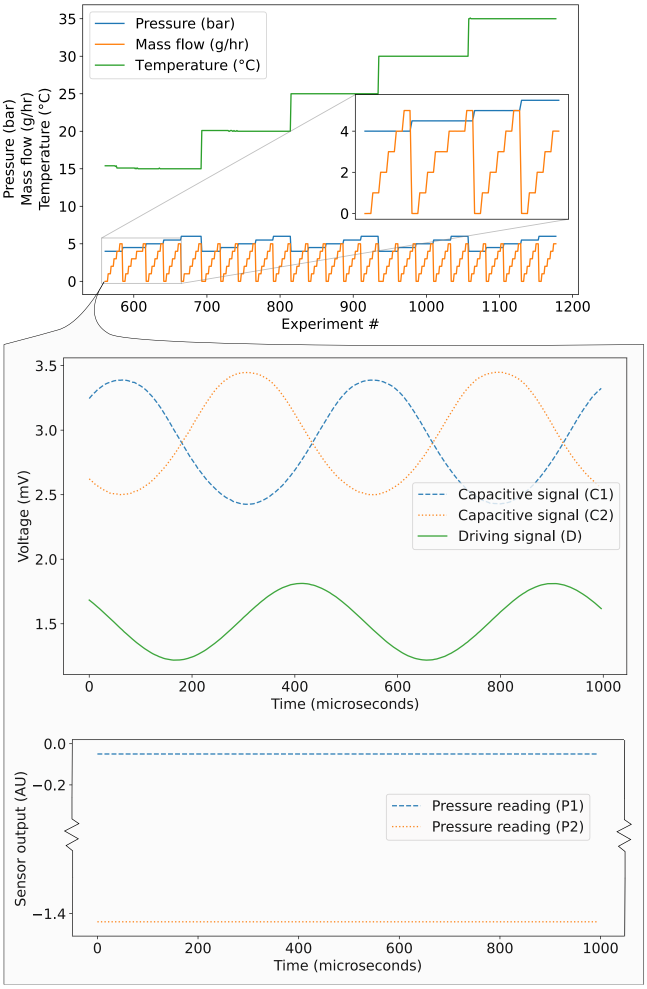

Figure 4: Top: applied conditions to the chip (in this case water), bottom: for each condition, the signals $C1$, $C2$, $P1$, $P2$ and D were recorded.

Using conventional calibration using only the phase shift $\Delta\varphi \propto \dot{m}$ results in an average full-scale accuracy of 5% between liquids. This would also require leaving out nitrogen due to an observed higher sensitivity compared to liquids. Using a weighted sum of linear combination of the derived features (LR), the performance is improved by a factor of 2 compared to the conventional method. However, a similar complication appears when trying to estimate nitrogen mass flow. This is solved by finding the most significant polynomial feature, which is modelled as

$$\dot{m} = \gamma_0 + \gamma_1 \Delta\varphi + \gamma_2 (\Delta\varphi \cdot f_0) + \gamma_3 R_{\text{track}} + \gamma_4 P_1 \quad (3)$$

where γ_0 to γ_4 denotes the weights of individual features optimized by least squares. Taking $\Delta\varphi \cdot f_0$ as a feature directly compensates for the different nitrogen sensitivity. This improves the accuracy by a factor of 2 when nitrogen has been included in the dataset, and by a factor of 2.5 when nitrogen is excluded.

Table 1: Pearson correlation coefficients between features and mass flow $\dot{m}$.

Feature		Correlation with $\dot{m}$
Phase shift	$\Delta\varphi$	0.99
Resonance frequency	f_0	-0.32
Resistance	R	0.04
Upstream pressure	P_1	0.40

The performance can be further improved by a factor of 4 by using a kernel-based method. This results in a full-scale ($5\,\mathrm{g\,h^{-1}}$) accuracy of $\approx 1.1\%$ shown in Figure 5. This method maps the measurements into a feature space, modelling interactions between features. The individual feature impact is shown in Figure 6. Table 2 summarizes the model performances.

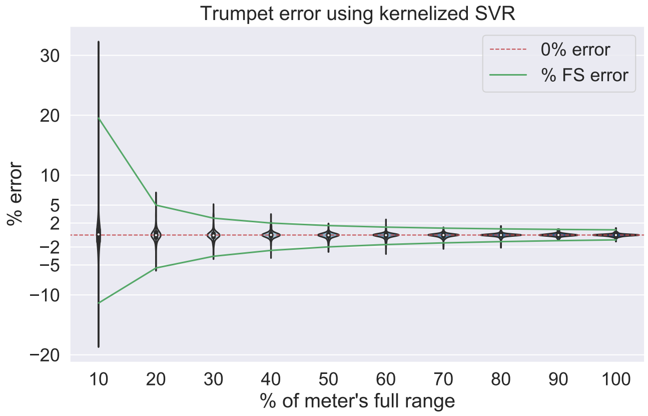

Figure 5: Trumpet curve based on kernelized SVR of the mass flow, showcasing the maximum error for measurements performed under varying conditions using the test dataset (70%). Full-scale is $5\,\mathrm{g\,h^{-1}}$ for this dataset.

Table 2: Summary of model performances.

Regression method	Full-scale accuracy
$\Delta\varphi \propto \varphi_m$ (excl. N2)	5%
Linear Regression	2.5%
Support Vector Regression	1.1%

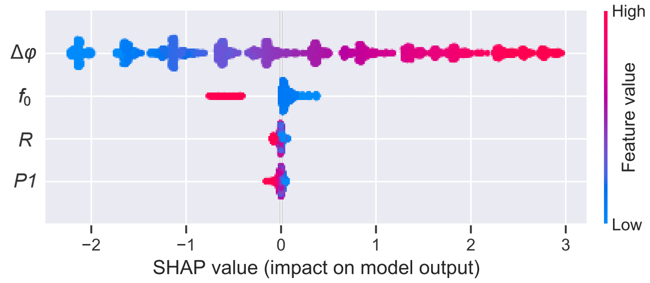

Figure 6: SHAP figure indicating individual feature interactions on the data, with SHAP value indicating positive or negative impact on the output based on feature values.

CONCLUSION

Two machine-learning regression methods, LR and SVR, have been applied to a microfabricated CMFS with integrated pressure-dependent and temperature-dependent sensing structures to improve robustness against external influences for mass flow estimation. Significant correlation has been found between mass flow and features (> 0.3) from integrated non-CMFS signals, which suggests that (a) non-ideal CMFS dependencies can be compensated for and (b) the integrated non-CMFS structures are also dependent on mass flow. Either way, estimation of mass flow by using this multi-feature approach shows a factor 4 improvement in accuracy with respect to conventional methods.

REFERENCES

[1] M. Dijkstra *et al.*, *Journal of The Optical Society of America B-optical Physics - J OPT SOC AM B-OPT PHYSICS*, 01 2006.
[2] S. Radhakrishnan *et al.*, *Materials Advances*, vol. 3, pp. 1874–1904, 2 2022.
[3] K. Makinwa *et al.*, in *ICECS 2001. 8th IEEE International Conference on Electronics, Circuits and Systems (Cat. No.01EX483)*, vol. 3, 2001, pp. 1505–1508 vol.3.
[4] N. Convery *et al.*, *Micro and Nano Engineering*, vol. 2, pp. 76–91, 2019.
[5] R. J. Wiegerink *et al.*, vol. 1, 9 2009, pp. 1455–1458.
[6] P. Enoksson *et al.*, in *Proceedings of Ninth International Workshop on Micro Electromechanical Systems*. IEEE, 1996, pp. 156–161.
[7] Y. Zhang *et al.*, in *Transducers' 01 Eurosensors XV: The 11th International Conference on Solid-State Sensors and Actuators June 10–14, 2001 Munich, Germany*. Springer, 2001, pp. 1432–1435.
[8] J. Haneveld *et al.*, *Journal of Micromechanics and Microengineering*, vol. 20, no. 12, 2010.
[9] T. et al., in *2018 IEEE Micro Electro Mechanical Systems (MEMS)*, 2018, pp. 218–221.
[10] J. Groenesteijn *et al.*, in *2016 IEEE 29th International Conference on Micro Electro Mechanical Systems (MEMS)*. IEEE, 2016, pp. 193–196.
[11] D. Alveringh *et al.*, *Sensors and Actuators A: Physical*, vol. 271, pp. 212–216, 2018.
[12] D. Alveringh *et al.*, *Sensors and Actuators A: Physical*, vol. 363, p. 114762, 2023.
[13] R. Zubavicius *et al.*, in *2024 IEEE 37th International Conference on Micro Electro Mechanical Systems (MEMS)*. IEEE.
[14] D. Alveringh *et al.*, *Journal of microelectromechanical systems*, vol. 26, no. 3, pp. 653–661, 2017.
[15] V. Vovk, "Kernel ridge regression," in *Empirical Inference: Festschrift in Honor of Vladimir N. Vapnik*. Springer, 2013, pp. 105–116.

CONTACT

* D. Alveringh, d.alveringh@utwente.nl

THEORY OF SELF-MONITORING OF PIEZOELECTRICALLY DRIVEN MICROPUMPS

M. Richter, K. Axelsson, J. Häfner
Fraunhofer Institute for Electronic Microsystems and Solid State Technologies EMFT,
Munich, Germany

This paper presents a novel method for monitoring piezo-driven micropumps by analyzing the actuation signal during operation without any additional sensors. While the indirect piezo effect is used for micropump actuation (electrical load performs mechanical work), the direct piezo effect is exploited to monitor micropump behaviour in real time (transient change of pump chamber pressure *dp/dt* induces an additional current I_p, which is measured). This method has been theoretically investigated and the electromechanical coupling has been linked to micropump theory. In addition to the self-sensing effect, a large signal behaviour of the piezo can be observed. An electronic system for measuring the self-sensing signal was developed, and the theory was verified in a first experiment. Subsequently, the transient self-sensing signal was measured for different disturbances such as gas bubbles or back pressure changes.

Background/ State of the Art

Since Harald v. Linteln published the first MEMS micropump in 1988 [1], 35 years of micropump research have taken place worldwide. However, there has been no breakthrough in this technology comparable to that of MEMS sensors. For critical applications like drug delivery or industrial applications obstacles such as free flow, bubbles, particles or phase changes have to be overcome. To monitor these effects for safe and accurate operation, flow, pressure or bubble sensors are required in addition to the micropump. But those are making the system complex, expensive and bulky.

To overcome these obstacles, a novel method of monitoring the micropump during operation by simply analyzing the control signal in real time has been developed and is presented here.

Micropump theory and time dependent pump chamber pressure

The piezo diaphragm transducer performs a volume displacement V when either the pressure difference at the actuation diaphragm p-p_0 (assuming, that there is atmosphere pressure at the piezo) or the Voltage difference U-U_0 changes. This volume displacement V can be calculated as follows:

$$V(p,U)=C_p(p-p_0)+C_E^*(U-U_0)$$

The coefficient C_p represents the "fluidic capacity" of the diaphragm transducer, i.e. how much the displaced volume changes when the pressure difference between the top and bottom of the membrane changes. The coupling factor C_E^* describes how much the displaced volume changes when the Voltage (difference of the electrical potential) U - U_0 changes.

The displacement ΔV of a micropump without back pressure, which is driven between the voltage levels of a negative voltage U- (e.g. U- = -40 V, the diaphragm is deflected "upwards", i.e. away from the bottom of the pump chamber) and a positive voltage U+ (e.g. U+ = *100 V*, diaphragm is deflected downwards), is calculated from equation 1 as follows:

$$\Delta V=C_E^*(U_- - U_+)$$

This volume is also called "stroke volume" of the micropump. In order to calculate the time behaviour of the pump chamber pressure, the differential equation can be set up by considering the volume flow changes of the inlet and outlet valves [2] (fig. 1).

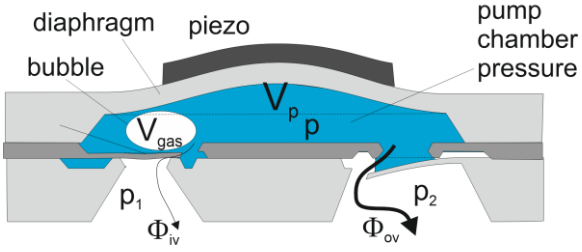

Fig. 1: model to derive the equation of p(t).

$$\frac{dp}{dt}=\frac{1}{C_p+C_{gas}}\left(-p\left(\frac{1}{R_{EV}}-\frac{1}{R_{AV}}\right)-C_E^*\frac{dU}{dt}\right)$$

In addition to the fluidic capacity of the drive diaphragm C_p, the fluidic capacity of an (optional) gas bubble C_{gas} has been taken into account. It is assumed for the course of the drive voltage that the electrical capacitance C_{el} charges via a charging resistor R_{el} in order to build up the voltage ΔU.

$$U(t)=\Delta U\left(1-e^{-\frac{t}{\tau_a}}\right),\ \text{with}\ \ \tau_a=C_{el}R_{el}$$

If the differential equation is solved (without back pressure ($p_1 = p_2 = p_0$), and neglecting the leakage rates of the inlet valve, the following special solution for the pump chamber pressure *p(t)* is obtained (initial condition: $p(t{=}0) = p_0$):

$$p(t)=\frac{C_E^*}{C_p+C_{gas}}\Delta U\frac{1}{1-\frac{\tau_a}{\tau_p}}\left(e^{-\frac{1}{\tau_a}t}-e^{-\frac{1}{\tau_p}t}\right)$$

The pump chamber pressure increases with the (electrical) time constant τ_a and decreases again with the (fluidic) time constant τ_P. The term in front of the bracket represents the maximum pressure generated in the pump chamber. This pressure opens the outlet valve. However, the presence of a gas bubble causes the pressure amplitude to decrease. The damping effect of the gas bubble means that a lower pressure amplitude is available.

Here, the "typical stroke time" τ_p can be defined. It is the product of the fluidic resistance of the outlet valve R_{OV} multiplied by the sum of the fluidic capacitance C_p of the diaphragm and the gas bubble C_{gas}:

$$\tau_p = R_{AV}\left(C_p + C_{gas}\right)$$

The typical stroke time of the pump is proportional to the flow resistance of the valve, i.e. a higher flow resistance requires more time to push the liquid through the outlet. However, the stroke time is also proportional to the flow capacities. If there is a large gas bubble in the pump chamber, the micropump requires more time to perform the pump stroke. A gas bubble in the pump chamber therefore leads to a reduction in the pressure amplitude and to a delay in the equalization process (fig 2.).

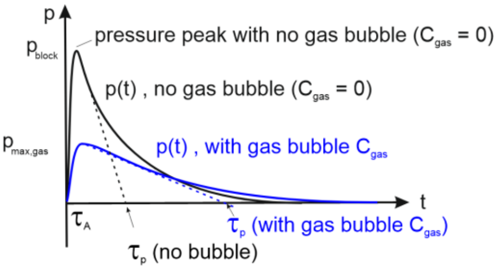

Fig. 2: Time dependent pump chamber pressure during the pump stroke, with and without a gas bubble.

Self-sensing principle of micropumps

The piezo effect combines inherently both (fig. 3) the indirect piezo effect (which is used to achieve a volume displacement V upon application of a voltage U) as well as the direct piezo effect.

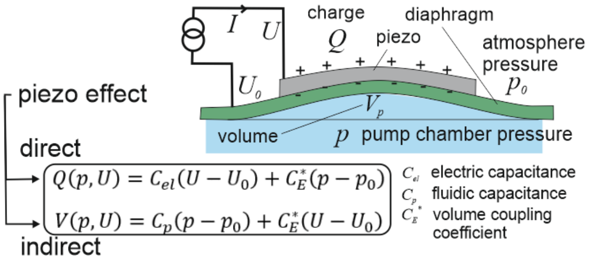

Fig. 3: Electromechanical coupling of piezo actuator.

The pressure change *dp/dt* in the pump chamber induces additional electrical charges Q to the piezo, which can be measured as electrical "self-sensing current" I_p. This signal is superposed by the current I_U to charge the capacitance and the current I_{piezo} which represent big signal effects of the piezo.

$$I = \frac{dQ}{dt} = C_{el} \cdot \frac{dU}{dt} + (U - U_0) \cdot \frac{dC_{el}}{dt} + (p - p_0) \cdot \frac{dC_E^*}{dt} + C_E^* \cdot \frac{dp}{dt} = I_U + I_{piezo} + I_p$$

Because the time to load the capacitance τ_a is usually shorter, compared to the fluid flow through the pump chamber τ_p, an electronic was developed to measure the self-sensing signal on a millisecond time scale, when the load current I_U already disappeared.

This time dependent signal gives a real time "fingerprint" of the micropump behaviour for every pump and supply mode of an actuation cycle.

Superposition of different physical effects by excitation with square wave voltage

When a square-wave voltage is applied to the drive diaphragm, different subsystems are excited which are essentially independent of each other, resulting in different step responses of the subsystem which added up due to superposition. These are:

- The electrical time constant within the piezo capacitance is charged. This can be a few microseconds for a low-impedance piezo amplifier and several hundred microseconds for battery-operated electronics (current I_U).
- The slow big-signal effects of piezoceramics associated with the growth of domains as the electrical field strength changes (in the low millisecond range, current I_{piezo}).
- The effect of the charge displacement on the piezoceramic when the pump chamber pressure changes according to the pump dynamics current I_p).

All these effects are superimposed to form a total current. At this point it must be emphasized that the pump chamber pressure *p(t)* can change not only due to the pump dynamics discussed in the last section, but also due to a variety of other effects:

- The resonance frequency of the drive diaphragm, which is in the order of 10 kHz (corresponding to 5 microseconds) depending on the geometry of the diaphragm bending transducer.
- The resonance frequency of the valve flap, which is in the range of a few kHz depending on the geometry.
- The fluidic resonance that occurs, for example, when the inertia of the fluid mass in the supply tubing couples with the fluidic capacity of the drive diaphragm.

As those effects are influencing the pump chamber pressure, they are also changing the self-sensing signal. Those effects may not be relevant at all operation conditions of a micropump, but must be taken into account by interpreting the self-sensing signal I_p. Within that, the self-sensing principle is a powerful tool to have a detailed insight into the pump dynamics of a piezoelectric micropump.

Calculation of the total current

The following is an analytical consideration of the time-dependent current signal, whereby the piezo large signal terms are neglected. The total current consists of the charging current of the capacitance (assumed to be constant) and the current induced by the pump chamber pressure change:

$$I(t) = I_U + I_p = C_{el} \cdot \frac{dU}{dt} + C_E^* \cdot \frac{dp}{dt}$$

If the characteristics of the special solution are used for the voltage curve and the pressure curve, the following expression is obtained for the total current:

$$I(t) = +\frac{1}{\tau_P} \frac{1 (C_E^*)^2}{C_p + C_{gas}} U e^{-\frac{t}{\tau_P}} + \left(C_{piezo} - \frac{(C_E^*)^2}{(C_p + C_{gas})} \right) \frac{U}{\tau_A} e^{-\frac{t}{\tau_A}}$$

The sensor current I_p starts negative (since dp/dt is there positive and C_E^* is always negative), crosses the zero line at time t_1 (when the pumping chamber pressure is maximum), has its maximum at time t_2, and then falls exponentially with the time constant τ_p. This current is superimposed on the total current, which is initially dominated by the charging current of the capacity. The slope of the total current is monotonically decreasing, so the sensor current is difficult to extract from the total current. It can be noticed, that The amplitudes of the total current I_0 at $t=0$ (about 100 mA), the sensor current at $t=0$ ($I_{p,0}$ about -6 mA) and the maximum of the sensor current ($I_{p,max}$ about 60 µA at $t=t_2$) scales with:

$$I_{p,max} = -\frac{\tau_a}{\tau_p} I_{p0} = -\frac{\tau_a}{\tau_p} k^2 \frac{C_M}{C_M + C_{gas}} I_0 \; ; \; (C_E^*)^2 = k^2 C_{el} C_M$$

k represents the piezoelectric coupling factor, and is connected with the volume coupling factor C_E^*, the capacitance C_p and fluidic capacity C_p.

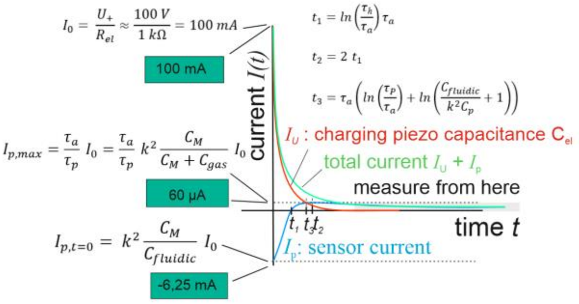

Fig. 4: Analytically total current I, consisting of charging current I_U and sensor current I_p.

The total current is always positive and decreases monotonically. This sensor current is superimposed on the total current, which is initially dominated by the charging current of the capacity. The slope of the total current is monotonically decreasing, so the sensor current is difficult to extract from the total current. However, you can take advantage of the fact that the charging current with τ_A drops much faster than the sensor current (with τ_p). After a time t >> τ_A the remaining signal consists just of the sensor current, which contains fluidical information like flow resistance, fluidic capacitance or pressure information.

Experimental

In the following section two sets of experiments has been designed. In a first experiment the superposition of the signals was investigated, to distinguish between the big signal current I_{piezo} and the self-sensing current I_p. To verify (or falsify) the hypothesis of the superposition of those effects, a second experiment with disturbances like gas bubbles or back pressure change was introduced to investigate the effect on the self-sensing signal. The piezo driven micropump consists of an actuation unit (piezo glued to a diaphragm), and two passive check valves for inlet and outlet. Two types of micropumps has been investigated, a silicon micropump (size 5x5x0.6 mm^3, for experiment A) and a metal micropump (size OD 20 mm, thickness 2 mm, for experiment B).

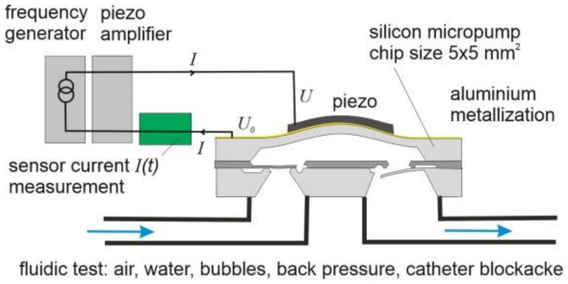

Fig. 5: Set-up to measure transient self-sensing signal.

A) Experiment to investigate the superposition of Ipiezo and the self-sensing current Ip

To investigate the self-sensing effect, a set-up according to fig. 5 was built up. Self-sensing signal I_p as well as big signal piezo response I_{piezo} are superposed and have been measured and separated by appropriate fit function (model 2, fig.3).

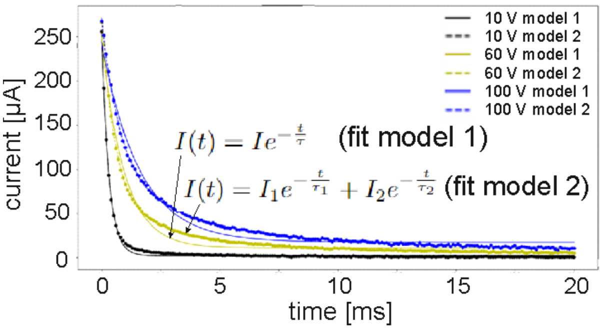

Fig. 6: Raw data of self-sensing signal from 5x5 mm^2 silicon micropump pumping air. Model 1 does not fit well. Model 2 (according hypothesis of superposition) fits very well to raw data, and separates I_p from I_{piezo}.

The extracted fluidic time constant τ_p (fig. 6) for the supply was in the same order of magnitude compared to micropump theory.

Measuring τ_p electrically gives detailed insight to the transient fluidic behaviour of the micropump. The increase of τ_p with voltage can be explained by the increase of flow resistance, as the diaphragm gets closer to the pump chamber bottom by higher voltages. The measured time constant of about 0.4 ms fits very well to the calculated time constant by analytical theory (fig. 7).

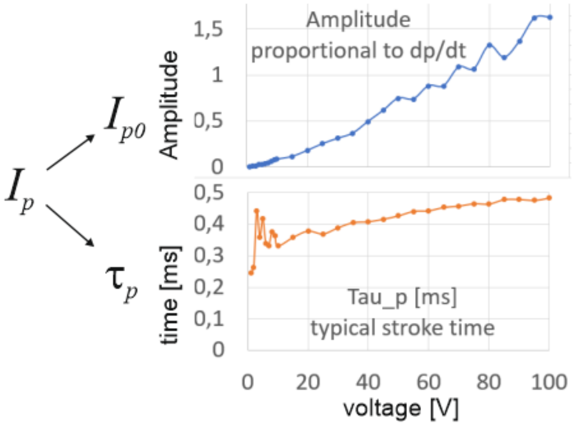

Fig. 7: Fluidic parameter extraction from raw data fit for supply mode of 5x5 mm^2 silicon micropump. From the same raw data we get parameter for I_{piezo} (not shown).

B) Experiment to investigate disturbances like bubbles and back pressure change

In figure 9 a real-time measurement of the self-sensing signa is shown. Each line is measured while the stroke of the supply mode. The pump actuates at a frequency of 10 Hz. A fluidic resonance is observable (nr. 1 in fig. 9), which shows the coupling of liquid inertia in the tubing with the fluidic capacitance of pump diaphragm.

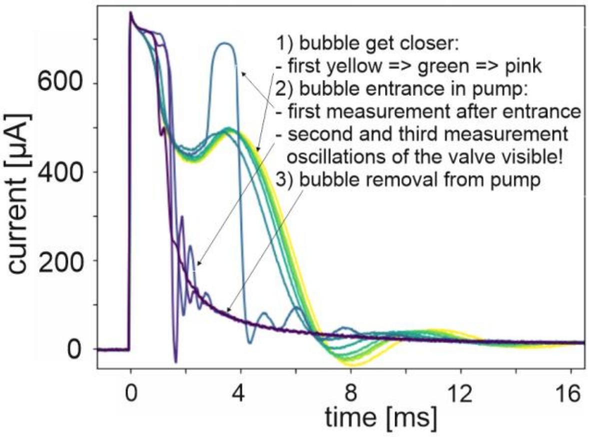

Fig. 9: Bubble transition from the inlet, through the pump chamber and outlet valve of the micropump.

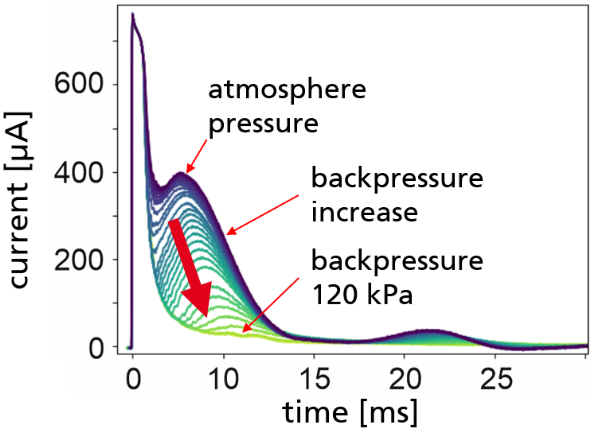

Fig. 10: Measured back pressure response on self-sensing signal.

The movement of a gas bubble was observed (nr. 2 in fig. 9). For every pump stroke, the fluidic resonance changes its frequency while the gas bubble is approaching the inlet valve of the micropump. If it enters the pump chamber, the signal changing heavily, and oscillations can be observed. Their origins will be investigated in future work.

Furthermore, it is possible to detect back pressure by self-sensing signal (fig. 10). If the back pressure exceeds the blocking pressure of the metal micropump (120 kPa), the actuator cannot open the outlet valve, therefore the resonance is disappearing.

Outlook

As described in this publication, the self-sensing signal is to be understood as a “fingerprint” of the current system state. The highly complex fluid-mechanical couplings are leading to a broad spectrum of different manifestations of the Self-Sensing signal. These are challenging to differentiate and classify by using classical techniques. Therefore, we propose a novel approach for this purpose - the use of artificial intelligence methods (AI-methods). For this, the following system solution is designed:

Currently, the piezoelectric micropump is driven by a boost-converter. Additionally, the self-sensing signal is amplified through a load-free current-to-voltage-converter circuit and sampled by an analog-digital-converter (ADC) of the microcontroller in the driver circuit. On this controller, AI-methods are also implemented to analyze the diverse and complex signal forms of the self-sensing signal in real-time. For an application-oriented utilization of the self-sensing property, the AI-methods are trained with suitable measurement data. This training data is generated on a testbench developed for this purpose at Fraunhofer EMFT. Various fault conditions, such as changes in viscosity, gas bubbles, alterations in system pressures, blockages, and electronic errors, can thus be deliberately induced and clearly associated with the measurement signal. This concept was first presented at the MST Congress in 2023 [2].

REFERENCES

[1] H.T.G. van Lintel, F.C.M. van der Pol, S. Bouwstra, A piezoelectric micro pump based on micromachining of silicon, Sensors & Actuators 15, 1988, S. 153-167.

[2] R. Zengerle and M. Richter, Simulation of microfluid systems, J. Micromech. Microeng. 4 (1994) pp. 192-204, UK 1994 (https://iopscience.iop.org/article/10.1088/0960-1317/4/4/004)

[2] Self-Sensing of Piezoelectric Actuators: Integrated Bubble Detection for Reliable Drug Dosing K. Axelsson, A. bin Tariq, G. Zerbib, M. Richter, C. Kutter ISBN: 978-3-8007-6203-3

MICRODROPLETS PLATFORM FOR BIOMOLECULES ENGINEERING

E. Tanumihardja[1]*, A. Tekath*[1]*, A. Heidari*[2]*, T. Segers*[3]*, and A. Rentmeister*[1]

[1] Institute of Biochemistry, University of Münster, Münster, Germany
[2] Institute of Physiological Chemistry and Pathobiochemistry, University of Münster, Münster, Germany
[3] BIOS Lab-on-a-Chip group, University of Twente, Enschede, the Netherlands

ABSTRACT

Microdroplets are an excellent display option for high-throughput biomolecule engineering, such as directed evolution. This project aims to establish an emulsion platform to create various monodisperse double emulsions for diverse biomolecule engineering to be operated by non-experts. A commercial system is modified to enable efficient injection and mixing of reagents in low microlitre volumes. Several stable constructions of double emulsions have been obtained and tested. A simple directed evolution experiment has been setup to show the proof of concept and technological readiness. The individual steps of the DE cycle have been tested successfully. The steps will be performed together in the near future.

KEYWORDS

Double emulsion, directed evolution, molecule engineering, high-throughput

INTRODUCTION & AIM

Directed evolution (DE) is a method devised to engineer biomolecules by natural selection simulation. The process alternates between gene diversification and selecting the functional gene variants. [1] It is desired to screen a vast library of genes at high throughput and to apply evolution pressures for effectiveness and productivity [2].

This project aims to use microdroplets as reactors for DE to allow use of (semi)synthetic materials and for the prospect of high-throughput [3], [4]. Genes can be compartmentalised in picoliter water droplets and expressed via an in-vitro transcription and translation (IVTT) process. The droplets with functional proteins can then be sorted using high-throughput systems. Seeing the intended users of this platform will be non-microfluidic experts; we choose double emulsion (water-in-oil-in-water droplets) construction to enable the use of a familiar, commercial cell sorter.

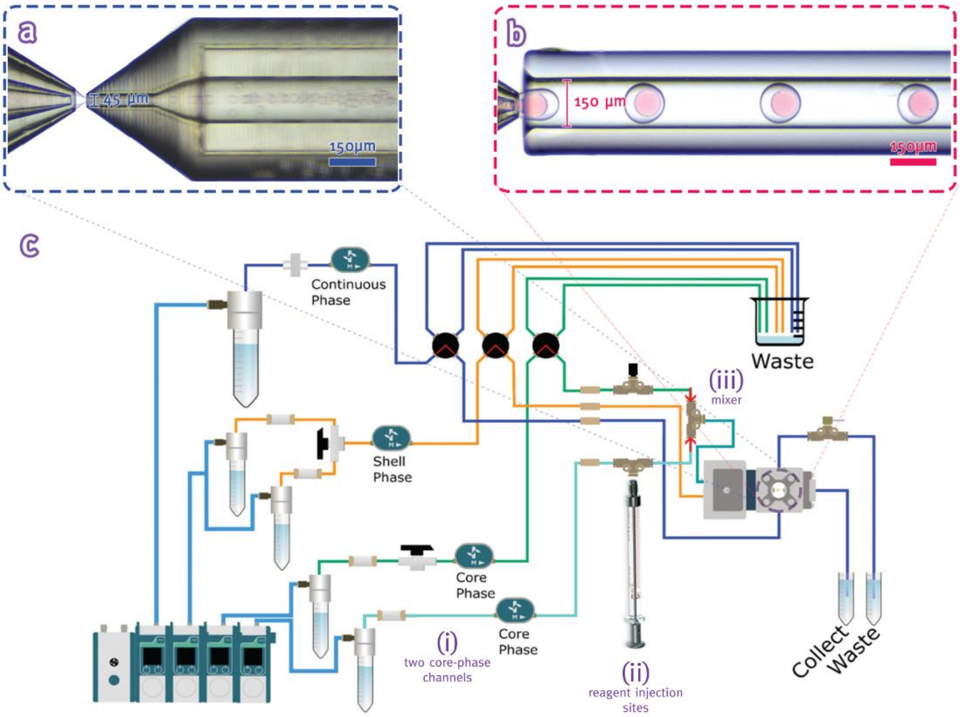

Figure 1: Overview of the microdroplet generation platform. RayDrop chip nozzle with (a) the small (45 µm) and (b) the big (150 µm) counter nozzle during droplet generation. (c) Schematic of the modified platform flow path: (i) 2 core phases channels with comparable flow resistance, (ii) two reagent injection sites which allow in-line injection of 10-50 µL reagent each, (iii) a mixer is added shortly before the nozzle, with check valves for dosing ease and in-line filter (Ø 0.5 µm) to prevent clogging.

SETUP & OPERATION

Microdroplets are generated on a modified commercial double emulsion platform (RayDrop platform, Secoya). Features are introduced to the platform to enable encapsulation of dosed two core phases in minute (10-20 µL) volumes (Fig. 2).

The platform operates on pressure pumps with flow sensors in the flow paths. Due to the elaborate flow paths, flow rate-controlled methods perform poorly as they suffer significant feedback latency. Pressure control is therefore used for all experiments, and dosing is achieved by manually adjusting the pressure and based on the measured flow rates. This dosing process has been made significantly more intuitive by having comparable flow paths between the two core phases.

T-junctions are added to the core phase lines as low-cost in-line injection sites. Threaded syringes can be directly connected to the lines, and tens of microlitre reagents can be injected practically loss-free. The injected core phases mix within 2 minutes before the nozzle to minimise transcription or translation before encapsulation. Therefore, the genotype-phenotype correlation within each droplet can be preserved.

In-line check valves are added immediately before the mixer to prevent backflow and further facilitate dosing. Stainless steel filters are often added before the mixer to prevent nozzle clogging.

DROPLETS & PROOF OF CONCEPT

Several droplet constructions have been explored for different projects. Stable water-in-oil-in-water (WOW) droplets are achieved using fluorinated oil (HFE7500) and 1% fluo-surfactant (FluoSurf, Emulseo) as shell phase. Highly monodisperse samples (CV <2%) can be generated in two size ranges (Ø 20-50 µm (Fig. 2a) and Ø 80-150 µm (Fig. 2b)) at relatively high throughput (~1 kHz). When osmotically matched, the WOW droplets are sufficiently stable for >6 hours of incubation at 37°C, also under agitation. At 4°C, the WOW droplets are stable for months.

To prove the concept and technologies involved, we have designed a simple DE workflow (Fig. 4b). A red-fluorescent protein (mScarlet-I) has been mutated using site-directed mutagenesis to create a non-fluorescent variant (Fig. 4a). A randomised library has been created from this protein variant, plasmids from the library will be put in droplets (~100 copies each droplets) to express the coded proteins. Based on their fluorescent signals, the droplets will be sorted and analysed.

A commercial IVTT kit (S30 T7 High-Yield Protein Expression System, Promega) was used to express wild-type mScarlet-I in WOW droplets. After 4 hours of incubation at 37°C, excitation and emission spectra matching mScarlet-I's were measured from the droplets (Fig. 3). Based on practical considerations, a flow cytometer will be used to sort the droplets. The smaller WOW droplets (Ø 20 µm) have been successfully sorted using a commercial flow cytometer (Sony SH800) at ~300 Hz.

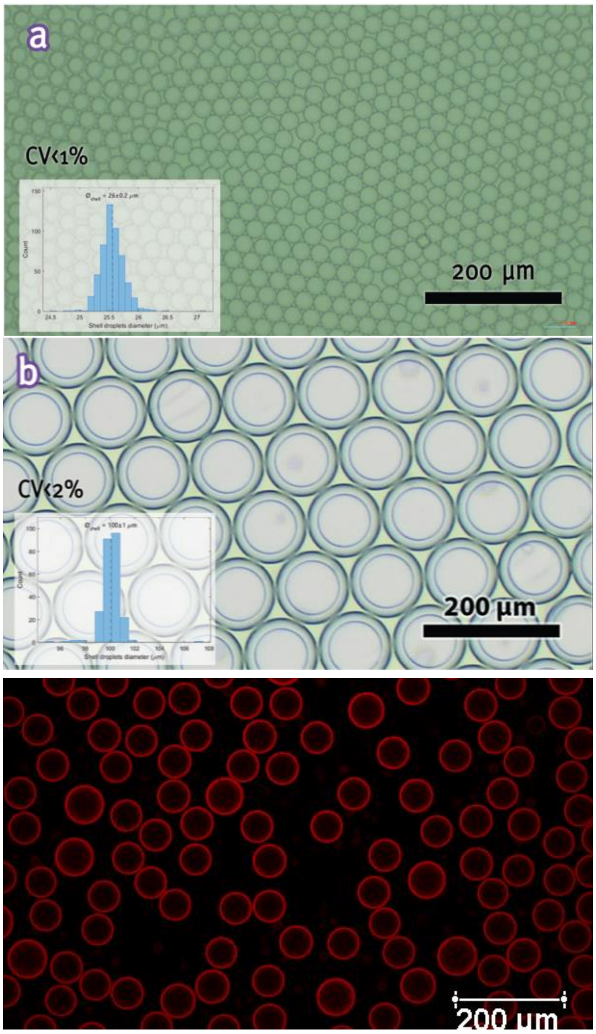

Figure 2: The different types of generated WOW droplets: (a) small (Ø 20-50 µm) and (b) large (Ø 80-150 µm). Insets show size distribution analysis of the droplets, both showing high monodispersity (CV<2%). (c) Giant unilamellar vesicles (Ø 40-50 µm) with a CV of ~5%.

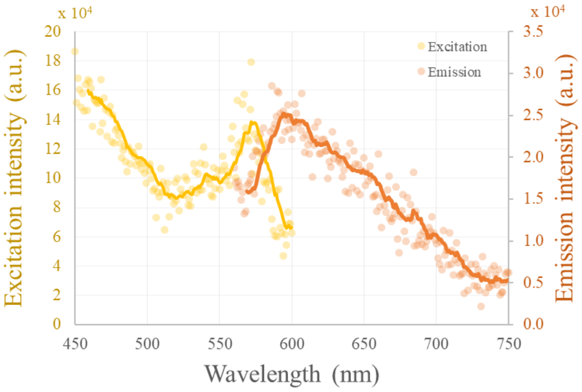

Figure 3: Excitation and emission spectra of mScarlet-I expressed in WOW droplets, measured in a well-plate reader after 4 hours of incubation at 37°C.

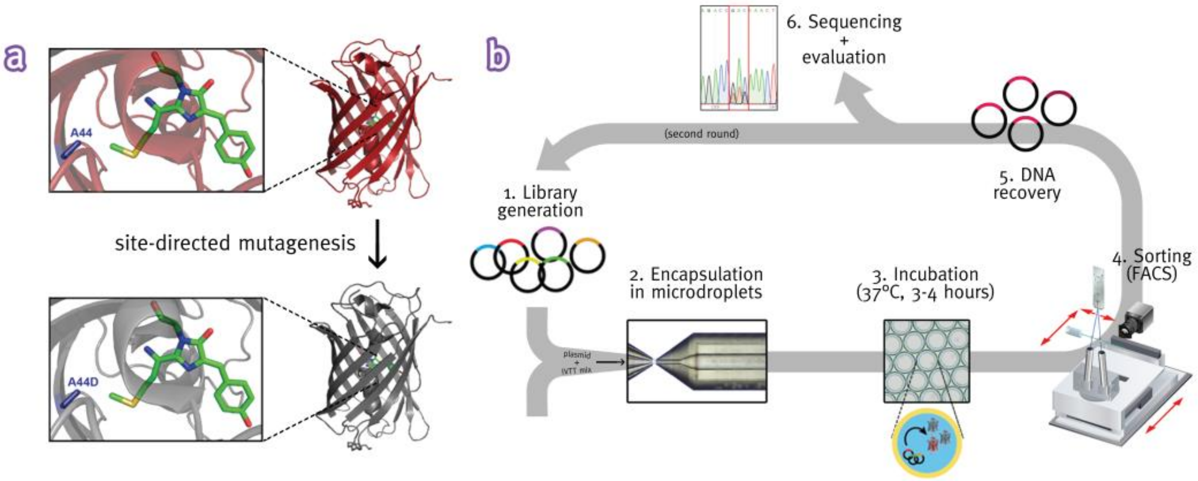

Figure 4: (a) Site-directed mutagenesis performed to obtain a non-fluorescent variant of mScarlet-I. (b) Simplified DE designed to prove the concept and the technological readiness to perform DE for biomolecule engineering.

We have also established giant unilamellar vesicles (GUV) construction for projects requiring more molecularly complex droplet lining. An established octanol-assisted liposome assembly protocol was used to generate and assemble GUVs rapidly [5]. With the addition of surfactant (50 mg/mL Poloxamer188) in the shell phase, the GUVs are stable for >1 week at 4°C. In generating the GUVs, controlling the pinch-off is more difficult due to the higher viscosity of octanol. The resulting GUV batches typically have a higher CV of around 5%. We plan to introduce an external force to destabilise the octanol stream and achieve smaller size ranges as well as better monodispersity.

CONCLUSION & OUTLOOK

A double emulsion microfluidic platform for biomolecule engineering has been achieved based on a commercial platform. Modifications are made to enable the injection and dosing of two core phases. Different droplet constructions have been tested and are altogether suited for a wide variety of applications.

As a proof-of-concept, DE will be performed using the droplets to evolve back a ‘dark’ variant of mScarlet red fluorescent protein. The library generation, encapsulation, in-droplets protein expression, and sorting are successfully tested separately. The different parts are to be tested together in the near future.

The same setup has been used to generate stable GUVs successfully. However, size range and monodispersity are still to be improved.

ACKNOWLEDGEMENTS

This work has been funded by the Alexander von Humboldt Foundation. The setup was funded by Deutsche Forschungsgemeinschaft (DFG, German Research Foundation) through the SFB 1459 – Intelligent Matter.

We would also like to thank Sabine Hüwel, Maria Dittmar, Sony, and Fluigent for the technical support with the various setups or experiments.

CONTACT

e.tanumihardja@uni-muenster.de (or)
e.tanumihardja@utwente.nl

REFERENCES

[1] U. T. Bornscheuer, B. Hauer, K. E. Jaeger, and U. Schwaneberg, “Directed Evolution Empowered Redesign of Natural Proteins for the Sustainable Production of Chemicals and Pharmaceuticals,” *Angewandte Chemie - International Edition*, vol. 58, no. 1, pp. 36–40, 2019, doi: 10.1002/anie.201812717.

[2] H. Xiao, Z. Bao, and H. Zhao, “High throughput screening and selection methods for directed enzyme evolution,” *Ind Eng Chem Res*, vol. 54, no. 16, pp. 4011–4020, 2015, doi: 10.1021/ie503060a.

[3] A. Manteca *et al.*, “Directed Evolution in Drops: Molecular Aspects and Applications,” *ACS Synth Biol*, vol. 10, no. 11, pp. 2772–2783, 2021, doi: 10.1021/acssynbio.1c00313.

[4] J. M. Holstein, C. Gylstorff, and F. Hollfelder, “Cell-free Directed Evolution of a Protease in Microdroplets at Ultrahigh Throughput,” *ACS Synth Biol*, vol. 10, no. 2, pp. 252–257, 2021, doi: 10.1021/acssynbio.0c00538.

[5] S. Deshpande, Y. Caspi, A. E. C. Meijering, and C. Dekker, “Octanol-assisted liposome assembly on chip,” *Nat Commun*, vol. 7, Jan. 2016, doi: 10.1038/ncomms10447.

TRANSFER VOLUME MODELING FOR FEEDBACK-FREE, AUTOMATED SINGLE SPHEROID DEPOSITION USING DROPLET-GENERATED MICROFLUIDIC FLOW

V. Zieger[1], D. Frejek[2], S. Zimmermann[1], P. Koltay[1], R. Zengerle[1,2] and S. Kartmann[1,2]
[1] Laboratory for MEMS Applications, IMTEK – Department of Microsystems Engineering,
University of Freiburg, Freiburg, Germany
[2] Hahn-Schickard, Freiburg, Germany

ABSTRACT

We present a microfluidic system that automates transfer of multicellular spheroids from a reservoir to designated target wells in well-defined quantities. Spheroids are transported through a disposable capillary with a microfluidic flow driven by a droplet dispenser at the end of the capillary. To dispense spheroids individually, the number of droplets required to deliver a spheroid can be predicted for a given dispensing droplet volume. In this way, we achieve a single spheroid deposition accuracy of 100% with a throughput of 13 spheroids per minute. This makes the platform a powerful tool for selective and accurate number controlled spheroid deposition.

KEYWORDS

3D cell culture, spheroids, feedback-free, single-spheroid-deposition

INTRODUCTION

Multicellular spheroids used as three-dimensional (3D) *in vitro* models are powerful tools for replicating *in vivo* conditions, particularly in drug screening and personalized therapy approaches [1]. However, standard spheroid cultivation techniques provide little ability to control and adjust the exact number of spheroids and their size in a test well for a drug screening. However, these parameters can have a significant impact on the drug response. In addition, many manual steps limit the throughput and precise reproducibility of test conditions.

To address these challenges, efforts have been made to automate the handling and controlled deposition of individual spheroids. One example is the Pick-and-Place method [2]. For this technique, negative pressure is used to draw spheroids into a pipette tip. Releasing the pressure again achieves precise repositioning of the spheroids. A major drawback of this method is the low throughput of only two to four spheroids per minute. A promising alternative is non-contact dispensing through Drop-on-Demand methods [3, 4]. For this method, spheroids are delivered to target positions encapsulated in droplets. Problematic with this approach is the fact, that the sample reservoir is placed above the dispensing nozzle and sample components are reaching the nozzle in an uncontrolled way. Depending on the sample concentration, sedimentation effects or impurities can make single spheroid deposition challenging and nozzle clogging is more likely to happen than in the system presented here.

In this article, we present an innovative yet simple label-free platform for automated single spheroid deposition. Reliable and fully automated deposition of individual spheroids is achieved through straightforward microfluidic flow rate regulation, using droplet dispensing to ensure a controlled and predictable spheroid transfer.

MATERIALS AND METHODS

Cell and spheroid culture

For this study, we cultured the MCF7 human breast cancer cell line obtained from the BIOSS Center for Biological Signaling Studies in Freiburg, Germany. We used Dulbecco's Modified Eagle Medium (DMEM) with high glucose, GlutaMAX™ Supplement, and pyruvate from ThermoFisher Scientific, USA, supplemented with 10% fetal bovine serum (FBS) from Biochrom AG, Germany, and 1% penicillin/ streptomycin from Thermo Fisher Scientific, USA (complete culture medium). Spheroids were generated using Corning Elplasia 12K flasks (Corning, USA) according to the manufacturer's instructions. Cells were harvested and resuspended in 25 ml of complete culture medium before being placed in the Elplasia flasks, where they settled into micro cavities. After four days of incubation, spheroids had formed and could be harvested by washing the flasks with PBS, collecting, and resuspending the sample in complete culture medium.

The Pick-Flow-Drop principle

The Pick-Flow-Drop principle is a novel approach for the controlled manipulation of 3D cell aggregates such as spheroids (Fig. 1 A, B) [5]. It combines elements of the Pick-and-Place technique and the Drop-on-Demand approach. In brief, the sample containing the spheroids is placed in a reservoir, e.g. a Petri dish. The spheroids are allowed to sediment and can be imaged at the bottom of the Petri dish with the platform. Suitable spheroids can then be selectively aspirated using a polyimide capillary with 250 µm inner diameter. This is accomplished by moving the reservoir with a motorized stage so that the selected spheroid is positioned below the capillary opening. The capillary is lowered and a microfluidic aspiration flow draws the spheroid into the capillary. A non-contact droplet dispenser (PipeJet, P9, BioFluidix GmbH, Germany) at the other end of the capillary, which continuously dispenses nanoliter droplets, generates this flow. The capillary forces create a constant capillary refill and thus an aspiration flow in the reservoir. With each ejected droplet, spheroids aspirated into the capillary are transported further through the capillary until they reach the dispensing nozzle. Each spheroid is then deposited at a target position confined in an ejected droplet.

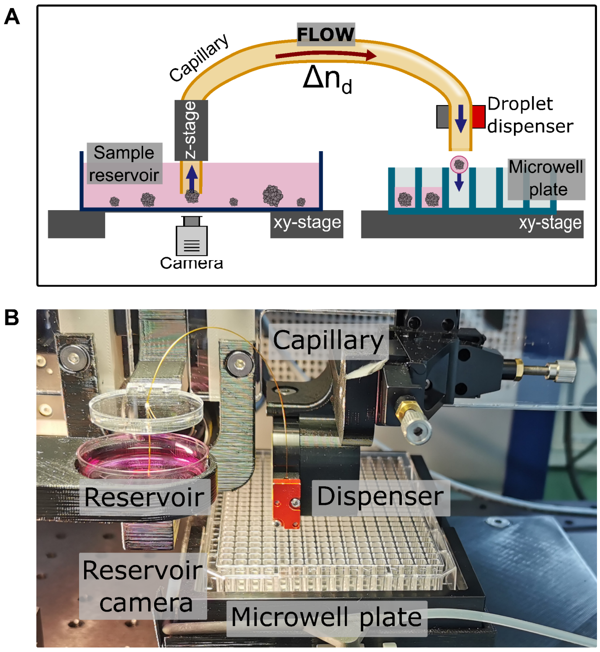

Figure 1: Schematic A) and photo B) of the spheroid deposition platform.

Drop volume measurement

In order to quantify the average flow rate, which determines transfer velocities of spheroids, the volume of ejected droplets has to be quantified. For this purpose, images of ejected, free-flying droplets are recorded with a camera. The images are then processed using a computer-based image analysis algorithm to calculate the droplet volume according to the method described in detail in ISO 23783-2:2022 [6]. The flow rate of the microfluidic transfer flow can be estimated from the droplet volumes as follows:

$$V_{\mathrm{r}} = V_{\mathrm{d}} \cdot f \tag{1}$$

where V_{d} is the volume of an ejected droplet and f is the droplet dispensing frequency. Both variables can be controlled via PipeJet parameter adjustment. Within this work, the considered droplet volume was in a range between 13 nl and 35 nl. The considered droplet dispensing frequency was between 4.4 Hz and 10.7 Hz.

Data presentation and statistical analysis

Values state the mean values ± standard deviation. Box plots extend from first to third quartile of the data, the median is shown as centerline. The whiskers extend from the edges of each box to the last data point in the 1.5 x interquartile range and outliers are shown as circles. Bar plots show the mean value with error bars equal to the standard deviation.

RESULTS AND DISCUSSION

Feedback-free spheroid deposition

Automated spheroid deposition with precise control over the amount of spheroids deposited requires knowledge of the position of the spheroid in relation to the nozzle orifice of the dispenser. One way to achieve this is via image-based spheroid detection in the nozzle of the dispenser shortly before the ejection [3, 4]. However, this usually requires complex detection algorithms, as the nozzle material, bubbles or spheroids that are too close together can cause distortions and detection errors. We are therefore pursuing the approach of detecting spheroids in a flat reservoir, e.g. a Petri dish, where good optical conditions can be created for optimal imaging. This allows not only the detection and selection of spheroids with favorable properties for the intended use, but also the detection of the aspiration time point of the selected spheroid. By knowing the droplet size and the droplet ejection frequency, the average flow rate can be calculated, which determines the transfer velocity of an aspirated spheroid, from which its position can be calculated at any time. Within this work, we aim to model and predict the required number of ejected droplets n_D for a successful transfer of a spheroid from the reservoir through the capillary to the dispensing nozzle. The less variable the required number of ejected droplets n_D for different spheroids, the more precise and rapid will be the feedback-less spheroid deposition.

Possible variance sources for spheroid transfer

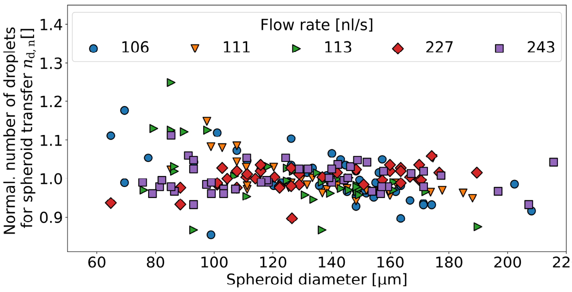

Figure 2. Normalized number of droplets required for spheroid transport depending on spheroid size with varied flow rates.

Initially, we assessed the factors contributing to variations of n_{d}. For this, we measured the number of dispensed droplets required to transfer MCF7 spheroids through the capillary. We varied droplet volumes, dispensing frequencies, capillary lengths l_{C}, and spheroid sizes within a diameter range from 60 µm to 220 µm. Interestingly, we observed that the spheroid diameter had limited impact on n_{d}, with greater variation noted for spheroids smaller than 100 µm (Fig. 2).

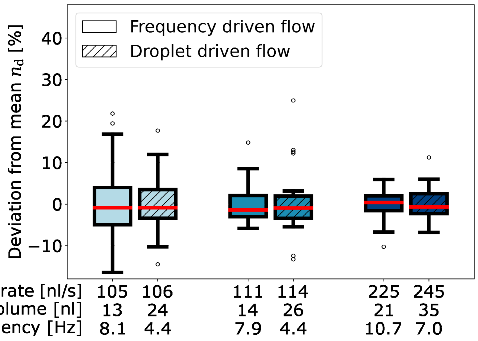

Figure 3. Effect of dispensing frequency or drop volume on the variance of the measured required number of ejected droplets n_D to transfer a spheroid (n≥34).

In a next step, we evaluated if droplet volume or dispensing frequencies had effects on the variability of n_{d}. In this context, a frequency driven flow means that the flow is generated with rather small droplets but a high frequency. Droplet driven flow means that the flow is generated with rather large droplets but a lower frequency. For low flow rates, a frequency driven flow increased slightly the variance compared to a droplet driven flow (Fig. 3). However, this effect was not visible for higher flow rates.

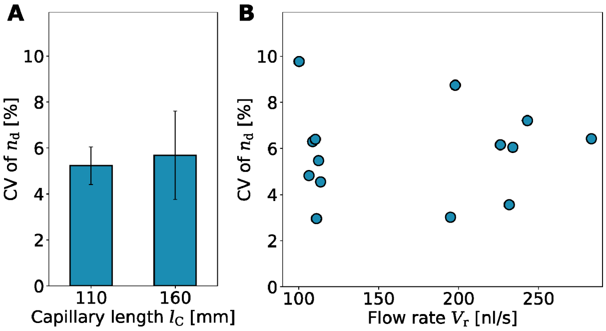

Figure 4. Coefficient of variation (CV) of n_d depending on capillary length l_C (A) and flow rate (B).

Subsequently, we investigated whether the capillary length l_c could lead to increased or decreased variance. We reduced l_C from 160 mm to 110 mm and measured for both lengths n_D for different flow rates. We then calculated the coefficient of variation (CV) (Fig. 4A). Further, we also measured the CV of n_D for different flow rates (Fig. 4B). In general, CVs were in the range of 3% to 9%. Increasing the flow rate did not reduce this variation.

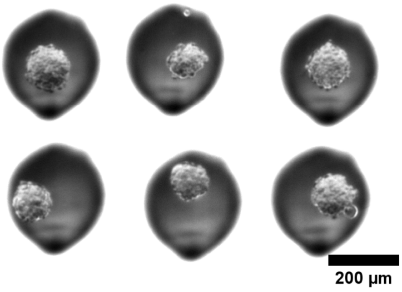

Figure 5. Representative examples of spheroid position under the capillary opening (large black circle) prior to aspiration. Differing positions of spheroids with respect to the capillary center will lead to different positions of the spheroid within the flow profile perpendicular to the flow direction after aspiration.

In summary, our investigations lead to the hypothesis that the primary source of n_{d} variation is related to the different positions of spheroids within the flow profile perpendicular to the flow direction. This variability originates mainly from the automated spheroid placement under the capillary opening using the motorized stage before aspiration (Fig. 5). In particular, the fact, that no severe increase of n_{d} variation with increasing capillary length was observed in Fig. 4A justify the assumption, that spheroids also change their position within the flow profile during the transfer. Otherwise, the effect of different starting velocities due to differing initial positions along the flow profile would add up and increase n_{d} variations with increasing capillary length. A position change of the spheroid along the flow profile during the transfer can happen due to uneven spheroid shape and sedimentation effects leading to a non-streamlined trajectory.

Transfer volume prediction for single spheroid deposition

The experiments reported before allow for the generation of a linear prediction curve for n_{d} for different droplet volumes V_{d} (Fig. 6). The gray area shows the range between the measured minimum $n_{\mathrm{d,min}}$ and maximum $n_{\mathrm{d,max}}$ number of dispensed droplets required to successfully transfer a spheroid. The variability range of required droplets to transfer a spheroid is characterized with $n_{\mathrm{VR}} = n_{\mathrm{d,max}} - n_{\mathrm{d,min}}$. To enable single spheroid deposition, n_{VR} characterizes the number of the droplets that must be dispensed before the next spheroid can be aspirated. Using the prediction curve in Fig. 6, it is possible to calculate the variability range n_{VR} for any desired droplet volume.

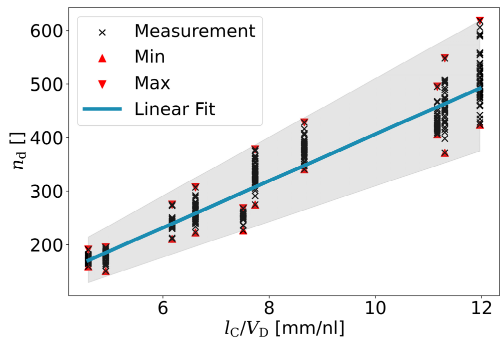

Figure 6. Measurements and linear fit as prediction for n_d for different droplet volumes V_d with respect to the capillary length l_C.

With that, we were able to establish a single spheroid deposition efficiency of (100 ± 0)% (N=3, n=36), meaning that exactly one spheroid was placed in each target well. The spheroid throughput scales with the frequency of dispensing. We operated at a minimum throughput of 13 spheroids per minute. In case that no single spheroid deposition is required, but a defined number of spheroids n_S is to be deposited into a specific target well, n_S spheroids are aspirated one after another. This is done without waiting n_{VR} droplets after each aspiration event. Only after the n_Sth spheroid aspiration, n_{VR} droplets are dispensed, before the next round of spheroid aspiration for the next well is started. In this way, it is possible to increase the spheroid throughput. As the maximum achievable aspiration rate of the system is 21 spheroids per minute, the spheroid throughput approaches this maximum rate as n_S is increased (Fig. 7).

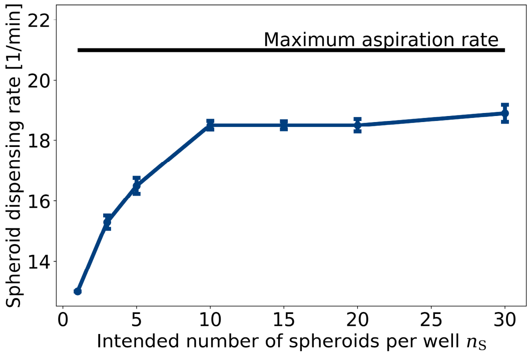

Figure 7. Measurement of the spheroid throughput depending on the defined number of spheroids n_S that are to be deposited into individual target wells.

CONCLUSION

Our microfluidic system based on spheroid aspiration and transport through a thin capillary is capable of well-controlled spheroid deposition. So far, only large and bulky laboratory platforms were able to accomplish this, however, usually providing even a lower spheroid throughput of only around < 10 spheroids per minute. Within this work, we showed that by predicting the number of droplet ejections required to transport a spheroid through the capillary, it is possible to enable highly accurate single spheroid deposition. As no further feedback is required to enable the deposition, the platform can be kept very simple and small in size. In general, controlled and automated spheroid handling will increase accessibility, throughput and reproducibility of 3D cell culture research and will therefore help to understand drug responses, disease pathways and tissue development.

REFERENCES

[1] Duval, K., Grover, H., Han, L.-H., Mou, Y., Pegoraro, A. F., Fredberg, J., and Chen, Z. “Modeling Physiological Events in 2D vs. 3D Cell Culture,” *Physiology (Bethesda, Md.),* 4, 32, 2017, 266–277.

[2] Ayan, B., Heo, D. N., Zhang, Z., Dey, M., Povilianskas, A., Drapaca, C., and Ozbolat, I. T. “Aspiration-assisted bioprinting for precise positioning of biologics,” *Science Advances,* 10, 6, 2020, 5111.

[3] Dornhof, J., Zieger, V., Kieninger, J., Frejek, D., Zengerle, R., Urban, G. A., Kartmann, S., and Weltin, A. “Bioprinting-based automated deposition of single cancer cell spheroids into oxygen sensor microelectrode wells,” *Lab on a chip,* 22, 22, 2022, 4369–4381.

[4] Gutzweiler, L., Kartmann, S., Troendle, K., Benning, L., Finkenzeller, G., Zengerle, R., Koltay, P., Stark, G. B., and Zimmermann, S. “Large scale production and controlled deposition of single HUVEC spheroids for bioprinting applications,” *Biofabrication,* 2, 9, 2017, 25027.

[5] Zieger, V., Frejek, D., Zimmermann, S., Miotto, G. A. A., Koltay, P., Zengerle, R., and Kartmann, S. “Towards label-free standardization in 3D cell culture: Automated, selective and gentle high-throughput handling of spheroids and organoids via novel Pick-Flow-Drop principle,” *Advanced Healthcare Materials*, 2024, Accepted for publication.

[6] ISO, 2023. *ISO 23783-2:2022 Automated liquid handling systems Part 2: Measurement procedures for the determination of volumetric performance.* https://www.iso.org/standard/76958.html. Accessed 25 December 2023.

CONTACT

* V. Zieger, viktoria.zieger@imtek.uni-freiburg.de

INNOVATIONS IN GAS FLOW CONTROL APPLICATIONS: SURFACE CHANNEL TECHNOLOGY, PRESENCE AND FUTURE

D.A.P. Oudejans[1], *V. Hengeveld*[1], *J.C. Lötters*[1,2]
[1] Bronkhorst High-Tech B.V., Ruurlo, The Netherlands
[2] University of Twente, Integrated Devices and Systems, Enschede, The Netherlands

ABSTRACT

This article discusses an unprecedented microfluidic innovation in gas flow control. During the development of this innovation, market study and search for a technological solution went hand in hand. 'Surface Channel Technology' became the heart of the development and has inspired building a new product line from the ground up, which resulted in the FLEXI-FLOW product line of Mass Flow Controllers of Bronkhorst High-Tech. Several useful features have been created for a wide group of gas flow control applications. Here, the reader is introduced to such gas flow control applications, user needs and the applied technology, while also discussing recommendations for future innovation.

KEYWORDS

Gas flow control, mass flow control, microfluidics, MEMS, LEAN product development, market study

INTRODUCTION

A number of gas flow control applications have been studied to find what users need and desire within their application. The study concentrated on applications that likely benefit from MEMS technology and in specific, an innovation that was started by the University of Twente and Bronkhorst High-Tech, called ‘Surface Channel Technology’. From the collected information, a vision was formulated for a new product line, which has served as a guideline for full technical product development. It can be concluded that in many flow control application fields, there are trends that require higher efficiency and performance of flow control devices. The presented innovation is targeted to meet those requirements.

GAS FLOW CONTROL

In industry, certain manufacturing processes involve gaseous media. For example, gases are used to cool, heat, flush, feed or react in order to enable these manufacturing processes. The same goes for analytical and testing type processes. The amounts of gaseous media in these processes are often controlled by gas flow controllers. Gas dosing is taking place, where a gas flow sensor is measuring the gas flow rate and a proportional valve is controlling it. The flow controller follows an externally given setpoint. The figures 1 and 2 show a picture and a schematic diagram of an electronic gas flow controller in the form of P&ID symbols (Piping & Instrumentation Diagram).

Figure 1. Example of an electronic gas flow controller. Photo courtesy of Bronkhorst.

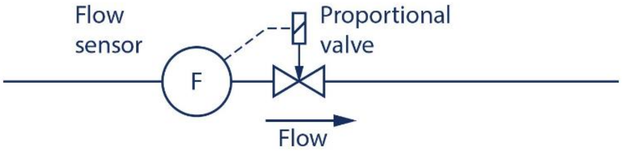

Figure 2. P&ID symbols that denote a gas flow controller, also known as a mass flow controller. The proportional valve is controlling the gas flow rate by means of a closed feedback loop, including a flow sensor.

GAS FLOW CONTROL APPLICATIONS

There is a wide group of industrial and instrumental applications that need gas flow control. Some examples are given here. One could think of analytical equipment that determines the concentration of elements in environmental samples. Another example is production of vaccines in a bioreactor by the help of bacteria [1]. A form of surface treatment is reactive sputtering, which is for instance used to apply anti-reflective coating to glass panels [2]. An emerging application is hydrogen flow control for automotive and stationary fuel cells. Another application is testing of industrial parts and consumer products for gas leaks with the help of pressure and flow control instruments [3]. Heating by burning a controlled gas mixture is applied in glass and steel manufacturing, as for some gluing and plastic processes. Last but not least, there is the wide variety of gas flow control applications in the field of research [4].

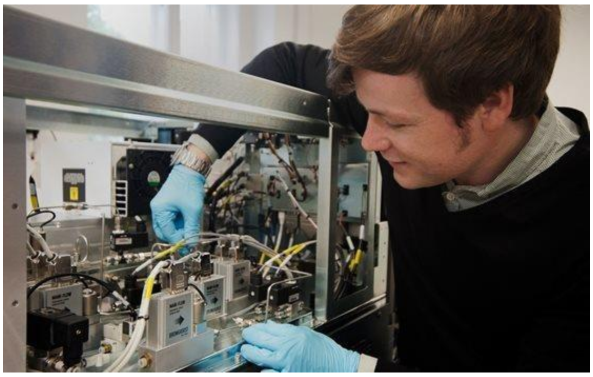

Figure 3. Gas flow controllers are installed in an analytical installation. Long-term stability is desired to meet the user's need to "fit and forget". Photo courtesy of Bronkhorst.

Figure 4. Gas flow control in burner applications for glass manufacturing. Fast ratio control of gases within the mixture results in a consistent flame temperature. Photo courtesy of Bronkhorst.

MARKET STUDY

In many flow control application fields, trends can be expected that require improved performance of flow control devices. Therefore, continuous market monitoring is performed by Bronkhorst High-Tech's strategic marketing department to collect such information. It has the goal to anticipate on these trends by product innovation and dedicated marketing. Because MEMS sensor technology is known to excel in stability, speed and compactness, market studies are performed that are targeted on these properties. So, parallel to the development of an innovative MEMS gas flow sensor, the needs of users, related applications and related business cases have been collected that match the potential performance of MEMS technology. As part of LEAN product development, a 'Core Hypothesis' is formulated that encapsulates the vision for a new product line [5, page 95]. The Core Hypothesis is validated against the collected market information and technical possibilities. It has subsequently served as a guideline for technical product development.

MARKET STUDY RESULTS

Our market study has shown that users highly value the speed of flow control, the ability to control a wide range of flow rates and a wide range of gas types, the long-term stability and the compactness of flow control systems. It is understandable that users are helped by improvement of these features, since industrial and laboratory equipment is pushed to become increasingly precise and time, space and cost efficient. Besides, equipment is meant to be used for many years with a minimum of maintenance, which corresponds to the user's need to 'fit and forget'. Additionally, users, such as researchers and equipment manufacturers, look for flexibility. Flexibility broadens the spectrum of use for researchers and enables equipment manufacturers to efficiently keep product stock that maintains its value.

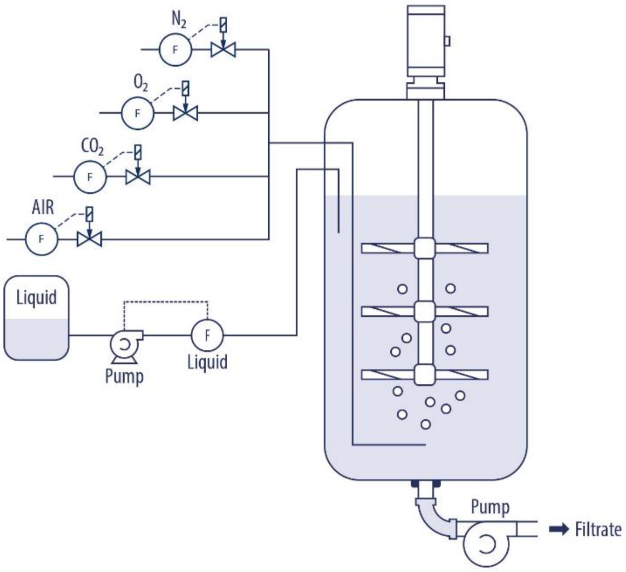

Figure 5. Gas dosing of N_2, O_2, CO_2 and Air to a bioreactor. For equipment manufacturers, a large dynamic range of flow control enables to keep stock of devices and react fast to an end-user request with specific flow rates. For end-users, it enables to use the same bioreactor system for different types of biological experiments.

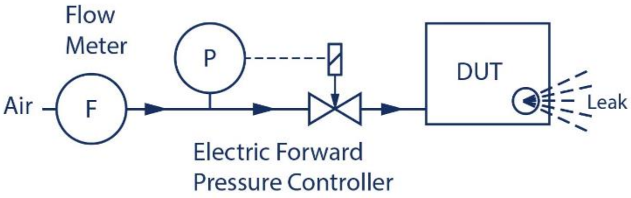

Figure 6. Leak testing of parts and products involves gas flow and pressure instruments. Flow & pressure functionality in a single device is beneficial for compactness and cost-efficiency.

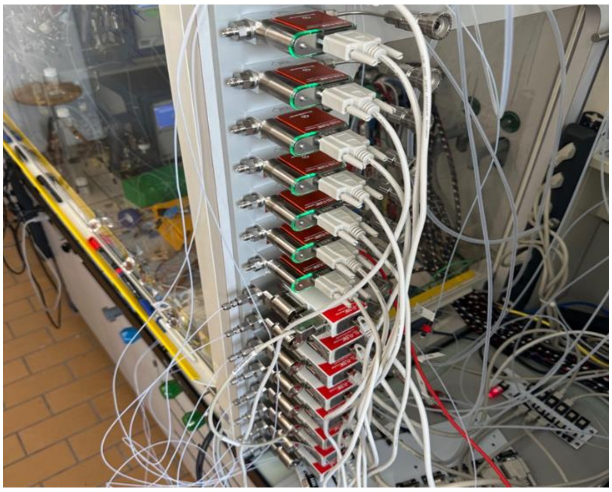

Figure 7. In research, an on-board gas database simplifies the use of gas flow controllers by offering flexibility. A different research experiment might require different gas types. With an on-board gas database, each gas flow controller can be set to the right gas type by the researcher. Photo courtesy of Bronkhorst.

DESIRED PROPERTIES

Table 1 shows relationships between gas flow control applications and typically desired properties.

Table 1. Table with gas flow control applications and desired properties for gas flow control. The check marks give the relation between applications and typically desired properties.

		Properties						
		Fast Response	Large Dynamic Range	Long-term Stability	Compactness	Flow & Pressure	Gas database	Data logging
Applications	Analytical			✓	✓			✓
	Biotechnology		✓	✓	✓	✓	✓	✓
	Surface Treatment	✓						
	Fuel Cell Testing	✓	✓	✓				
	Leak Testing	✓	✓		✓	✓		
	Burners	✓						
	Research	✓	✓	✓		✓	✓	✓

INNOVATION

As a technology push and inspired by market insights, Bronkhorst and the University of Twente further developed 'Surface Channel Technology', which originated at the University of Twente [6]. It is used to create a unique type of microfluidic MEMS chip sensors (figure 8). MEMS processes are applied to create on-chip microfluidic capillaries with heaters and temperature sensors for sensing the flow rate of the gas that is passing through the capillaries. A large advantage of flow sensing by capillaries is the ability to perform accurate calculation of the flow rate for different gas types on the basis of a nitrogen calibration and an on-board gas database [7].

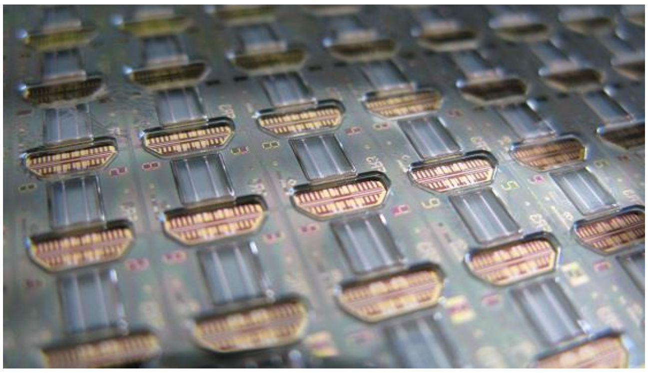

Figure 8. A wafer of MEMS flow sensor chips, made with Surface Channel Technology. Each flow sensor chip contains capillaries that sense the gas flow rate. The capillaries are encapsulated by a transparent protection. The open areas are for electrical connections. The bottom side, which is not visible in this picture, contains fluidic connections for the gas. Photo courtesy of Bronkhorst.

Through the use of stable materials and deposition methods and a dual capillary topology, the flow sensor obtains its exceptional stability. It provides the sensor a large dynamic range and long-term stable behaviour [7]. Therefore, it enables users to measure and control over a broad flow range and postpones the moment of recalibration. Since the capillaries are thin-walled and thus have a low thermal mass, the sensor responds very quickly to changes in gas flow [7]. Table 2 shows an overview of specifications that could be achieved by applying 'Surface Channel Technology'.

Table 2. Overview of gas flow control specifications that could be achieved by applying "Surface Channel Technology".

Repeatability	< ±0.2 % Rd
Dynamic range	1:1000
Long-term stability	< 0.5 % FS over a period of 3 years
Control settling time	< 150 ms
Multi gas	22 unique gases
Pressure resistance	17 bar(a) Full Scale
Dimensions (mm)	70 x 60 x 20

‘Surface Channel Technology’ initiated the engineering of a completely new product line called FLEXI-FLOW (figure 9). The goal has been to integrate the previously mentioned features, but also to respond to the customer's need for flexibility. A built-in gas database allows switching between a wide range of gas types, and pressure sensors at the inlet and outlet provide additional functionality within a single device. Figure 10 shows a P&ID schematic of the internals of a FLEXI-FLOW flow control device.

Figure 9. Compact gas flow control devices from the FLEXI-FLOW product line. A number of useful features have been created for a wide group of gas flow control applications. Photo courtesy of Bronkhorst.

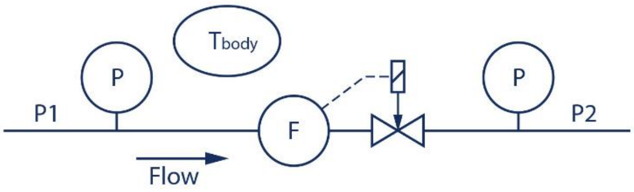

Figure 10. P&ID of the FLEXI-FLOW gas flow controller with gas pressure functions. P stands for pressure measurement. F stands for flow measurement. T stands for temperature measurement.

CONCLUSIONS

A collaboration between the University of Twente and Bronkhorst High-Tech resulted in the development of an innovative and unique gas flow sensor, based on MEMS ‘Surface Channel Technology’. Through market study, a match is found between user needs in a selection of gas flow control applications and the potentials of MEMS ‘Surface Channel Technology’. This has inspired to develop a completely new product line, called FLEXI-FLOW of Bronkhorst High-Tech, that contains a dedicated set of features to serve selected gas flow control applications.

RECOMMENDATIONS FOR FUTURE INNOVATION

This extended abstract is targeted to inform, but also to inspire microfluidic technology researchers to work on innovations in gas flow control solutions.

An extension of compatibility towards corrosive and humidity-sensitive gases would be beneficial to combine with the fast and stable performance of microfluidic MEMS. The use of better chemically resistant materials in sensor chip packaging and the elimination of elastomer sealing would for instance help in semiconductor CVD and etch applications, as well as reducing elastomers, out-gassing and moisture in any application.

PID-control is a common method to control a system to a desired setpoint. Machine-learning could enable a user- and process- independent flow control loop at the fastest response time without setpoint overshoot and control-instability.

Gas type recognition to enable gas-independent thermal flow measurement is a holy grail in the world of gas flow control and would lead to efficiency in any application.

Researchers and developers are encouraged to continue their useful work in microfluidics and contribute to a next generation of gas flow control products.

CONTACT INFORMATION

Dion Oudejans: d.oudejans@bronkhorst.com

REFERENCES

[1] Z. Fang et al., “Application of bioreactor technology for cell culture-based viral vaccine production: Present status and future prospects”, *Frontiers in Bioengineering and Biotechnology, 2022*

[2] S.J. Nadel et al., “Equipment, materials and processes: a review of high rate sputtering technology for glass coating”, *Thin Solid Films, V442, I1-2, 2003*

[3] Bronkhorst High-Tech, “Flow control used for leakage test of air ducts”, *Application Note A053*

[4] Bronkhorst High-Tech, “Accurate flow control for cancer research”, *Application Note A082-ME09*

[5] K. Radeka, “The shortest distance between you and your new product”, *ISBN:9780979532160, 2017*

[6] R.J. Wiegerink et al., “Thermal and Coriolis type micro flow sensors based on surface channel technology”, *Eurosensors XXIII, Lausanne, 6 Sept. 2009*

[7] W. Sparreboom et al., “Truly calorimetric flow sensor chip based on surface channel technology”, *MFHS 2014, Freiburg, 8 Oct. 2014*

TOWARDS A FULLY INTEGRATED FLUID HANDLING SYSTEM FOR AN INTRAVAGINAL WEARABLE DEVICE

J.J.A. Lozeman[1]*, J. Kaptein*[1]*, M. Odijk*[1]

[1] University of Twente, BIOS Lab-on-a-Chip group, Enschede, The Netherlands

ABSTRACT:

In this article, we report on fabricating a proof-of-concept device to be used as a fluid handling system for an intravaginal wearable sampling device. This device operates with one-way valves combined with a single peristaltic pump. We can introduce a sampling or cleaning buffer into a measurement chamber by changing the peristaltic pump's flow direction. We discuss the fabrication of the one-way check valves using readily available materials and their integration into the fluid handling system. Finally, we show the measurements performed to determine the opening pressure of the valves, followed by the first measurement performed using a food dye, proofing the operating principles of the device.

INTRODUCTION:

Historically, the participation of females in clinical trials has been underrepresented [1], [2]. For example, in the US, between 1977 and 1993, most women of "childbearing potential" were banned from participating in clinical studies[3]. Although the participation of women in clinical trials has improved in recent years, there still is an underrepresentation of women, even in the most relevant fields, such as cardiologic[4] and cancer[5] research. This underrepresentation causes discrepancies in knowledge about gender-specific medication, medical treatments, and toxicities of certain medications[1].

One field of gender-specific research that has been underrepresented is vaginal drug delivery and diagnostics. Drug absorbance in the vagina avoids the hepatic first-pass effect; it gets directly absorbed into the bloodstream [6]. The extensive vascularization of the vagina makes it not only an excellent place for drug delivery but also for diagnostic purposes.

In this project, we work on a fluidic sampling device connected to a sensing chamber for diagnostic purposes. The device is intended to be placed in a commercially available vaginal ring, namely the

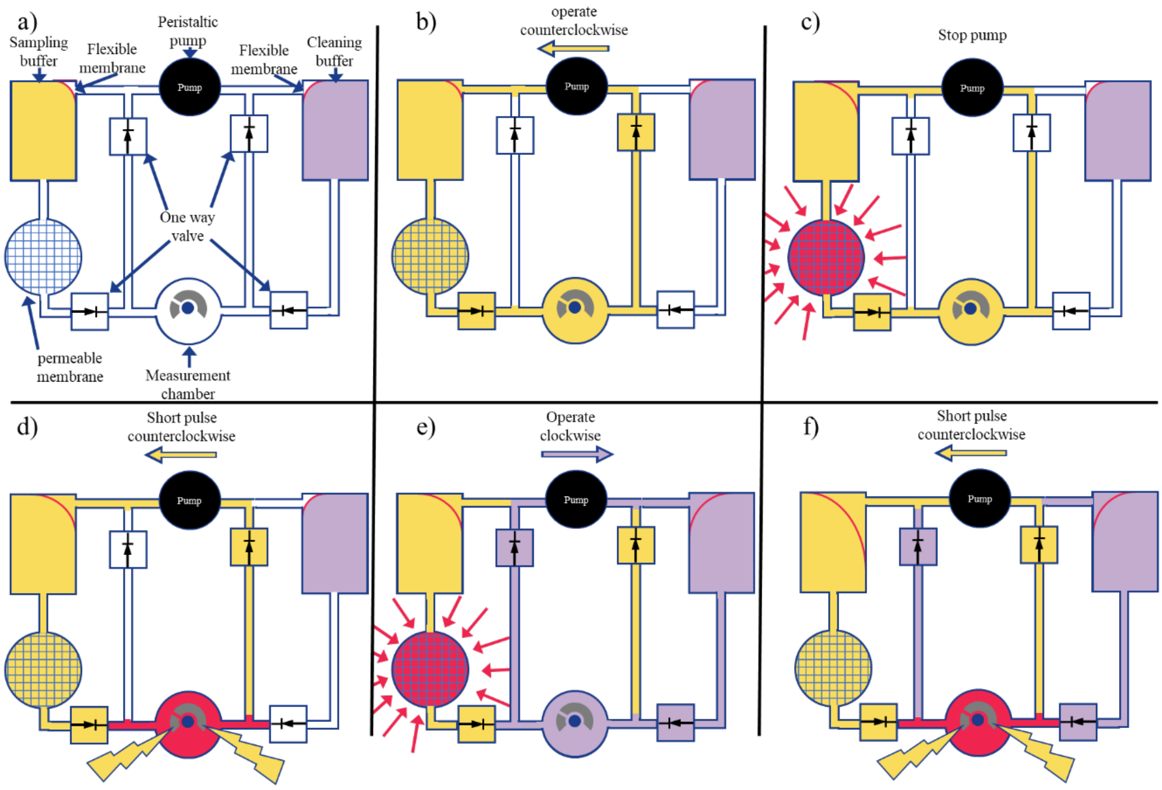

Figure 1. Schematic representation of the microfluidic sampling device (not to scale) and the operating mode explained. a) empty device with legend of the components. b) pumping in the counterclockwise mode flushes the system with the sampling liquid. c) stopping the pump for a pre-determined amount of time so the analyte can diffuse through the permeable membrane (analyte-containing buffer in pink). d) pump the analyte-containing sample buffer into the sensing chamber and perform the analyses. e) operate the pump in the clockwise mode, rinsing the system with the cleaning buffer. At the same time, the analyte can start diffusing into the sample buffer. f) the cycle can be repeated; pump the analyte-containing sample buffer into the sensing chamber and perform the analyses.

LiGalli MedRing. This end goal gives us certain restrictions in the device design and fabrication, most notably:

1) **Size**: The footprint of the entire device should be small enough to fit in a standard LiGalli Med ring
2) **Lifetime**: The device must be usable for 30 days. The drain on the battery should be minimal.
3) **Fabrication**: in the end, the design needs to be cost-effective and capable of being mass-produced.
4) **Robustness**: the device will be implanted in a human and should be robust enough to survive for 30 days
5) **Safety**: the device should be able to be operated safely, especially with chemical and electrical dangers in mind.

Fig. 1 shows the conceptual design of the final device for this project. Fig. 1a shows an empty, unused device. In practice, the device would be filled with a buffer, but for ease of explaining, the device is drawn as if empty. In Fig. 1a, we can see the peristaltic pump in the middle top of the figure. There are two buffer reservoirs filled with their respective buffers. A flexible membrane in the buffer reservoir separates the used buffer from the fresh buffer. Also visible are the four one-way valves used to control the flow path. A permeable membrane covers the sampling area to collect the analyte. The measurement chamber is located in the bottom center of the figure, where electrochemistry will be used to perform the analysis. Fig. 1b shows the first operating step. By operating the pump counterclockwise, the sampling buffer flushed the system. In Fig. 1c, the flow is stopped by a pre-determined amount of time, allowing an equilibrium to be created by the analyte in the vagina and the sampling buffer solution. After an equilibrium has been established, we activate the pump again, shown in Fig. 1d, to pump the sample plug into the measurement chamber, where the analyses will be performed. After the analysis, the system is operated in the clockwise mode, flushing it with the cleaning

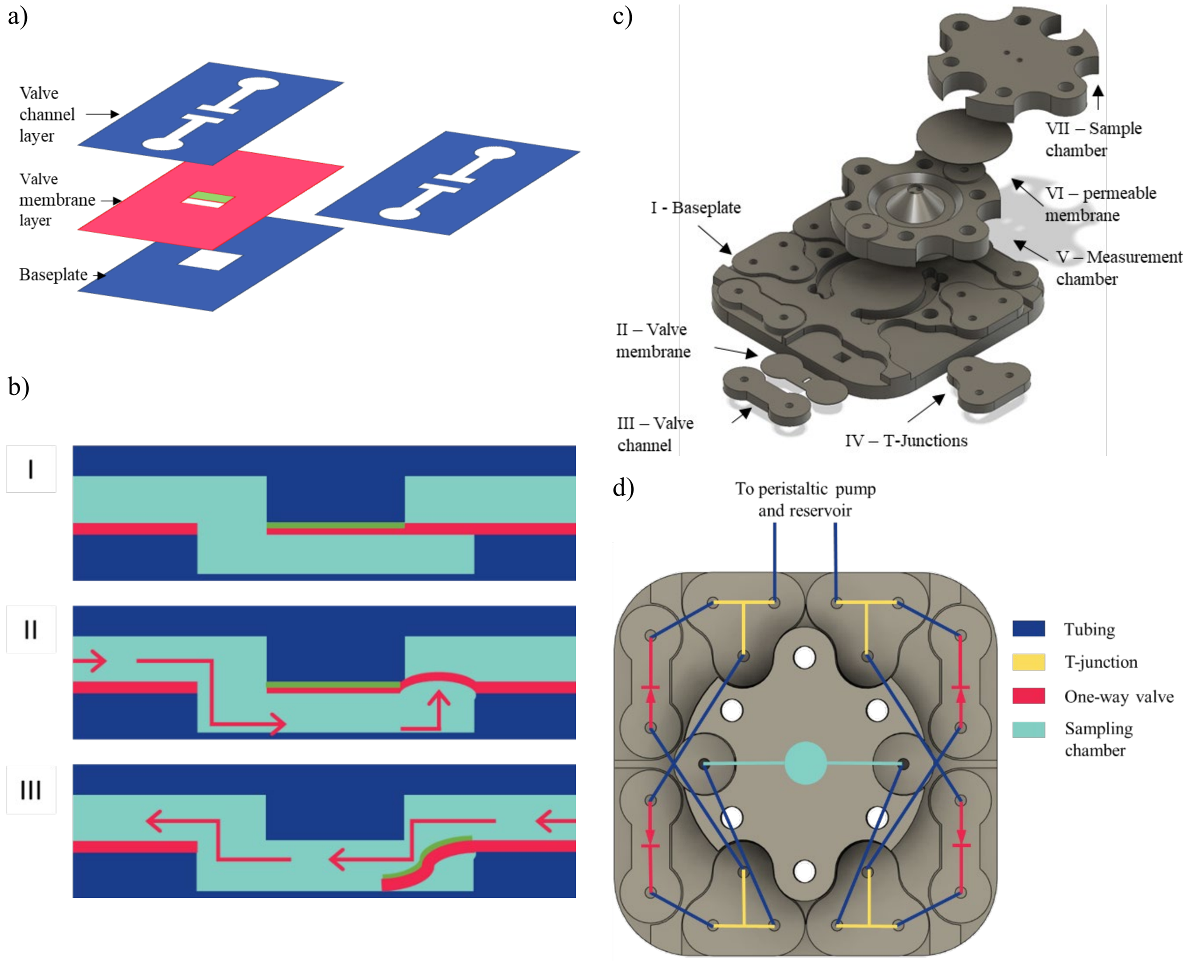

Figure 2. Schematic representation of a,b) the valve and c,d) the complete device. 2a and b show the valve layers, with the channel layer (blue) on top, the valve membrane layer (red) in the middle and the baseplate (blue) on the bottom. Note that the green area in the valve membrane layer indicates where the adhesive has been removed. a shows an exploded and assembled top view of the valve layer. b-I shows a side view of the membrane without flow. b-II shows a flow against the allowed flow direction, causing the valve to be sealed. b-III shows the flow in the allowed flow direction, the pressure opening the valve. c) shows the fusion 360 file of the assembly, with the device's dimensions being 5.0 x 5.0 x 1.5 cm. d) shows the routing of the liquid through the system.

buffer, as shown in Fig. 1e. At the same time, a new equilibrium can be established. Now, the cycle can be repeated till the buffer reservoir runs empty.

The work presented in this manuscript focuses on the one-way valves in combination with the bi-directional flow of the peristaltic pump. The goal is to prove that by changing the operating direction of the peristaltic pump in combination with the one-way check valves, we can rinse the measurement chamber with either the sampling buffer or the cleaning buffer. The design used for the current work is shown in Fig. 2b

METHOD:

A simple yet effective microfluidic check valve has been designed for this work. A schematic representation of the designed valve is shown in Fig. 2a. The device comprises two layers of PMMA with a layer of acrylic adhesive tape (Adhesive Research, Inc. ARcare 90445q) as the valve layer. The valve is integrated into the modular microfluidic sampling device as shown in Fig. 2b. The modular microfluidic sampling device consists of several components, namely a baseplate (Fig., 2b-I), 4 valve membrane layers (Fig. 2b-II), 4 valve channel layers (Fig. 2b-III), 4 T-junctions (Fig. 2b-IV), the measurement chamber (Fig. 2b-5V, the permeable membrane (Fig 2b-VI) and the sample chamber (Fig. 2b-VII). All the components, except the valve membrane layers, have been fabricated by micro-milling (DATRON Neo) a piece of PMMA polymer. The designs (made in Autodesk Fusion 360) were loaded in the milling machine, after which the program controls the mill (smallest tool used for the most delicate features in this design: ϕ 0,5 mm at 25.000 RPM and a feed rate of 300 mm min^{-1}. Larger tools were used for less delicate features, ϕ 1.0, 2.0 and 4.0 mm, where operated at 20.000 RPM and a feed rate of 400 mm min^{-1}). The device's dimensions are 5.0 x 5.0 x 1.5 cm (l, w, h). The valve channel pieces are 2.0 x 0.8 x 0.2 cm (l, w, h), with the actual valves being 0.18 x 0.18 x 0.18 cm (l, w, h). The adhesive layer used as the valve material was cut in the designed shape with a cutting machine (Cricut Maker) using the standard blade. Next, the adhesive tape is attached to the valve channel layer, and a nonstick area is created to prevent the sticking of the valve in specific areas (as shown in Fig. 2a). The removal of the adhesive layer has been

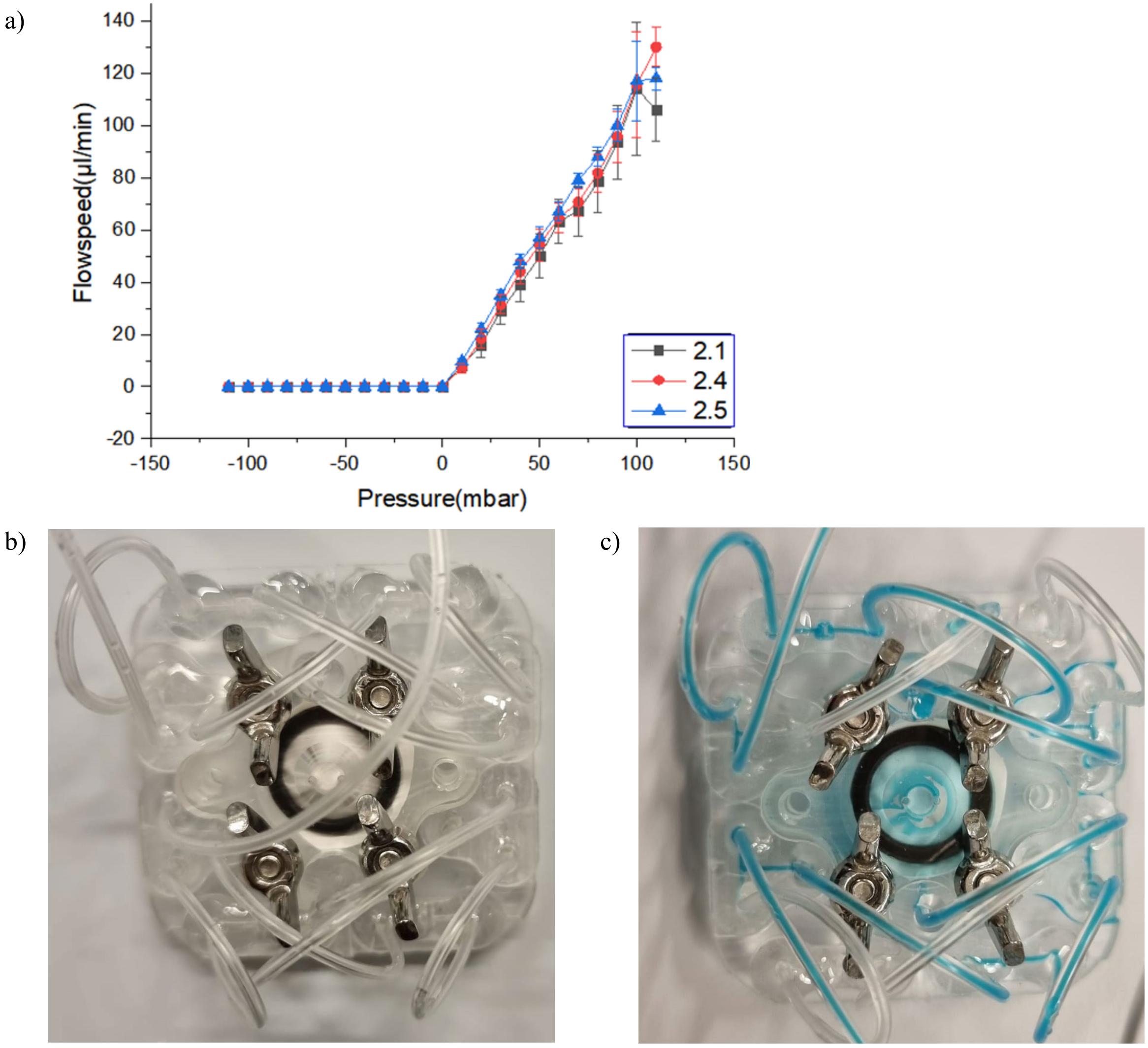

Figure 3. Test results of three one-way check valves. Positive pressure is pressure applied in the flow direction; negative pressure is pressure applied against the flow direction. b) Empty fabricated device. c) device filled with blue-coloured food dye

achieved with three different methods:

Method 1: Scratch and peel the adhesive layer of the carrier layer using a tweezer. The advantage of this method is that the area in which the adhesive layer is removed is easily controlled. A disadvantage is that the carrier layer can easily be damaged.

Method 2: Makes use of ethanol on a cotton swab to remove the adhesive layer. The advantage of this method is that it is difficult to damage the carrier layer this way. However, controlling the area where the adhesive layer gets removed is difficult.

Method 3: Inspired by the work of Amador-Hernandez et al.[7], makes use of nail varnish to passivate the adhesive layer. Nail varnish is easily applied and does not damage the carrier layer. It does require some time to cure, and the resulting valves often leak due to the shape of the cured droplet of nail polish. For the work shown in the document, the adhesive layer was removed using method 1.

After removing a specific area of the adhesive layer, the valve membrane layer is compressed between the valve channel layer and the baseplate (Fig. 2a-I). Compression is achieved by clamping the different layers together in a vice and waiting for 5 min. Next, the rest of the device is assembled. The T junctions are mounted on the baseplate using the same adhesive tape as used for the valve layers. The measurement chamber is clamped into position on the baseplate, and the permeable membrane is placed on top of the measurement chamber. Next, using 4 screws, the permeable membrane is clamped between the measurement chamber and the sample chamber. An O-ring in between the different layers is used to prevent leaking. Finally, Tygon tubing, in combination with Norland Optical Adhesive, was used to connect the modules, resulting in the device shown in Fig. 3b.

PRELIMINARY RESULTS:

In Fig 3. The first experimental results are shown. In the graph shown in Fig. 3a, the test results of 3 valves are shown. Each point averages three measurements, and error bars show the standard deviation. As seen in this graph, the valves open in the allowed flow direction at 10 mbar and stay closed with a flow against the allowed flow direction till at least 100mbar. In Fig. 3b, one can see an empty device. As can be observed, all the valve layers are empty. In Fig. 3c, we see the result after operating the pump for several minutes with a blue-coloured food dye in the counterclockwise operating mode. Valves II and IV are coloured blue, while valves I and III are transparent. Indicating an operational device,

CONCLUSION AND OUTLOOK:

The separate valves' results, shown in Fig. 3a, match the goals set for the minimum opening pressure in the flow direction and the minimum opening pressure in the counter flow direction. The initial results from the assembled device are promising and reason to further miniaturize the system. The following steps include further miniaturization of the device and improving the fabrication workflow to fit a production environment better.

ACKNOWLEDGMENTS

LiGalli B.V. funded this work. The authors would like to thank Victor Nickolson, Maarten Wiegerinck, and Willem de Laat for our fruitful discussions and their support of the project. We would also like to thank Sevil Sahin for our discussions and input on the device's design.

REFERENCES

[1] A. Z. Sosinsky, J. W. Rich-Edwards, A. Wiley, K. Wright, P. A. Spagnolo, and H. Joffe, "Enrollment of female participants in United States drug and device phase 1–3 clinical trials between 2016 and 2019," *Contemp Clin Trials*, vol. 115, p. 106718, Apr. 2022, doi: 10.1016/J.CCT.2022.106718.

[2] C. M. Mazure and D. P. Jones, "Twenty years and still counting: Including women as participants and studying sex and gender in biomedical research," *BMC Womens Health*, vol. 15, no. 1, pp. 1–16, Oct. 2015, doi: 10.1186/S12905-015-0251-9/TABLES/4.

[3] R. B. Merkatz, "Inclusion of Women in Clinical Trials: A Historical Overview of Scientific Ethical and Legal Issues," *Journal of Obstetric, Gynecologic & Neonatal Nursing*, vol. 27, no. 1, pp. 78–84, Jan. 1998, doi: 10.1111/J.1552-6909.1998.TB02594.X.

[4] C. Melloni *et al.*, "Representation of Women in Randomized Clinical Trials of Cardiovascular Disease Prevention," *Circ Cardiovasc Qual Outcomes*, vol. 3, no. 2, pp. 135–142, Mar. 2010, doi: 10.1161/CIRCOUTCOMES.110.868307.

[5] K. Kwiatkowski, K. Coe, J. C. Bailar, and G. M. Swanson, "Inclusion of minorities and women in cancer clinical trials, a decade later: Have we improved?," *Cancer*, vol. 119, no. 16, pp. 2956–2963, Aug. 2013, doi: 10.1002/CNCR.28168.

[6] M. M. El-Hammadi and J. L. Arias, "Nanomedicine for vaginal drug delivery," in *Theory and Applications of Nonparenteral Nanomedicines*, Elsevier, 2020, pp. 235–257. doi: 10.1016/B978-0-12-820466-5.00011-9.

[7] J. U. Amador-Hernandez, P. E. Guevara-Pantoja, D. F. Cedillo-Alcantar, G. A. Caballero-Robledo, and J. L. Garcia-Cordero, "Millifluidic valves and pumps made of tape and plastic," *Lab Chip*, vol. 23, no. 20, pp. 4579–4591, Oct. 2023, doi: 10.1039/D3LC00559C.

FLAT INTEGRATION OF PIEZOELECTIRC MICRO DIAPHRAGM PUMP IN FLEXIBLE CARRIER

E. Ahmed[1] *and A. Bußmann*[1]
[1] Fraunhofer Institute for Electronic Microsystems and Solid State Technologies EMFT, Munich, Germany

ABSTRACT

Many applications, such as drug delivery, organ-on-chip or micro total analysis systems require the precise movement of fluids. Especially if space is limited, piezoelectric micro diaphragm pumps are an adequate fluidic actuator. However, the electric and fluidic integration of the pump often requires a lot of space. To allow extreme miniaturization of dosing units, a space efficient integration method is crucial. In this work, we present the fluidic and electric integration of a micropump into a flexible foil stack. The fluidic inlet and outlet port are connected via channels that can be flexibly routed towards i.e., a reservoir. The positive and negative electrode of the piezoelectric actuator ceramic are connected via cupper electrodes. This integration allows to build extremely compact and flat system and therefore enables the development of dosing units with extreme special restrictions.

Key words: piezoelectric micro diaphragm pump, foil integration, flexible substrate, flexible electronics, laser structuring, laser ablation

INTRODUCTION

Micro diaphragm pumps enable the precise dosing of liquid or gas volumes. Their exact fluidic properties depend on the exact pump geometry, actuation mechanism and driving signal [1]. This flexibility in design makes them a suitable microfluidic actuator for various applications. Examples of gas transport are the sample transport for gas sensors, or scent dosing. The dosing of small amounts of liquids or generation of continuous small flow rates is required in many biomedical applications, such as drug delivery or organ-on-chip devices [2, 3].

Especially for biomedical application, the size of the overall delivery system can be extremely relevant. For instance, organ-on-chip devices optimally match the format of a standard multi well plate and thus require an extremely flat dosing unit. Another example are patch pumps for continuous drug delivery: current patch pump systems are bulky, often visible under clothing and can disturb the patient during sleeping, sports or showering [4]. A flat dosing can improve the patients' comfort and compliance and thus increase the treatment outcome.

Unfortunately, a very flat fluidic and electric integration of a micro diaphragm pumps is challenging. Housings require a minimal size to allow for manufacturing and sufficient stability. The housed micropump is often bulky and the flat dimensions of the diaphragm pump are lost with the housing [5, 6]. To optimize microfluidic dosing systems for the use in applications that require flat packages, a thin electrical and fluidical integration of the pump is necessary.

The aim of this work is to enable a flat integration of a piezoelectric micropump. The fluidic as well as the electric connection needs to be reliable and customizable to fit the requirements of different applications. Especially for the use in patch pumps, a flexible substrate is preferable. That allows for the overall patch to remain supple and offers more comfort to the patient.

MATERIALS AND METHODS

To evaluate the possibility of flat pump integration, the Fraunhofer EMFT silicon micropump of 5x5 mm² size is used. It was first introduced by Leistner et al. [7]. It consists of a silicon chip with a pump chamber and two passive flap valves (Figure 1). The piezoelectric actuator is glued on top of the actuation diaphragm.

Actuation is achieved with the indirect piezoelectric effect: An oscillating electric field causes the piezoelectric ceramic to contract and expand. This elongation causes the bending actuator (piezoelectric ceramic glued on top of the diaphragm) to bend upwards and downwards. The movement expands and compresses the pump chamber, which, in combination with the passive flap valves, leads to an effective fluid flow.

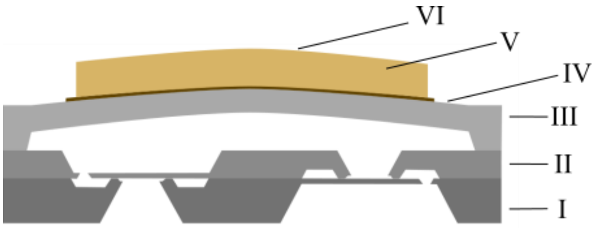

Figure 1 Silicon micro diaphragm pump with its outlet valve wafer (I), its inlet valve wafer (II), the actuation diaphragm wafer (III) and glued piezoelectric actuator (V) with the top electrode (VI) and bottom electrode (IV). Adapted from [8]

The micropump is well suited for drug delivery applications: With 5x5x0.6 mm³ it is extremely small. The piezoelectric actuation is energy efficient with a required power of few mW. The fluidic properties of the pumps match the requirements of drug delivery. For example, the delivery of 10 units of insulin is achieved in approximately 90 s, which is in the range of delivery units on the market [8]. An evaluation of the repeatability of package dosing of this pump with water and insulin solution shows that deviations are lower than the generally accepted 5% [8].

Electric and fluidic integration of the device is challenging. To drive the pump, the ground has to be connected to the bottom electrode. The bottom electrode of the ceramic is in contact with an aluminum layer on top of the actuator diaphragm wafer. This aluminum electrode expands to the edge of the pump and can thus be contacted on the outer rim. The top electrode is more challenging, since it has to be contacted on top of the actuator ceramic. This part of the pump moves in use and the motion should be as little restricted as possible to limit the impact on the pump's performance.

A good fluidic integration is also challenging, as it requires high precision. For optimal fluidic performance, it is advantageous to place the valves closely together. However, that limits the sealing area for fluidic integration. A tight connection, that prevents cross leakage is therefore crucial. However, the foils structure must also not block the inlet and outlet valve, which requires precise manufacturing and handling.

Integration materials

Polyimide (PI) is one of the most commonly used commercially available substrates for flexible electronics. This material possesses lightweight, excellent mechanical strength, chemical resistance, and thermal stability, PI ensures the final product maintains optimal flexibility and bendability without compromising its electrical properties, making it the best candidate as a substrate for the micropump integration in flexible carrier.

To ensure a good electrical contact to the micropump electrodes, a thick layer of electroplated copper (3-5 µm) is structured on the 50 µm thick PI, which is later electrically contacted to the electrodes.

For the purpose of stacking multiple layers, a 50 µm thick double-sided adhesive is employed. Its small thickness makes it optimal for this use case, facilitating flexibility within the system while maintaining mechanical stability.

The flexible carrier system is divided into four main parts. The 1st layer, at the bottom, encompasses fluidic channels for the micro-pump's inlet and outlet. This design ensures that the fluidic material exclusively contacts the bare PI layer within the system, preventing any contamination. The 2nd layer, the filler layer, with the same thickness as that of the micro-pump. Its primary functions are to improve the mechanical stability of the system and act as a bridge between different layers. The 3rd layer, the insulator layer, plays a critical role in preventing shortcuts or interconnections between the two electrodes. The 4th layer consists of copper electrodes, precisely cut to function as two flexible individual layers within the pump area. The first electrode aligns precisely around the hexagon structure, while the second electrode travels over the insulator layer, establishing contact with the ceramic area.

MICROPUMP INTEGRATION

After precisely preparing each layer through processes such as laser ablation for the copper electrodes, applying double-sided adhesive and conductive adhesive to each layer according to its intended purpose, and laser cutting to achieve the precise size required for the micropump, the integration process commences.

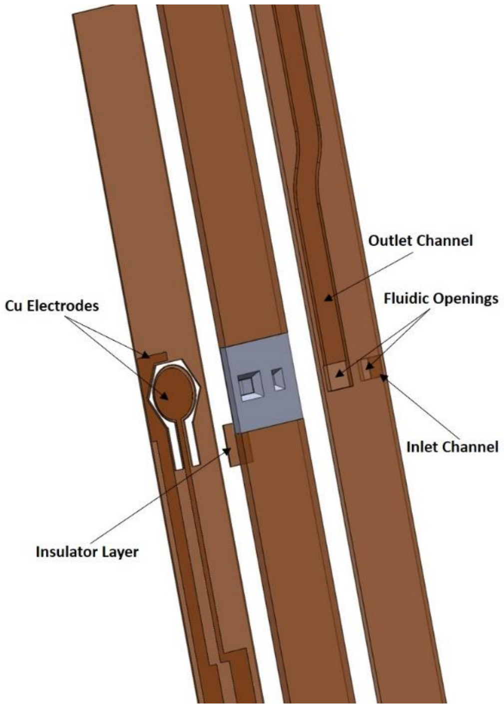

Figure 2 Bottom view of the different layers design for integration into flexible carrier

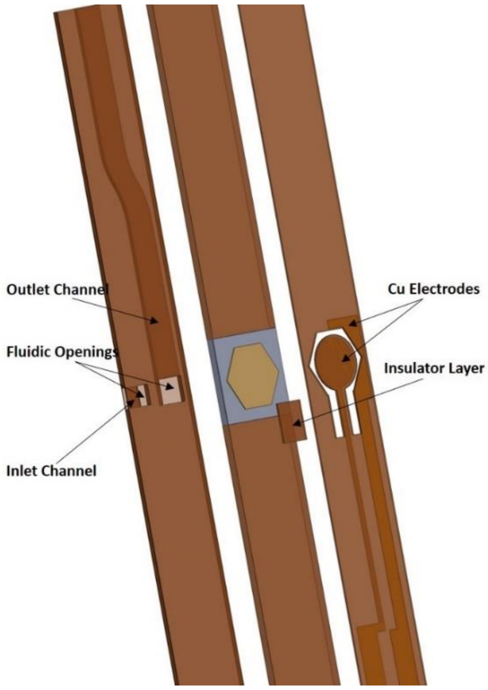

Figure 3 Top view of the different layers design for integration into flexible carrier

This process begins with the initial application of the fluidic channels layer, where high precision is employed to align the inlet and outlet valves with the channel holes, ensuring a completely sealed system (Figure 2).
Subsequently, the filler layers are applied, followed by the insulator layer. Finally, the Cu electrodes layer is accurately applied, guaranteeing a precise electrical connection for both electrodes (Figure 3).
For initial evaluation of the integration process, two functional piezoelectric micro diaphragm pumps were integrated into a flat foil stack. The results of preliminary evaluation of this integration are presented here below.

EVALUATION OF INTEGRATION RESULT

The integrated micropump is shown in Figure 4 and Figure 5. The silver aluminum surface of the pump is visible at the edges of the package. Furthermore, the hexagonal piezoelectric actuator is evident. Its top electrode is contacted with the round Cu electrode. The contact of the ground electrode is visible on the left side.
The bottom view of the foil layers shows the inlet valve (left side) and outlet valve (right side) as well as the short channel from the side of the package to the inlet as well as the long outlet channel towards the top of the image. The area between the valves is a critical point of integration. The adhesion needs to be tight and seal the outlet valve from the inlet. The image shows no air bubbles or leaks and suggests successful fluidic integration.

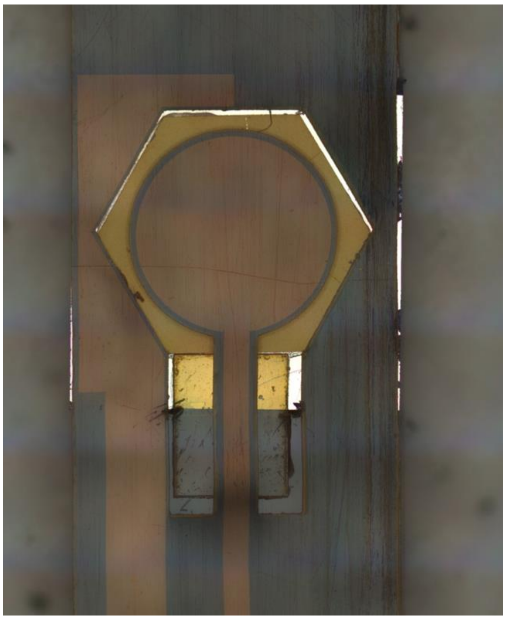

Figure 4 Top view on the micropump integrated into a flat foil stack with the visible hexagonal piezoelectric ceramic and contacting electrodes.

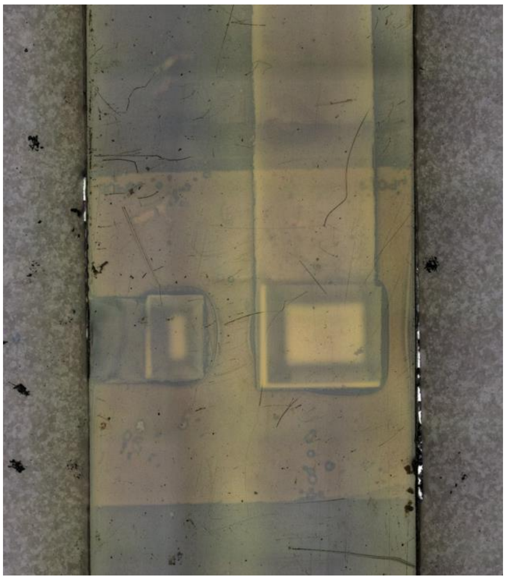

Figure 5 Bottom view of the foil layer comprising the silicon pump. The inlet and outlet valve, as well as fluidic channels are visible

The first measure of successful electric integration is the capacitance of the actuator ceramic. After the piezoelectric actuator is mounted to the silicon chip, it has a capacitance of 2.1 nF. The pumps after integration still show a capacitance of 2.1 nF. This confirms successful electrical contact to both electrodes. Furthermore, it shows that the piezoelectric ceramic has not been damaged.
One important measure for the pump’s functionality is its actuator stroke. The stroke is the movement of the diaphragm, when exposed to an electrical field. The stroke height directly determines the stroke volume, which is the amount of liquid that is transported in one suction and pumping cycle. If the foil integration limits the actuator movement, as it adds passive structures to block the ceramic’s elongation, the fluidic performance of the pump decreases. This is especially problematic for the bubble tolerance of the dosing unit, since a smaller stroke reduces the compression ratio. Other than reduced flow rates, this effect cannot be compensated by higher actuation frequencies.
The exemplary stroke measurement of one of the samples is depicted in Figure 6. Compared to a stroke of the bare silicon micropump of 15 µm +/- 1.1 µm [8], the total stroke is similar. The integration does not affect the diaphragm movement considerably. The used foils are thin and their stiffness is low compared to the mechanical stiffness of the silicon diaphragm.
For preliminary evaluation of the fluidic integration, a qualitative function test is performed. The ability of the pumps to transport air is shown by pumping into water. The usual dependence of the pumping rate on the actuation frequency is visible.

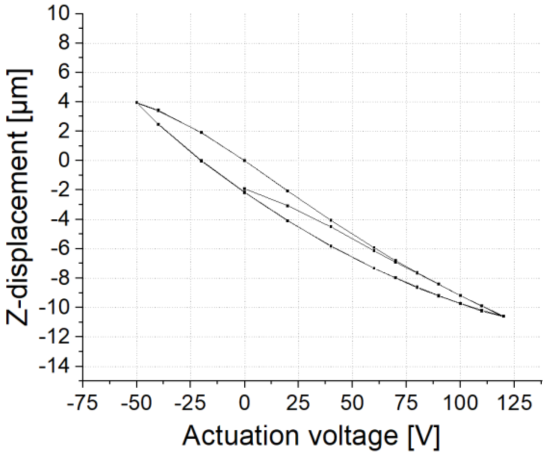

Figure 6 Stroke measurement of the silicon micropump integrated in a thin foil stack

In future work, the exact evaluation of integration requires quantitative analysis of the fluidic performance. This characterization will include the frequency dependent air flow rate, the maximal backpressure capability, and backwards leakage through the device. The characterization data can then be compared to the initial performance of the pump that has been measured before integration.

Furthermore, dynamic stroke measurements will be performed. The static actuator stroke presented above shows promising results. However, the velocity of the actuator movement and whether it can still reach its maximal displacement at higher frequencies is crucial for the use of this integration. The evaluation of the dynamic stroke over several million cycles can further more give information on the stability of the foil stack.

CONCLUSION

The preliminary evaluation is this work shows very promising results. The electric contact to the bottom and top electrode of the actuation ceramic is viable. Furthermore, the electromechanical characterization of the actuator movement shows little influence of the foil cover. This indicates that the pump's functionality remains unaltered. Furthermore, initial fluidic testing shows encouraging results.

The first samples show potential for optimization in the exact geometry of the layer design. A good trade of between a reliable electric contact and sufficient spacing to ensure electric isolation of the two electrodes is a crucial optimization parameter. Furthermore, for long term applications with many pump cycles, a slightly larger design that prevents lateral shift of the pump, might be required.

The overall results of this study are extremely encouraging as they prove the technical feasibility of micropump integration in an extremely flat package. This flat and to a certain extend flexible design offers the opportunity of improved dosing units for many industrial and biomedical applications, such as ultra-thin patch pumps.

ACKNOWLEDGEMENT

This work was funded by the NewLife project and is supported by the Chips Joint Undertaking (Grant Agreement No. 101095792). The authors extend their thanks to Dieter Bollman, Manishkumar Santoshkumar Pandey and Martin Wackerle for their technological contributions.

REFERENCES

1. Laser DJ, Santiago JG (2004) A review of micropumps. J. Micromech. Microeng. Doi:10.1088/0960-1317/14/6/R01
2. Bußmann AB, Grünerbel LM, Durasiewicz CP, Thalhofer TA, Wille A, Richter M (2021) Microdosing for drug delivery application—A review. Sensors and Actuators A: Physical. Doi:10.1016/j.sna.2021.112820
3. M. Mastrangeli, H. Aydogmus, M. Dostanic, P. Motreuil-Ragot, N. Revyn, B. De Wagenaar, R. Dekker, P. M. Sarro (2021) In: 2021 21st International Conference on Solid-State Sensors, Actuators and Microsystems (Transducers), pp 102–107
4. Henry Anhalt and Nancy J.V. Bohannon Insulin Patch Pumps: Their Development and Future in Closed-Loop Systems
5. Cheng M-H, Yang CY, Tee R, Hong Y-T, Lu C-C (2019) Efficacy validation of a lymphatic drainage device for lymphedema drainage in a rat model. Journal of surgical oncology. Doi:10.1002/jso.25707
6. Peng T, Guo Q, Yang J, Xiao J, Wang H, Lou Y, Liang X (2019) A high-flow, self-filling piezoelectric pump driven by hybrid connected multiple chambers with umbrella-shaped valves. Sensors and Actuators B: Chemical. Doi:10.1016/j.snb.2019.126961
7. Leistner H, Wackerle M, Congar Y, Anheuer D, Roehl S, Richter M (2021) In: Schlaak H (ed) Actuator 2021: International Conference and Exhibition on New Actuator Systems and Applications GMM conference, February 17-19, 2021, online event. VDE Verlag GmbH, Berlin, Offenbach, pp 113–116
8. Bußmann A, Leistner H, Zhou D, Wackerle M, Congar Y, Richter M, Hubbuch J (2021) Piezoelectric Silicon Micropump for Drug Delivery Applications. Applied Sciences. Doi:10.3390/app11178008

MONOLITHIC INTEGRATION OF A CALORIMETRIC MICROFLUIDIC FLOW SENSOR USING FLAT PANEL DISPLAY TECHNOLOGY

Bjorn de Wagenaar[1,2]*, Frennie Bens*[1]*, Alfredo Mameli*[1]*, Auke Kronemeijer*[1]*,*
Agnes Bußmann[3]*, Bogdan Firtat*[4]*, Massimo Mastrangeli*[2]*, Albert van Breemen*[1]
[1]TNO Holst Centre, Eindhoven, The Netherlands
[2]Delft University of Technology, Delft, The Netherlands
[3]Fraunhofer Institute for Electronic Microsystems and Solid State Technologies
EMFT, Munich, Germany
[4]National Institute for Research and Development in Microtechnologies IMT,
Bucharest, Romania

ABSTRACT

This abstract describes the design, simulation and experimental characterization of a thin film thermal flow sensor fabricated using flat panel display technology. Patterned microelectrodes were successfully applied as a thermal flow sensor, showing good correlation between experimental and simulated data. The use of flat panel display technology could provide an interesting option for cost-effective integration of flow sensing in Organ-on-Chip technologies.

KEYWORDS

Organ-on-Chip, microfluidics, thermal flow sensor, monolithic integration, flat panel display technology.

INTRODUCTION

Over the last decennium, Organ-on-chip (OoC) has shown to be a rapidly expanding field [1]. Although OoC technology holds great promise, the lack of standardization in, among other aspects, fabrication methodologies, chosen fabrication materials, device footprints, required peripheral systems, and operational protocols has hampered its widespread adoption.

Design and use of open technology platforms can provide a solution to improve on standardization. An example is the Smart Multi-Well Plate (SMWP) [2]. This platform combines modularity and configurability by choice of functional components such as OoC devices, sensors and pumps in a well-plate format with embedded functionality including in-line perfusion, electrode stimulation, sensor read-out and wireless communication.

An attractive feature of the SMWP is the in-line perfusion by integrated micropumps, which obviates the need for external pneumatics and tubing. To accurately control the micropumps (sensor-pump feedback loop) and monitor their performance over time, in-line flow sensing is required. Although flow sensor technology is well-known and available, it is challenging to upscale and multiplex this technology in a cost-effective manner. Flat panel display (FPD) technology provides a solution to this challenge [3]. Microelectrodes and microfluidic channels - either on thin flexible films or glass - can be cost-effectively fabricated in high resolution.

In this proof-of-concept study, patterned Au microelectrodes in a microfluidic channel make up a flow sensor based on a thermo-resistive, calorimetric principle. In this approach, a set of sensing microelectrodes are situated up- and downstream with respect to a central heater electrode (Fig. 1). The flow of liquid over this heater results in transport of heat towards the downstream electrode, causing an increase in its electrical resistance, which provides an indirect measure of the fluid flow rate.

MATERIALS AND METHODS

COMSOL Multiphysics simulations

To study and optimize the flow sensor performance, a COMSOL Multiphysics (5.2) 3D model was constructed (Fig. 2). This model, shown in figure 1b, is based on the geometry of the physical sensor and includes and combines all relevant physics: electric current, heat dissipation and fluid flow. A biasing electric current is applied to the microelectrodes (10 mA to the heater, 1 mA to the sensors), in which the middle electrode acts as a heater. By means of conduction and convection, heat is dissipated to the liquid. The flow of liquid inside the microchannel is defined to be laminar. These physics were coupled together (multiphysics) by the electromagnetic heating and non-isothermal flow modules. To minimize the complexity of the model and to optimize simulation time, the thin electrodes (100 nm) were represented as a 1 layer conductive shell. The temperature of the liquid at the inlet was set to room temperature (20 °C), the outlet was defined as a fluidic and thermal outflow. The fluid flow rate was determined by a parametric sweep, varying the flow rate between 1 and 100 µL/min.

Prototype design

The design of the prototype is shown in figure 1. The fluidic parts is fabricated by TNO Holst Centre (figure 2), consisting of three layers of dry foil resist (TOK, 45 µm). The first layer contains embedded microelectrodes (Au 75 nm) for flow sensing, the second layer contains the microfluidic channel features (width 300 µm, height 45 µm) and the third seals the fluidic circuit and provides access to the microfluidic channel.

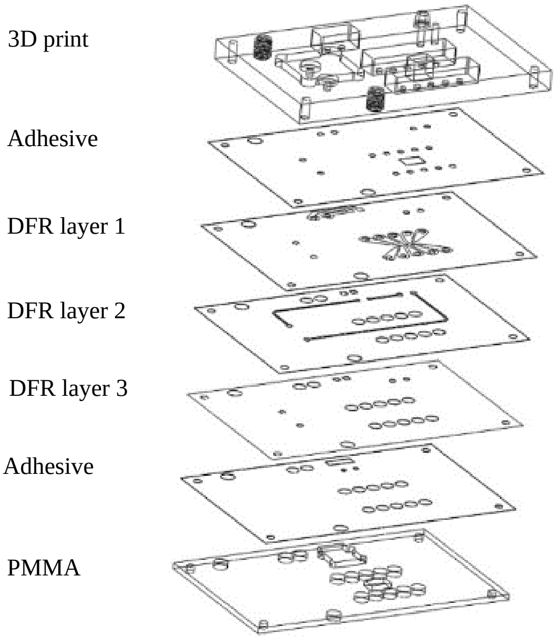

Figure 1: Exploded view of the flow sensor design. The fluidic layer consists of 3 layers of dry foil resist, which is bonded in between a 3D printed and a bottom PMMA layer using laser-cut pressure sensitive adhesive.

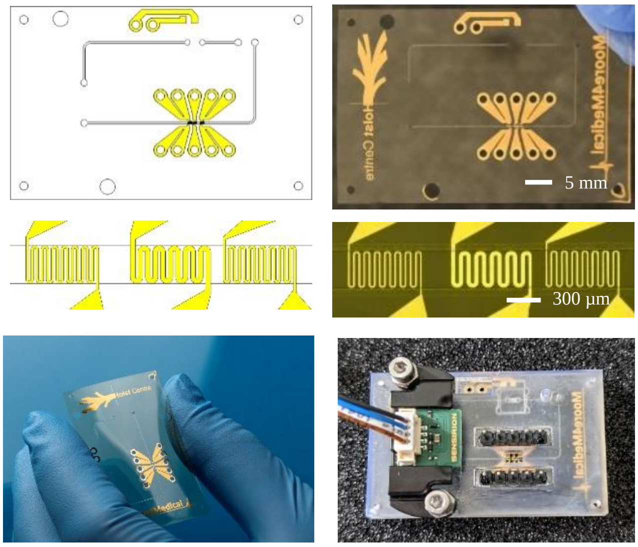

Figure 2: Design (top left) and fabrication (top right) of the fluidic layer (DFR) containing microelectrodes. Bottom: assembled prototype including the Sensirion flow sensor with head-stage.

The fluidic stack is sandwiched in between a 3D print (Asiga Max X27, Moiin Tech Clear) and a lasercut PMMA layer (thickness 1 mm) to allow integration of the flow sensor and connection to an external pump. Effective bonding between the different layers is accomplished using laser-cut pressure sensitive adhesive (PSA). A conductive silver paste was used to electrically connect the gold electrodes to the pin headers, which were glued in place using epoxy glue. The Sensirion flow sensor will be used to benchmark the embedded thermal flow sensor and to optimize its performance.

Experimental setup

A piezoelectric micropump assembly (µP030, EMFT Fraunhofer) was fluidically connected to the inlet of the prototype (figure 3) to supply a fluid flow of DI water at ± 21°C (Extech SDL200). The flow rate was varied by adapting the actuation signal (waveform, amplitude and frequency) provided by a custom piezo-actuator and software. A flow sensor (Sensirion LPG10-1000) and head stage were mounted on the 3D print. A current source (BK precision 9130) was connected to the heater electrode, providing a constant current condition. A digital multimeter (HP3478A) was used to measure the resistance of the down-stream sensor electrode. As a control, a Fluke 115 multimeter was used to monitor the resistance of the upstream electrode. Presented results indicate the increase of downstream sensor resistance after drift compensation.

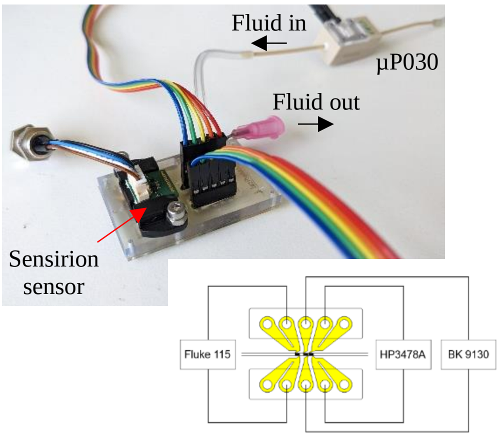

Figure 3: Experimental setup showing the fluidic and electric connections to the flow sensor prototype.

RESULTS & DISCUSSION

The 3D COMSOL model is shown in figure 4. A laminar flow condition is applied at the channel inlet, resulting a simulated fluid flow over the upstream sensor, heater and downstream sensor towards the channel outlet. The selected flow rates for simulation (figure 5) are based on the experimental obtained values (figure 6).

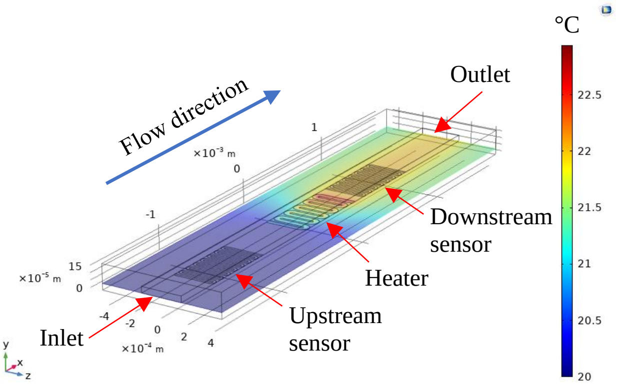

Figure 4: 3D COMSOL Multiphysics model of the thermal flow sensor embedded in a microfluidic channel (channel dimensions h x w x l: 45 x 300 x 3000 µm, flow rate: 24.8 µL/min, electrode current: 8 mA).

Figure 4 shows the concept of thermal flow sensing. Due to a constant current condition at the heater, the liquid heats up, resulting the downstream sensor to heat up as well, resulting in an increase of electrical resistance. Using this model, the temperature development in the channel was investigated at different flow rates (figure 6).

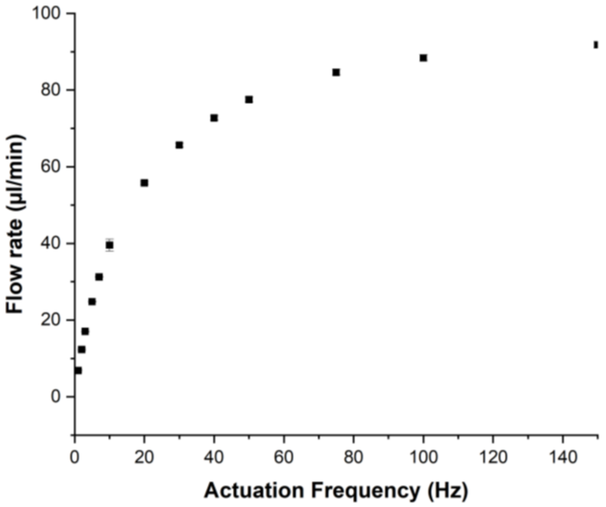

Figure 5: Measured flow rate (Sensirion) versus pump actuation frequency (rectangular waveform, 100/-20V amplitude).

Before simulations were performed, the pump performance was benchmarked using the external flow sensor (Sensirion) using fixed actuation frequencies (figure 4). The resulting flow rates were used in COMSOL simulations (figure 5).

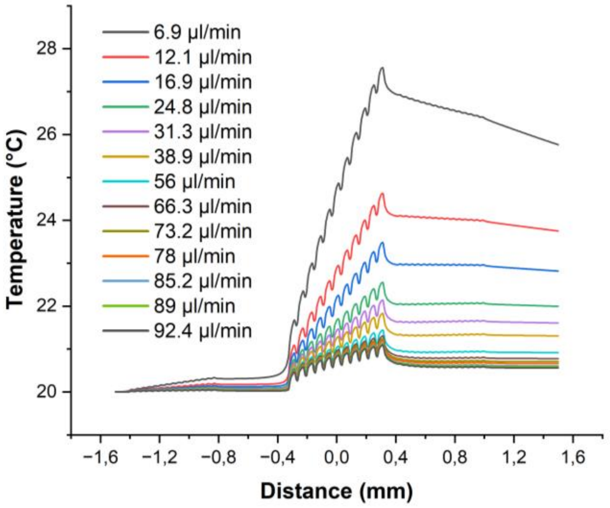

Figure 6: Simulated fluid temperature distribution on the bottom (electrode) plane of the microfluidic channel from channel inlet to outlet at different fluid flow rates (8 mA constant current).

Simulations show that at fluid flow rates above 12 µL/min heat dissipation is dominated by convection, preventing diffusion of heat towards the upstream sensor (anemometric regime). Increasing fluid flow results in more effective “cooling” of the heater, yielding a decrease in fluid temperature at the downstream sensor.

Before experiments were initiated, the resistance of the heater and sensor microelectrode was measured to check the electrical connection to the microelectrodes. Measured resistance was 150 Ω and 50 Ω respectively; simulated resistance values were 72.5 and 25 Ω respectively. Simulated values only account for the resistance of the microelectrode itself rather than the resistance of the electrical leads in total. Furthermore, the width of the sensing microelectrode (±17 µm) was slightly smaller than the design and simulated value (20 µm), further increasing its effective resistance.

The results of the experimental characterization of the flow sensor are shown in figure 7. The experimental data is normalized to an increase of electrical resistance (ΔR) for better comparison with the simulated values.

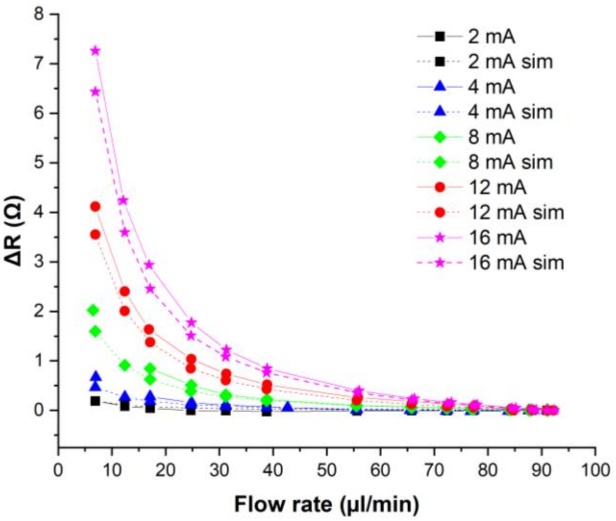

Figure 7. Experimental (straight line) and simulated resistance change (dashed line) of the downstream electrode versus flow rate at 5 different constant current conditions.

At low flow rates, heat transfer from heater to sensor is most efficient resulting in a large increase in resistance. Furthermore, increasing the applied current will result in more heat generation and a larger increase in sensor resistance. A good correlation of simulated and experimental data is observed, proving the functionality of the thin film-based, monolithically-integrated thermal flow sensor and the validity of the COMSOL model.

CONCLUSIONS

This abstract shows the proof-of-concept of a monolithic integration of a thermal flow sensor inside a microfluidic channel using thin film technology. This approach could prove be very interesting for flow sensing in integrated setups including micropumps. Future work will focus on optimizing the design of the flow sensor to achieve proper sensor functionality in the relevant flow rate regime typically used for Organ on Chip applications (1-100 µL/min). Furthermore, the use of different electrode materials will be investigated to make the sensor more robust and to allow more cost-effective integration.

REFERENCES

[1] M. Mastrangeli et al., *ALTEX - Alternatives to animal experimentation*, 36(4), pp. 650–668, 2019. doi: 10.14573/altex.1908271.

[2] Philips, ECSEL JU, *Moore4Medical consortium website (2020)*, accessed on 8 October 2023, <https://moore4medical.eu/organ_on_chip>.

[3] A. Mameli et al., *Microelectronic Engineering* 277, 112016, 2023, doi: 10.1016/j.mee.2023.112016

CONTACT

* B. de Wagenaar, bjorn.dewagenaar@tno.nl

A readout method of a micro-Coriolis mass flow sensor using integrated optical components

Anneirudh Sundararajan[1*], Remco J. Wiegerink[1], Remco G.P. Sanders[1], Joost C. Lötters[1,2]

[1]Department of Integrated Devices and Systems, MESA+ Institute for Nanotechnology, University of Twente, Enschede, The Netherlands
(*corresponding email: a.sundararajan@utwente.nl)

[2]Bronkhorst High-Tech BV, Ruurlo, The Netherlands

Novelty

This paper presents a novel readout of a micro-Coriolis mass flow sensor based on a differential optical reflective method, using chip based integrated optical components like VCSEL (vertical cavity surface emmiting laser) diode and two photodiodes . We measure the phase shift between the two photodiode signals with respect to the input flow rate of gas flow inside the suspended microchannel under actuation. Such a setup offers non-contact, low cost and robust sensing method. This can potentially increase the feasibility in integrating optical methods to existing miniaturized multiparameter flow sensor platform.

Background

A micro-Coriolis mass flow sensor with a reflective mirror, illustrated in Figure [1], consists of a vibrating tube fabricated with silicon-rich silicon nitride very thin (1.2 µm) channel walls using micromachined Surface Channel Technology [1]. The basic operating principle is based on the change in the velocity of the mass flow inside the microchannel, when subjected to external vibration by Lorentz actuation using the metal tracks deposited along the channel. The resulting Coriolis forces (F_c) are obatained by the ratio between the swing and twist mode ($\acute{\omega}$) amplitude which is directly proportional to the mass flow (φ_m) and is expressed by, $F_c=-2L\acute{\omega}$ x φ_m. Such devices are used to measure fluid flow down to a few nl/min [2]. Existing micro-Coriolis flow sensor uses capacitive detection methods with higher sensitivity. However their complex interdigitated comb structure results in a relatively fragile sensor during water hammering effects.

In this paper we propose to use an optical readout method using chip based laser diode (VCSEL) as a source and two photodiodes, to receive the signal that will detect the change in the phase of Coriolis forces induced vibrational amplitude corresponding to rotation and displacement of the sensor.

Description of the New Method or System

The basic structure and operating principle are illustrated in Figure 2. Such a method was previously demonstrated using optical fibers [2]. The differential reflected intensity from the receiving optical fibers were used to detect angular displacement of a reflecting metal surface. In this case, we have replaced the optical fibers with a VCSEL and two photodiodes that detect the reflected light from the actuation metal track of the Coriolis mass flow sensor. The sensor has an order of magnitude of 0.114° rotation with displacement of approximately 10 µm at the corner and 16 nm due to Coriolis forces (swing mode) at maximum flow of 1g/h when actuated in twist mode with 1.5 V amplitude. The two photodiodes are positioned at 400 µm on the either side of the VCSEL source of 850 nm wavelength as shown in Figure 3. The two photodiode signals are both proportional to both modes, but the twist mode gives a differential signal and the swing mode gives a common signal. The resulting phase shift, arising from the mass flow between the two photodiode signals, is directly proportional to the mass flow rate.

Experimental Results

The optical measurement setup is shown in Figure 4. The integrated optical components (VCSEL and PD's) of dimensions 200 x 200 µm and a typical thickness of 160 µm, were aligned and flip-chip bonded on glass chip fabricated with gold metal pads for wire bonding, as illustrated in Figure. Lorentz force is used to actuate the sensor at a resonance frequency of twist mode at 3.148 Khz by using magnets. Measurements for such a setup is yet to be realized. More improvement can be done to reduce the noise and develop a complete stable packaging for future integrated optical micro-Coriolis mass flow sensors.

REFERENCES

1. "Micro Coriolis mass flow sensor with integrated capacitive readout.", Haneveld, J., et al., 2009 IEEE 22nd International Conference on Micro Electro Mechanical Systems. IEEE, 2009.
2. "Towards nanogram per second Coriolis mass flow sensing.", J. Groenesteijn, R. G. P. Sanders, R. J. Wiegerink and J. C. Lötters 2016 IEEE 29th International Conference on Micro Electro Mechanical Systems (MEMS), 2016,
3. "A differential reflective intensity optical fiber angular displacement sensor.", Jia, Binghui, et al., Sensors 16.9 (2016): 1508.

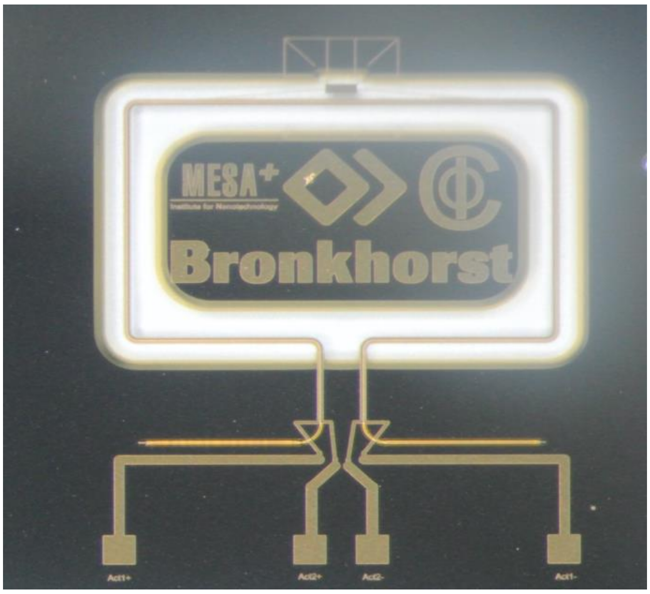

Figure 1: Photograph of a fabricated rectangle-shaped Coriolis flow sensor with a extended reflective surface

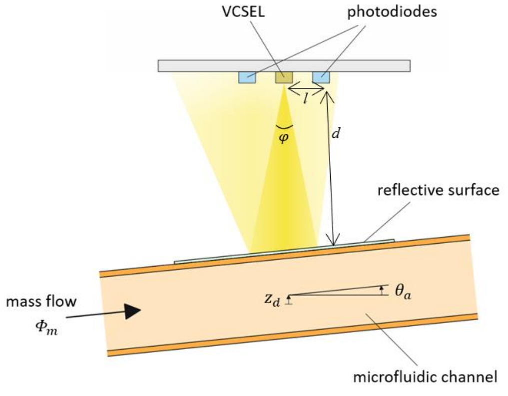

Figure 2: Basic operating principle of the readout method using integrated optical components (VCSEL and PD)

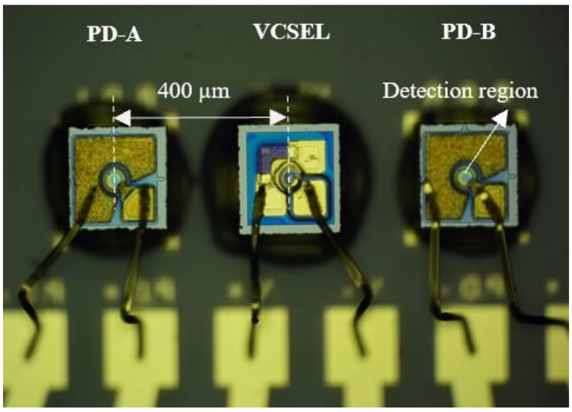

Figure 3: Integrated optical components VCSEL and PD flip-chip bonded on glass chip fabricated with gold metal pads for wire bonding

MINIATURIZED THERMAL FLOW SENSOR FOR MODULAR ORGAN-ON-CHIP APPLICATIONS

A. Paul[1], *W. Spareboom*[2], *J.C. Lötters*[2,3] *and M.Odijk*[1]
[1] University of Twente, BIOS- Lab-on-Chip Group, Enschede The Netherlands
[2] Bronkhorst High-Tech BV, Ruurlo, The Netherlands
[3] University of Twente, Integrated Devices and Systems, Enschede, The Netherlands

Introduction

Modular microfluidic systems have been explored for decades in lab-on-chip and Micro Total Analysis systems (µTAS). The advantages of plug and play systems have the advantage of lowering the gap between lab and industry while reducing design cycles by building on previous frameworks. Recently, ISO 22916:2022 has been established as an international guideline to making interoperable microfluidic components.[1]

This aligns well with the immediate needs in the field of Organ-on-Chip (OoC) where cell culture systems are replicated in 3D microfluidic environments. This also implies several constraints on footprint encountered from imaging setups and incubators which makes the ISO an ideal starting point to design modules and interfacing connections. This also enables developers of sensors, OoCs and platforms to interface with a wider library of modules (Figure1). Currently, a functional OoC environment mostly requires investment in peripheral from specific brands which can later limit the choice of accessories. Instead, an open source community can help build an ecosystem of interchangeable microfluidic parts akin to the electronics industry.

The control of micro-environments is vital for OoCs and sensors for oxygen, flow, pressure, glucose, pH are highly desired. Circulation of the medium often improves physiological relevance concerning shear stresses experienced by different types of cells. The flow rates can vary between 0-50 µL/min for common channel dimensions in OoC devices (~20 - 500 µm) [2]. Cells are often sensitive to variations in flow rate (shear stress), making flow sensors essential in monitoring and controlling pumping systems. Commercial flow sensors tend to have a measurement range of 1 or 2 orders of magnitude, thus requiring different sensors depending on the desired flow rates and cell culture conditions. Therefore, miniaturized flow sensors are needed to measure over a wider range while being biocompatible and modular.
This work reports a calorimetric flow sensor measuring 3 orders of magnitude. (0-50 µL/min). The sensitivity is experimentally shown to be 0.2µL/min. The flow sensor chip has a footprint of 1x1 cm, which can be housed in a module compatible with the ISO2296:2022 standard established for OoC devices. The temperature measured at the heater is compatible with cell culture viability.

A calorimetric flow sensor by principle requires less energy than other thermal flow sensing mechanisms like hot wire anemometry and has lower fabrication costs than Coriolis flow sensors. Calorimetric thermal flow sensor designs avoid narrow microfluidic channels which can get clogged with biological samples while still being compact enough to be packaged for modularity.

We demonstrate a simple COMSOL model that depicts the temperature difference detected at the thermal sensors on either side of the heater in Figure 4. This model can optimize the flow sensing range by changing parameters like the heater temperature, height of the microfluidic channel, and space between sensing electrodes.

Methods

The working principle of a calorimetric flow sensor involves measuring the temperature difference between two sensing electrodes either side of a heater (Figure 2). In this case the dimensions of the electrodes and the channel is as shown in Figure 3. The chip in total has a footprint of 1cm x 1cm which can then be housed in an ISO compatible module of 1.5cm x 1.5cm. The flow sensor is a commercial Bronkhorst IQ+Flow gas flow sensor chip repurposed for a modular OoC platform. (Figure 2b).

The sensor was connected to a Nemesys pump (Cetoni GmBH) in which flow profiles were programmed. The readout was then observed in the FlowPlot software. The output was the raw measured voltage for a certain value of flow rate. This can then later be converted into flow rate after careful calibration steps with respect to the manifold and final setup. The heater in the COMSOL simulation was set at 380K before plotting he difference between the adjacent electrodes. The channel height is 200um with a flow rate condition of $7.5*10^{-11}m^3/s$ (4.5 µl/min). The simulation is a 2D so the width of the channel is neglected in the simulation.

Results

Experimental

The initial test was conducted with a flow profile varying from 0 to 100 µL/min in steps of 10 µL/min. (Figure 4a). This was mainly to test the maximum flow rate that could be measured. We observe that the voltage detected starts to plateau around 60 µL/min. The amount of noise at higher flow rates can be reduced by signal processing or by some optimization in the test setup. In general, a value was clearly visible between flow rates varying from 0-50 µL/min.

Similar test was conducted with a programmed flow profile ranging from 0-10 µL/min with step size of 1 µL/min. In this case, there are step profiles visible however there is too much noise at flow rates closer to 10 µL/min. Considering this is the unprocessed data, it appears the sensor is able to detect flow rate in the range of 0-10 µL/min. A final test was conducted for a flow profile ranging from 0-1 µL/min with a step size of 0.2 µL/min. In this case, the step responses are visible implying that this is a range the flow sensor can give a readout.

Simulation

The geometry of the 2D simulation resembles the schematic in Figure 3. The central electrode is set as a heat source with a temperature of 380K. The materials selected are copper for the electrodes, borosilicate for the substrate, a 50µm layer of parylene and water as liquid. The flow is set as creeping flow at a flow rate of 4.5 µL/min. A temperature difference of 6 degrees is observed. Depending on the required temperature difference for a meaningful readout, the heater temperature or channel geometry can be changed. This can provide a scalable approach for multiple applications by changing power or the external manifold housing the sensor chip.

Conclusion and Outlook

An existing commercial flow sensor was repurposed to check the viability as a modular liquid flow sensor. The sensor chip was tested experimentally with flow rates ranging from 0-100 µl/min. The tests indicate a capability to measure flow as low as 0.2 µL/min and up to a maximum flow rate of 50 µL/min. This shows that the sensor can detect flow rates across 3 orders of magnitude while having a concise footprint that can be placed in ISO compatible modules. The response is non-linear and the higher noise levels in all experiments points to an external source rather than a limitation of the sensor itself. Further calibration and characterization of the sensor needs to be done to understand the accuracy of the sensor. Signal processing and setup optimization can be used to obtain cleaner signals. The sensor can then be implemented onto a fluidic circuit board as a module to conduct incubator tests to verify functionality in an environment common to OoC culture.

The working principle and dimensions of the channels are compatible with biological samples. The concept can be further fine tuned by simulating various parameters like heater temperature and geometry to fit specific requirements. Overall, the combination of above mentioned factors hold promise for a rapidly growing need for miniaturized flow sensors for modular microfluidic and Organ-on-chip applications.

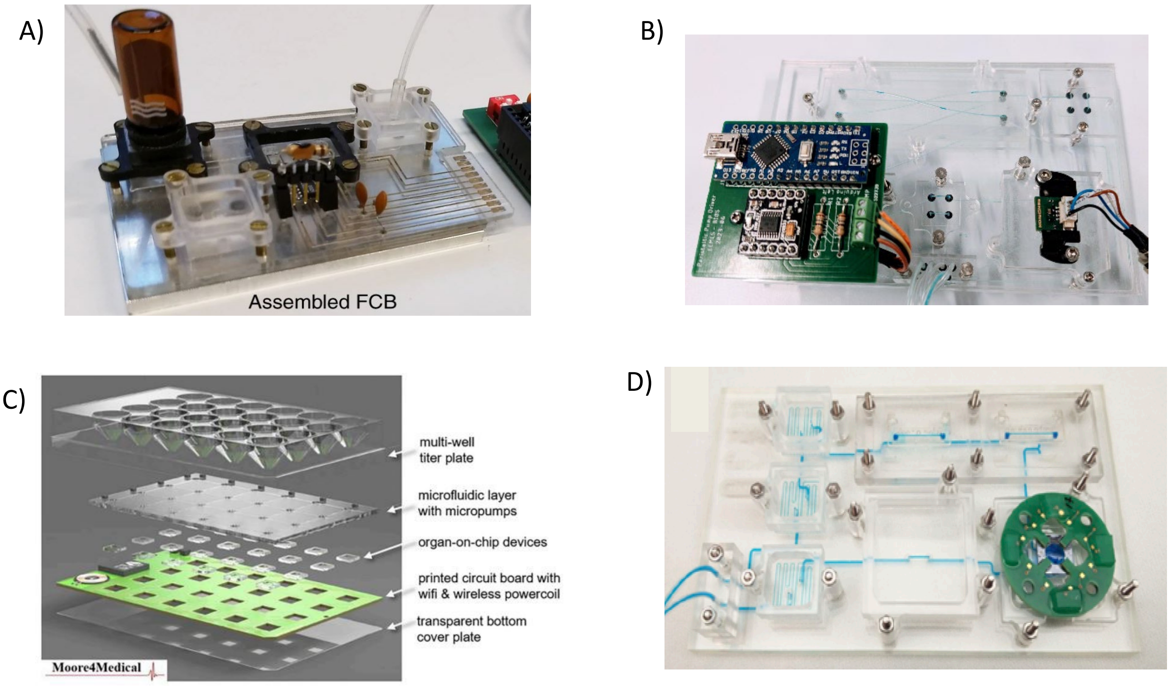

Figure 1: Examples of ISO compatible FCBs and modules A) A modular FCB with integrated electronics for impedance sensing. [3] B) Commercial pumps and sensors interfaced as modules onto a FCB. C) Schematic of a fully integrated Smart cell culture platform [4]. D) An academically developed pH sensor modules interfaced onto a FCB. [5]

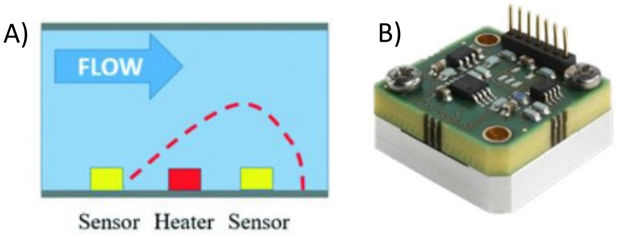

Figure 2: A)Working Principle of Calorimetric flow sensors. Red dashed line represents temperature distribution. [6] B) Image of a IQ+ sensor chip with manifold

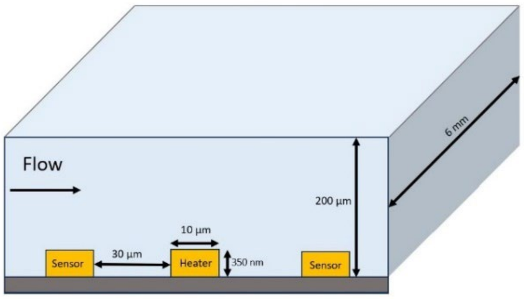

Figure 3: Layout of the sensing chip electrodes and microfluidic channel

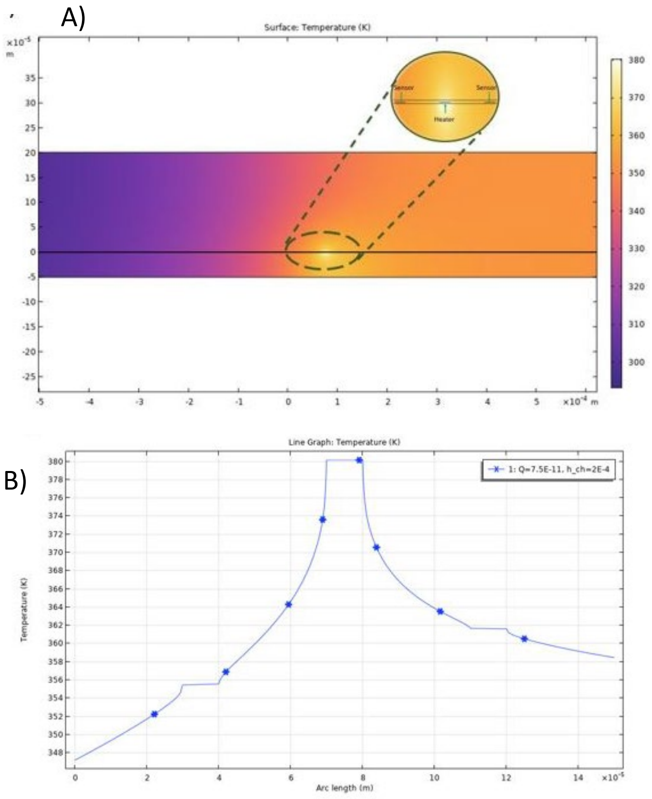

Figure 4: A) Temperature variation across the channel with heater and sensor electrodes under flowing water conditions. B) Temperatures of heater and sensor electrodes

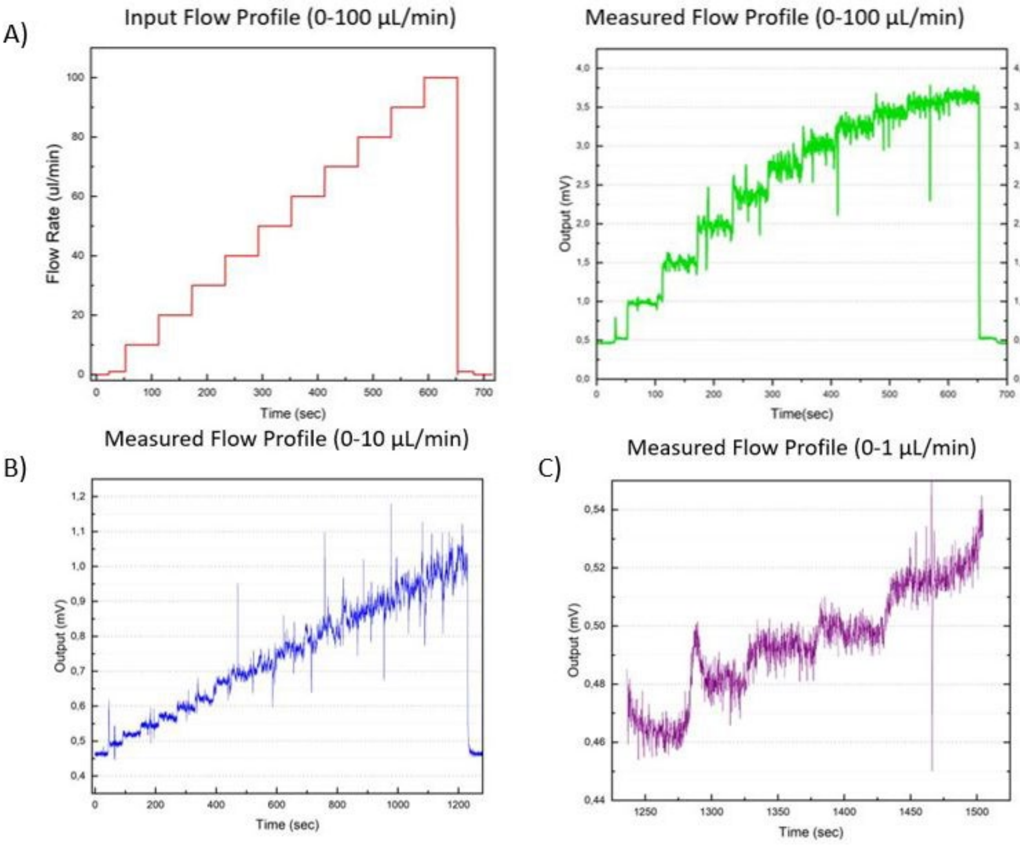

Figure 5: Panel with flow measurements. A) input flow profile vs measured flow profile. B) Measured flow profile with input flow in steps of 1 µL/min. C)Measured flow profile with input flow in steps of 0.2 µL/min

REFERENCES

[1] ISO 22916:2022

[2] Pisapia F *et al*. Organ-on-a-Chip: Design and Simulation of Various Microfluidic Channel Geometries for the Influence of Fluid Dynamic Parameters. ***Applied Sciences***. 2022; 12(8):3829

[3] S. Dekker et al, Microsyst Nanoeng 4 34 (2018)

[4] Mastrangeli, M. *et al*. (2021). Organs-on-chip: The way forward. Stem Cell Reports. 16. 2037-2043. 10.1016

[5] Vollertsen, A. *et al*. (2022). Connecting labs for higher level organ-on-chip systems: integration of a pH sensor and a blood vessel-on-chip on a standardized platform. Paper presented at EUROoCS Annual Meeting 2022

[6] C. Cavaniol, *et al*. “Flowmetering for microfluidics,” *Lab on a Chip*, vol. 22, no. 19, pp. 3603–3617, Sep. 2022

Miniaturized on-chip optical gas sensor

Dexter Manalili [1], Amir Khodabakhsh [1], Arnoud Everhardt [2], Dimitri Geskus [3], Wilson Tsong [3], David van Duinen [4], Joost Lötters [5], Sacco te Lintel Hekkert [6], Simona Cristescu [1,6,]*

[1] Life Science Trace Detection Laboratory, Radboud University, 6525 XZ Nijmegen, The Netherlands
[2] LioniX International, 7521 AN Enschede, The Netherlands
[3] Chilas BV, 7521 AN Enschede, The Netherlands
[4] PHIX Photonics Assembly, 7522 NM Enschede, The Netherlands
[5] Bronkhorst High-Tech BV, 7261 AK Ruurlo, The Netherlands
[6] Sensor Sense, 6525 ED Nijmegen, The Netherlands
[*] Author to whom correspondence should be addressed.
E-mail: s.cristescu@science.ru.nl

Abstract

There is a need for continuous measuring and regulating flow speed in gases in an affordable manner and several commercial solutions are available. However, in some cases not only the flow speed, but also the concentration of the different components in the gas play an important role. Continuous monitoring of the ratio between methane and carbon dioxide in biogas is a measure of the caloric level of the gas and determines the quality and the price of the biogas supplied to the gas network. Therefore, implementing a miniaturized sensor to measure these concentrations in the Bronkhorst flowmeter will fulfill the demand from the end-user market and have a great market potential. In the OP Oost EFRO project SensorChip, Radboud university and Sensor Sense are using evanescent wave spectroscopy to develop such a sensor based on the PIC technology developed by Lionix in combination with broadband tunable laser on the chip from Chilas and system integration at PHIX. Preliminary results on the gas sensor development and its performances will be presented.

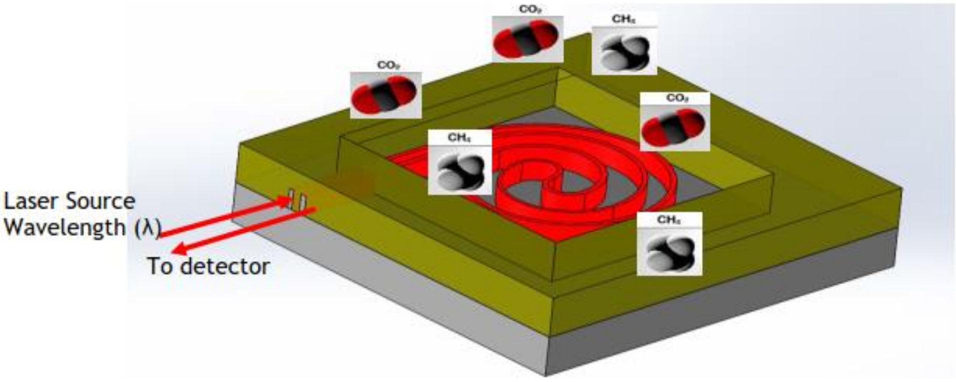

The evanescent laser light from a spiral on a chip is absorbed by methane and carbon dioxide molecules. The decrease of laser light coming out of the spiral is a measure for the concentrations of the gases.

PREDICTING MEDIUM IN LOW FLOW THERMAL GAS SENSORS

V. Winnen[1], J. Groenesteijn[1] and W. Sparreboom[1]
[1] Bronkhorst High-Tech BV, Ruurlo, The Netherlands

ABSTRACT

Thermal flow sensors are used in multiple fields of applications. This sensor determines the flow of a gas due to thermal energy transfer between the gas and a heating element. These sensors have to be calibrated for each different gas, therefor there is interest in automatic detection of the medium inside the flow sensor. This problem is approached by simulations and measurements of applying an Alternating Current (AC) signal on the thermal elements of the sensor. This allows for the determination of the thermal properties of the system via to the third harmonic of the signal.

KEYWORDS

Low flow thermal gas sensors, medium prediction, heat transfer coefficient, specific heat capacity, 3ω method

INTRODUCTION

Thermal flow sensors are applied in all kind of industries with different applications. For the sensor to be used in a different application with different gases, this sensor needs to be re calibrated or manually adjusted with a conversion model to select a different gas. An automatic gas detection method could radically improve this situation. Since thermal sensors rely on the thermal interaction with the flowing gas, the sensitivity of the sensor depends on the thermal properties of the gas. When the heating element is actuated with and Alternating Current (AC) it allows for the determination of thermal properties surrounding the heating element. This AC signal at a certain frequency ω induces joule heating at 2ω. An extra product of this actuation occurs at 3ω, this third harmonic contains the temperature oscillations (δT_h) of the heating element. The amplitude of these oscillations is dependent on the surrounding thermal properties. With the oscillations at the third harmonic it is possible to determine the thermal properties of the thermal system. The system used in this research is shown in figure 1, this consist of two suspended channels. These channels have a circular cross section but have a flat top where the heating elements are placed. With the geometry of the channel multiple mediums are influencing thermal measurements. These are the air surrounding the suspended channel, the channel wall and the gas inside the channel. When fitting δT_h at different frequencies, the thermal properties of the system can be determined.

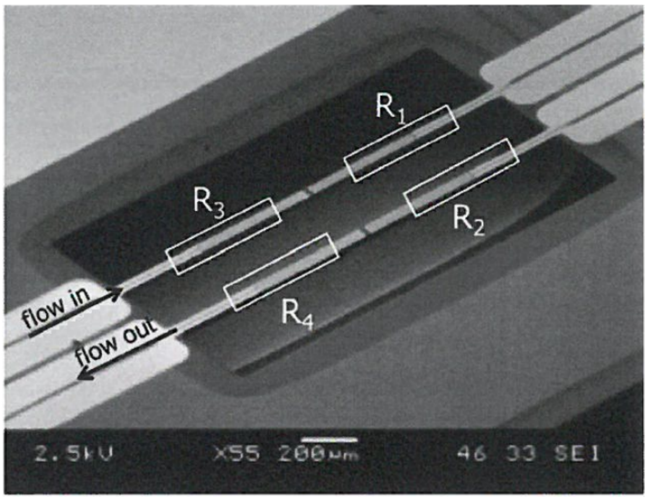

Figure 1: Overview of device used in this research. The flow direction is shown with the arrows and the heating elements are shown with R1-4 (Image taken from [1]).

3ω METHOD

When using an oscillating signal the penetration depth of this signal in the system depends on both the frequency and the material this signal encounters. This is shown with the equation of the penetration depth [2].

$$\lambda_p = \sqrt{\frac{\alpha_D}{\omega}} \quad (where\ \ \alpha_D = \frac{k}{\rho C_p}) \tag{1}$$

Where λ_p is the penetration depth, ω the applied frequency, α_D is the thermal diffusivity coefficient consisting of k the thermal conductivity, ρ the density and C_p the heat capacity. Because the thermal signal is omnidirectional, the described parameters are influenced by the surrounding air, the channel walls and the gas inside the channel. This gas can be varied and thus influence the total parameters. Therefor each gas will have their own response. Equation 1 shows a inverse relation between the frequency and the penetration depth. Higher frequencies result in a smaller penetration depth, this has to be taken into account. When the penetration depth is too low the temperature oscillations do not reach the gas inside the channel. Thus only probing the channel top wall. When the frequency is too low, the penetration depth will be too high. Resulting in a large volume of air outside the channel which is probed and thus small contribution of the gas in the channel.

Table 1: Properties of gases determining the penetration depth of the thermal signal (k at 300K and 1 bar) [3] (C_p & ρ at 293K and 1 bar) [4].

Gas	k $[mW/(m{\cdot}K)]$	ρ $[kg/m^3]$	C_p $[kJ/(K \cdot kg)]$
N_2	26.0	1.165	1.04
Ar	17.7	1.661	0.520
CO_2	16.8	1.842	0.844
He	155.7	0.1664	5.19

The selection of gases was made due to the difference in thermal properties where helium has the biggest deviation. The penetration depth of helium and nitrogen are shown in figure 2. This shows the large dependence on thermal properties. To distinguish nitrogen, argon and carbon dioxide via their thermal conductivity or ρ C_p product is a hard task due to the small separation between values. To separate these gases the specific heat capacity needs to be determined.

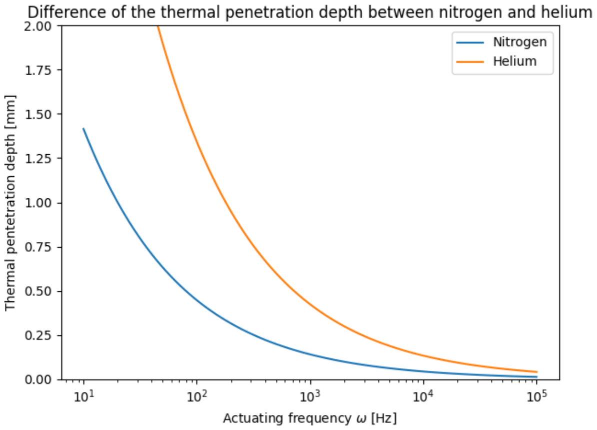

Figure 2: The influence of thermal properties to the thermal penetration depth when comparing nitrogen and helium.

Depending on the heating elements geometry and the penetration depth of the signal regimes with different thermal behavior can be defined. The first regime where the penetration depth is larger than the heater width b_h ($\lambda_p >> b_h$), the δT_h is inversely dependent on the thermal conductivity (equation 2 [2]). The second regime where the penetration depth is smaller than the heater width ($\lambda_p << b_h$) is dependent on the inverse square root of the product between the thermal conductivity and the specific heat capacity (equation 3 [2]). The regimes are visualized in figure 3 [5]. With both regimes it is possible to determine first the thermal conductivity at the linear regime and use this to determine the specific heat capacity.

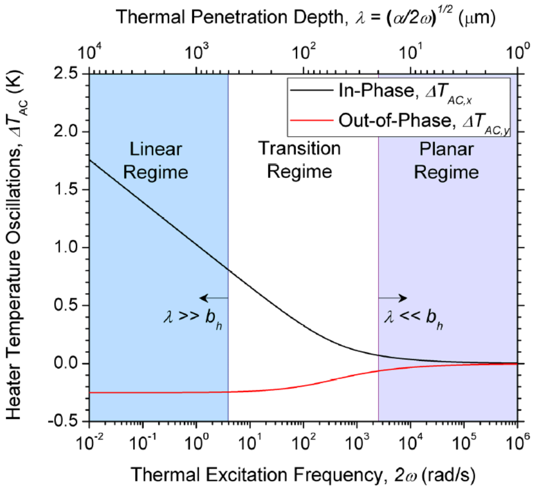

Figure 3: The different regimes in the 3ω response. Where the ratio between the penetration depth (λ) and the heater width (b_h) are the determining factors. [5]

The temperature oscillations in the different regimes from figure 3 can be fitted, where equation 2 fits the linear regime and equation 3 fits the planar regime.

$$\delta T_h = \frac{P}{l\pi k}[-ln(2\omega) - ln(\frac{b^2}{\alpha_D}) - i\pi/4] \qquad (2)$$

$$\delta T_h = \frac{P}{l2b_h}\frac{1}{\sqrt{2\omega C_p k}}e^{-i\pi/4} \qquad (3)$$

Where: l is the length of the heating element, b_h is the width of the heating element, P is the applied power to the heating element.

The temperature oscillations can be rewritten as a function of the voltage measured at 3ω [2]:

$$\delta T = \frac{2V_{3\omega}}{IR\alpha_R} \qquad (4)$$

Where I is the applied current on the heater, R is the resistance of the heater and α_R is the thermal coefficient of resistance. The used value for α_R is 0.00218 [1/K].

DEVICE

The device is fabricated using surface channel technology as seen in figure 4, this fabrication process is described in [6]. Where the device consists of a channel where gas flows through. This channel is suspended where the surrounding gas is air. The heaters are located on the suspended part of the tube, these heaters are thermistor's because the resistance is highly dependent on the temperature of the heater. Due to the channel being suspended the thermal signal penetrates the air surrounding the heater, the channel wall and the gas in the channel.

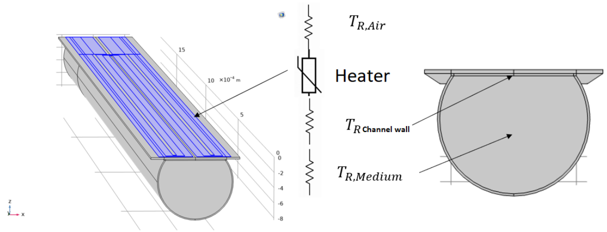

Figure 4: Simulated channel with the domains surrounding the geometry where the medium is varied by the gases mentioned.

When using the geometry of the heating element in the 3ω method it should be located in the linear and planar regime, which is ideal for this purpose.

COMSOL

The channel as shown in figure 4 was simulated in COMSOL. The surrounding air and material of the channel was taken into account. Simulations were performed to determine if the suspended channel was thermally isolated from the substrate. From these simulation no leakage of heat to the substrate was observed, therefor only the suspended part of the tube was simulated. The simulation was validated by simulating the channel filled with nitrogen at 1 bar and comparing it to actual measurements of 1 bar of nitrogen in the device under test. This resulted in figure 5 which shows the same trend in both the in and out phase part of the data.

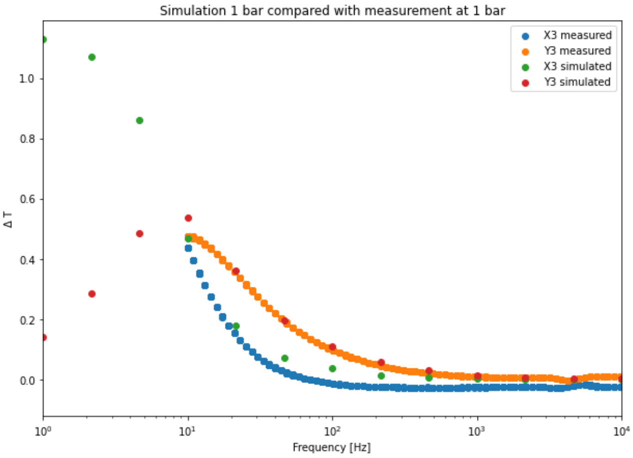

Figure 5: Simulation results compared to measurement results with nitrogen in the channel. X3 is the in phase signal measured at 3ω and Y3 is the out phase signal at 3ω.

SETUP

The measurement setup consist of a pressure controller, the device under test, mass flow controller, lock in amplifier and current source. The pressure controller controls the gas pressure before the device under test. This pressure causes the gas to flow through the device under test. The mass flow controller controls the flow through the device under test.

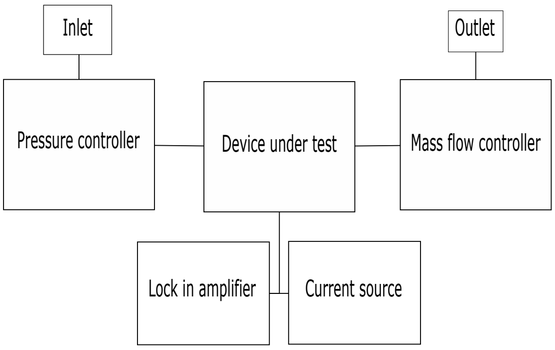

Figure 6: Schematic overview of the measurement setup. First gas enters the pressure controller which sets the pressure to the specified pressure. Then the gas flows through the device under test to a mass flow controller which sets the desired flow speed. The device under test is connected to two lock in amplifiers and a oscillating current source.

The frequency range of the current source was taken to extract both regimes defined in figure 2 from the measurements. The in and out of phase part were collected separately with the lock in amplifiers. A frequency sweep was done from 10 to 10000 Hz to address both regimes defined in figure 2. Both regimes are visible as seen in figure 5.

Before each measurement the channel was flushed for 30 seconds with the intended gas. After the 30 seconds the measurement starts where the gas pressure is kept at 2 bar. For each frequency 10 measurements were performed where the voltage at the third harmonic is collected.

RESULTS

The analysed gases were nitrogen, helium, argon and carbon dioxide (properties shown in table 1). The difference in response between different gases show a possibility to label the gases using the in and out phase response at 3ω. This is visualized by the measurement done with flow through the device under test as shown in figure 7.

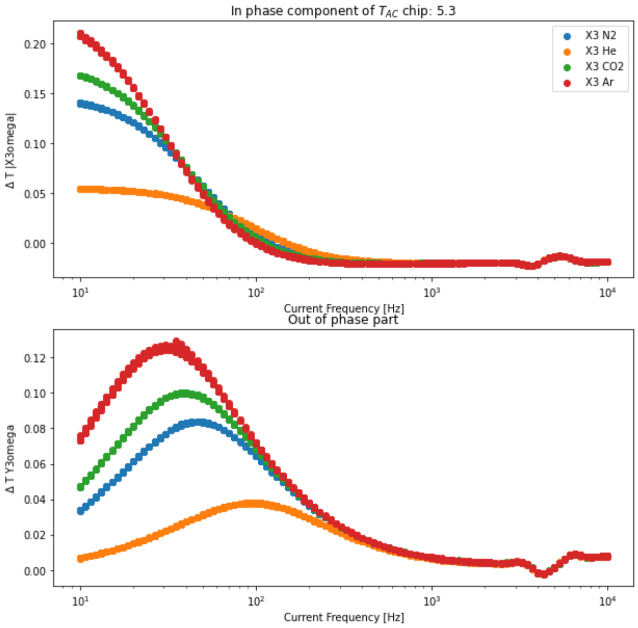

Figure 7: This figures contains the measurement data with flow in the device under test. The top graph shows the in phase component of the measured third harmonic for nitrogen (blue), helium (orange), carbon dioxide (green) and argon (red). The bottom graph shows the out of phase response of the third harmonic. Both graphs have the same order.

With the in phase results it is possible to determine the thermal conductivity of the system. This was done by extracting the slope from the top plot between 20 to 80 Hz. This value was then later reused in equation 3 to fit for the C_p value of the system.

One notable point in figure 7 is the order of the gases. Because the thermal conductivity is inversely related to the slope in the in phase plot. Therefor it should have the order from smallest to highest k value: carbon dioxide, argon, nitrogen and helium. From the plot we obtain: argon, carbon dioxide, nitrogen and helium. Here the carbon dioxide and argon are switched.

In the out of phase plot the of the different thermal diffusivity is visible when comparing the peak of helium and nitrogen. The helium plot has an lower amplitude and shifted to around 100 Hz compared to the nitrogen at around 28 Hz. Comparing each gas shows a change in amplitude and peak location on the frequency axis. This combination between amplitude in δT_h can be used to identify the medium.

CONCLUSION

With this technique it was shown different gases can be separated based on there thermal properties. This can be done with the peak in the out of phase plot, where the amplitude and frequency value of the peak is gas depended.

REFERENCES

1. Sparreboom, W., van der Wouden, E., Lammerink, T. & Lötters, J. *Truly calorimetric flow sensor chip based on surface channel technology* in *Proceedings of the Second International Conference on MicroFluidic Handling Systems, MFHS 2014* (University of Freiburg, Oct. 2014), 53–56.
2. Bhardwaj, R. G. & Khare, N. Review: 3- ω Technique for Thermal Conductivity Measurement—Contemporary and Advancement in Its Methodology. *International Journal of Thermophysics* **43.** ISSN: 15729567 (9 Sept. 2022).
3. Huber, M. L. & Harvey, A. H. *Thermal conducTiViTy of gases Thermal conductivity in mW m-1 K-1 100 K 200 K 300 K 400 K 500 K 600 K Ref* ().
4. Kadoya, K., Matsunaga, N. & Nagashima, A. Viscosity and Thermal Conductivity of Dry Air in the Gaseous Phase. *J. Phys. Chem. Ref. Data* **14** (1985).
5. Koninck, D. D. *Thermal Conductivity Measurements Using the 3-Omega Technique: Application to Power Harvesting Microsystems* (2008).
6. Groenesteijn, J., de Boer, M. J., Lötters, J. C. & Wiegerink, R. J. A versatile technology platform for microfluidic handling systems, part I: fabrication and functionalization. *Microfluidics and Nanofluidics* **21.** ISSN: 16134990 (7 July 2017).

CONTACT

Victor Winnen
v.winnen@bronkhorst.com

A PORTABLE NUCLEAR MAGNETIC RESONANCE (NMR) DEVICE FOR MICROFLUIDIC FLOW MEASUREMENT AND SAMPLE DETECTION

E. Aydin[1], D.M. Polishchuk[2,3], J.G.E. Gardeniers[2], K.A.A Makinwa[1]
[1]Electronic Instrumentation Laboratory, Delft University of Technology, Delft, The Netherlands
[2]Mesoscale Chemical Systems Group, University of Twente, Enschede, the Netherlands
[3]Institute of Magnetism, NAS of Ukraine and MES of Ukraine, 03142 Kyiv, Ukraine

Precise control and sensing of flow rates are essential in various lab-on-a-chip applications [1]. MEMS thermal flow sensors are widely utilized for their simplicity, scalability, low power consumption, high sensitivity, and practicality [2]. The growing popularity of MEMS Coriolis flow sensors is attributed to their fluid-independent sensing capability and simplified calibration [3]. However, it is important to note that both types of sensors necessitate physical contact with the fluid, introducing complexities to the fluidic setup, altering the flow profile, and causing pressure drops. Moreover, these sensors may be susceptible to corrosive or scalding liquid damage.

Ultrasonic [4] and electromagnetic [5] flowmeters operate without physical contact. Nonetheless, their functionality relies heavily on the fluid's distinct acoustic or electrical properties, respectively. Additionally, they are not compatible with the narrow tubes (< 1mm diameter) commonly employed in microfluidic settings [6]. In contrast, Nuclear Magnetic Resonance (NMR) flowmeters offer a non-contact solution adaptable to a diverse range of fluids and capable of fluid composition analysis. This feature proves particularly advantageous in biomedical applications.

Previously, NMR flowmeters were associated with large-scale fluidic applications [7]; recently, it has been shown that these techniques can also be applied to microfluidics using permanent magnets and low-noise electronics [8]. On the other hand, the portability of the proposed prototype was limited by the size of the magnet and its PCB-based electronics.

This paper will outline recent advances in the development of portable NMR microfluidic flowmeters. First, we will describe the basic principles of NMR and NMR-based flowmeters. Following that, we will discuss the new developments in the design of the associated magnet and electronics. Finally, the paper will conclude with a discussion of future prospects.

NMR-BASED FLOW MEASUREMENT

The term NMR refers to the resonant interaction between an RF magnetic field (B_1) and nuclei in the presence of a static magnetic field (B_0). As shown in Figure 1-a, the randomly distributed magnetic moments of the protons in a sample will align themselves with the external field (Figure 1-b). This alignment will be disturbed by an external RF field (B_1) that is perpendicular to B_0 (Figure 1-c) at the so-called Larmor frequency f_{Larmor} given by:

$$f_{Larmor} = \gamma B_0 \qquad (1)$$

Where γ is the gyromagnetic ratio and is a material-dependent parameter, and equals 42.58 MHz/T for protons. The duration of the RF field determines the angle of misalignment, which should be 90° for maximum effect (Figure 1-d). When the RF field is turned off, the magnetic moments will re-align themselves with B_0 and emit an NMR signal (Figure 1-e). The decay time constant of the NMR signal depends on the spin-spin relaxation (T_2) mechanism, which is sample-dependent.

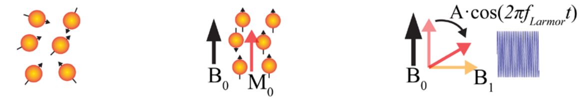

a) Randomly distirubuted magnetic moments.

b) Protons are magnetized with the B_0 field.

c) Magnetization is disturbed by the B_1 field at f_{Larmor}.

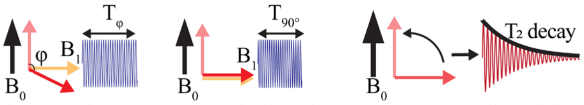

d) Magnetic moments are misaligned at a certain angle φ depending on the excitation duration T_φ. The maximum NMR signal is obtained when φ=90°.

e) Protons realign their magnetic moments with B_0 and emit NMR signal after B_1 is removed.

Figure 1. Illustration of the NMR Principle.

Inhomogeneity in the B_0 field will cause different spins to have different Larmor frequencies, which will decrease the coherence of the NMR signal and shorten the decay time constant (T_2^*). One way around this problem is the use of spin-echo measurements. After a $T_{90°}$ pulse, applying a $T_{180°}$ pulse will invert the magnetic moments, causing the decaying spins to gradually re-align and emit a so-called echo signal. As shown in Figure 2, Carr and Purcell [9] proposed a pulse sequence that exploits this spin-echo phenomenon. It consists of a $T_{90°}$ pulse followed by a train of $T_{180°}$ pulses. The interval between the $T_{180°}$ pulses is twice the interval between the $T_{90°}$ and the first $T_{180°}$ pulse. The T_2 decay can then be accurately estimated from the peaks of the echo signals.

Another important phenomenon in flow measurement is spin-lattice relaxation, the so-called T_1 relaxation [10]. It refers to the time it takes for the nuclear magnetization (M_0) to build up or recover along the direction of the B_0 after being perturbed or the sample inserted inside B_0. When a sample is introduced into a static magnetic field (B_0), the nuclear spins within the sample align with this field, causing an increase in longitudinal magnetization (M_z) and reaching its final value M_0 with the time constant T_1, as shown in Equation 2. Less time allocated for the sample in B_0 will decrease the amplitude of the received NMR signal since less magnetization is built up.

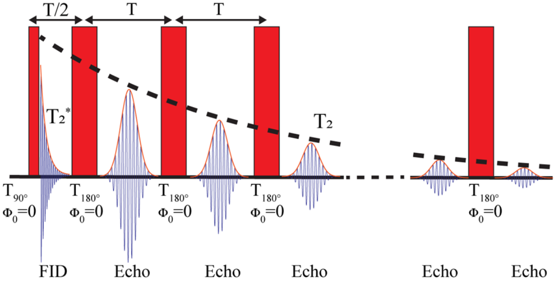

Figure 2: Illustration of Carr-Purcell pulse sequences; the red rectangles represent the RF excitation moments.

Like T_2 relaxation, T_1 relaxation is a molecule-dependent parameter. Understanding those parameters is crucial to obtaining both flow-related and molecule-related information from NMR signals.

$$M_z = M_0 \cdot (1 - e^{-T_1/t}) \qquad (2)$$

Flow measurements can also be done by using Carr-Purcell pulse sequences. In the absence of flow, the typical exponential T_2 decay is observed. However, in the presence of flow, the decay accelerates as the magnetized fluid volume moves away from the RF detection coil. Consequently, the exponential decay is modulated by an additional flow-rate dependent decay, denoted as $f(t)$. This decay can be derived by normalizing the measured decay with the decay observed in the absence of flow (T_2 normalization) [11]. The normalization eliminates the T_2 dependency of the obtained NMR signal under flow. Figure 3 depicts an illustrative plot of the resulting signals at various flow rates.

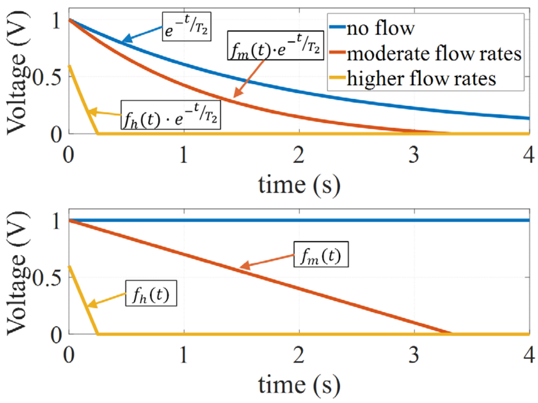

Figure 3: Effect of flow on T2 decay (top: T2 decay, bottom: T2 normalized signal f(t)). The peak value of f(t) decreases with the flow rate since the shorter exposure to the B_0 field results in the magnetization of fewer molecules.

The average normalized slope of $f_n(t)$, where "n" indicates the flow rate is directly proportional to the flow rate. This can be determined by dividing the maximum value of $f_n(t)$ by the area under the $f_n(t)$ curve:

$$normalized\ slope_n = \frac{\max(f_n(t))}{\int_0^\infty f_n(t)dt} \qquad (3)$$

NMR FLOWMETER HARDWARE DEVELOPMENT

The block diagram of an NMR flowmeter system is shown in Figure 4. It typically includes a magnet, a transceiver, and a system that acquires the data from the electronics and analyzes them. The ultimate portability can be achieved by having a portable magnet and making the electronics smaller using integrated circuit (IC) technologies.

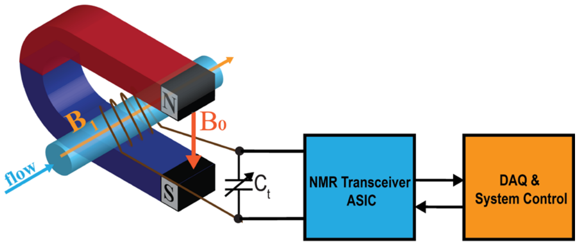

Figure 4: Illustration of an NMR flowmeter

a) Magnet Development

A magnet is an essential component of an NMR system as it is the source of static magnetic field. For miniaturized NMR systems, permanent magnets are a natural choice as they can provide sufficient field strength (up to 2 T) and homogeneity. The main hurdle in designing such a permanent magnet system is achieving sufficient field homogeneity while keeping it as compact, efficient, and simple in assembly and tuning as possible, and with little or no electrical shimming.

We have developed a compact permanent magnet system [12] specifically for microfluidic flow measurements, shown in Figure 5. The magnet is 3.5x3.5x8.0 cm^3 in size and has a 5 mm high airgap, provides a field strength of 0.5 T, and sufficient field homogeneity (<200 ppm) for NMR relaxometry measurements in capillaries up to 1.6 mm inner diameter and 20 mm long. The key components that enable good static field homogeneity are soft-magnetic steel inserts, which are slightly shorter than the total magnet length. By displacing the inserts, it is possible to improve (to shim) the B_0 homogeneity sufficiently and without needing further electrical shimming or repeating the procedure afterward. The "C" shape allows access from the side, and the 5-mm airgap provides enough space for additional electronics or microfluidic fixtures inside. At the same time, the C-shape yoke encloses the magnetic stray fields outside the air gap, thus preventing strong interaction with the environment.

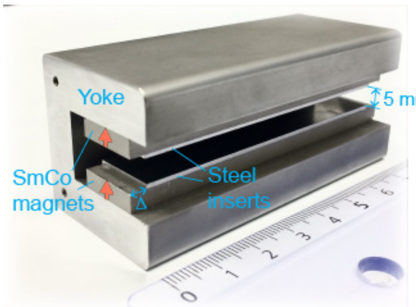

Figure 5: A photograph of the developed magnet for flow measurements

b) Development of Electronics

An NMR system can be regarded as a radio transceiver that operates at the Larmor frequency. The B_1 field is applied to the sample by an RF coil, also used to pick up the NMR signal. A transmitter drives the coil, and a receiver detects the NMR signal.

To develop a portable device, an Application-Specific Integrated Circuit (ASIC) was designed and implemented using a 65 nm CMOS technology. The designed chip's block diagram is shown in Figure 6. This chip incorporates an H-bridge power amplifier that drives the coil to excite the samples. The designed transmitter operates with a 3.3 V supply and can draw a maximum current of 150 mA.

On the receiver side, the chip features a signal chain responsible for amplifying the NMR signals, followed by an 8-bit Successive Approximation Register (SAR) Analog-to-Digital Converter (ADC) to digitize them. The receiver dissipates 36 mW of power from a 1.2 V supply and exhibits a spectral noise density of 1 nV/sqrt(Hz) at 21 MHz. A micrograph of the designed chip wire-bonded to a 7mm x 7mm QFN package is shown in Figure 7.

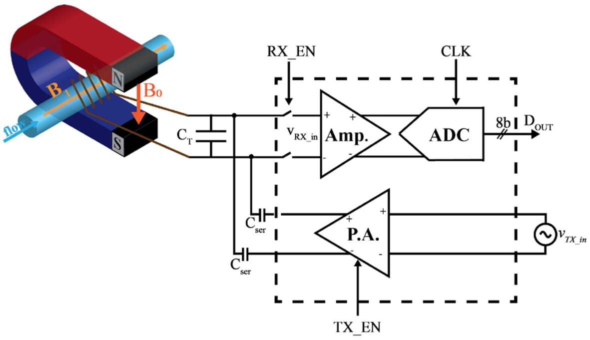

Figure 6. Block diagram of the designed ASIC

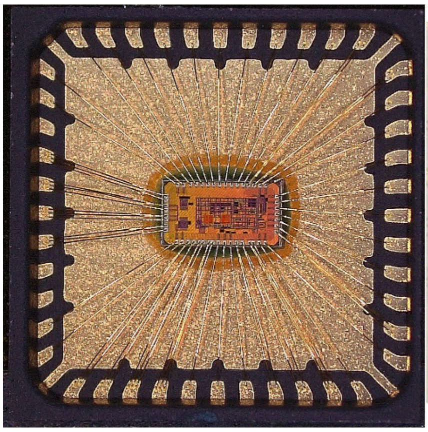

Figure 7: The micrograph of the designed NMR ASIC wire-bonded to a QFN package

MEASUREMENT RESULTS

To demonstrate the capabilities of such a compact NMR system, we first combined the magnet and sample probes, made based on a solenoid coil wound around the capillary of desired inner diameter (up to 1.6 mm), and a commercial NMR control unit (Pure Devices GmBH).

Figure 8 shows measurement examples of the flow curves (inset) and flow measurements at different set flow rates. Changing the probe's size makes it possible to measure in a desired flow-rate range; here, three probes of varying solenoid lengths were used. These proof-of-concept measurements cover a range of 5-orders of magnitude wide, from 100 nL/min to 20 mL/min.

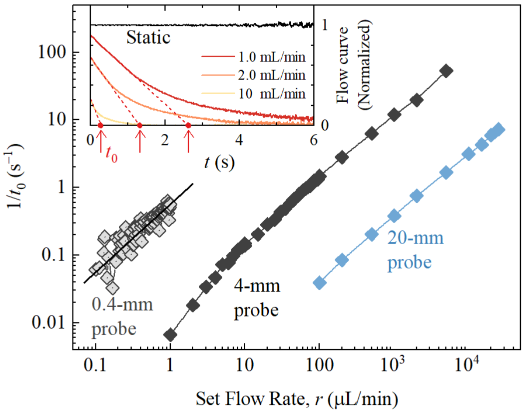

Figure 8: Proof-of-principle flow measurements using the C-shape magnet and sample probes of different diameter

CP measurements were performed to test the developed magnet's and the ASIC's functionality. The test setup is shown in Figure 9. A PTFA microfluidic tubing with a 1.6 mm outer and 0.8 mm inner diameter was filled with tap water. The coil size was 6 mm, and the coil was hand-wound using 0.25 mm copper wires. The resulting NMR signal measured from the digital output of the ASIC is shown in Figure 10.

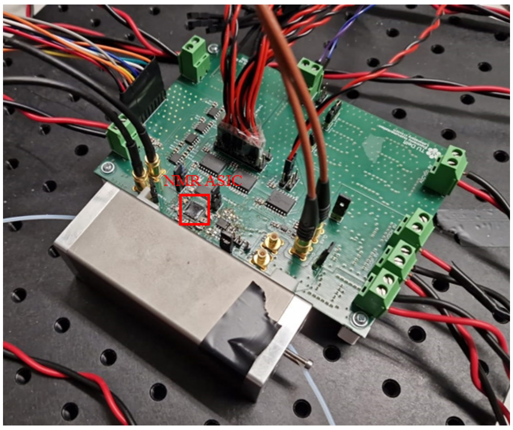

Figure 9: The NMR measurement setup with the developed ASIC and the magnet.

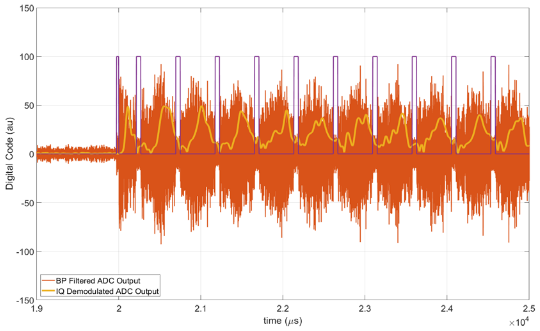

Figure 10: The NMR signal measured using the developed ASIC and the magnet with a xx μl sample.

CONCLUSION

This paper presented some recent progress in the development of portable NMR microfluidic flowmeters portable. A small magnet was designed specifically for flow measurement. Flow measurements using this magnet show that it is possible to measure microfluidic flows ranging from 100 nL/min to 20 mL/min.

We also describe the architecture of a recently developed NMR ASIC for NMR flowmeters. The resulting chip achieves state-of-the-art performance and occupies only 2.2 mm^2 area. It is also shown that the developed chip and developed magnet can be used together for NMR measurements.

All in all, research in the development and miniaturization of NMR microfluidic flowmeters is still ongoing both in magnet design and electronics design. With its specific advantages over other flow measurement techniques, the use of NMR flow sensing in both scientific and industrial applications has a bright future.

ACKNOWLEDGMENTS

This work is a part of the research program FLOW+ under project number 15025, which is co-funded by the Netherlands Organization for Scientific Research (NWO), Bronkhorst High-Tech, and Krohne.

REFERENCES

[1] H. A. Stone, A. D. Stroock, and A. Ajdari, “Engineering flows in small devices: Microfluidics toward a lab-on-a-chip,” Annu Rev Fluid Mech, vol. 36, no. 1, pp. 381–411, Jan. 2004.
[2] J. T. W. Kuo, L. Yu, and E. Meng, “Micromachined Thermal Flow Sensors—A Review,” Micromachines (Basel), vol. 3, no. 3, pp. 550–573, Jul. 2012.
[3] A. C. De Oliveira, *et al.*, “A MEMS Coriolis Mass Flow Sensor with 300 µ g/h/ √Hz Resolution and ± 0.8mg/h Zero Stability,” in 2021 IEEE International Solid- State Circuits Conference (ISSCC), IEEE, Feb. 2021, pp. 84–86.
[4] Y. Chen, Y. Chen, S. Hu, and Z. Ni, “Continuous ultrasonic flow measurement for aerospace small pipelines,” Ultrasonics, vol. 109, p. 106260, Jan. 2021.
[5] L. Ge *et al.*, “Study on a New Electromagnetic Flow Measurement Technology Based on Differential Correlation Detection,” Sensors, vol. 20, no. 9, p. 2489, Apr. 2020.
[6] Y. Yu and G. Zong, “Note: Ultrasonic liquid flow meter for small pipes,” Review of Scientific Instruments, vol. 83, no. 2, p. 026107, Feb. 2012.
[7] A. M. Bilgic *et al.*, “Multiphase flow metering with nuclear magnetic resonance,” Technisches Messen, vol. 82, no. 11, pp. 539–548, Nov. 2015.
[8] E. Aydin and K. A. A. Makinwa, “A Low-Field Portable Nuclear Magnetic Resonance (NMR) Microfluidic Flowmeter,” 21st International Conference on Solid-State Sensors, Actuators and Microsystems, TRANSDUCERS 2021, pp. 1020–1023, Jun. 2021.
[9] H. Y. Carr and E. M. Purcell, “Effects of diffusion on free precession in nuclear magnetic resonance experiments,” Physical Review, vol. 94, no. 3, pp. 630–638, May 1954.
[10] F. Bloch, W. W. Hansen, and M. Packard, “The Nuclear Induction Experiment,” Physical Review, vol. 70, no. 7–8, pp. 474–485, Oct. 1946.
[11] T. M. Osán *et al.*, “Fast measurements of average flow velocity by Low-Field 1H NMR,” Journal of Magnetic Resonance, vol. 209, no. 2, pp. 116–122, Apr. 2011.
[12] D. Polishchuk and H. Gardeniers, “A compact permanent magnet for microflow NMR relaxometry,” Journal of Magnetic Resonance, vol. 347, p. 107364, Feb. 2023.

PRESSURE DECAY TESTBENCH FOR AIR LEAKAGE CHARACTERIZATION OF MICROPUMPS OR MICROVALVES

D. Anheuer[1,*], *P. Debera, M. Richter*[1], *C. Kutter*[1]
[1] Fraunhofer EMFT, Hansastraße 27 D, 80686 Munich, Germany

ABSTRACT

Microvalves as components of micropumps have been developed, improved and used in different areas of industrial and medical technology [1, 2]. Reliable active or passive microvalves as standalone components enable a variety of different microfluidic systems and applications by regulating or switching fluid flows [1]. For gas applications such as micro vacuum pumps or micro compressors, the leakage rate is an important parameter for proper functioning of the microfluidic system. In order to improve the performance of valves in relation to the leakage rate, a comprehensive evaluation of the valves is important. Often these low gas flow rates below 0.1 cm³/min cannot be accurately measured with conventional flow sensors. This paper presents a small and low-cost test rig for measuring gas leakage rates accurately below 0.1 cm³/min with the pressure decay method. Exemplary results of the leakage rate measurement with the pressure decay method combined with reference measurements of a conventional flow sensor are shown using a silicon micropump with two passive silicon flap valves.

Keywords: Silicon, microvalve, leakage, pressure decay, experimental characterization, flap valves.

INTRODUCTION

The gas or liquid leakage rate of valves or pumps is detrimental to their performance and in most cases undesired. However, measuring such leakages for micropumps or microvalves is typically challenging with known characterization setups such as mass flow sensors due to the very small flowrates involved, especially for gases. In the following, a cost-effective and simple measurement set-up is presented, which allows the reliable measurement of smallest gas flowrates below 0.1 cm³/min. The lower resolution limit varies according to the measuring range of the pressure sensor employed and its resolution.

Fraunhofer EMFT develops and manufactures silicon microdiaphragm pumps with piezoelectric actuators and passive flap valves as depicted in Figure 1 [3]. The generation and maintaining of high air pressure differences of more than 50 kPa with a single micropump is particularly challenging and relevant for use in applications such as vacuum micropumps [4]. The valve leakage rate therefore plays a significant role in this context and can be defined as an undesired fluid flow against the pumping direction. For micropumps, the leakage rate reduces important parameters such as flow rate and back pressure capability [5], which impairs the performance of the pump. In the case of microdiaphragm pumps with passive flap valves, this is especially important, since the actuator movement generates alternating positive and negative pressure. This pressure is then applied to the closed valve causing undesired leakage rates.

In this study, a leakage rate test bench with the pressure decay method for gases is presented. Exemplary results of leakage rate measurements are shown using a silicon micropump in order to determine the quality of its silicon microvalves.

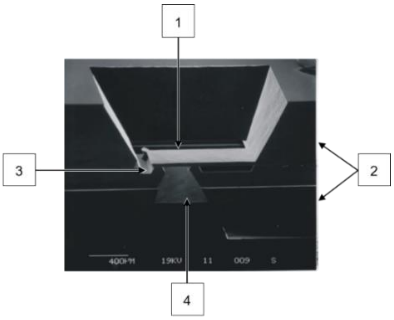

Fig. 1: SEM image of silicon a microvalve. (1) Valve flap and outlet opening, (2) silicon substrates, (3) valve seat, (4) inlet opening.

FUNDAMENTALS

This chapter provides a brief overview on micropumps and microvalves and possible causes of leakage rates in those devices.

Silicon microvalves and micropumps

Figure 2 illustrates the silicon micropump developed and manufactured by Fraunhofer EMFT [3]. It consists of two identical valve wafers that are inverted and bonded to each other by a silicon dioxide direct bond. On the bottom side of substrate 3, the cylindrical pump chamber is etched into the silicon and the residual membrane is thinned to a thickness of $30 - 100$ µm, depending on the required pump parameters. On the top side of substrate 3 is the bonded piezoelectric actuator.

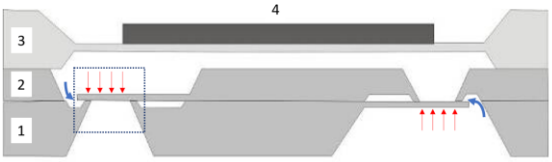

Fig. 2: Schematic cross section of a piezoelectrically-driven silicon micropump. (1) Lower valve wafer, (2) thinned upper valve wafer, (3) pump chamber wafer, (4) piezoelectric actuator. Blue arrows show leakage flow around silicon microvalves, red arrows indicate the applied closing pressure. Blue dotted area is shown in Fig. 1.

The operating principle of this diaphragm pump is based on the inverse piezoelectric effect. As a result of an electrical actuation signal, the piezoelectric ceramic expands and deflects the silicon diaphragm upwards, thus, increasing the volume in the pump chamber. The resulting underpressure opens the inlet valve and fluid flows in the pump chamber. Reversing the actuation voltage causes the piezoelectric actuator to move down towards the valve wafer, causing an overpressure in the pump chamber, which opens the outlet valve and pushes the fluid out of the chamber, and therewith completes the pump cycle.

Leakage Rate

A leakage rate is the undesired flow of fluid against the flow direction of the microvalve. The fluid flows past the valve flap and the valve seat and reduces the achievable flow rate as well as the ability to generate high pressures. High leakage occurs especially as a combination of the following four causes:

1. In the pressure-balanced state, there is an initial gap of roughly 150 nm between valve seat and valve flap due to the manufacturing process, which cannot be changed easily without accepting multiple different process risks. With an applied backpressure, this initial gap between valve flap and valve seat starts to close at the front part of the valve flap. With increasing pressure differences this gap closes further and further until flap and seat are in contact over the entire flap seat. When the valve is exposed to a very small pressure difference in blocking direction that is not yet sufficient to press the valve flap onto the valve seat (closing the initial gap), the medium can flow through the initial gap in blocking direction.
2. Depending on the valve geometry, pressure differences result in the flap being pressed onto the valve seat in the direction of the inlet opening, which causes a deformation of the flap in certain areas. These resulting gaps in the edges of the valve flap, here called remaining gaps, cause leakages.
3. Contaminants, such as particles and fibres, that are located between valve flap and valve seat can cause leakage rates and are difficult to avoid.
4. Valve flap and valve seat are made of silicon and form a hard-hard contact in the closed state. The silicon surface roughness of the contact areas is in the nanometre regime, nevertheless this contact creates additional gaps that lead to leakages.

TESTBENCH DEVELOPMENT

In this section, the development of a testbench in order to precisely measure gas flow rates is shown. Volume flows smaller than 0.1 cm³/min can be measured and displayed reliably with this method. First, a comparison of different measurement methods for leak testing is presented. Furthermore, the implemented test procedure and system design are described in detail.

Comparison of Measurement Procedures

The pressure decay measurement is the classic method of industrial leak testing. Here, a chamber is filled to a certain test pressure and the pressure drop across a given device caused by a leak is measured with a pressure sensor. A quality classification of the tested device by comparing only the pressure drop is possible, in this case the volume flow for a quantitative comparison is of interest. This flow can be calculated from the known internal volume V and the pressure drop rate $\Delta p/\Delta t$. By accurately determining the test volume and using a pressure sensor with sufficiently high resolution, this measurement method can be used to calculate low leakage rates such as those found in silicon microvalves. Alternatively, the necessary gas flow to maintain a certain pressure in the fluidic system can be measured as the leakage rate. In this scenario, the object's volume just needs to be constant and not known numerically and monitored with a flow and a pressure sensor. The expected leakage rates for silicon microvalves at pressure differences < 10 kPa are difficult to be measured with standard flow sensors. For instance, the mass flow meter EL-FLOW Select F-110C from Bronkhorst is suitable for accurate measurement of flow ranges between 0.014 cm³/min and 0.7 cm³/min [6]. Below 0.01 cm³/min, the measurement accuracy of classic flow sensors decreases significantly for gases, whereas pressure can be measured precisely up to smallest pressure differences.

Another leak test procedure is the pressure build-up measurement, where the test pressure is first applied to a volume tank, for example with an integrated active valve. After reaching the target pressure, for example 50 kPa, the active valve switches and applies the pressure to the device under test (DUT). In the pressure chamber, connected to the DUT, the pressure increase is measured, which corresponds to the leakage rate of the DUT. This requires additional components such as a volume tank and an active valve, which are not required for the pressure decay measurement. This means there are additional connections in the pressure build-up measurement from which unwanted leaking rates can occur. A disadvantage of the described pressure increase or decrease method is the difficulty in deducing the volume flow from the recorded pressure data. Fewer components in the fluidic system are particularly important to reduce the risk of undesired leaks. At the same time, the test bench needs to remain modular to allow easy replacement of the DUT. These advantages, together with the low-cost realization and the possibility to calculate leak rates using a pressure sensor and a specific volume, leads to the decision to use the concept of a pressure decay measurement test bench.

System Design

The test bench, depicted in Figure 3, includes a pressure generator CPC4000, which is connected to the test valve or micropump housing (2) via a capillary (1). To prevent leakages around the DUT, an additional silicone sealing gasket is inserted into the housing. This sealing was tested with a blank silicon chip without valve to ensure the tightness of the sealing. After several minutes no pressure loss is detected hence the overall system is considered free of leakages.

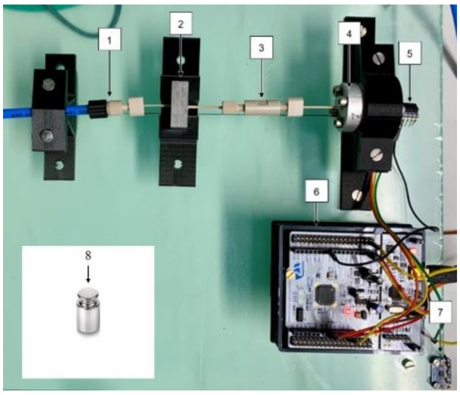

Fig. 3: Pressure decay system setup: (1) Fluidic connection to pressure generator CPC4000, (2) Aluminum housing for silicon-microvalve, (3) Capillary with connector, (4) Aluminum housing with integrated test volume, (5) Pressure sensor HSC-DRRN600MD2A3, (6) NUCLEOF411RE microcontroller, (7) MCP9808 temperature sensor, (8) calibration test weight.

The DUT can be replaced easily, quickly and non-destructively. A capillary (3) connects the housing with a pressure chamber (4) for pressure build-up and inserting the test volume for a defined volume reduction with a calibration weight. A pressure sensor (5) is bonded directly to this housing to avoid further connections and thus possible leakages. Attached to the test bench is a temperature sensor MCP9808 (7) to record temperature fluctuations of the ambient air for the calculation of the leakage rates. The ambient air temperature is assumed to be the gas temperature of the leakage flow. Sensor data is processed by a STM microcontroller NUCLEO411RE (6) and transferred to a computer for post processing.

Data Processing and Flow Calculation

A 1 g steel calibration test weight, depicted in Fig. 3 (8), as a defined volume for a defined volume reduction of the pressure chamber is used to determine the volume of the pressure chamber. We assume that the test volume has a precisely determinable volume, which can be calculated based on temperature $T = 20°\mathrm{C}$, density $\rho = 7859$ kg/m³ and weight $m_{1g} = 1e^{-3}$ kg and results in $V_D = V_{1g} = 1.272e^{-7}$ m³. This weight of the test volume is verified with a laboratory balance. The described test procedure is depicted in Figure 4.

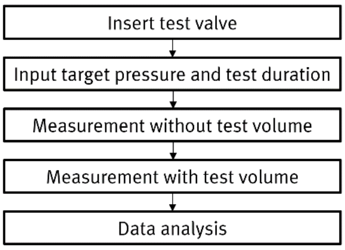

Fig. 4: Simplified flow diagram of testing procedure. Measurement with defined volume reduction due to the test weight is used for the determination of the volume of the pressure chamber and periphery.

Two consecutive pressure decay measurements are necessary to compute the volume of the pressure chamber and periphery, as depicted in Figure 5.

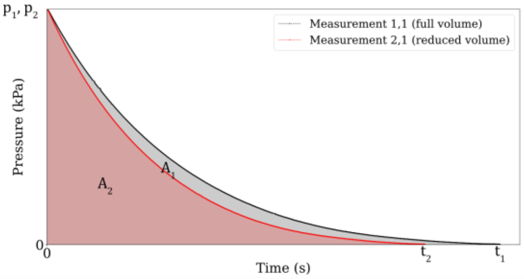

Fig. 5: Schematic pressure decay measurements with full volume (1,1) and reduced volume (2,1). Starting pressures p_1 and p_2, atmospheric pressure at times t_1 and t_2. Area below black graph (A_1) and area below red graph (A_2).

One measurement with inserted test volume for the defined volume reduction in the pressure chamber (Measurement 2,1) as well as one measurement without inserted test volume is performed (Measurement 1,1). The temperature is constantly measured and observed in the controlled lab environment. All necessary steps to calculate the leakage volume flow from those pressure decay measurements are explained in the following. The ideal gas equation

$$n(t) = p(t)\,\frac{V}{R \cdot T} \qquad (1)$$

depicts the substance amount n of air in relation to the volume V. Assuming a constant temperature T, the substance amount n in the volume V at a certain similar pressure level p is obtained. The ratio r (at the same temperature T and pressure p) can be compared and assumed to be equal.

$$r(p) = \frac{n_1(t_1)}{V_1} = \frac{n_2(t_2)}{V_2} \qquad (2)$$

By integrating over the measurement time t, until atmosphere pressure is reached, from the beginning of the pressure decline, the area under the curve is obtained and gives a relation to the volume V of the pressure chamber and periphery.

$$\int_0^{t_1} p_1(t)dt = \frac{V_1}{V_2}\int_0^{t_2} p_2(t)dt \qquad (3)$$

A_1 and A_2 represent the integrated area under measurement 1 or measurement 2. The ratio between A_1 and A_2 is assumed similar as the ratio between volume V_1 and volume V_2. The combined heuristic formula used for the volume determination is obtained.

$$\begin{aligned} A_1 = \int_0^{t_1} p_1(t)dt &= \frac{V_1}{V_2}\int_0^{t_2} p_2(t)dt \\ &= \frac{V_1}{V_2}\cdot A_2 \end{aligned} \qquad (4)$$

As explained above, measurement 2 has a defined reduced volume V_D due to the inserted calibration weight, which defines the test volume. To compute our unknown chamber volumes V_1 and V_2 from which the pressure decrease is measured, V_2 gets replaced with $V_1 - V_D$.

$$\frac{A_2}{A_1} = \frac{V_2}{V_1} = \frac{V_1 - V_D}{V_1} \qquad (5)$$

With equation 5 the unknown volumes V_1 and V_2 are calculated, as seen in formula 6 and 7.

$$V_1 = V_D \frac{A_1}{A_1 - A_2} \qquad (6) \text{ and } V_2 = V_D \frac{A_2}{A_1 - A_2} \qquad (7)$$

Assuming an ideal gas and using the calculated volume of the pressure chamber V to receive the substance amount $n(t)$ for a defined time step Δt.

$$n(t) = \frac{-\Delta p \cdot V}{R \cdot T} \qquad (8)$$

The obtained amount of substance $n(t)$ leads to the mass flow q_m.

$$q_m(t) = \frac{n(t) \cdot M}{\Delta t} \qquad (9)$$

Necessary for determining the volume flow $q_v(t)$ is the pressure dependent fluid density of air $\rho(t)$.

$$\rho(t) = \frac{p(t) \cdot M}{R \cdot T} \qquad (10)$$

From the mass flow $q_m(t)$ the volume flow $q_v(t)$ can be determined by considering the fluid density of air $\rho(t)$.

$$q_v(t) = \frac{q_m(t)}{\rho(t)} \qquad (11)$$

RESULTS

In the following chapter, first results obtained with this measurement method are presented. The repeatability of this method was demonstrated by three consecutive measurements with the same housed $5x5$ mm² silicon micropump from Fraunhofer EMFT (uP029) [7]. Each of the three measurements consist of one measurement with test volume (reduced volume) and one measurement without test volume (full volume). The result in each case is a time-decreasing function of pressure over time, depicted in Figure 6. Prior to each measurement, the entire fluidic system was dismantled and re-assembled and an overpressure of 50 kPa relative to the atmosphere was generated inside the pressure chamber. Due to the leakage rate of the micropump and periphery, this overpressure equalises to atmospheric pressure after $270 - 330$ s.

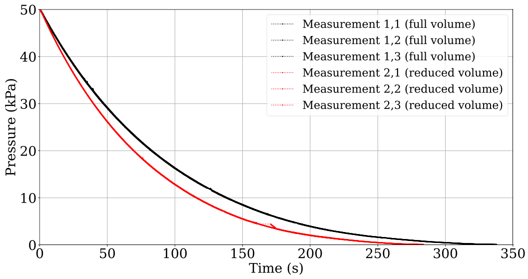

Fig. 6: Pressure decay measurements with housed micropump uP029. Data recorded three times with test volume $V_D = V_{1g} = 1.272e^{-7}$ *m³ or* $m_{1g} = 1e^{-3}$ *kg (reduced volume) and three times without test volume (full volume). Setup was dissembled after each cycle.*

The volume flow of the test object is determined using the methodology described in section 3.3. Each of the three measurements with test weight is compared to the measurement without test weight and the volume of the pressure chamber (without test volume) was determined and is shown in Table 1.

Table 1: Resulting volumes from measurements depicted in Figure 6. Calculated full chamber volumes V_1*, mean chamber volume* $\bar{V}$ *and percentage deviation from the mean chamber volume.*

Measurement	**1**	**2**	**3**
Volume V_1 (cm³)	0.81	0.77	0.80
$\bar{V}$ (cm³)	0.797		
$\lvert V_i - \bar{V} \rvert$ (%)	0.98	1.03	0.99

The calculated mean and the percentage difference from the mean is also depicted. Deviation from the mean is approximately 1% in all three measurements. The total error band of the used pressure sensor (Honeywell HSC-DRRN600MD2A3) is 1% and can therefore be considered as the minimum error of this measurement method.

Figure 7 illustrates the calculated leakage rate of the three consecutive measurements. The maximum volume flow obtained with the pressure decay method is ~0.225 cm^3/min at a pressure difference of 40 kPa. Every 50th pressure sensor value (slice 50) is recognised for the computation. All three consecutive measurements with the pressure decay method (Fig. 7, Measurement 1-3) show a high reproducibility. Two reference measurements of the same DUT were recorded using the mass flow meter EL-FLOW Select F-110C from Bronkhorst (Fig. 7, Reference measurement 1-2). All measurements of the same sample generally correlate, although the reference measurements indicate a higher volume flow of the leak rate and shows an offset.

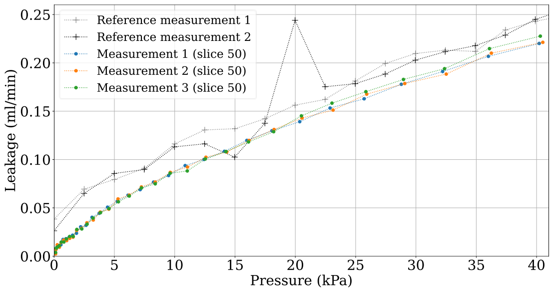

Fig. 7: Calculated leakage volume flow from the same DUT for measurements depicted in Fig. 6 (Measurement 1-3, dot markers). Reference measurement 1 and 2 (+ markers) measured with conventional mass flow meter.

CONCLUSIONS

This publication shows a straightforward and cost-effective test bench for the precise determination of smallest gas flows below 0.1 cm^3/min using the pressure decay method. In this process, flow rates below the resolution limit of flow sensors can be measured reliably, shown exemplarily with housed silicon micropumps with integrated silicon microvalves. For measurements on samples with lower leak rates compared to the measurements presented above, an alternative pressure sensor with a reduced operating range can be selected to allow the detection of leakage rates below 0.01 cm^3/min with high resolution. The accurate calculation of the test volume is elaborate and ensures reproducible measurements. Further steps will include extensive measurements with changing specimen and leakage improved passive silicon microvalves and micropumps in order to develop micropumps for gas applications with challenging leakage requirements.

ACKNOWLEDGEMENT

This research was funded by Deutsche Forschungsgemeinschaft (German Research Foundation) with grant number KU 3410/1-1.

REFERENCES

[1] K. W. Oh and C. H. Ahn, "A review of microvalves," *J. Micromech. Microeng.*, vol. 16, no. 5, R13-R39, 2006, doi: 10.1088/0960-1317/16/5/R01.

[2] A. B. Bußmann, L. M. Grünerbel, C. P. Durasiewicz, T. A. Thalhofer, A. Wille, and M. Richter, "Microdosing for drug delivery application—A review," *Sensors and Actuators A: Physical*, vol. 330, no. 6, p. 112820, 2021, doi: 10.1016/j.sna.2021.112820.

[3] H. Leistner, M. Wackerle, Y. Congar, D. Anheuer, S. Roehl, and M. Richter, "Robust Silicon Micropump of Chip Size 5x5x0.6 mm3 with 4 ml/min Air and 0.5 ml/min Water Flow Rate for Medical and Consumer Applications," in *Actuator 2021: International Conference and Exhibition on New Actuator Systems and Applications : GMM conference, February 17-19, 2021, online event*, 2021, pp. 113–116.

[4] Martin Richter, Daniel Anheuer, Axel Wille, and Yuecel Congar and Martin Wackerle, "Multistage Micropump System towards Vacuum Pressure," *Actuators*, 2023.

[5] C. P. Durasiewicz, S. T. Güntner, P. K. Maier, W. Hölzl, and G. Schrag, "Piezoelectric Normally Open Microvalve with Multiple Valve Seat Trenches for Medical Applications," *Applied Sciences*, no. 11, p. 9252, 2021. [Online]. Available: https://doi.org/10.3390/app11199252

[6] BRONKHORST DEUTSCHLAND NORD GMBH, *DATASHEET F-110C: EL-FLOW Select F-110C.* [Online]. Available: https://www.bronkhorst.com/de-de/produkte/gas-durchfluss/el-flow-select/f-110c/ (accessed: Jan. 3 2023).

[7] A. Bußmann *et al.*, "Piezoelectric Silicon Micropump for Drug Delivery Applications," *Applied Sciences*, vol. 11, no. 17, p. 8008, 2021, doi: 10.3390/app11178008.

CONTACT

*Daniel Anheuer,

daniel.anheuer@emft.fraunhofer.de

SILICON-BASED PIEZO MICROPUMPS ENABLE FULLY FLEXIBLE DRUG DELIVERY PATTERNS

D. Plano[1], S. Kibler[2], N. Rudolph[1] and J. Dressman[1]
[1] Fraunhofer Institute for Translational Medicines and Pharmacology ITMP, Frankfurt, Germany
[2] Fraunhofer Institute for Electronic Microsystems and Solid-State Technologies EMFT, München, Germany

PURPOSE

The rate and extent to which an active pharmaceutical ingredient (API) is released from a drug product is crucial to optimal therapy [1] In some cases API release should be fast, but in others it should be delayed, sustained or site-specific. It would therefore be advantageous to generate dosage forms with flexible pharmaceutical release profiles.

This study focuses on the ability of a silicon-based piezo micropump to generate a wide variety of release patterns [2]. Metoprolol tartrate, a commonly used antihypertensive drug, was chosen as the model compound for testing the micropump [3].

METHODS

A solution of 200 mg/ml metoprolol tartrate in 20 mM phosphate buffer at pH 6.5 was freshly prepared, filtered through a Cytivia 0.02 µm Anotop Plus filter (Little Chalfont, UK), degassed and maintained at 20°C. Experiments were conducted on 5x5 mm^2 piezo based silicon micropumps embedded in a PEEK housing developed at Fraunhofer EMFT (Munich, Germany [2, 3]), which was controlled using a Keysight A 33500B waveform generator (Böblingen, Germany) and a Piezosystemjena SVR1000/3 high voltage amplifier (Jena, Germany). The flow rate was obtained using a Bronkhorst LiquiFlow L13 in-line flow-through sensor (Ruurlo, Netherlands) (Figure 1). In a first step, the micropump was primed by pumping the API solution at a rate of 0.5 ml/10 min. Next, the API solution was pumped according to one of five protocols: i) immediate-release profile of 0.5 ml/10 minutes over 20 minutes, ii) pumping the solution five times at a rate of 0.5 ml/min (stress test), iii) extended-release profile at 0.5 ml/12h, iv) a modified-release profile by alternating six times between a pump rate of 0.1 ml/10min and 0.5 ml/10min every 15 minutes and v) a modified-release profile increasing the pump rate every 15 minutes (Figure 2). Metoprolol tartrate was analyzed qualitatively between 200 and 700 nm using a ThermoFisher GENESYS 50 spectrophotometer (Karlsruhe, Germany) and quantitatively using a HPLC-UV system (VWR, Darmstadt, Germany) with a Phenomenex Gemini-NX reversed-phase C18, 150 mm x 4.6 mm, 5 µm column (Aschaffenburg, Germany). All experiments were performed in triplicate.

RESULTS

Protocols i) and ii) showed reliable and consistent mean pumping rates. Signal noise or slight variations in pumping rate can be attributed to differences in individual pump performance and small air bubbles in the experimental set-up, but did not affect the mean flow rate.

In Experiment iii), a constant and nearly linear pumping rate was observed, indicating accurate dosing over 12 hours. Due to the low pumping rate, the mean flow rate varied by up to 15% among the three individual experiments. Moreover, at this low pumping frequency, the micropump was more sensitive to air bubbles, resulting in intermittent flow rates.

Experiment iv) demonstrated reliable pulsatile release over 2 hours. The micropump returned to its previous pump performance after each cycle, with temporary deviations caused by small air bubbles adsorbed in the tubing and air accumulation in front of the micropump's built-in filter.

Experiment v) showed some variability at the lowest pump rates of 0.5 µl/min and 5 µl/min. Pumping at higher rates reduced the frequency of outliers, decreased the sensitivity against air bubbles, and stabilized the mean flow rate (Figure 3).

Qualitative UV-Vis and quantitative HPLC analysis confirmed the compatibility and stability of metoprolol during the experiments (Table 1).

CONCLUSION

The results demonstrate that the piezo micropump is well suited to provide individual and adjustable dosing profiles without compromising the quality of the API over a wide range of flow rates.

Word Count: 570

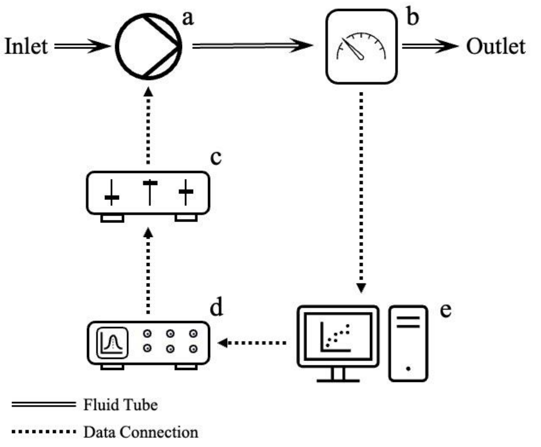

Figure 1: Schematic of the experimental micropump setup with a) micropump, b) flow-through sensor, c) amplifier, d) waveform generator and e) computer.

Table 1. Concentration of metoprolol tartrate before and after pumping experiments i) - v).

	Exp.	c (before) [mg/ml]	c (after) ± SD [mg/ml]
Metoprolol	i	190.9 ± 1.8	178.5 ± 3.9
	ii		186.4 ± 8.5
	iii		180.4 ± 0.1
	iv		177.4 ± 1.8
	v		182.9 ± 2.3

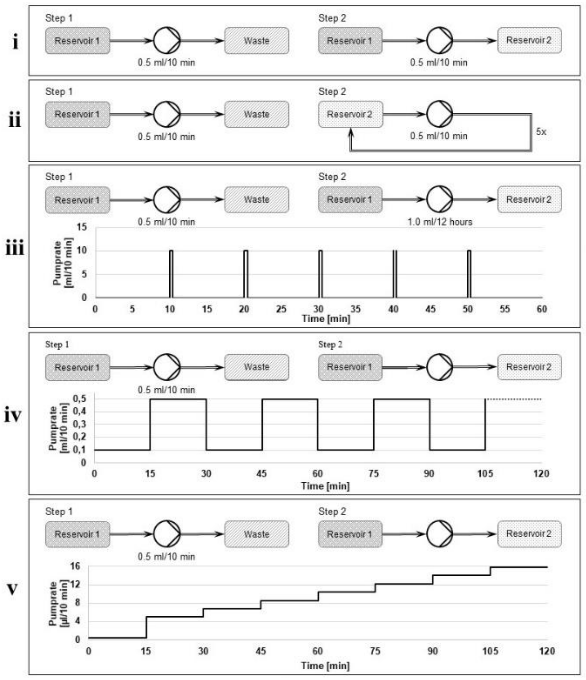

Figure 2. Schematic of the pump experiments i) – v) along with the pump rates applied in the studies.

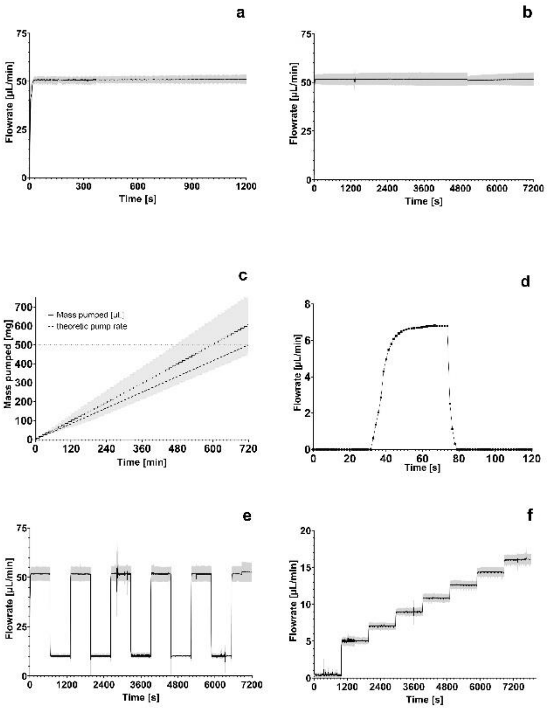

Figure 3. Mean pump rates of the pump experiments with a 5 x 5 mm^2 micropump and metoprolol tartrate solution:

- *(a) Mean flow rate of Experiment i) (immediate-release) with standard deviation (grey)*
- *(b) Mean flow rate of Experiment ii) (stress test) with standard deviation (grey)*
- *(c) Cumulative pumped volume of Experiment iii) (extended-release) with standard deviation (grey) and theoretic pumped volume (dotted line)*
- *(d) Flow rate of pump 1 in Experiment iii) (extended-release) between minute 363 and 365 of the protocol*
- *(e) Mean flow rate of Experiment iv) (modified-release) with standard deviation (grey)*
- *(f) Mean flow rate of Experiment v) (modified-release) with standard deviation (grey).*

REFERENCES

[1] A. T. Florence and P. U. Jani, “Novel oral drug formulations. Their potential in modulating adverse effects,” *Drug safety*, vol. 10, no. 3, pp. 233–266, 1994, doi: 10.2165/00002018-199410030-00005.

[2] A. Bußmann *et al.*, “Piezoelectric Silicon Micropump for Drug Delivery Applications,” *Applied Sciences*, vol. 11, no. 17, p. 8008, 2021, doi: 10.3390/app11178008.

[3] Henry Leistner et al., *ACTUATOR 2021: International Conference and Exhibition on New Actuator Systems and Applications GMM Conference, February 17-19, 2021, Online Event*, 113rd ed. [Berlin]: VDE Verlag, 2021.

CONSTRUCTION AND CHARACTERIZATION OF MICROFLUIDIC PLATFORM FOR HIGHLY PARALLEL SINGLE CELL ISOLATION

M. Kümmerle[1], V. Zieger[1], S. Kartmann[1, 2] and P. Koltay[1, 2]
[1]Laboratory for MEMS Applications, IMTEK – Department of Microsystems Engineering,
University of Freiburg, Freiburg, Germany
[2] Hahn-Schickard, Freiburg, Germany

Single cell isolation provides many advantages such as a noise free environment without any paracrine signaling. This can provide insights into cellular heterogeneity, cellular behavior and disease mechanism [1]. This paper explores our advancements in single cell isolation techniques, highlight their principles, advantages and applications. We cover the design, construction methods, characterization of the fluidic device and improvement strategies to further improve the single cell isolation platform.

Current solutions in literature report single cell trapping via gravitational and hydrodynamic forces, for example for drug screenings.[2, 3] However, screenings or downstream studies have to be carried out on-chip which limits the possible applications. Here, we report a microfluidic trapping structure for low cell concentration samples with the ability to dislocate trapped cells from the trapping site and dispense them in a highly parallel manner into individual wells of a micro well plate.

For microfluidic cell trapping, we investigated hydrodynamic trapping. The system is shown in **Fig. 1** and is designed as follows: A fluid reservoir is connected to a PMMA substrate chip through a rigid PEEK tube that is connected with luer-connectors. The trapping structures are micro milled into the base chip with Micro HD (Kern Microtechnik, Germany). The base chip is covered with a dispensing cover that seats a nozzles over each individual trap. The nozzles have the dimensions to provide a surface tension great enough to not leak during the trapping process and open up into an aperture. The nozzles and trapping structures are placed to fit over the individual wells of a standard 384 micro well plate. The cell suspension is transported through the channel by pressure and passes the trapping structures that are based on hydrodynamic forces. The hydrodynamic traps are U-shaped indents into rectangular blocks sitting in the center of a flow speed reduction chamber as shown in **Fig.2**. The trapped cells can then escape the isolation device with the help of centrifugal forces into the micro well plate as in **Fig.1**. The microfluidic platform operates as a standalone chip so it can be placed in a centrifuge to transfer the cells from the microfluidic trapping structure into a micro well plate. The device is low cost in production and can therefore be used as consumable. The system is optimized to provide high throughput and high quality single cell isolation.

First, we tested the trapping concept with various trapping structure geometries. A flow rate variation was investigated with the help of a Nemisys syringe pump (cetoni GmbH, Germany). Further variables that were investigated are concentration and volume. The prototype chips were characterized by Isolation Efficiency (IE), defined by the amount of set traps divided by the total amount of traps and Multiplet Rate (MR), defined by the amount of multiplet state traps divided by the amount of set traps.

During the initial research the experiments were conducted with the help of polystyrol beads with similar size and density as cells. Electrostatic effects are considered when investigating the results of experiments carried out with a bead suspensions as particle clusters are formed. The results of these experiments provided insight to the behavior of the particle isolation dependent on the implemented trapping concepts and lead us to focus on hydrodynamic U-trapping structures as presented in **Fig.3, Fig.4, Fig.5** and **Fig.7**. It is clear to see that the IE reaches a maximum at $4.8 \cdot 10^4\ \mathrm{ml}^{-1}$ at a flow rate of $c = 50\,\frac{\mathrm{\mu l}}{\mathrm{min}}$. During the flow rate variation it shows the best results at a flow rate of $Q = 110\,\frac{\mathrm{\mu l}}{\mathrm{min}}$. The multiplet rate is lower at lower concentrations, yet does not show a trend with varying flow rates

During the construction process, we have shown that a consumable microfluidic platform for isolation and dispensing of single cells can be machined by micro milling trapping structures and dispensing nozzles in two separate PMMA substrates and then joining them. We therefore have a chip that isolates single particles from a suspension at trapping locations and dispenses them into a micro well plate. We can conclude, that it is feasible to structure and join such a chip from PMMA at low costs and provide a highly parallel single cell isolation platform.

Word Count: 686

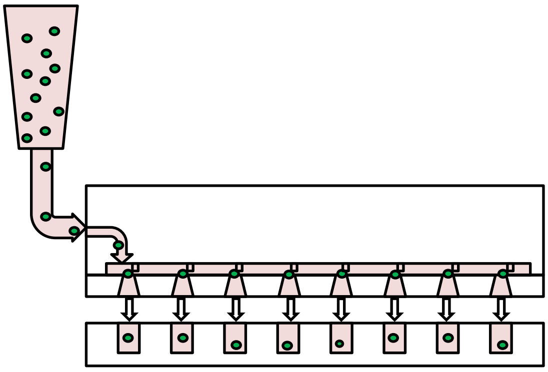

Figure 1: Concept of the entire trapping and dispensing device. The microfluidic chip is connected to a suspension reservoir and placed above a micro well pate.

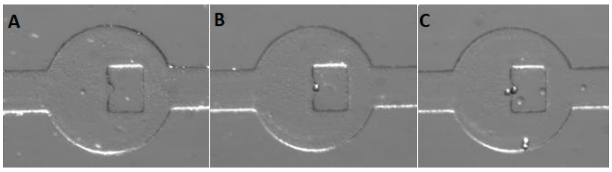

Figure 2: Top view of the U-trap within the channel. Suspension flow from left to right. Possible states of U-trap. A: *unoccupied* B: *single occupation* C: *multiplet occupation*

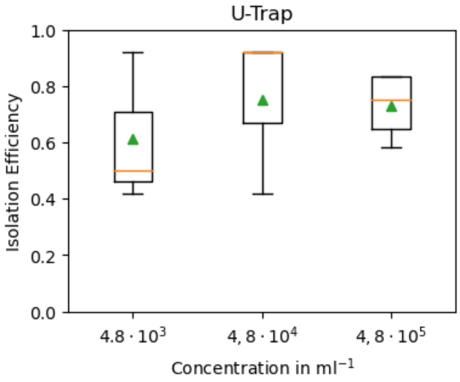

Figure 3: Isolation Efficiency depending on the particle concentration of the hydrodynamic U-trap channel. n=5

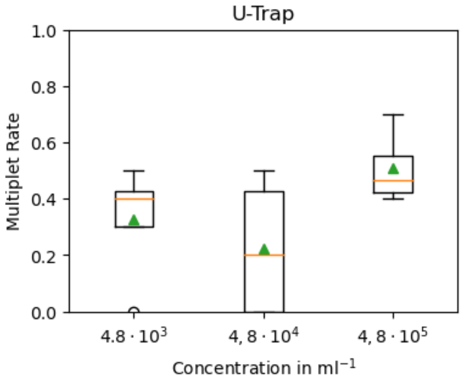

Figure 4: Multiplet Rate depending on the particle concentration of the hydrodynamic U-trap channel. n=5

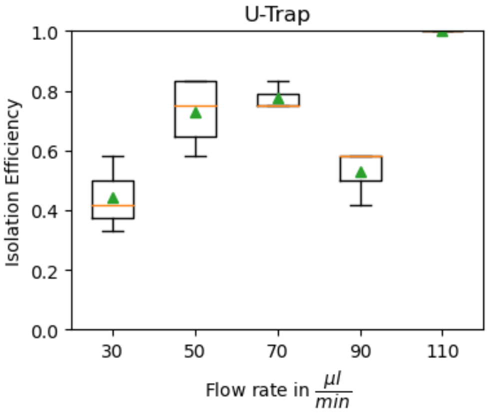

Figure 4: Isolation Efficiency depending on the flow rate for the hydrodynamic U-trap channel. n=5

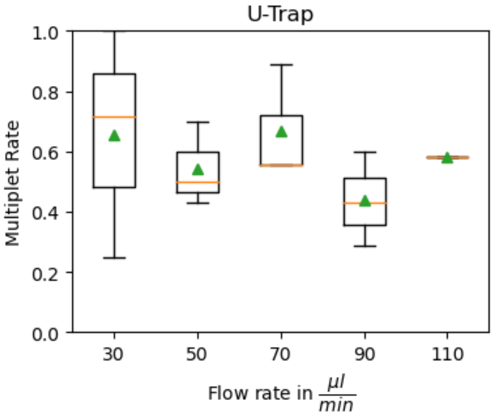

Figure 5: Multiplet Rate depending on the flow rate variation for the hydrodynamic U-Trap channel. n=5

REFERENCES

[1] M. Tellez-Gabriel, B. Ory, F. Lamoureux, M.-F. Heymann, and D. Heymann, “Tumour Heterogeneity: The Key Advantages of Single-Cell Analysis,” *International Journal of Molecular Sciences*, vol. 17, no. 12, p. 2142, Dec. **2016**, doi:10.3390/ijms17122142.

[2] R. M. Johann, “Cell trapping in microfluidic chips”, Anal Bioanal Chem (**2006**) 385: 408–412, doi:10.1007/s00216-006-0369-6

[3] J. R. Rettig, A. Folch, “Large-Scale Single-Cell Trapping and Imaging Using Microwell Arrays” Anal Chem (**2005**) 77, 5628-5634

CONSISTENT EXPERIMENTAL EVALUATION METHODS FOR MICROFLUIDIC MIXERS

O. Blaschke[1], J. Kluitmann[1], X. Xie[1], J. Elsner[1] and K. S. Drese[1]
[1] Institute for Sensor and Actuator Technology, Coburg University of Applied Sciences and
Arts, Am Hofbräuhaus 1B, 96450 Coburg, Germany.

ABSTRACT

This study presents a unifying methodology for characterizing micromixers, integrating both experimental and simulation techniques. Focusing on Dean and H-mixer designs, it employs an optical evaluation for experiments and a Mixing Norm for simulations, yielding a unified characteristic parameter for each mixer. The results demonstrate consistent mixing performance trends across both methods. The paper also proposes enhancements in the evaluation process to improve accuracy and reduce noise impact. This approach provides a valuable framework for optimizing micromixer designs, essential in advancing microfluidic technologies.

KEYWORDS

Micro mixer, mixing measures, mixing performance, simulation, microfluidics

INTRODUCTION

The integration of mixers is a critical step in developing new microfluidic applications and products, often dictating the overall performance of microfluidic chips. Despite extensive research and numerous innovations in fluid flow optimization, the quest for an ideal mixer remains unfulfilled due to varying application-specific requirements. Mixer design poses challenges including compactness, minimizing dead volume, and maximizing mixing efficiency. Factors such as mixing quality, energy consumption, production technology, and material choice further complicate the design process. Consequently, custom mixer designs are frequently necessary, necessitating thorough characterization to ensure suitability for specific applications and to facilitate scaling for increased production without compromising speed or quality.

Therefore, a fast and efficient mixer characterization scheme has been developed. Different experimental approaches on Dean- and H-mixer designs were used for characterization and the experimental results were also compared with simulations of the chips. A main difference to nearly all approaches in the literature is, that not only the performance at the outlet, but the development along the mixing channel was taken into consideration.

MATERIALS AND METHODS

Experimental setup and data collection

For the experiments, multilayer polycarbonate bonding was used to create mixer designs with different mixing elements, including Dean mixers and H-type split and recombine (SAR) designs [1], as shown in Fig. 1.

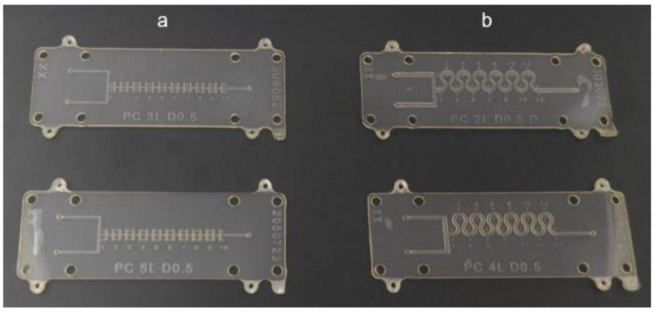

Figure 1: Microfluidic polycarbonate chips with different mixing elements.

These designs were chosen for their well-understood fluid mechanics and mixing processes, facilitating a fundamental evaluation scheme. Studies were conducted using ink-coloured water and $Fe(SCN)_3$ solution at various Reynolds numbers to observe mixing efficiency. The ink-based experiments tracked homogenization through chaotic advection and diffusion, while the $Fe(SCN)_3$ solution experiments provided insights into solvent boundary layer behaviour, considering the Beer–Lambert law.

Two key experiments were conducted: one with green ink diluted in deionized water (volume ratio 4:100), and another with a colour reaction forming a red $Fe(SCN)_3$ complex from 20 mM $Fe(NO_3)_3$ and 60 mM NaSCN in 99.5% ethanol. The ethanol was used to minimize bubble formation in microchannels [2]. Observations under a bright field microscope with a mounted camera showed effective ink dilution and the progressive darkening of the channel in the colour reaction experiment.

The volume flow rates were adjusted by the usage of syringe pumps to realize the necessary Reynolds numbers between 20 and 400 for the Dean mixers. The H-type SAR mixers were limited to a Reynolds number of 200 avoiding too high pressures.

For analysis, a Python code identified channel markers on the chips, and grey scale values of pixels along a defined line between these markers were calculated as depicted in Fig. 2. These values indicated mixing levels in ink dilution studies becoming more uniform over the mixing length and also the extent of chemical mixing in colour reaction experiments because of progressive darkening.

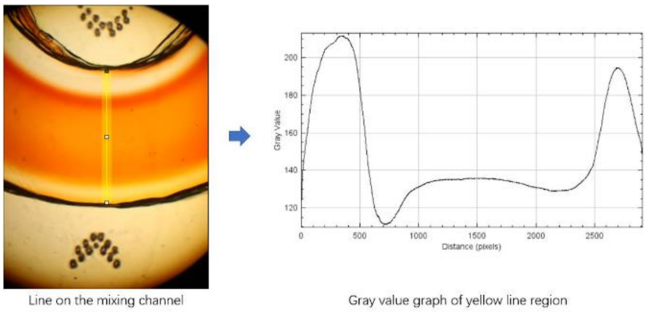

Line on the mixing channel

Gray value graph of yellow line region

Figure 2: Optical measurement from the top of a mixing channel and grey value interpretation across a defined inter-channel section line.

Simulation setup

For comparison of experimental data, finite element (FEM) simulations were done in COMSOL Multiphysics software. The focus was on determining the extent to which simulations can reproduce the real mixer behaviour of the chips. This is of relevance as computational experiments, with their easy access to cross-sectional data and insights into velocity profiles and fluid dynamics, can aid mixer development when linked with real experiments.

Dean and H-type mixers were modelled with actual dimensions and equivalent Reynolds numbers as in the experiments. However, only the ink-dilution experiment was simulated, as the colour reaction required specific chemical parameters not fully detailed in literature. The simulations used water properties at 20 °C, matching our experimental conditions. The inflow boundary was split into two sections with different concentrations to replicate the experiments.

For the Dean mixer, the symmetry of the structure was exploited by modelling only the lower half of the channel and then mirroring it in postprocessing, resulting in a mesh of about 1.37 million elements. The H-type SAR mixer, lacking symmetry due to its inflow conditions, was modelled in its full geometry with approximately 2.9 million elements. Both models used aligned hexagonal elements, which align better with streamlines than tetrahedral elements. Consistent stabilization schemes were also applied to reduce numerical diffusion and enhance the realism of the mixing process simulations [3].

Evaluation scheme for experiments

The datasets of grey values were processed in a way that at first a gaussian filter was applied to eliminate the high frequency noise, containing the original shape of the grey value profiles. Second, multiple statistical measures were computed for the data. The first set determined the positional characteristics and therefore the mean, median and Shamos estimator were evaluated. From these, the mean was the most consistent. The other two measures failed to give a reliable estimate in datasets where the middle region contained a high gradient in grey vales, as they were then sensitive to an asymmetrical distribution. The second set of estimators were applied to measure the amount of dispersion along the mixer. Therefore, the standard deviation (SD), median absolute deviation (MAD) and Hodges-Lehmann estimator were selected. In addition, a Sobolev norm of negative index was calculated as these types of norms can quantify the amount of dispersion and thus mixing [4]. The benefit of this method comes from the ability to not only measure mixing through convection through local variations in grey value gradients, but also takes the diffusion into account by including the information about the absolute values. This makes the so-called Mixing Norm a multi-measure for mixing. In this one-dimensional line-interpretation it was determined that it had a very similar behaviour as the standard deviation, therefore the latter one was selected as relevant measure because of convenience reasons. The MAD and Hodges-Lehmann estimator performed worse as they rely on the median which is not ideal for this use case as stated before.

The evaluation led to mean and SD curves over the mixer length which represented an exponential decline as can be seen in Fig 3. A logarithmic transformation led to the linearization of these curves and made the fitting of a linear model possible. The absolute value of the gradient of these linear models was then plotted against the Reynolds number of the corresponding experiment resulting in a map of the mixer performance for the certain mixing geometry.

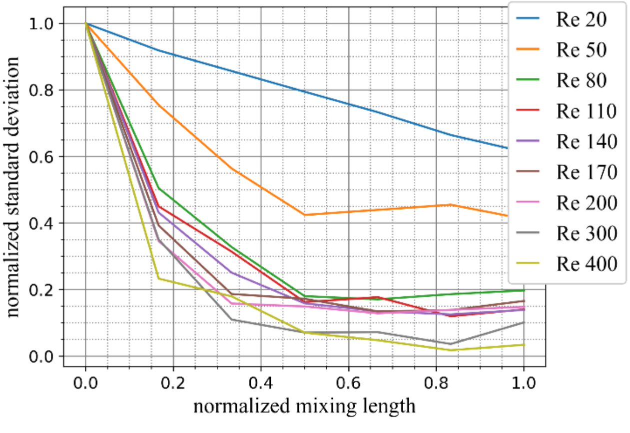

Figure 3: Normalized curves of standard deviation across the mixer structure over normalized mixing length. Dean mixer experiment with ink dilution.

Evaluation scheme for simulations

The evaluation of simulation data differed significantly from the experimental approach. In simulations, the data was represented in a two-dimensional cross-section of the channel, focusing on the change in concentration profile. A crucial step involved weighting the concentration profile by the local mass flow, similar to calculating the Nusselt number in thermodynamics. This was necessary to account for the throughput of mixed or unmixed fluid in the system. The concentration profile c was multiplied with the normalized velocity profile of the main flow direction u_x, with the mean concentration subtracted to center the field around zero.

$$c_{weight} = (c - c_{mean}) \cdot \frac{u_x}{\max(u_x)} \qquad (1)$$

In this case the Mixing Norm is a useful tool to calculate the amount of mixing. The Mixing Norm, mathematically a Sobolev norm of negative index, can be described as an extension of the L2 norm incorporating information about not only the size of a function but also the size of its derivatives, allowing statements about the function's decay. The general form of a Sobolev norm for a function which is represented as a Fourier series is given as:

$$\|f\|_{H^s} = \left(\sum_{k=-\infty}^{\infty}(1 + |2\pi\, k|^2)^s\, |c_k|^2\right)^{1/2} \qquad (2)$$

Here, c_k are the Fourier coefficients with the corresponding indexes k which represent the concentration profile. Using the factor 2π transforms the wavenumber k into the circular wave number which makes the underlying physical length scale more accessible. The exponent s is the index of the Sobolev norm which is -1/2 for the Mixing Norm indicating the evaluation of the half derivation in the negative Sobolev space. In theory, this smoothing makes it possible to evaluate functions which are usually not differentiable. The use of a 2D Fast Fourier Transform algorithm allowed for easy computation of the underlying function of numerical data.

In the analysis, the Mixing Norm values were plotted against the normalized mixing length and linearized through logarithmic transformation. The absolute values of the gradients of these linear representations were then correlated with the Reynolds number and compared to the experimental results.

RESULTS

The evaluation yielded four experimental results for two mixer designs with two mixing processes, and also two simulation results. The performance map for the Dean mixer, shown in Fig. 4, includes both experimental and simulation data for ink-based and colour reaction processes. In simulations, mixing performance increased with the Reynolds number, plateauing between 110 and 300 Re, and then sharply rising above Re = 300. This correlates with the formation of additional vortex pairs in the flow pattern at higher Reynolds numbers as depicted in Fig. 5. Experimentally, the ink mixing showed a similar performance plateau and rise above 200 Re, while the colour reaction remained consistent up to 400 Re. A data inconsistency in the ink experiment around 170-200 Re was attributed to noise in the data.

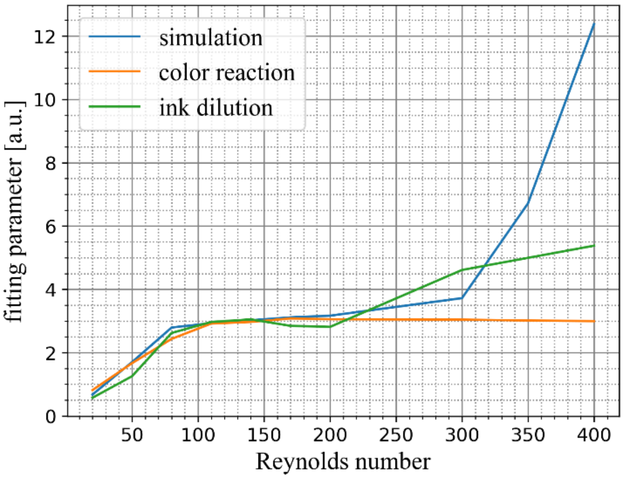

Figure 4: Mixing map for the Dean mixer showing mixing performance at different Reynolds numbers. Comparison between experiments and simulation.

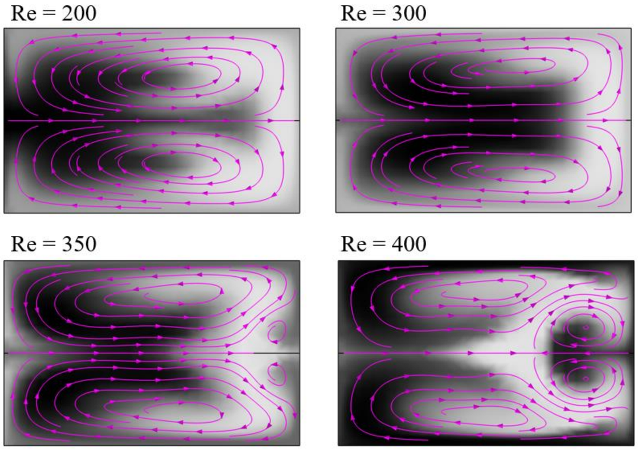

Figure 5:Secondary flow pattern of same evaluation position from Dean mixer simulations at different Reynolds numbers. Concentration profile as grey scale map with black equals high concentration and white low concentration.

As for the H-type SAR mixer, a higher noise in the experimental data made logarithmic scaling of the dispersion curves unfeasible. Therefore, the parameter a of an exponential fit with function $f(x) = e^{-a*x}$ of the measured dispersion curves was used in Fig. 6. Both experiments exhibited higher absolute values for the fitting parameter, particularly at increased mixing lengths, which were significantly higher than those in the simulation. To address this, the data was scaled to a range between zero and one. In this scaled format, both simulation data and experimental results indicated a similar increase in mixing performance with rising Reynolds numbers, except for an outlier at Re = 170 in the ink-based experiment.

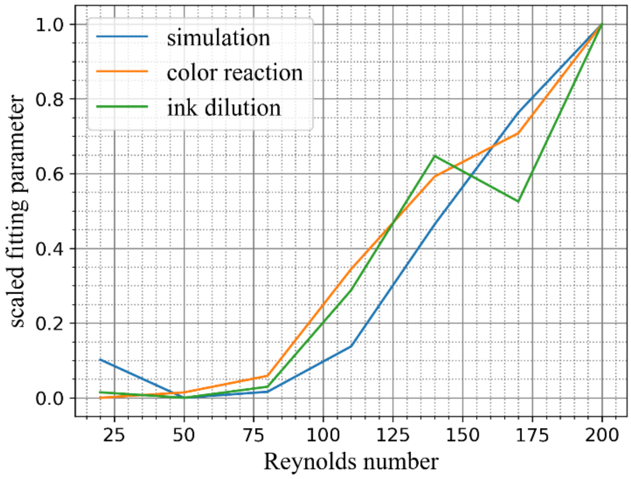

Figure 6: Mixing map for the H-type SAR mixer showing mixing performance at different Reynolds numbers. Comparison between experiments and simulation.

DISCUSSION

This study introduces a method for evaluating micromixer performance in both experimental and simulation setups, assessing mixing not just at the outlet but throughout the entire mixer geometry for a more comprehensive approach. The experiment relies on an optical evaluation scheme, tracking the change in pixel grey values and derivation of a single characteristic fitting parameter for the complete mixer at a given Reynolds number, whereas the simulations evaluate the two-dimensional cross sections along the mixer with the Mixing Norm and also lead to the same kind of parameter. It had been shown that there is a similar trend for the mixing performance in both experiments and simulations demonstrating the potential of this method for understanding and optimization of mixing structures. In the colour reaction experiment with the Dean mixer, the mixing performance plateaued at higher Reynolds numbers, possibly due to the limitation of the methodology. In instances where significant mixing occurs at the initial measurement positions, the fitting method becomes ineffective due to the loss of information in coarse resolution. Enhancing the resolution of measurement positions would be a beneficial modification to address this issue. Additionally, the H-type mixer experiments showed higher fitting parameter values than simulations, likely due to manufacturing asymmetries and artefacts causing chaotic mixing at a higher extent as in idealized simulations. Future simulations may include these asymmetries for more accurate results. Finally, the grey value evaluation method could be improved by analysing more lines or conducting area evaluations to reduce sensitivity to local noise like microbubbles and particles.

The next phase in the evaluation involves correlating mixing performance with the energy consumption required for mixing. This is crucial for assessing efficiency and comparing different mixers. Energy consumption, indicated by the pressure drop across the mixers was recorded in experiments and simulations, and will be a focus in future work.

FUNDING

The development of this work was funded by the Federal Ministry for education and research (BMBF) (funding reference 031B1124B, BioQuant project).

REFERENCES

[1] X. Hu, F. Yang, M. Guo, J. Pei, H. Zhao, Y. Wang, “Fabrication of polyimide microfluidic devices by laser ablation based additive manufacturing”, Microsystem Technologies 2020;26(5):1573–83.

[2] Shen B, Hamazaki T, Ma W, Iwata N, Hidaka S, Takahara A et al. Enhanced pool boiling of ethanol on wettability-patterned surfaces. Applied Thermal Engineering 2019;149:325–31.

[3] M. B. Okuducu and M. M. Aral, “Performance analysis and numerical evaluation of mixing in 3-d t-shape passive micromixers,” Micromachines, vol. 9, no. 5, 2018.

[4] G. Mathew, I. Mezic, and L. Petzold, “A multiscale measure for mixing”, Physica D: Nonlinear Phenomena, vol. 211, no. 1-2, pp. 23–46, 2005.

CONTACT

* O. Blaschke, Oliver.Blaschke@hs-coburg.de

POINT-OF-CARE MICROFLUIDIC CHIP FOR PROTEIN ANALYSIS USING ELECTROCHEMICAL CELLS

J. Vírostko[1], *P. Fecko*[2] *and R. Hrdý*[2]
[1] Department of Microelectronics, Brno university of Technology, Brno, Czechia
[2] Central European Institute of Technology (CEITEC), Brno university of Technology, Brno, Czechia

The ongoing project is trying to solve a complex problem of separating protein samples and subsequent scanning of electroanalytical signals in microfluidic configurations using optimized micro-electrode array (MEA). [1] We designed and fabricated a proof-of-concept microfluidic device for blood cell lysis and analysis of the cell proteins using a two-electrode configuration of four electrochemical cells (EC).

Red blood cells (erythrocytes) are suspended in a liquid medium and run through a 400 µm wide and 20 µm deep channel. The channel contains two separate chambers, one containing an array of blades 20 µm long and 1.5 µm wide, and the other chamber is utilized for the electrochemical counter-part. Blades are sized and organized to puncture and break down the cell wall to release proteins for further analysis. [2] The outline of the channel with the enlarged section of the channel blades is shown in Figure 4.

Micromachining of the silicon chip consists of two separate photolithographic and etching steps. The first photolithography transfers the channel and chamber layout, which is subsequently etched into the SiO_2 layer using reactive ion etching with fluorine chemistry RIE-F to create a hard mask for later etching. The second photolithography involves transferring the layout for through-silicon inlets and outlets using thick photoresist (PR) film. Through-silicon holes are etched using the Bosh process of deep reactive ion etching (DRIE). As a last step, the SiO_2 hard mask is etched to a depth of 20 µm. The wafer was cleaned and diced into 30 x10 mm^2 chips, seen in Figure 3 on the left.

Fabrication of the electrochemical counter-piece is divided into five main photolithographic steps. First, a metallic tri-layer of Titanium, Copper and Platinum is shaped using a lift-off on a negative PR layer. To cover the tri-layer, a SiO_2 layer is grown and shaped to cover all but the electrodes and contact pads. The soldering properties of platinum pads are not optimal; therefore, gold is evaporated and lifted off on the pads. Afterwards, a thin Parylene C layer is grown and etched to open electrodes and pads. The last step consists of magnetron sputtering of a carbon-boron composite on the working electrode (WE) shaped by lift-off. The Pyrex glass substrate was then diced using a dicing saw, and the result can be seen in Figure 3 on the right.

The final part of the lab-on-a-chip (LoC) chip is to bond the previous two pieces together using the softening of Parylene C. The surfaces of the silicon microfluidic chip and the Parylene-C-coated Pyrex slides were treated with O_2 plasma to activate the surfaces. Then, the silicon chip was placed onto a hotplate set to 230°C, and the Pyrex slide (with electrodes facing down) was aligned with the silicon chip and pressed with a Teflon roller to achieve optimal bonding strength. Refer to Figure 5 for the complete chip.

The next development step will be separating intracellular particles using deterministic lateral displacement (DLD). DLD uses asymmetric branching of laminar flow using micro-posts. The periodicity of the displaced array of posts is denoted by N, and the flow (which direction is determined by the sidewall) between two adjacent posts is split into N streams. The width of the fluid stream close to the post near the channel bottom wall can be expressed roughly by

$$\beta = \sqrt{\frac{N}{3}} \cdot \frac{d}{N}, \tag{1}$$

where d is the diameter of the post. [3] The critical diameter of the particle that can be sorted by DLD is $D_c = 2\beta$ and if the diameter of a particle is less than this value, it will flow in a zig-zag pattern to the top wall of the separator channel.

Word Count: 589

REFERENCES

[1] R. Hrdý, H. Kynclová, I. Klepáčová, M. Bartošík, and P. Neužil, ”Portable Lock-in Amplifier-Based Electrochemical Method to Measure an Array of 64 Sensors for Point-of-Care Applications,” Anal. Chem., vol. 89, no. 17, pp. 8731–8737, Sep. 2017, doi: 10.1021/acs.analchem.7b00776.

[2] L. Nan, Z. Jiang, and X. Wei, “Emerging microfluidic devices for cell lysis: a review,” Lab on a Chip, vol. 14, no. 6, pp. 1060–1073, 2014, doi: 10.1039/C3LC51133B.

[3] P. Sajeesh and A. K. Sen, ”Particle separation and sorting in microfluidic devices: a review,” Microfluid Nanofluid, vol. 17, no. 1, pp. 1–52, Jul. 2014, doi: 10.1007/s10404-013-1291-9.

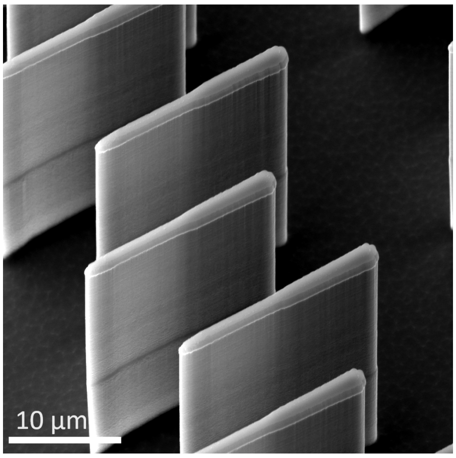

Figure 1: A scanning electron microscopy (SEM) image close-up of lysis blades in the microfluidic channel etched using DRIE.

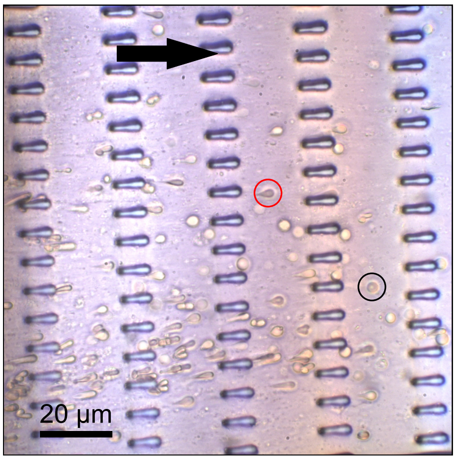

Figure 2: Performance of silicon blades in the lysis chamber with an inflow of cell medium. The black arrow shows the flow direction. A ruptured cell is circled in red, and an undamaged cell is circled in black.

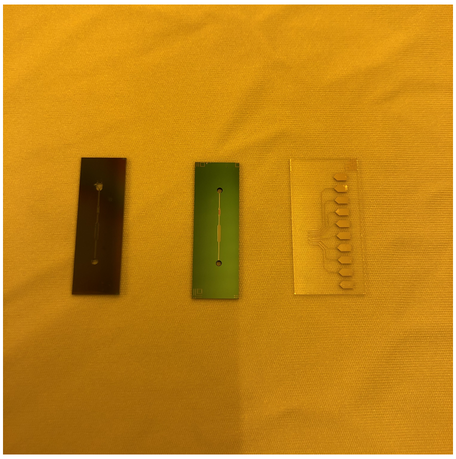

Figure 3: Diced chips (microfluidic part -left and middle, EC part - right) after complete fabrication ready for bonding.

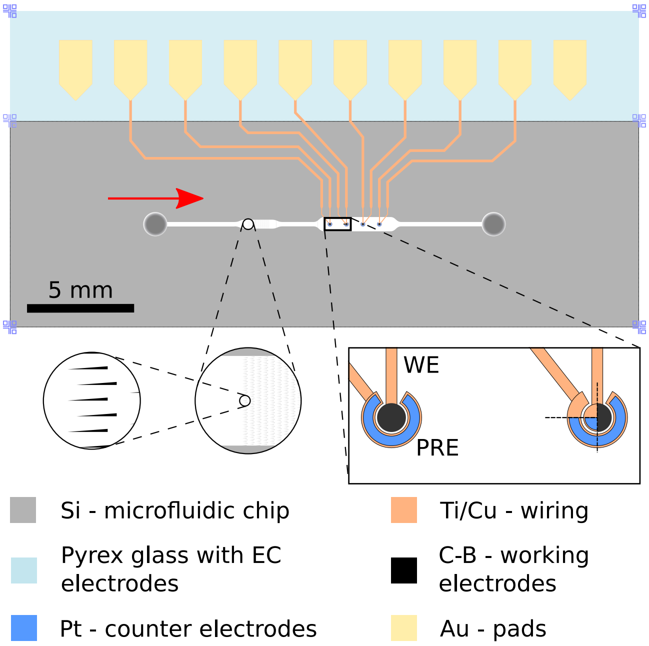

Figure 4: This layout shows a top view of a completed microfluidic chip. The widths of the lysis chamber and the reactor chamber are 400 µm and 650 µm, respectively. The red arrow marks the flow direction. The inlet and the outlet are through silicon vias so that the chip can be connected to capillaries from the bottom side. The lysis chamber is enlarged to show the detailed arrangement of the slicing blades. The electrodes in the reactor chamber are also shown in detail; the diameter of the working electrode (WE) is 105 µm, and the inner and outer diameters of the pseudo-reference electrode (PRE) are 120 µm and 220 µm, respectively.

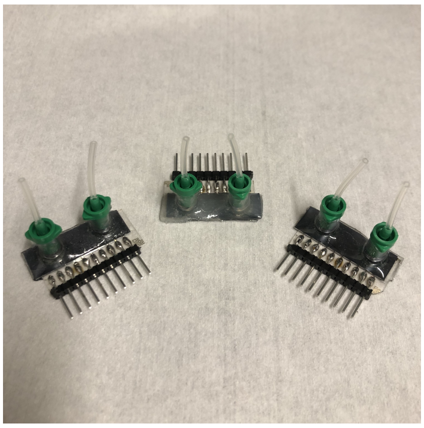

Figure 5: The two parts (left and middle in Figure 3) are bonded into a single chip.

A MULTI-PARAMETER MEASUREMENT SYSTEM FOR MEMS ANEMOMETERS FOR DATA COLLECTION WITH MACHINE LEARNING OUTCOMES

T. L. Hackett, D. Alveringh, R. G. P. Sanders, T. E. van den Berg, J. Schmitz
MESA+ Institute, University of Twente, Enschede, The Netherlands

ABSTRACT - In order to generate consistent and comprehensive datasets for the application of machine learning algorithms to MEMS thermal flow sensors, a measurement set up was created. This system allows automatic data collection of large datasets involving parameters such as the angle of attack, humidity, temperature and flow speed. The electrical output signals in both the time and frequency domain can be measured for both AC and DC actuation. The setup has been able to fully characterize an anemometer by exposing it to flows of 0 to 5 m/s in steps of 0.02 m/s under angles from -45 to 45° in steps of 5° at a constant temperature of 25 °C and humidity of 30 %RH and complete the measurement in 8 hours.

Key Words – MEMS, Machine Learning, thermal, anemometer, microfluidics, flow sensor.

INTRODUCTION

The measurement of flow through the use of MEMS thermal anemometers is a well-established field [1]. Thermal anemometers measure the heat transfer rate from a heat source to a fluid as a measure of the flow rate. Provided the fluid is cooler than the heat source, heat flux increases with higher flows. A hot-wire anemometer is perhaps the simplest example of this type of device. Another family of thermal sensors uses at least one sensing element placed downstream from the heat source to measure the heat transfer from the heater, through the fluid, and back to the sensing element. These types of sensors are known as calorimetric anemometers [1].

Superficially both types of sensors are simple, however there are many physical principles that make determining the flow velocity from sensor data more complicated. Some of these complicating factors include thermal inefficiencies such as heat flux into the mechanical scaffolding of the heater, temperature variations of the fluid, or changes in gas composition which leads to different thermal diffusivities and heat capacities [2]. There might also be heat leaking into the sensing elements through other means or condensation on the sensing element surface if there is a condensable gas present.

It is often the case that these practical complications are circumvented by measuring the device response to changing flow experimentally and calculating a calibration curve in very specific conditions such as at room temperature, low humidity and perpendicular flow conditions [3]. Though this is not necessarily a bad practice it does limit the scope of the device. On the other hand it is also nigh impossible to make a fully comprehensive theoretical model from which to develop a set of equations which perfectly model the device.

To relate sensor signals to specific flow speeds in varied conditions one could train a machine learning (ML) model. This has indeed been done before, and has shown to be better at characterizing measurements than traditional calibration curves [4].

To be able to train a ML model well, a common approach is to provide a complete and comprehensive learning and test set for all the conditions in which the device should be able to measure accurately. The larger and more complete the learning set, the more accurate the models tend to be. In order for it to be a comprehensive dataset many combinations of different physical conditions should be applied to the sensor.

This work aims to make the collection of such a large dataset in the context of applying ML to thermal MEMS anemometers more achievable for research labs. Testing time in commercial wind tunnels can be expensive and limited, meaning that a smaller lab-based system should be produced. A small wind tunnel has the added benefit of being highly customizable and able to apply more physical conditions than a commercial one.

This system has several important requirements. It should be highly automated in order to prevent excessive time use for the researchers and eliminate user error. It should also be able to provide consistent conditions including ambient temperature and humidity as well as constant heater temperatures or powers.

Additionally the system should also be able to apply different independent variables, which for these types of sensors would be the magnitude (0-2.3 ms^{-1}) [5] and angle of attack (AoA) (±45°) of the flow velocity. Some of the control variables could also become independent variables for multi-parameter devices including the ambient temperature and humidity as well as the gas composition.

The system should be able to simultaneously measure as many dependent and independent variables as possible for each datapoint. It should also be able to resolve different sensor signals in the time and frequency domains as additional information could be stored in either domain.

MACHINE LEARNING BENEFITS

There are several types of devices that can have ML applied to them in order to provide more accurate measurement results, as well as testing and characterizing multi-parameter chips.

Improved Accuracy

Machine Learning has shown to improve measurement accuracy for MEMS thermal anemometers already. In a paper by J. Amaral *et al.* K-nearest neighbor regression (KNNR) was able to reduce the maximum error from 20.4% to 1.7%, while measuring water flow with a central heater and thermocouple measuring elements [4].

This approach could also be applied to non-thermocouple based thermal flow the sensor presented in Alveringh *et al.* where resistors are used as the measuring elements has previously been measured in a similar set-up [6].

Multiple parameters

Devices like the one presented in Azadi *et al.* would benefit from using a measurement system capable of providing varied conditions as humidity, gas composition and temperature can have negative effects on the accuracy of results [7]. The gas independent sensor presented in the work would be easily characterized in the system.

Sensors that have structures to decrease their dependence on external conditions as well as devices without these additions could potentially reveal information about the external conditions with the aid of a properly trained model, which indeed requires a larger data set than a single variable model due to the increased complexity.

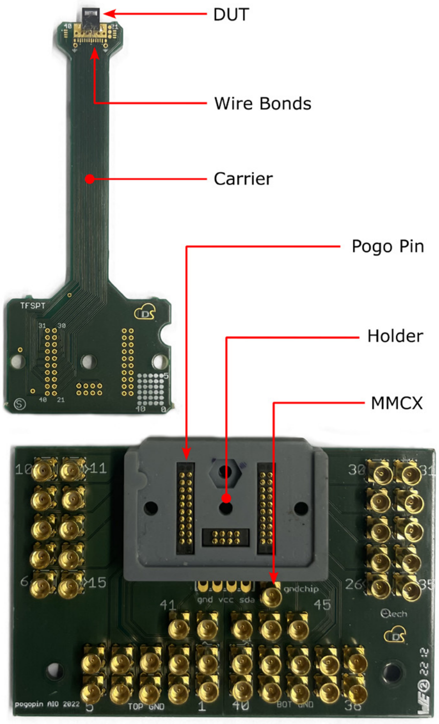

Figure 1: The carrier and holder PCBs used to place the DUT in the stream of the wind tunnel.

MEASUREMENT SYSTEM

The device under test (DUT) is held near the center of the wind tunnel using a custom built PCB which allows for the DUT to stick out 5 cm from the side wall through an elongated carrier PCB shown in Figure 1.

The DUT can be interfaced through the use of wire bonds from the DUT to the carrier PCB. The carrier PCB is affixed to the holder PCB using a 3D printed mounting system, which uses some screws to press the carrier to the holder's pogo pin connectors. These then connect through to MMCX connectors allowing the DUT to interface with the electronics outside of the climate cabinet.

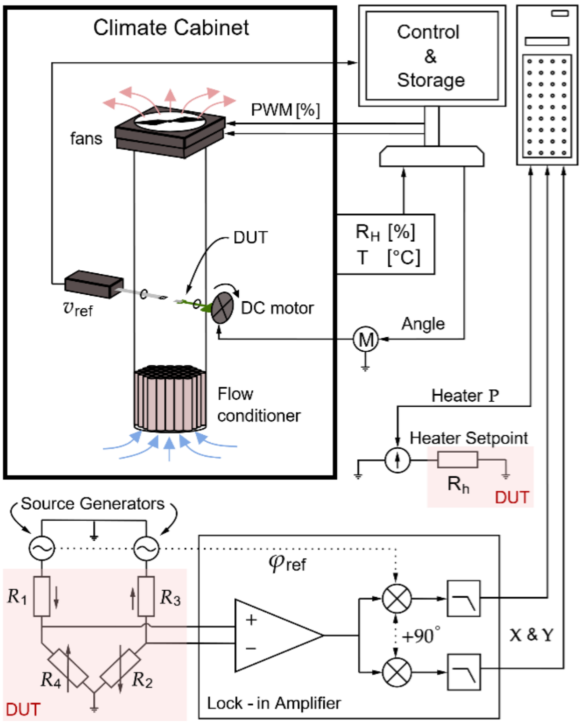

Figure 2: A schematic of the measurement system in the case of a calorimetric anemometer with a Wheatstone bridge readout.

The holder is mounted on a DC servo motor (Newport M-495 ACC) which using its controller (Newport ESP 300) is able to rotate the holder, carrier and DUT within a precision of 0.001°. The MMCX connections to the holder PCB can be put under strain when the DC motor rotates the DUT more than 45°, in order to prevent this the cables were affixed to the rotating portion of the set-up with ample of leeway.

The wind tunnel itself is a 1.5 m long PMMA tube with an inner diameter of 114.5 mm. The bottom of the wind tunnel has a flow conditioner and a dust filter to make sure that the incoming velocity profile is flatter and free of any debris that could damage the DUT. The flow conditioner consists of 292 parallel tubes, 10 cm in length with an inner diameter of 5.55 mm and outer diameter of 5.95 mm.

At the other end of the wind tunnel are two pulse-width modulated (PWM) fans that draw air through the wind tunnel. The first fan (Scythe SU1225FD12MR-RHP) is able to provide a lower range of flow speeds between 0.02 and 0.4 m s^{-1} while the second fan (Delta Electronics PFR1212UHE-SP0) can provide higher flow speeds of 0.4 to 5 m s^{-1}. Both fans are controlled via an Arduino UNO from the LabVIEW program.

To measure the reference flow velocity at the DUT a reference flow meter is placed symmetrically opposite the DUT through a small hole in the wind tunnel (Voltcraft PL-135HAN) around 2 cm away from the DUT.

An seal is required at the point of entry of the carrier PCB and the reference sensor into the wind tunnel to minimize air leakage. The noise in the reference flow measurement decreases significantly when no flow enters the wind tunnel from the side. Additionally the flow velocity range within the tube at the measurement height increases when the seal is made better, as higher flow speeds can be achieved.

The entire wind tunnel is placed within a climate controlled cabinet (ESP PRC 1200 WL) which is able to vary the temperature and humidity effectively in the ranges of 10-50 °C and 20-80 %RH. These values are measured using a reference sensor (Dracal USB-PTH-450) placed in the cabinet.

Though the DUT can vary the holder has many possible MMCX connectors that allow for multiple electronic configurations to be tested. As an example Figure 2 shows a DUT consisting of 4 measuring resistors placed in a Wheatstone bridge and one heating resistor.

The system has two in phase signal generators (Agilent 33220A) that allow for any fabrication related asymmetries in the bridge to be compensated. In case of DC measurement these can also be set as DC voltage sources. The bridge is measured using a lock-in amplifier (Stanford Research Systems SR830) locked into to the phase of the source generators. The X, Y, R and θ of the lock-in amplifier are recorded in the LabVIEW program.

The heating resistor is powered by a source measurement unit (Keithley 2400) which can be run in two modes using the LabView program. Constant power, which can sweep a given set of powers, or constant temperature, which works to keep the temperature of the heating element constant.

The LabVIEW program is able to automatically record and sweep over the flow velocity (v), AoA (θ), heating power supplied (P), while measuring the lock-in's in phase (X), quadrature (Y), amplitude (R), and phase (φ), the heater's volage (V) and current (I), and the climate cabinets temperature (T) and humidity (%RH). All of the variables above are recorded as one data entry in a CSV file for easy post processing, while being shown live during the experiment.

Simulation

The flow velocity profile in the wind tunnel must be as flat as possible to allow for reproducible measurements. This is because small variations in the flow velocity profile could result in incongruent results due to small misalignments within the wind tunnel. This can be simulated for by using COMSOL Multiphysics®.

The expected flow speeds induced by the dual fans is around 0.04 to 4 m s^{-1} and with the inner diameter of the wind tunnel being 114.5 mm the Reynolds number is given by the equation below [8]:

$$\mathrm{Re} = \frac{uL}{\nu}$$

Where u is the flow velocity, L is the tube diameter and ν is the kinematic viscosity. The resulting Reynolds number is between 310 and 31,000 assuming a kinematic viscosity of 1.83E-5 m s^{-2} at room temperature, meaning that the flow regime spans from laminar to turbulent [9].

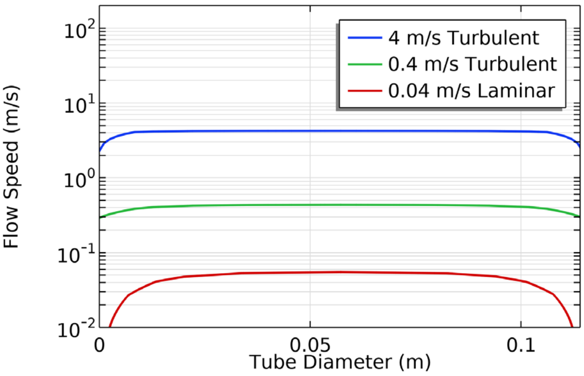

Figure 3: Simulated velocity profiles within the laminar and turbulent flow physics modules.

Turbulent flow velocity profiles tend to be quite flat, while laminar flow profiles are parabolic [10]. This is confirmed by the simulation results shown in Figure 3. The COMSOL Multiphysics® laminar flow module was used for flows with $Re < 1000$ while the turbulent flow module was used for flows with $Re > 1000$.

The inlet of the wind tunnel is given a flat flow profile boundary condition due to the flow conditioner. Figure 3 shows the flow velocity profiles at 50 cm from the flow conditioners given by the laminar flow physics module in COMSOL Multiphysics®.

The central 6 centimeters of the flow velocity profile vary by about 1% for flows of 0.4 m s^{-1}. This allows for some tolerance with regards to the placement of the DUT in the wind tunnel without loss of accuracy.

Measurement Protocol

The most efficient order of measurement is to first vary the flow speed, followed by the angle, temperature, and finally humidity, since the latter variables require a longer time to adjust compared to the flow rate.

Due to the length of the wind tunnel it takes time for the flow velocity of a PWM set point to be achieved. This takes longest (60 s) when doing a zero flow measurement as it can take up to a minute before the flow is fully stopped. Therefore it is good to include a stability control script, which can start a measurement while the reference flow is consistently within a range of ±0.01 m/s from the last 20 measurement values.

A further stability control script can be used for any heating elements in the sensor. This is because the element must also compensate for heat flow away from the chip into the PCB. Furthermore using a proportional integral control for the heater set point is recommended in order to maintain consistent heating conditions.

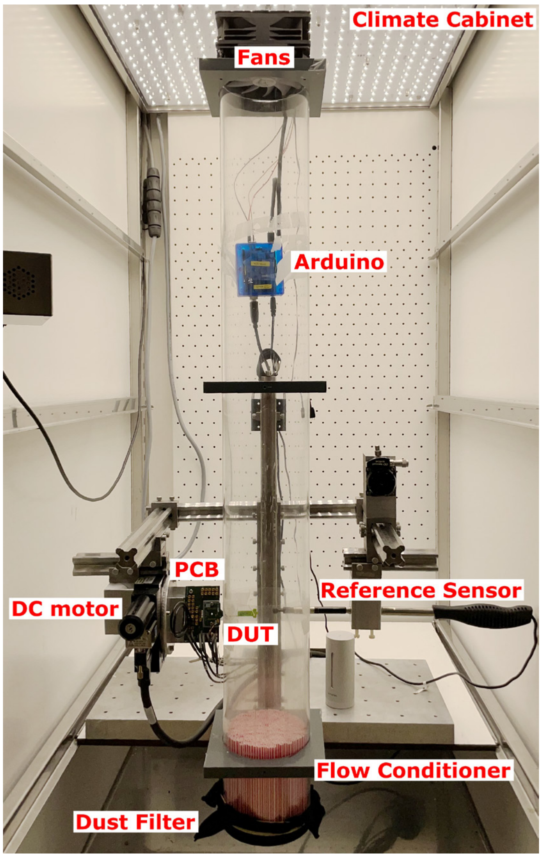

Figure 4:The system as placed within the climate cabinet, with a the DUT placed within the wind tunnel.

Integrating these stability arrays and PI controllers into the same program used for data collection allows for more control over the experiment including the step sizes for each variable as well as the amount of measurements per specific condition.

RESULTS

The measurement system was built and run in the climate cabinet as shown in Figure 4. The system is able to produce very large datasets without supervision. A continuous measurement of 24 hours can be run without issue. A typical measurement takes around 12 hours and will yield a large enough dataset for ML purposes.

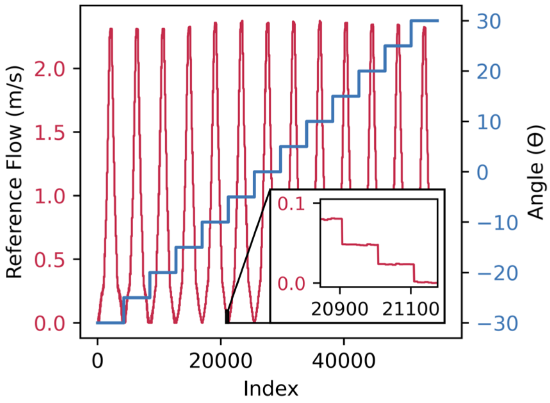

Figure 5: Data from a test run taking 8 hours.

As shown in Figure 5, a measurement at one temperature and humidity set point with 13 individual angles and 5% changes in PWM with 100 measurements per condition would yield 54,600 datapoints. If this was also done for 5 humidities and 5 temperatures this number reaches above the 1.3 million. The chips presented in Azadi *et al.* [7] and chips similar to the one presented in Alveringh *et al* [6] were successfully measured in the wind tunnel, providing a dataset over 10 million datapoints for future ML research and publication.

CONCLUSION

The system provides reliable and automated datasets with high controllability of physical conditions. An anemometer was automatically measured over a range of flows (0 – 5 $\mathrm{ms^{-1}}$) over 90° of AoAs and in several humidities (30-80 %RH) at a controlled temperature (20 °C). Different types of hot wire and calorimetric sensors have been tested in it automatically each with large datasets containing more than 1 million datapoints. These large datasets allow for the next step in the development of these devices as there is plenty of data for both learning and testing sets for all devices. Both single and multiple parameter chips can also be characterized for non ML purposes as an added benefit.

REFERENCES

[1] Kuo, J.T.W.; Yu, L.; Meng, E. *Micromachines* **2012**, *3*, 550-573.

[2] Khamshah, N.; Abdalla, A. N.; Koh, S.; Rashag, H.F. *Int. J. Phys. Sci.* **2011,** 6, 3270-3327.

[3] Motallebi, F. *Prog. Aerosp Sci.*, **1994,** 30, 267-294.

[4] Amaral, J.; Silva, J. R. C.; de Andrade, D. S. M.; Ferreira, L. T. ; Quirino, T. M.; Quirino, J. *INSCIT*, Sao Paulo, Brazil, **2019**, 1-6.

[5] Nguyen, N.T. *Flow Meas. Instr.*, **1997**, 8, 7-16.

[6] Alveringh, D.; Bijsterveld, D.G.; van den Berg, T.E.; Veltkamp, H-W.; Batenburg, K.M.; Sanders, R. G.P.; Lötters, J. C.; Wiegerink, R.J. *2022 IEEE Sensors*, Dallas, TX, USA, **2022**, 1-4.

[7] S. A. Kenari; R. J. Wiegerink; R. G. P. Sanders; J. C. Lotters *MEMS 2023*, Munich, Germany, **2023**, 767-770.

[8] LaNasa, P. J., Loy Upp, E. *Fluid Flow Measurement*, 3rd Edition; Butterworth-Heinemann: 2014; pp. 19-29.

[9] Bond, W. N. *Proc. Phys. Soc.,* **1937**, 49, 205-213.

[10] *DOE Fundamentals Handbook Thermodynamics, Heat Transfer, and Fluid Flow*, 3rd Edition; US Department of Energy: Washington, D.C., USA, 1992; pp. 18.

CONTACT

Thomas Hackett
t.hackett@utwente.nl

DEEP LEARNING BASED MICROFLUIDIC SENSING DEVICE FOR VISCOSITY MEASUREMENT

Muneeb Ullah[1], *Xiaodong Yang* [1], *Nan Zhao* [1], *Shihan Dai* [1]
[1] School of Electronic Engineering, Xidian University, Xi’an, Shaanxi, China, 710071.

Abstract: Microfluidic sensing device that integrates in fluid-structure interactions with advanced machine learning (ML) and deep learning (DL) techniques to determine the viscosity of Newtonian fluids. The device's core innovation lies in its utilization of micro sensor deflection analysis, prompted by fluid flow within a micro channel. This paper focusing on glycerol/water solutions as representative Newtonian fluids, the study spans a viscosity range of 5–100 centipoises (cP) and examines fluid flow at rates between 15–105 mL/h (γ = 60.5–398.4 s^(-1)), using sample volumes from 80–400 μL.A pivotal aspect of our research is the application of Artificial Neural Networks (ANNs) and Convolutional Neural Networks (CNNs) to process and analyze micro sensor deflection data derived from video footage. In addition, the novelty of this research is indicated by video-based deflection data for viscosity measurement. These study findings are significant, with ANNs achieving an overall average accuracy of 90% and CNNs excelling with a remarkable 98% accuracy in classifying the viscosity of Newtonian fluids. It demonstrates the feasibility of using ML and DL models for precise, real-time viscosity measurements. The ANNs and CNNs in interpreting deflection data from video analysis represent a major advancement in fluid dynamics research, offering a novel and efficient approach for viscosity measurement in various scientific and industrial applications.

Introduction: Dynamic viscosity, central to understanding the behavior of fluids under stress, is intricately linked to numerous scientific and industrial applications. This resistance to flow, pivotal in fluid mechanics, chemical engineering, biomedical sciences, and environmental studies, influences a broad spectrum of processes, from the design of intricate transportation systems to the delicate balance required in pharmaceutical formulations [1, 5]. Research discussed the dynamic viscosity in depth and investigate its role in fluid dynamics in-depth look at dynamic viscosity, delving into its critical role in fluid dynamics. This study investigates the primary measurement techniques used for the quantification e.g., capillary viscometers and rotational viscometers, also based on the solid physical principles, offer a window into understanding their complex property. Furthermore, this research categorizes dynamic viscosity into various types e.g., Newtonian fluids, non-Newtonian fluids, and complex fluids, each characterized by distinct responses under shear stress, such categorization is necessary for customized fluid handling process across different industries. This classification, encompassing Newtonian fluids, non-Newtonian fluids, and complex fluids, is indispensable for tailoring fluid handling processes across different industries. To investigate the difference between these fluids are equally important for practitioners and researchers, there are variety of challenges and applications for each category which come across on daily basis. [12, 13].

This research draws on a wealth of scholarly sources and empirical data, aiming to bridge the gap between theoretical understanding and practical applications of dynamic viscosity by examining real-world examples and case studies [14, 17].In the landscape of viscosity measurement, traditional methods like capillary and rotational viscometer have long stood as pillars in both research and industry. Capillary viscometer, depends on the time it takes for a fluid to flow through a narrow tube under gravity or controlled pressure, that is particularly suited for Newtonian fluids. On the contrasy Rotational viscometer, make use of rotating spindle to measure the torque required to maintain a constant angular velocity, accommodate both Newtonian and non-Newtonian fluids [18,22]. The traditional techniques, with innovative methods to measure viscosity in efficient and economical ways. The advent of portable and handheld viscometers, for instance, has revolutionized viscosity measurement. The Utilization of principles eg., vibration, ultrasonic, or microfluidics, these devices provide rapid, on-site viscosity assessments without the need for extensive laboratory setups [23, 27]

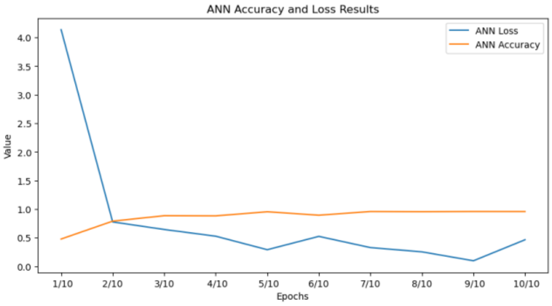

Figure 3, ANN's evolving performance in viscosity classification across the epochs

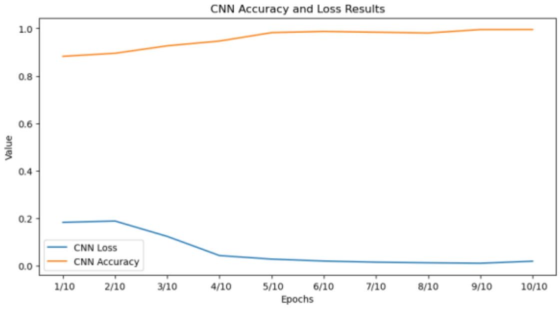

Figure 4 graphically represents the CNN's

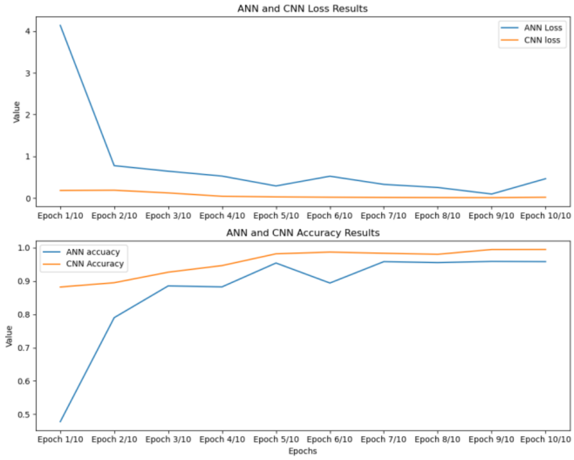

Figure 5: representing the accuracy and Loss of both models.

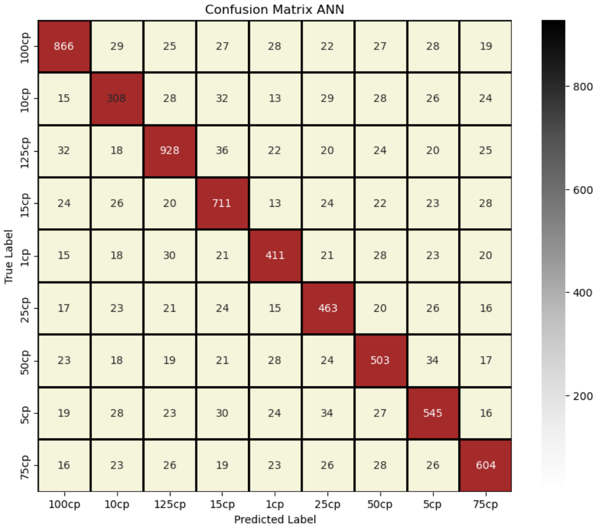

	100cp	10cp	125cp	15cp	1cp	25cp	50cp	5cp	75cp
100cp	866	29	25	27	28	22	27	28	19
10cp	15	308	28	32	13	29	28	26	24
125cp	32	18	928	36	22	20	24	20	25
15cp	24	26	20	711	13	24	22	23	28
1cp	15	18	30	21	411	21	28	23	20
25cp	17	23	21	24	15	463	20	26	16
50cp	23	18	19	21	28	24	503	34	17
5cp	19	28	23	30	24	34	27	545	16
75cp	16	23	26	19	23	26	28	26	604

Figure 6: ANN model confusion matrix.

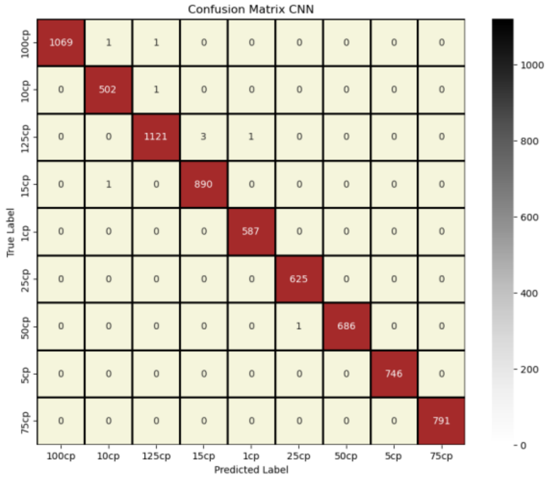

	100cp	10cp	125cp	15cp	1cp	25cp	50cp	5cp	75cp
100cp	1069	1	1	0	0	0	0	0	0
10cp	0	502	1	0	0	0	0	0	0
125cp	0	0	1121	3	1	0	0	0	0
15cp	0	1	0	890	0	0	0	0	0
1cp	0	0	0	0	587	0	0	0	0
25cp	0	0	0	0	0	625	0	0	0
50cp	0	0	0	0	0	1	686	0	0
5cp	0	0	0	0	0	0	0	746	0
75cp	0	0	0	0	0	0	0	0	791

Figure 7: ANN model confusion matrix.

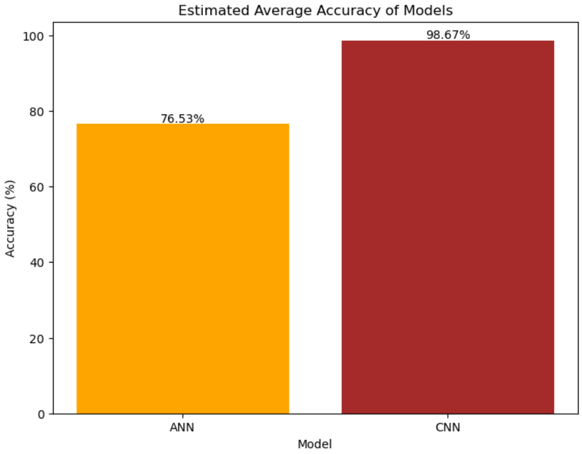

Figure 8, CNN And ANN model over all avvuracy representation.

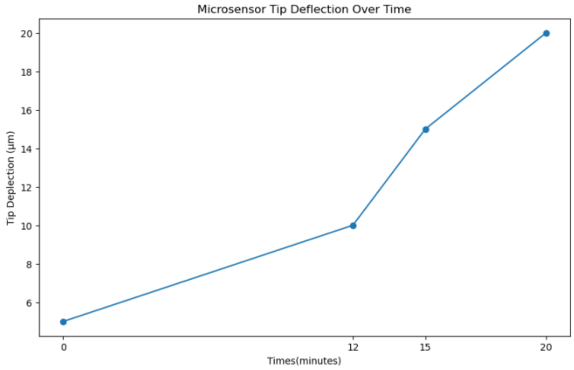

Figure 9: micro deflection over time

REFERENCES

1. Munson, B. R., Young, D. F., Okiishi, T. H., & Huebsch, W. W. (2006). Fundamentals of Fluid Mechanics, John Wiley & Sons. *Inc., USA*.

2. Bird, R. B., Stewart, W. E., & Lightfoot, E. N. (2007). Transport Phenomena, 2nd Edn. New York, NY: John Wilwe & Sons.

3. Batchelor, G. K. (1967). An introduction to fluid dynamics. Cambridge university press.

4. White, F. M. (2016). Fluid Mechanics 7th Edition in SI units.

5. Barnes, H. A. (2000). *A handbook of elementary rheology*. University of Wales, Institute of Non-Newtonian Fluid Mechanics..

6. Macosko, C. W. (1994). Rheology principles. *Measurements and Applications*.

7. Barnes, H. A., Hutton, J. F., & Walters, K. (1989). *An introduction to rheology* (Vol. 3). Elsevier.

8. Mezger, T. (2020). *The rheology handbook: for users of rotational and oscillatory rheometers*. European Coatings..

9. WALTERS, Kenneth. Rheometry, industrial applications. *(No Title)*, 1980..

10. Tadros, T. F. (2011). *Rheology of dispersions: principles and applications*. John Wiley & Sons..

11. Steffe, J. F. (1996). *Rheological methods in food process engineering*. Freeman press..

12 . Larson, R. G. (1999). "The Structure and Rheology of Complex Fluids." Oxford University Press.

13. Dealy, J. M., & Larson, R. G. (2006). Molecular structure and rheology of molten polymers. *Hanser, Munich*..

14. Holman, J. P. (1966). Experimental methods for engineers.

15. Gunstone, F. D. (2001). *Minor oils, specialty oils, and super-refined oils* (pp. 185-208). Marcel Dekker, New York..

16. Steffe, J. F. (1996). *Rheological methods in food process engineering*. Freeman press..

17. McKenna, B. M., & Lyng, J. G. (2001). Rheological measurements of foods. In *Instrumentation and sensors for the food industry* (pp. 425-452). Woodhead Publishing, Cambridge, UK..

18. Jayamohan, H., Romanov, V., Li, H., Son, J., Samuel, R., Nelson, J., & Gale, B. K. (2017). Advances in microfluidics and lab-on-a-chip technologies. *Molecular Diagnostics*, 197-217..

19. Abdallah, A., Heinisch, M., & Jakoby, B. (2012). Viscosity measurement cell utilizing electrodynamic-acoustic resonator sensors: Design considerations and issues. *Procedia Engineering*, *47*, 160-164..

20. Nguyen, N. T., Wereley, S. T., & Shaegh, S. A. M. (2006). Fundamentals and applications of microfluidics, Artech House. *Inc.: Boston, MA, USA*..

21. Benninger, R. K., Hofmann, O., McGinty, J., Requejo-Isidro, J., Munro, I., Neil, M. A., ... & French, P. M. (2005). Time-resolved fluorescence imaging of solvent interactions in microfluidic devices. *Optics express*, *13*(16), 6275-6285.

22. Anderson, A. M., Bruno, B. A., & Smith, L. S. (2014). Viscosity measurement. *A A*, *2*(t3), 809..

23. Nguyen, N. T., & Wereley, S. T. (2006). Fundamentals and Applications of Microfluidics 2nd edn (Boston, MA: Artech House)..

24. Whitesides, G. M. (2006). The origins and the future of microfluidics. *nature*, *442*(7101), 368-373..

25. Tabeling, P. (2023). *Introduction to microfluidics*. Oxford university press..

26. Squires, T. M., & Quake, S. R. (2005). Microfluidics: Fluid physics at the nanoliter scale. *Reviews of modern physics*, *77*(3), 977..

27. Stone, H. A., Stroock, A. D., & Ajdari, A. (2004). Engineering flows in small devices: microfluidics toward a lab-on-a-chip. *Annu. Rev. Fluid Mech.*, *36*, 381-411.

TOWARDS HYBRID PRINTING OF INTELLIGENT DEVICES: CONDUCTIVE TRACES FROM BULK METAL FOR DIGITAL SIGNALS

Z. Khan[1,2]*, A. Saphala*[3]*, D. Straubinger*[1]*, S. Kartmann*[1,2]*, P. Koltay*[2,4]*, R. Zengerle*[1,2]*, O. Amft*[1,3]*,*
and Z. Shu[1,2]
[1] Hahn-Schickard, Georges-Koehler-Allee 103, 79110 Freiburg, Germany;
[2] Laboratory for MEMS Applications, IMTEK - Department of Microsystems Engineering, University of Freiburg, Georges-Koehler-Allee 103, D-79110 Freiburg, Germany;
[3] Intelligent Embedded Systems Lab., Dept. of Computer Science, Freiburg, Germany;
[4]Actome GmbH, Georges-Köhler-Allee 103, D-79110 Freiburg.

ABSTRACT

Multi-material additive manufacturing (MMAM) has unlocked new opportunities for producing intricate, tailor-made 3D devices while enabling the potential electronics integration to develop intelligent devices. Applying MMAM, conductive traces are formed on polymer substrates for digital signals using bulk molten metal microdroplets. Single traces at (240 ± 12) µm trace width, and length 90 mm, show minimum printing resolution of (281 ± 15) µm. For digital signal transmission, interference between adjacent single traces (crosstalk) is investigated up to 1 MHz frequency; along with reliability and robustness test against thermal shock showing 4.1% change in trace width.

KEYWORDS

Digital signals, microdroplets, additive manufacturing, bulk metal

INTRODUCTION

The utilization of 3D printing in electronic applications has been a subject of ongoing research [1]. MMAM has proven to be an efficient tool through its rapid and geometrically-intricate capabilities to produce smart structures and robust embedded systems [1, 2]. It is particularly attractive for applications like biomedical devices [3] and environmental monitoring [4]. MMAM allows us to customize device design, embed electronics, and provide interconnections all in one place to simplify supply chains and manufacturing processes[1]. In this direction, MMAM can provide neat solutions to eliminate traditional circuit boards and reduce the chemical waste biased fabrication methodologies [5].

To date various MMAM techniques have been explored, including methods like jetting and microdispensing of conductive inks, as well as integrating wires and connectors within the 3D printed substrates [2, 3]. However, they suffer from irregular shape fidelity and poor electrical performance from solution-based conductive ink traces [6], or deposition reliability in molten metal deposition approaches [7]. A recent study demonstrated MMAM for digital signal transmission [1]. However, the conductive traces showed failure when subjected to thermal characterization.

In order to mitigate the issues of poor conductance, deposition accuracy, robustness, and demonstrate the potential for digital signal transmission, we introduce a novel approach to MMAM by combining polymer dielectric substrates with bulk metal conductive traces. We investigate the minimum printable pitch (MPP) on our printing platform along with an analysis on its dimensional accuracy. Next, we evaluate the influence of crosstalk, if any, at different frequencies. Furthermore, we assessed the effect of thermal shock on the printed electrical traces.

MATERIAL AND METHOD

Hybrid printing platform

MMAM of bulk metal and polymer for 3D electronics is a novel printed electronics method, manifested on an in-house hybrid printing platform, see Fig. 1. The hybrid printer consists of two printheads, polymer printhead and metal printhead.

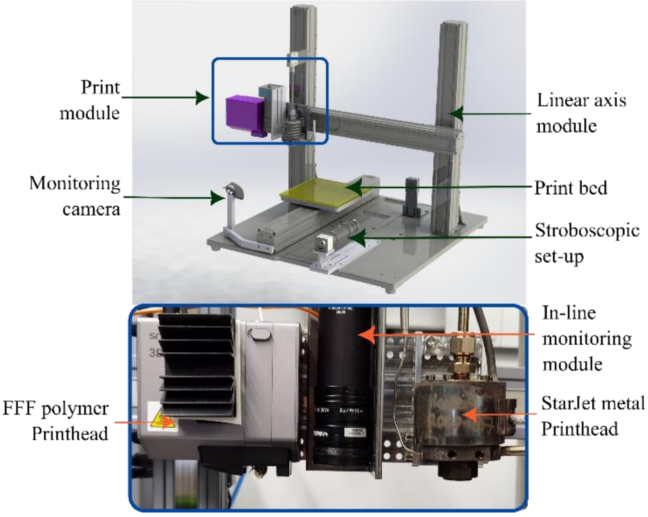

Figure 1: A) Schematic of our hybrid printing platform and B) Photo of the print module containing the two printheads.

Polymer printhead works on the extrusion principle to deposit molten filament in a layer-by-layer sequential manner on the print bed. The metal printhead works on the principle of pneumatic actuation of molten metal through a small orifice. This printhead, also referred to as the StarJet printhead from here on, was developed at the University of Freiburg[8]. The StarJet printhead is used to print molten metal microdroplets to form electrically conductive traces. Sequential printing of the two printheads to generate layer-by-layer 3D electronics was made possible by hardware, electronic, and software integration [9].

Materials and print parameters

Polyethylene Terephthalate Glycol Copolymer (PETG) (purchased from Prusa Polymers a.s., Prague, Czech Republic), filament are used to print the polymer substrate. Molten metal microdroplets are printed from flux-free solder SAC305 (Sn96.5Ag3Cu0.5) (purchased from STANNOL, Germany). The polymer filament was stored at room temperature. The filaments did not undergo any active or passive drying processes. There was no heated printing chamber for polymer printing.

The printhead parameters used during this work are stated in Table 1.

Table 1: Printhead parameters

StarJet parameters	Value	FFF parameters	Value
Reservoir temperature	320 °C	Polymer road width	450 µm
Orifice diameter	183 µm	Nozzle diameter	400 µm

Sample preparation and fabrication

A general flow for hybrid sample preparation is described in previous work [9]. Samples were prepared with substrate thickness of 600 µm and length of metal traces of 90 mm. 5 samples were used for each experiment analysis, each with 5 pairs of traces.

Characterization

Trace Imaging and image processing is done using LEICA M165C Optical microscope and ImageJ software, respectively. We use the KEITHLEY 1100V SourceMeter in current sweep mode to record 100 data points per measurement for 4-wire resistance measurement. Thermal characterization is done on VOETSCH, Voetsch Industrietechnik, Germany

Statistics and data analysis

The measurements illustrated on ‘violin’ plot represents the density of the data. The respective mean and standard deviation values are displayed. The box box-and-whisker plot provides information on quartiles, mean within a certain range. The whiskers depict the standard deviation while, the outliers are represented with dots. Linear fit with prediction band are represented using 95% prediction interval.

RESULTS AND DISCUSSION

The hybrid printing platform enables the printing of 3D electronics on a single platform without any pre- or post-processing of either the polymer substrate or the conductive material. Features of conductive traces and their characterization are explained in the next section.

Printing resolution and dimensional accuracy

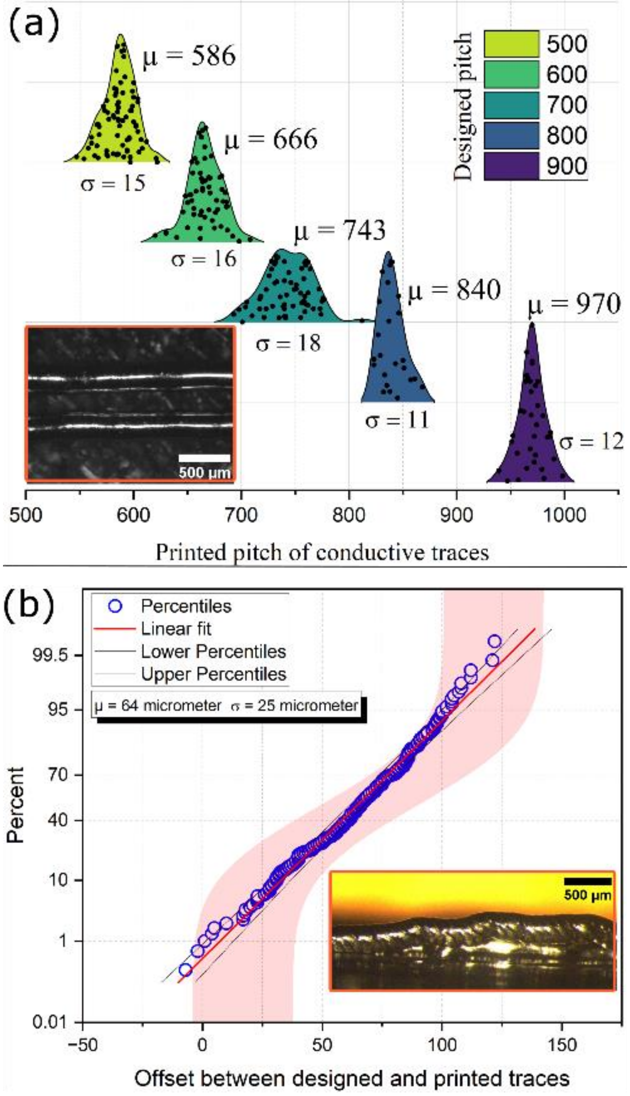

Figure 2: A) Trace pitch distribution curve, inset shows traces at MPP. μ=mean, σ=standard deviation. Y-axis=data count, B) Prediction curve for trace pitch printability.

Conductive traces were printed at a droplet deposition frequency of 18 Hz and droplet pitch of 100 µm. In order to guarantee the reliable printing, we achieved full continuity by optimizing the droplet pitch in previous work [9]. The metal droplet diameter printed on the polymer was measured at (289 ± 28) µm while single trace width was measured at (240 ± 12) µm[9]. To estimate the MPP with a 183 µm nozzle orifice, 90 mm long traces are designed at varying pitches from 500 µm to 900 µm with a step size of 100 µm. The measurement of MPP is taken from the center of one trace to the center of an adjacent trace. If none of the 25 printed traces makes contact with each other, the pitch is considered to be at its minimum. Printing resolution is demonstrated by MPP. The dimensional accuracy of the printing system is evaluated by comparing the designed MPP to printed MPP.

The normal distribution curves in Fig. 2a show uniformity in printed results for designed pitches 500 µm to 700 µm. It is worth noting that as the design pitch is increased, the curve becomes narrow. This could be due to the influence of polymer road printing. Nevertheless, the standard deviation of the printed trace pitch remained within 5% of the designed pitch. Trace printed at design pitch of 400 µm showed contact with neighboring trace and irregular printing. Inset image in Fig. 2b shows the side profile of traces printed at 400 µm design pitch. Therefore, the MPP was concluded at (586 ±15) µm. A sample trace at MPP can be seen as inset in Fig. 2a.

Next, we predict the dimensional accuracy of the hybrid printing by comparing the printed trace pitch to designed trace pitch. On applying linear fit to the designed pitch vs printed pitch data, we obtain a prediction of (64 ±25) µm as offset in the dimensional accuracy of the printing system, see Fig. 2b. Using the prediction curve, we can define the design parameter for trace pitch. This will benefit the designing of electrical traces and definition of semiconductor pin pitch for integrating 3D electronics on our printing platform.

Crosstalk in printed electrical traces

Prediction of trace pitch in previous section ensures no short in the electrical circuit. However, to ensure the usability of the traces as digital signals in electronic circuits, we estimate the influence of crosstalk between MPP. Crosstalk is electromagnetic coupling between closely spaced signal lines in dense circuits that limit the interconnect (electrical trace) performance [10]. The general crosstalk involves multiple traces and complex designs. In this work, we have simplified the design to two traces printed next to each other with (240 ± 12) µm trace width. We printed five different samples with five pairs of MPP, 90 mm long, and evaluated the trace gaps. The trace gap was measured to be (281 ± 15) µm, see Fig. 3a. We observed only 5% standard deviation in the trace gap, which affirms the trace shape fidelity, and reliability in trace dimensions for crosstalk analysis. Crosstalk analysis is done by passing the input signal through one trace (aggressor) and observe the effect on the neighboring trace (victim trace), see Fig.3b. The crosstalk is quantified using Eq. 1.

$$Crosstalk\ (dB) = 20\log\frac{\mathrm{V(victim)}}{\mathrm{V(aggressor)}} \qquad (1)$$

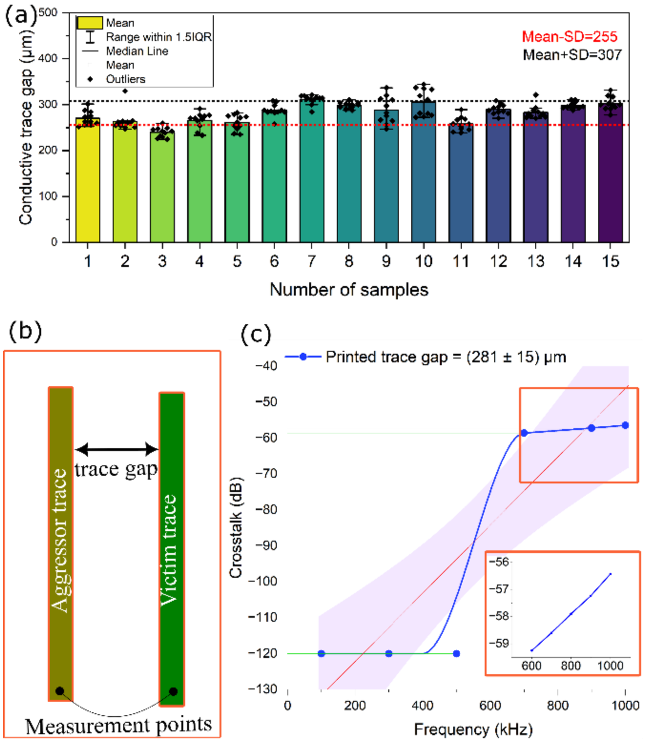

Figure 3: A) Printed trace gap distribution for MPP, B) Illustration of crosstalk measurement, C) Crosstalk (dB) for different signal frequencies.

Printed traces with trace width (240 ± 12) µm yielded a characteristic resistance of (285 ± 6) mΩ for a single trace. The input signal or aggressor signal is a sinusoidal signal with amplitude of 1000 mV. Upon applying the input signal, the waveform was observed at the victim trace by increasing the frequency from 100 kHz to 1000 kHz. Due to limitations on set-up, further examination at higher frequencies was not possible. Crosstalk remained in the range of -120 dB up to 600 kHz, see Fig. 3c. This can be regarded as noise since no clear waveform was observed. However, from 600 kHz to 1000 kHz, crosstalk was observed in small linear increments from -60 dB to -55 dB; see inset image Fig. 3c. Therefore, we can conclude that up to 600 kHz almost no crosstalk influence was observed for traces with low resistance of (285 ± 6) mΩ, trace width of (241 ± 12) µm, 90 mm long on a 600 µm thick PETG dielectric substrate (polymer). Such traces can be hypothesized to be suitable for real case testing of digital signal transmission within (100 – 600) kHz frequency range. Further analysis is needed to analyze the effect of trace gap on the crosstalk measurements, which is not in the scope of this work. A final assessment on printed trace performance for their use as digital signals is done by assessing the behavior under thermal conditions.

Thermal characterization of the printed traces:

Printed traces with defined printing parameters were observed for the effect of thermal shock on the trace width and trace resistance. For this test, the traces were subjected to two different temperatures, 60 °C and -40 °C, with a dwell time of 30 minutes each for 100 cycles. The higher limit of temperature is limited by the heat deflection temperature of PETG.

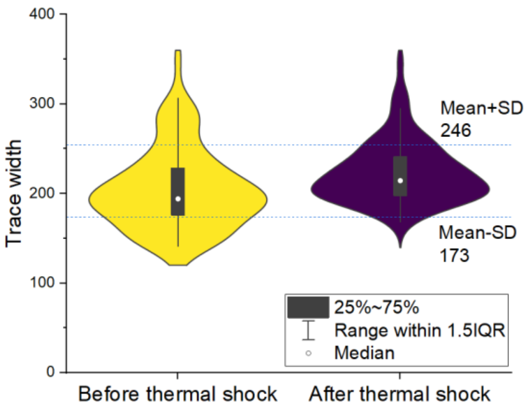

Figure 4: Influence of thermal shock on printed trace width

We observed that the mean trace width changed from (241 ± 12) µm to (251 ± 16) µm after thermal shock that amounts to 4.1%. The change in linewidth could be due to the influence of modification in the polymer substrate. We did not observe detachment of single traces from the polymer surface. This can be attributed to the good adhesion present between metal and polymer [9]. Therefore, we can hypothesize that this combination of metal and polymer printed via MMAM on our printing platform can find application for printed electronics in the market where operating temperature is less than 60 °C.

CONCLUSION

This work highlights the capability of our hybrid printing platform for 3D printed electronics in facilitating digital signal transmission.

Following conclusions are formed from the investigation:

- MMAM of 3D electronics is possible without additional sintering process or surface treatments on polymer.
- MPP of 2.4 times the printed trace width was possible for 90 mm long traces on MMAM samples. Additionally, we determined the prediction curve for ensuring 100% printing of any trace over the MPP.
- The crosstalk was negligible in the frequency range up to 600 kHz at 1 V input signal with the derived MPP; showcasing the applicability of the printed traces in additively manufactured electronics.
- Thermal characterization demonstrated trace width robustness with only 4.1% change likely influenced by substrate expansion and contraction.

Our one-stop printing platform highlights the practical viability of 3D printed electronics in real-world applications.

CONTACT

* Z. Khan, zeba.khan@imtek.uni-freiburg.de

REFERENCES

[1] H. Nassar and R. Dahiya, "Fused Deposition Modeling Based 3D‐Printed Electrical Interconnects and Circuits," *Advanced Intelligent Systems*, vol. 3, no. 12, 2021, doi: 10.1002/aisy.202100102.

[2] T. Rayna and L. Striukova, "The Impact of 3D Printing Technologies on Business Model Innovation," in Advances in Intelligent Systems and Computing, Digital Enterprise Design & Management, P.-J. Benghozi, D. Krob, A. Lonjon, and H. Panetto, Eds., Cham: Springer International Publishing, 2014, pp. 119–132.

[3] R. Dahiya *et al.*, "Large-Area Soft e-Skin: The Challenges Beyond Sensor Designs," *Proc. IEEE*, vol. 107, no. 10, pp. 2016–2033, 2019, doi: 10.1109/JPROC.2019.2941366.

[4] M. F. Farooqui, M. A. Karimi, K. N. Salama, and A. Shamim, "3D‐Printed Disposable Wireless Sensors with Integrated Microelectronics for Large Area Environmental Monitoring," *Adv. Mater. Technol.*, vol. 2, no. 8, 2017, doi: 10.1002/admt.201700051.

[5] J. A. Castrovilla, "The printed circuit board industry and innovations for the 1990s," *JOM*, vol. 41, no. 4, pp. 25–27, 1989, doi: 10.1007/BF03220194.

[6] J. Wiklund *et al.*, "A Review on Printed Electronics: Fabrication Methods, Inks, Substrates, Applications and Environmental Impacts," *JMMP*, vol. 5, no. 3, p. 89, 2021, doi: 10.3390/jmmp5030089.

[7] H. Merrow, J. D. Beroz, K. Zhang, U. P. Muecke, and A. J. Hart, "Digital metal printing by electrohydrodynamic ejection and in-flight melting of microparticles," *Additive Manufacturing*, vol. 37, p. 101703, 2021, doi: 10.1016/j.addma.2020.101703.

[8] N. Lass, L. Riegger, R. Zengerle, and P. Koltay, "Enhanced Liquid Metal Micro Droplet Generation by Pneumatic Actuation Based on the StarJet Method," *Micromachines*, vol. 4, no. 1, pp. 49–66, 2013, doi: 10.3390/mi4010049.

[9] Z. Khan, P. Koltay, R. Zengerle, S. Kartmann, and Z. Shu, "One‐Stop Hybrid Printing of Bulk Metal and Polymer for 3D Electronics," *Adv. Eng. Mater.*, 2023, doi: 10.1002/adem.202300922.

[10] L. B. Gravelle and P. F. Wilson, "EMI/EMC in printed circuit boards-a literature review," *IEEE Trans. Electromagn. Compat.*, vol. 34, no. 2, pp. 109–116, 1992, doi: 10.1109/15.135623.

AUTOMATIC DESIGN OF OPEN MICROFLUIDIC CHANNELS USING A ONE-DIMENSIONAL MODEL

T. Mitteramskogler[1] *, R. Ecker*[1] *, A. Fuchsluger*[1] *, R. Wille*[2]*, and B. Jakoby*[1]
[1] Johannes Kepler University Linz, Institute for Microelectronics and Microsensors, Linz, Austria
[2] Technical University of Munich, Chair for Design Automation, Munich, Germany

In the design of open microfluidic channels, one often has to follow simple design rules related to the channel's length, the minimal distance between neighboring channels and the maximum bending radius allowed. In addition, all the required components have to be connected, while staying within the chip's boundaries. While manually drawing microfluidic networks according to those specifications is possible, the creation of increasingly complex networks becomes more tedious. In the following, we show how the use of a routing tool [1] as shown in Fig. 1. for microfluidic chips can aid the design and present two applications thereof.

While the liquid flow in closed microfluidic channels can be driven by applying a pressure along the channel, the flow in open microfluidic channels is solely relying on surface energies. There, the open liquid surface allows for a wide range of possible morphologies, allowing the shape of the liquid front to differ from the bulk of the channel as shown in Fig. 2.

For fully established liquid flow, the effect of the liquid front can easily be separated from the bulk, so that the filling length L is proportional to the square root of the time t

$$L \sim \sqrt{t} \tag{1}$$

similar to Washburn's equation for closed microfluidic channels [2]. Here, the geometry of the cross-section of the channel is included in the proportionality factor. Employing this simple model, open microfluidic networks can be created.

This simple model depending on the cross-section of the microchannel can be used to create an open microfluidic device that measures the liquid contact angle between the substrate and a test liquid [3], [4]. To this end, several microchannels with different geometries have to be connected to a common reservoir as shown in Fig. 3. When the liquid to be tested is placed into this reservoir, the number of microchannels filled gives information about the contact angle between the liquid and the substrate. Due to the requirements on the maximum bending radius of the microgrooves and the requirement of the channels to have the same length for easier comparison, we employed our routing tool to design the microfluidic channels according to our specifications. This allows for easy adaption of the device, but also allows to easily expand the design to include more non-intersecting microchannels.

A second use-case of our tool lies in fabrication of high-resolution conductive tracks using open microfluidic chips as shown in Fig. 4. There, the open microchannels guide a nanoparticle ink, that acts as conductive path after subsequent drying and sintering. Similar to before, the length of the channel is of importance, since the maximal filling length is limited due to the evaporation of the solvent contained in the ink. Additionally, the radius of curvature has to be large enough to avoid that the liquid is drawn towards these sharp edges inside the channels. With our design tool specified electrical resistances between two contact points can be created through controlling the length of the conductive path and knowledge of the resistance per length. Similarly, more complex electrical networks can be created through integration of SMD (Surface Mounted Devices) as shown in Fig. 5.

Overall, we have shown how the routing tool can aid the design of open microfluidic chips on the basis of two illustrative applications.

Word Count: 542

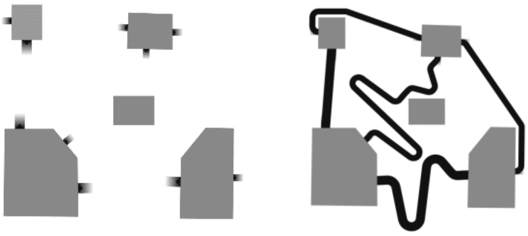

Figure 1: A routing tool for microfluidic chips connecting user-defined locations with microchannels having specified lengths, maximum bending radii and spacing between them.

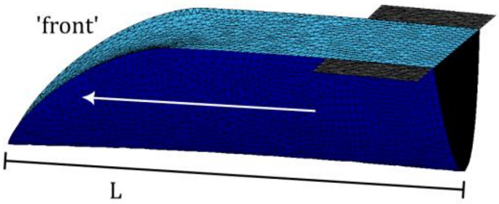

Figure 2: Surface Evolver simulation of a liquid (blue) inside a parabolic microchannel (partially shown, grey) connected to a pressure-free inlet (black). The flow-direction is indicated by the white arrow. Note, that the cross-section (black) after the liquid front remains constant for the entire channel length L.

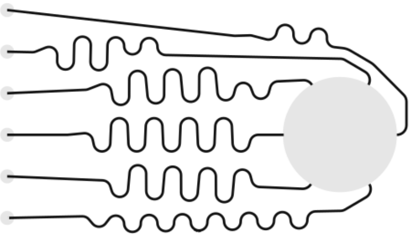

Figure 3. Design of a contact angle measurement device presented in [CITE] designed with our design tool. Note, that the meander structures ensure that every microchannel has the same length.

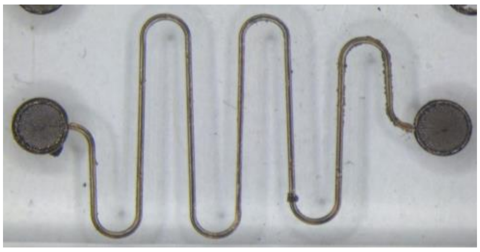

Figure 4. Conductive nanoparticle ink inside a laser-engraved open microchannel. After laser writing, the nanoparticle ink is placed inside the two reservoirs and fills the microchannel through spontaneous capillary flow. The meandering design ensures that the electrical resistance between those two points can be specified depending on the channel's length. Width of the image 15 mm.

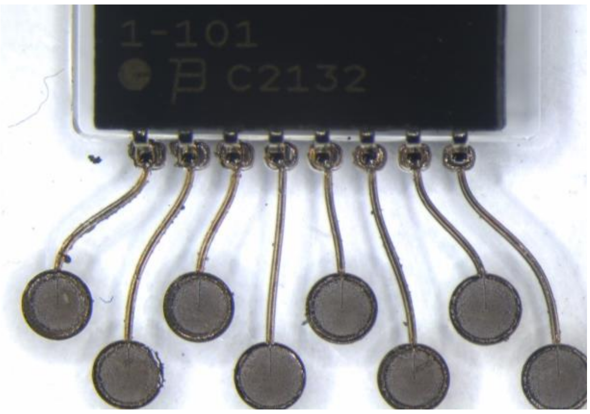

Figure 5. SMD integrated on a PMMA chip enabling the fabrication of complex electrical networks.

REFERENCES

[1] P. Ebner, G. Fink, and R. Wille, ‘Channel Routing for Microfluidic Devices: A Comprehensive and Accessible Design Tool’, *IEEE Trans. Comput.-Aided Des. Integr. Circuits Syst.*, pp. 1–1, 2022, doi: 10.1109/TCAD.2022.3179647.

[2] H. Bruus, *Theoretical Microfluidics*, Illustrated Edition. Oxford; New York: Oxford University Press, 2007.

[3] T. Mitteramskogler *et al.*, ‘An open microfluidic design for contact angle measurement’, *Micro Nano Eng.*, vol. 19, p. 100197, Jun. 2023, doi: 10.1016/j.mne.2023.100197.

[4] T. Mitteramskogler, K. Hingerl, and B. Jakoby, ‘A condition for spontaneous capillary flow in open microgrooves’, *Acta Mech.*, vol. 233, no. 10, pp. 3923–3939, Oct. 2022, doi: 10.1007/s00707-022-03289-1.